The University Of Sheffield.

Electronic and

Electrical Engineering

Electronic and Electrical Engineering

Doctoral Thesis

Design Simulation and Experiments on Electrical Machines for Integrated Starter-Generator Applications

Binan Lan

August 2018

Supervisors: Dr JAMES E GREEN and PROF. KAIS ATALLAH

A thesis submitted for the degree of Doctor of Philosophy

Design Simulation and Experiments on Electrical Machines for Integrated Starter-Generator Applications

Binan Lan

A doctoral thesis
In the department of
Electronic and Electrical Engineering
August 2018

ABSTRACT

This thesis presents two different non-permanent magnet machine designs for belt-driven integrated starter-generator (B-ISG) applications. The goal of this project is to improve the machine performance over a benchmark classical switched reluctance machine (SRM) in terms of efficiency, control complexity, torque ripple level and power factor. The cost penalty due to the necessity of a specially designed H-bridge machine inverter is also taken into consideration by implementation of a conventional AC inverter.

The first design changes the classical SRM winding configuration to utilise both self-inductance and mutual-inductance in torque production. This allows the use of AC sinusoidal current with lower cost and comparable or even increased torque density. Torque density can be further increased by using a bipolar square current drive with optimum conduction angle. A reduction in control difficulty is also achieved by adoption of standard AC machine control theory. Despite these merits, the inherently low power factor and poor field weakening capability makes these machines unfavourable in B-ISG applications.

The second design is a wound rotor synchronous machine (WRSM). From FE analysis, a six pole geometry presents a lower loss level over four pole geometry. Torque ripple and iron loss are effectively reduced by the use of an eccentric rotor pole. To determine the minimum copper loss criteria, a novel algorithm is proposed over the conventional Lagrange method, where the deviation is lowered from ± 10% to ± 1%, and the simulation time is reduced from hours to minutes on standard desktop PC hardware. With the proposed design and control strategies, the WRSM delivers a comparable field weakening capability and a higher efficiency compared with the benchmark SRM under the New European Driving Cycle, where a reduction in machine losses of 40% is possible.

Nevertheless, the wound rotor structure brings mechanical and thermal challenges. A speed limit of 11,000 rpm is imposed by centrifugal forces. A maximum continuous motoring power of 3.8 kW is imposed by rotor coil temperature performance, which is extended to 5 kW by a proposed temperature balancing method. A prototype machine is then constructed, where the minimum copper loss criteria is experimentally validated. A discrepancy of no more than 10% is shown in back-EMF, phase voltage, average torque and loss from FE simulation.

ACKNOWLEDGEMENTS

Foremost, I would like to extend thanks to my first supervisor Doctor James Green and second supervisor Professor Kais Atallah for their continuous encouragement and tremendous academic support throughout my PhD. study.

Similar, profound gratitude goes to Mr. Dave Snowden, Mr. Lawrence Obodo and Mr. Andrew Race for their wonderful assistance in prototyping and lab training.

I own my deep gratitude to my fellows of Electrical Machines and Drives Group at the University of Sheffield for their generous help and invaluable advice to my work.

I am also hugely appreciative to Federal-Mogul Controlled Power Ltd. for their sponsorship and aids to my PhD. study.

Finally, but by no means least, thanks go to my parents and wife for their almost unbelievable support. I am particularly indebted to my wife. I could not have accomplished this without her understanding, encouragement and unconditional support. They are the most important people in my world and I dedicate this thesis to them.

CONTENTS

List of Figures

List of Tables

List of Abbreviations and symbols

Acronyms

B-ISG	Belt-driven integrated starter-generator
CPSR	Constant Power Speed Ratio
CSRM	Classical switched reluctance machine
DSPM	Doubly salient permanent magnet machine
elec	Electrical
EMF	Electromotive force
EV	Electric vehicle
FE	Finite element
FP	Fully pitched
FRC	Fractional pitched classical
FRPM	Flux reversal permanent magnet machine
FSPM	Flux switching permanent magnet machine
HEV	Hybrid electric vehicle
ICE	Internal combustion engine
ICEV	Internal combustion engine vehicle
IM	Induction machine
IPF	Internal power factor
IPMNSM	Interior permanent magnet synchronous machine

ISG	Integrated starter-generator
MCFR	Mutually coupled fractional pitched
MC	Short pitched mutually coupled
mech	Mechanical
MMF	Magnetomotive force
MTPA	Maximum torque per ampere
MTPV	Maximum torque per volt
PF	Power factor
PM	Permanent magnet
PMaSynRM	Permanent magnet assisted synchronous reluctance machine
PMSM	Permanent magnet synchronous machine
RD	Radial direction
RMS	Root mean square
SIN	AC sinusoidal current
SPMSM	Surface mounted permanent magnet synchronous machine
SQ2	Bipolar square waveform a conduction angle of 120 electrical degrees
SQ3	Bipolar square waveform a conduction angle of 180 electrical degrees
SQ_x	Bipolar square waveform with a conduction angle of x electrical
SRM	Switched reluctance Machine
SynRM	Synchronous reluctance Machine

TD	Tangential direction
USQ	Unipolar square waveform with a conduction angle of 180 electrical degrees
VA	Voltage-Ampere
WRSM	Wound rotor synchronous machine

Roman letters

B	Flux density	M	Mutual-inductance
c	Fill factor	N	Number of turns per coil
e	Voltage induced by net flux	p	Number of pole pairs
F	Force	P	Power or Loss
H	Magnetic intensity	R	Resistance
i	Current	S	Cross sectional area
J	Current density	T	Torque
l	Length	V	Phase Voltage
L	Self-inductance	W	Energy

Greek letters

β	Angular displacement	λ	Flux
γ	Pole angle	μ	Magnetic permeability
δ	Angle between d-axis and net flux	ρ	Resistivity
ε	Saliency ratio L_d / L_q	σ	Stress

ζ	Rotor position	τ	Torque value
η	Conduction Angle	φ	Angle between current and voltage vector
θ	Load Angle	ω	Speed

Subscripts

a, b, c	Stator Phase A,B,C	min	Minimum
ag	Airgap	p	Peak
al	Axial	opt	Optimum
ave	Average	rad	Radius
b	Base	rbk	Rotor back iron
com	Common	re	Reluctance
cop	Copper	res	Resultant
d, q	d, q-axis	ripp	Ripple
e	Electrical	rp	Rotor eccentric pole radius
ew	End winding	rr	Rotor radius
exc	Excitation	rs	Rotor pole shoe
f	Rotor excitation field	rt	Rotor teeth
fun	Fundamental	rtd	Rated
fw	Field weakening	s	Stator
ini	Initial	sbk	Stator back iron

inst	Instantaneous	sbr	Stator bore radius
int	Interpolation	sf	Shaft
ir	Iron	sr	Stator outer radius
l	Loss	st	Stator teeth
m/mech	Mechanical	tan	Tangential
max	Maximum	VM	Von Mises
nor	Normal	0	Objective

1. Introduction

With a fast growing population and high demand on convenient transportation, increasing demands on vehicles has brought many challenges. Among them, environmental stress and high reliability on fossil fuels are the major concerns which have been widely expressed [1]. The main approach to a solution is the introduction of electrical propulsion system into conventional vehicles. Compared with conventional propulsion systems involving an internal combustion engine (ICE), an electrical propulsion system requires an electrical energy storage device (battery), an electrical-mechanical energy transformation device (electrical machine) and a bi-directional power train between them.

1.1 Research Background

1.1.1 Advantages of Electric Vehicle

Compared with conventional internal combustion engine vehicles (ICEV), the electric vehicle (EV) has the following advantages:

Firstly, it reduces the dependence on oil. Transportation accounts for one third of all energy usage [1], where oil is the main energy source. However, there is pressure to reduce oil utilisation due to decreasing reserves and overall increased demand. Studies have shown that half of the earth's oil has been consumed [2], and even the most optimistic estimation indicates the earths oil reserves will be depleted within this century [3]. The EV provides an alternative to oil, where electrical energy can be more widely used for transportation. The main sources for electrical power are shown in Figure 1.1.

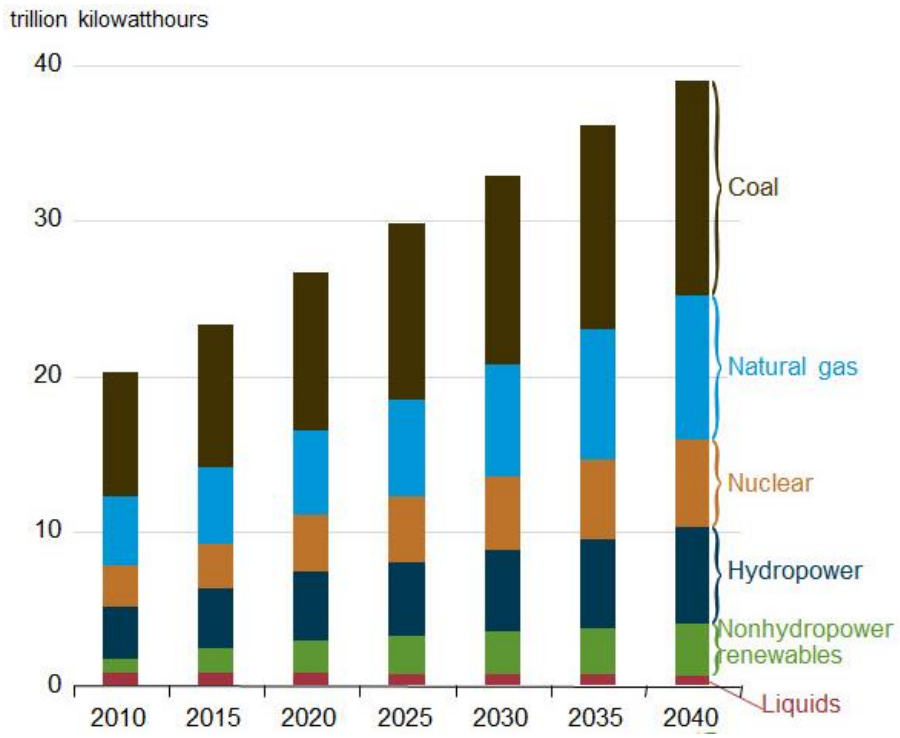

Figure 1.1 World net electricity generation by energy source from 2010 to 2040 [4].

Coal, natural gas, nuclear and hydropower are the main energy sources for electricity generation. Coal is estimated to have at least 100 years' worth of deposits for consumption without restriction [5], and it will be gradually replaced by cleaner and renewable energy sources thereby extending the time over which some coal can still be used. By using electricity in vehicles, the dependence of transportation on all fossil fuels will be greatly relieved.

The second advantage of EV is the increase in efficiency and decrease in energy consumption. Compared with the ICE, an electrical machine has a much higher efficiency with a wider operational range. The overall efficiency of the ICE is around 30%, and electrical machine is over 85% [6]. Despite this, EV shares a similar efficiency from crude oil to wheels as ICEV (15%-19% for ICEV and 14% to 20% for EV). With the use of new power line transmission technologies, this overall efficiency can be further increased [1, 7].

The third advantage of the EV is the reduction of pollution and carbon emissions. Carbon dioxide is a major cause of global warming and climate change. With electricity provided by nuclear, hydro, or other non-fossil power sources, carbon emissions from energy generation are

greatly reduced compared with crude oil refining [7]. It is estimated by the US Department of Energy that the total replacement of ICEV with EV will cut worldwide carbon dioxide emissions by half [1].

Pollution from increasing ICEV causes a large burden on the environment. This problem has two meanings: local pollution and overall pollution. First, the increasing pollutants from vehicles' exhaust fume is more severe in cities, where people and vehicles are both concentrated. Pollutants like carbon monoxide, nitrous oxides and particulates are harmful to human health. Electrical propulsion cuts waste fume emissions, alleviating the local pollution problem. Much of the emission problem is transferred to power stations in remote locations, where it can be more responsibly handled [7]. Second, in terms of overall pollutant emissions, it is estimated that a total replacement of ICEV with EV will slightly cut nitrogen oxides, and sulfur dioxide will be slightly increased. Other pollutants like waste oil and noise would be reduced [1]. To reduce overall pollution, cleaner power sources should be applied in electricity production.

1.1.2 Flaws of Electric Vehicle

Despite the promising advantages of the EV, it has never been considered as a rival to the ICEV until recently. The reasons for the greater success of the ICEV are understandable when we compare the features of batteries and gasoline.

The specific energy of gasoline for the ICE is around 9000 Wh/kg, whereas it is 30 Wh/kg for lead acid battery [7]. With the estimation of energy conversion efficiency of 20% for ICEV and 90% for EV, for the same power delivered by 1 kg of gasoline, 66.6 kg of batteries is needed. This low energy density problem severely restricts the cruising range of the EVs. Another major problem of battery is the long charging time and low cycle life. Fully charging the fuel tank for ICEV usually takes less than one minute, but fully charging battery usually takes several hours, making the EV less favoured for long journeys. Batteries also have a limited cycle life, so replacement maybe required before the end of the vehicle's life. To make the problem worse, the battery is usually expensive. For example, to give the same energy provided by 10 gal of gasoline, a lead acid battery of 2.7 tons is required, incurring a cost of about £8,000 [7].

Recent years, battery technology sees a greatly development with the wide implementation Lithium-ion battery [8]. Compared with lead acid battery, the power density, life cycle, charge time and life time cost have all been significantly improved [9] [10]. Despite a big improvement in EV technologies, the performance in the aforementioned area are still inferior compared with ICEV [11].

1.1.3 Hybrid Electric Vehicle: A Combination

The poor performance of electrical energy storage and high cost hamper the complete replacement of the ICE with an electric power train. Before these problems can be overcome, it is reasonable to utilize both electrical machines and ICE on the same vehicle to obtain some benefits of the electrical system and mitigate some of the problems of the ICE.

The hybrid electric vehicle (HEV) provides such a solution. An HEV is a type of vehicle that combines a conventional ICE system with an electrical propulsion system. By utilizing the high efficiency of the electrical system and the high power density of the gasoline, the fuel economy and dynamic performance of an HEV are both significantly improved over an ICEV [12]. In this way, the problems such as pollution, oil dependence and carbon emission of conventional vehicle are partially alleviated.

Hybrid systems can be categorized by the proportion of power provided by the electrical system as: micro hybrids, mild hybrid, full hybrid and plug-in hybrid [13]. Table 1.1 shows a common categorization standard for hybrid vehicles.

From table 1.1, micro to mild hybrid vehicles with integrated starter-generator (ISG) systems have the advantages of low cost, low weight and convenient implementation on a conventional ICEV. In an ISG system, a small electrical machine is used, assisting the ICE for starting, power boosting as well as energy recuperation. Since the electrical machine only contributes a small proportion of power, the size of the battery is usually small enough to be mounted on a conventional vehicle, and external battery charging is avoided [12]. Sometimes B-ISG are integrated in Full / Plug-in HEV as an additional power assistance.

Hybrids	Micro Hybrid		Mild Hybrid	Full Hybrid	Plug-in Hybrid/EV
	ISG Start/Stop	ISG Hybrid			
Engine	Conventional	Conventional	Downsized	Downsized	Downsized
Engine Motor Coupling	Belt Driven	Belt Driven/ Crank shaft	Belt Driven/ Crank shaft	Crank shaft	Crank shaft
Electrical Power (kW)	2-5	3-10	5-20	30-75	30-100
Operation Voltage (V)	12	12-42	60-200	200-600	
Fuel Economy Improvement	3-5%	5-10%	10-25%	25-40%	50-100%
Cost	Low		→		High
Examples	Fiat 500, SMART, Ford Focus		Toyota Prius	GM Volt	Nissan Leaf

Table 1.1. Hybrid vehicle types and features [13].

1.1.4 Rare Earth in Hybrid Electric Vehicles

The core of a hybrid electrical system is the battery and the electrical machine. The machine is the device that performs electrical-mechanical energy conversion. The performance of electrical machines can be evaluated in many ways, such as power density, torque density, efficiency, cost, etc. A high efficiency machine could increase the energy utilization and reduce overall emissions. A high torque or power density reduces the overall machine size for the same torque or power output, so the volume of the electrical system on an HEV can be reduced.

The invention of the electrical machine dates back to Michael Faraday. The development history over the intervening years has formed a trend of increasing power and torque density of machines with a reduction in cost, which has accelerated since the discovery and use of rare earth magnets. Electrical machines can be generally categorized into two types: permanent magnet (PM) machine, and non-permanent magnet machines. For a long time, non-permanent magnet machines dominated the industry [14]. The performance of permanent magnet machines was unsatisfactory due to the poor performance of the available PMs. The PM materials were usually aluminium iron (AlCoNi) magnets alloy or ferrite magnets. These materials have low maximum energy product and highly non-linear magnetization curve. The

performance of PMs took a big leap forward thanks to the advent of rare-earth samarium-cobalt magnets (SmCo) in 1960s, and Neodymium-Iron-Boron magnets (NdFeB) in 1983. Scientists discovered that these alloys have high remanence, high coercivity and a linear magnetization curve, bringing unique advantages in terms of power density, torque density, and efficiency in PM machines [15]. Specifically, NdFeB magnet material possesses an energy product about 2.5 times higher than SmCo magnet material and 7 - 12 times stronger than aluminium iron magnets [16]. Corrosion as well as limitation on the temperature of the PM can be overcome with addition of praseodymium (Pr), dysprosium (Dy) and terbium (Tb) [16]. Rare earth PM machines play an important part in the EV market nowadays [17]. They have greatly promoted the development of the EV industry, facilitating efficiency improvements and emission reduction [15].

1.1.5 Challenges for the HEV Industry

Along with the benefits previously outlined, reliance on rare earth magnets brings challenges, foremost among these is availability.

Besides EVs, rare earths play a major part in many other fields including domestic appliances such as smart phones, computers and air conditioners. It is also crucial in electricity production technologies including wind turbines and oil refineries [15, 18] .The fast development of these industries has added to the demand on the rare earth material like Nd and Dy, and further increase is predicted [16, 19].

In addition to the ever-increasing demand, the risk of near future supply shortages and cost fluctuation in rare earths are the most severe problems facing the magnet industry. China is the leading producer of rare earth materials. In 2008, 57% of the world's known deposits were inside China's borders and 97% of the world's rare earth material used in 2010 was mined there. In recent years, however, China has imposed a limit on rare earth exports due to issues such as environmental burden of extraction, smuggling, increase in domestic demand and political considerations, increasing the risk to the EV industry [18]. According to the 'US Department of Energy critical material strategy', Nd, Dy and Tb remain in the category of critical material

with high importance to clean energy, and high supply risk in medium term analysis (2015–2025) as shown in figure 1.2 [20]. The difficulties associated with supply and demand risks causing a significant increase in the price of rare earths for a period of time, which in turn adds to the cost of PM electrical machines. Figure 1.3 shows the price history of relevant rare earth oxides from 2010 to 2016 [21]. A prior investigation in 2010 [22], compares the prices of electrical machines used for vehicle traction, where a NdFeB PM machine costs 3.3 times more than a switched reluctance machine, and 1.7 times more than an induction machine. In the analysis, the rare earth PMs make up 70.6% of total PM machine cost.

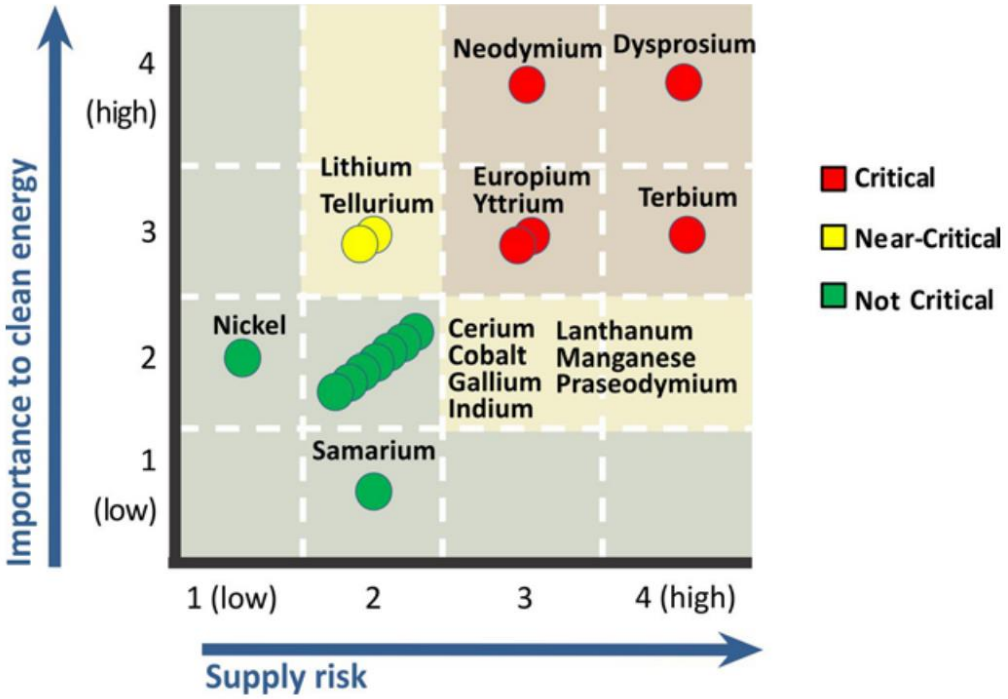

Figure 1.2. Medium term criticality matrix of rare earth elements from 'US Department of Energy critical material strategy' [20].

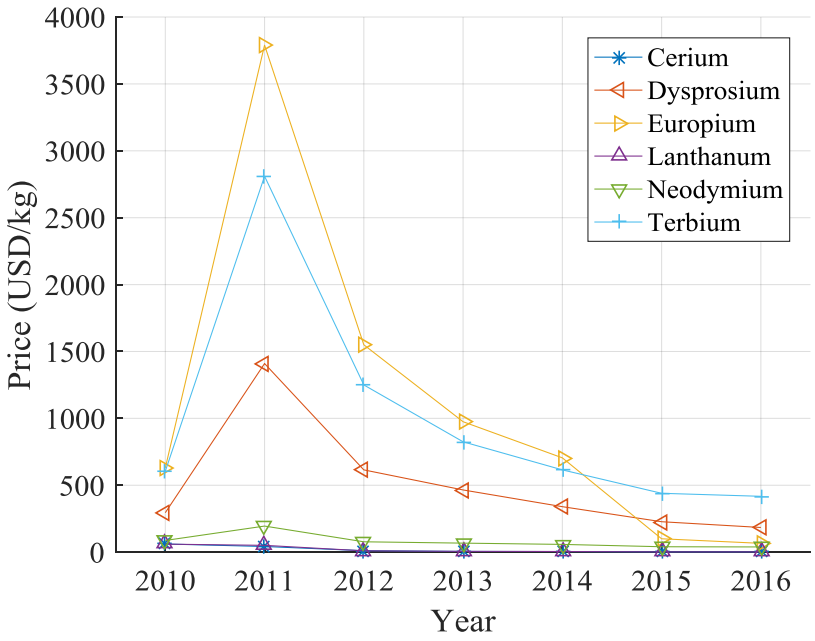

Figure 1.3. Historical rare earth oxides (Purity 99% min) prices from 2010 to 2016 [21].

The second challenge is the influence of temperature on rare earth PM. NdFeB is the most commonly used PM material, but neodymium magnets are very vulnerable to temperature increase, which cause coercive force and residual flux to reduce. A demagnetization characteristic of NdFeB Magnequench MQ2 magnets at various temperatures is shown in figure 1.4 [23]. The adding of dysprosium (Dy) helps to maintain coercive force, but maximum energy product decreases proportionally with the percentage of Dy used to replace Nd in magnet. It is estimated that in the next generation HEV with 200°C operation temperature, 40% of Nd needs to be replaced by Dy, resulting in a 40% smaller maximum energy product of PM compared with pure NdFeB magnet [15].

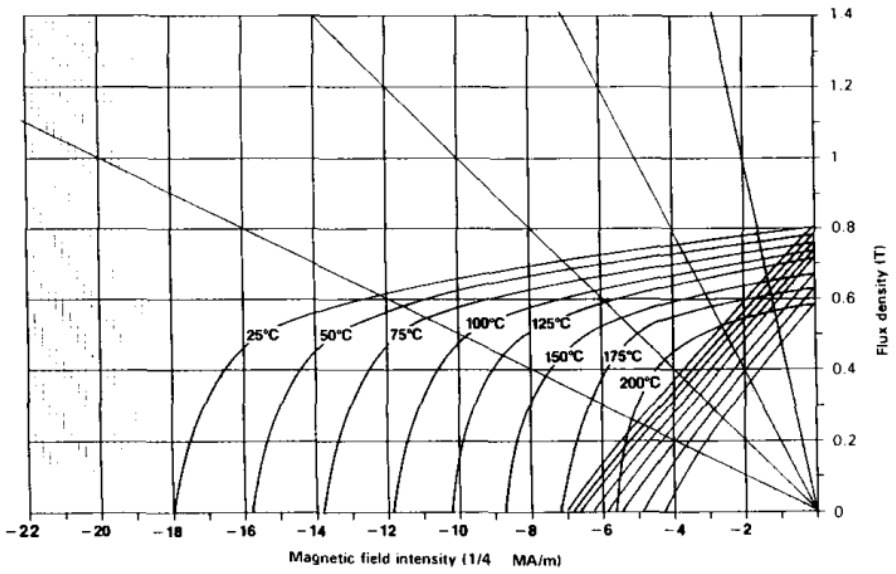

Figure 1.4. The demagnetization characteristics of NdFeB Magnequench MQ2 magnets at various temperatures [23].

1.2 Literature Review

From the prior section, the introduction of the integrated starter-generator provides increased fuel economy compared with ICE alone. This reduces pollutants, carbon emissions, and alleviates dependence on fossil fuels. Compared with EV, the ISG reduces the overall cost and avoids the reliance on the low energy density, high initial cost and long recharging time battery. However, manufacturing of electric machines often relies on the use of rare earth materials, which increases the cost and brings additional risk to the industry.

This section reviews the recent and archival literature that focused on the ISGs and electrical machines suited for ISG applications. Different types of machines are compared, where emphasis is placed on the requirements of rare earth PMs.

1.2.1 ISG System

ISG System introduction

The HEV has been vaunted as an effective solution for pollution problems caused by vehicle exhaust gasses [24]. An ISG is an electrical system that starts the ICE and generates electricity using only one electrical machine instead of two separate machines as in conventional vehicles. The concept of ISG was put forward in 1930s, but it took a long time to be realized because the

ISG motoring and generating modes have very different specifications, and the requirements for the power electronic system are challenging. Unlike the electrical system in an EV, an ISG is not designed to move the vehicle on its own, but assists its performance in several ways. A typical ISG system configuration is shown in figure 1.5 [25, 26].

An ISG has three main functions: electricity generation, stop/start, regeneration and power assistance.

Firstly, it replaces the AC alternator in a conventional vehicle, so the ISG is sometimes called integrated starter alternator (ISA). As a generator, it produces power for all of the electrical systems including lights, air-conditioning, radio, etc. Compared with a conventional AC alternator, the ISG has a higher efficiency, so the vehicle exhaust gas emissions are reduced.

Secondly, it allows complete stop of ICE when the vehicle stops, and restarts it when the vehicle starts moving. An ISG allows the vehicle to turn off the ICE completely when the vehicle comes to rest. To restart the ICE, the electrical machine provides the cranking torque and starting speed. This function is particularly useful in traffic or at lights, and is not generally possible with a traditional starter motor. Moreover, the machine in the ISG starts the engine faster and more quietly than a conventional starter, so a vehicle with an ISG system has a faster, quieter and more efficient restarting process than conventional vehicle [26].

Lastly, the ISG provides regeneration and power assistance. When braking is demanded by the driver, the ISG operates in regeneration mode. Instead of dissipating energy as heat in brake pads pressed onto metal disks, the mechanical energy is converted to electrical energy and stored in a battery or super capacitors. When acceleration is needed, the ISG operates in motoring mode, supplying additional power to the vehicle. As a result, the ISG improves vehicle efficiency and acceleration performance while reducing exhaust gas emissions.

In addition, as electrical machine is generally quieter than ICE, a reduction in noise and vibration of the overall drivetrain can be achieved. In certain cases, active damping of torque ripple and vibration noise throughout the entire powertrain is achieved by applying torque ripple

of electrical machine to counteract with the ripple generated by ICE [27], or rapidly switches ISG between motoring and generating mode [25].

Since the ISG can perform more functions than just starting and generating, vehicles with ISG systems are sometimes referred to as micro or mild HEVs.

ISG System Configuration

The electrical machine is the core of an ISG system that performs the conversion between electrical and mechanical energy. It is mechanically connected to the engine by either a belt or a clutch, and electrically connected to the battery via a power electronic inverter.

There are two common types of ISG configuration, belt driven and crankshaft. The belt driven ISG (B-ISG) uses a belt to couple the shaft of the electrical machine to the shaft of ICE. In the crankshaft ISG, shafts are directly coupled with one or more clutches and possibly a gearbox. The electrical machines for the two types of ISGs have different specifications due to their placement within the powertrain. Figure 1.6 shows diagrams of conventional separate starter/generator, B-ISG and crankshaft ISG. Compared with crankshaft ISG, the B-ISG has the following advantages. First, it can directly replace an alternator in a conventional vehicle without the need to redesign the system. Second, due to the damping effect of the belt, B-ISG system can tolerate a higher electrical machine torque ripple[25] [26]. Third, the belt transfer system allows the implementation of high speed and downsized machine without speed reducing gearbox between ISG and ICE. Fourth, the B-ISG allows direct drive of compressor without mechanical coupling with ICE.

Electrical Machine Requirements for ISG System

To achieve all the required functions of an ISG, the electrical machine needs to meet rigorous requirements. The main challenges and requirements for the electrical machine design in a ISG system are enumerated below [25, 26, 28-30]:

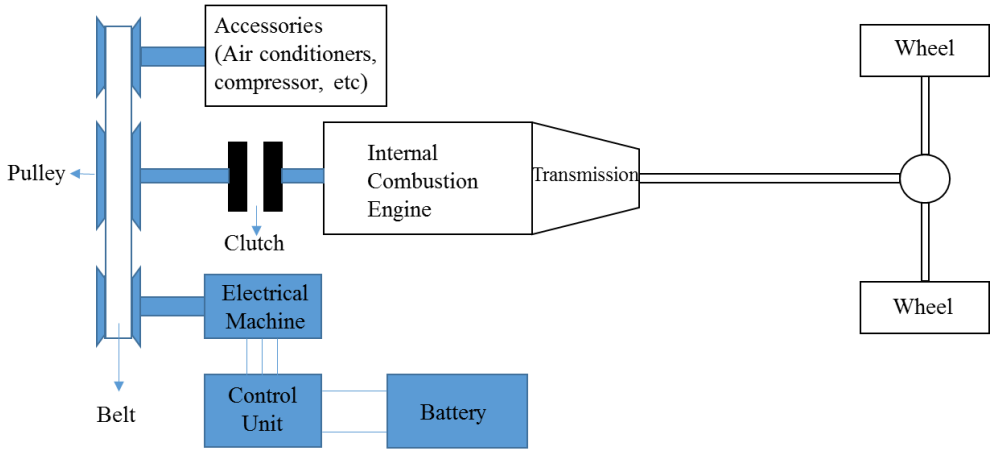

Figure 1.5. A typical belt drive integrated starter generator hybrid vehicle system [26].

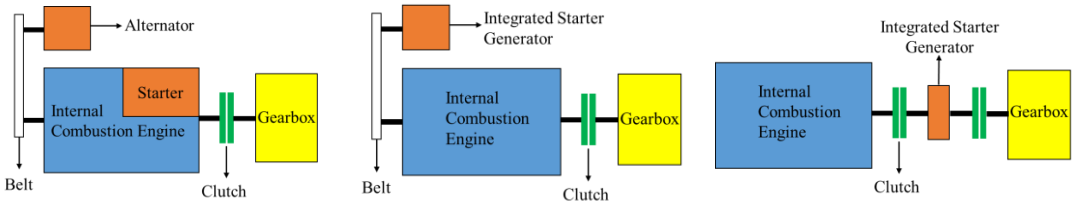

(a) *(b)* *(c)*

Figure 1.6. The diagram of (a) conventional separate starter and alternator system. (b) belt driven integrated stator generator system (B-ISG). (c) crankshaft integrated stator generator system [26].

Firstly, the limit of available voltage is the main restriction in machine design. The B-ISG system uses a vehicle mounted battery which, with aid of a power electronic system, supplies voltage and current to the machine. The preferred automotive voltages are 12 V, 36 V and 42 V. In a normal 42 V case, the available DC link voltage may run up to 48 V, and should not exceed 52 V [25]. This limitation calls for a high power factor and a wide speed range in machine to avoid excessive stator current, which increase copper loss and rating of inverter components.

Secondly, the B-ISG requires wide and efficient torque generation from engine start to red line speed. A typical belt ratio is between 2.3:1 - 3.2:1 [25]. For normal ICE operational speed, the speed range of the electrical machine starts from 0 to about 20000 rpm. From mechanical aspect, at high speed, a machine with a low rotor moment of inertia is favoured for its low centrifugal stress and fast response [31]. From electrical aspect, if the base speed is set at 2000 rpm, a constant power speed ratio (CPSR) of ten is required, suggesting a good field weakening capability is essential for the machine. Also, the power factor should be as close to one as

possible for good utilization of the limited voltage and inverter volume. The required efficiency in the normal range of operation (approximately 2000 – 10000 rpm) is often over 80% [25, 26].

Thirdly, a motoring overload capability is desired, where the machine is required to elevate the mechanical power above the nominal continuous power over the full range of motoring speed. This is sometimes called “boosting”. To overcome the engine static torque, the machine needs to provide 1.5 to 1.8 times the nominal cranking torque at low speed (up to 400 rpm), within a response time for of 1 - 3 seconds for B-ISG. At normal engine speed, extra torque is desirable for vehicle acceleration assistance, usually for between 3 and 15 seconds [25]. The time limit is sometimes imposed by thermal considerations.

A fourth requirement is an efficient continuous power generation from engine idle to maximum speed, with an overload capability. Specifically, the maximum demand electrical power output at engine idle speed is normally 35% to 60% higher than continuous generating output. For a short time (several minutes), the generator needs to provide about up to 30% - 40% more electrical power than continuous power rating for fast charging of batteries. The overall efficiency of generation should reach 80% [25].

A fifth requirement is the vibration caused by the ICE disturbances and deceleration fuel cut-off at low speed range should be reduced by the ISG. This requires ISG machine to have a low operational vibration and noise, and possibly a quick state switching strategy between motoring and generating for active noise damping [25].

Lastly, the machine needs good reliability in a harsh environment. Specifically, the machine is demanded to operate at a temperature range from -40°C to 125°C. If it is liquid cooled, the available coolant from the engine can go up to 150°C. This raises some challenges for a PM machine. Moreover, a long cycle life for stop/start and long operation time without malfunction is required.

Among these requirements for machines, the high power factor and good field weakening capability is the precondition for B-ISG applications, so these features should be emphasized

in machine selection.

1.2.2 Selected Machines

The introduction of rare earth PM raises many challenges into HEV industry. As a result, extensive investigations have been conducted into reduction and even elimination of rare earth materials in the electrical machines for HEV application. In this chapter, a variety of machine types both with and without rare earth PMs are investigated on an ISG applications.

Due to the rigorous requirements of the ISG, the machine needs to have the following features [22, 25, 32, 33]:

(1) High power factor
(2) Large CPSR with high efficiency
(3) High starting torque and low torque ripple
(4) Fast dynamic response
(5) Long cyclic life
(6) Good reliability and ability to work under unfavourable operating conditions
(7) Reasonable cost

The ISG systems currently on the market mainly use induction machines (IM) and permanent magnet synchronous machines (PMSM) [17, 30]. Although both machines meet the basic requirements for an ISG, each of them has their own drawbacks. As a result, there has been widespread interest in using alternatives to overcome these challenges in both machines and drive system for commercial use.

Table 1.2 lists the majority of machine types for traction and starter generator application in EVs and HEVs in the market. They are:

(1) Permanent Magnet Synchronous Machine (PMSM)
(2) Induction Machine (IM)
(3) Switched Reluctance Machine (SRM)
(4) Synchronous Reluctance Machine (SynRM)

(5) Wound Rotor Synchronous Machine (WRSM)

Figure 1.7 shows the typical cross-section configurations of these five types of machine. From the figure, PMSM, IM, SynRM and WRSM uses distributed stator windings, while SRM uses concentrated stator windings. Their typical drive inverter topologies are shown in figure 1.8. In this section, the merits and drawbacks of both machines and drives are discussed.

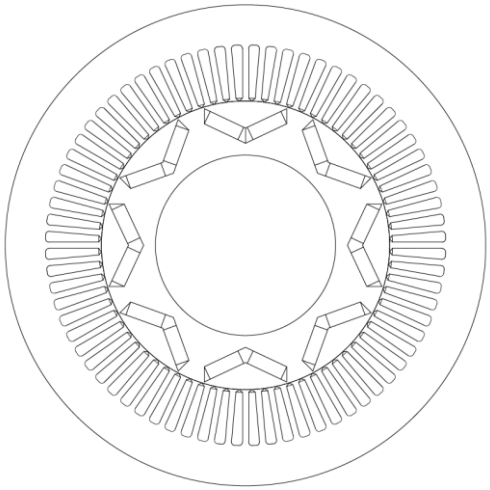

(a)

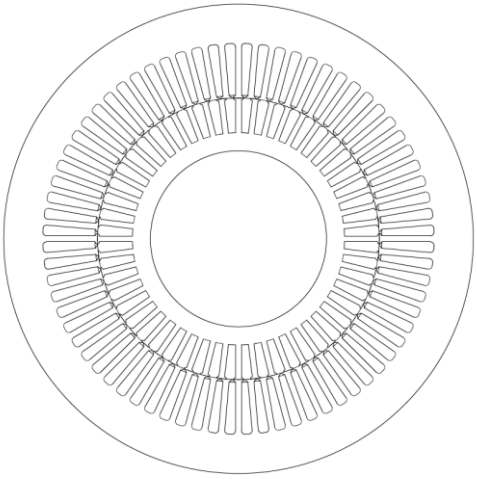

(b)

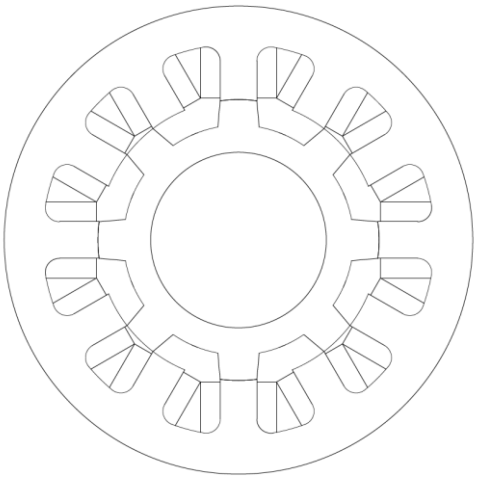

(c)

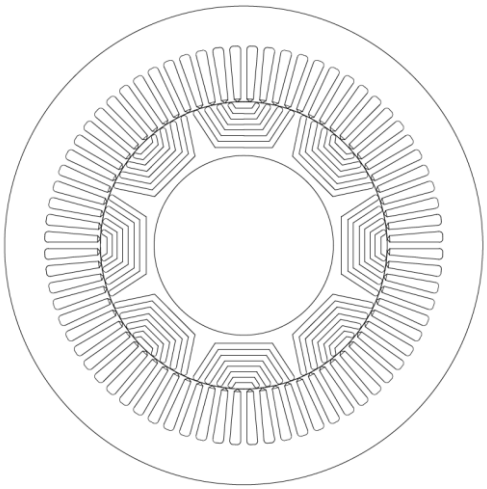

(d)

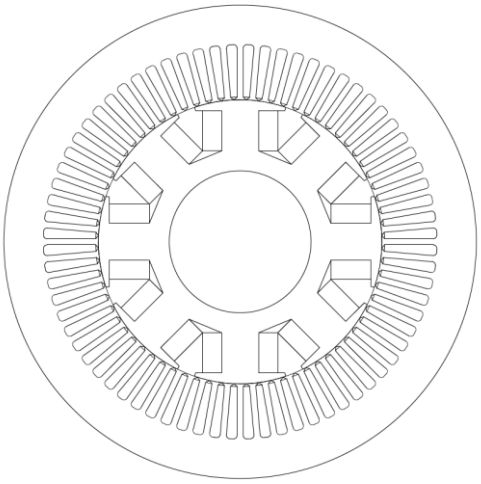

(e)

Figure 1.7. Cross-section configuration of different machine types (a) permanent magnetic synchronous machine (PMSM). (b) induction machine (IM). (c) switched reluctance machine (SRM). (d) synchronous reluctance machine (SynRM). (e) wound rotor synchronous machine (WRSM).

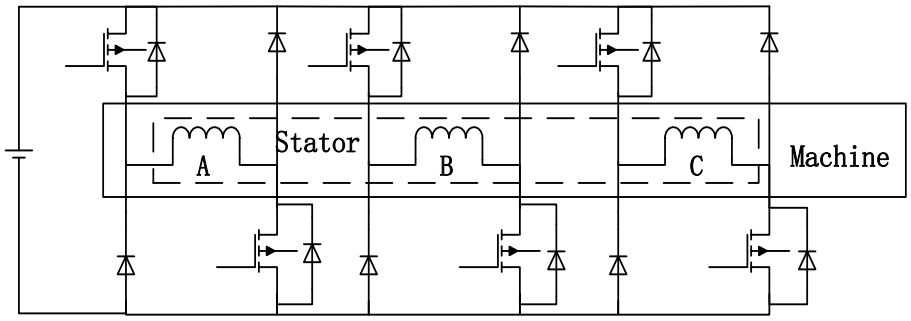

(a)

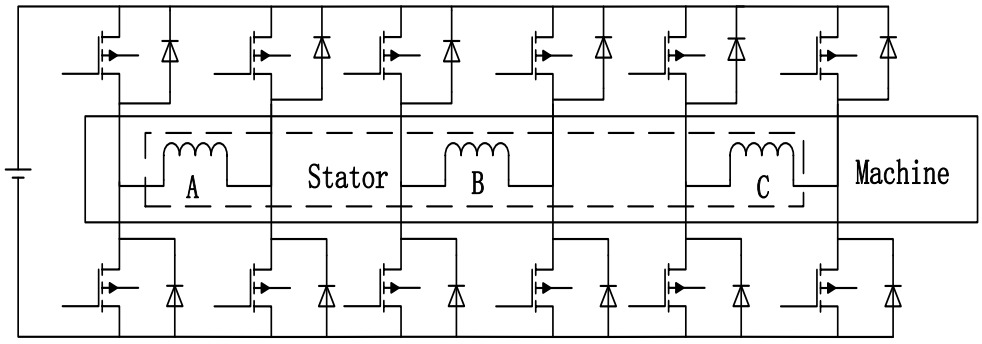

(b)

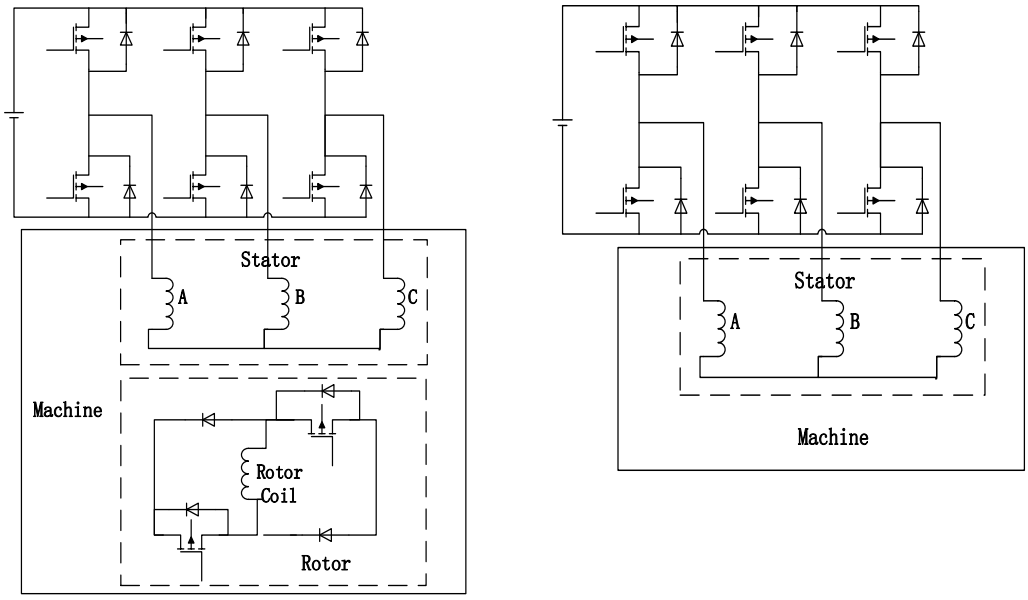

(c) *(d)*

Figure 1.8. Typical inverter topologies for different machine types (a) three-phase half bridge inverter for SRM; (b) three-phase H-bridge inverter for SRM. (c) three-phase AC inverter with separate rotor excitation for WRSM. (d) three-phase AC inverter for IM, SynRM and PMSM.

Vehicle Model	Machine	Vehicle Model	Machine
Kia Soul (S.Korea)	PMSM	**Honda Insight (Japan)**	PMSM
Toyota Prius (Japan)	PMSM	**Nissan Leaf (Japan)**	PMSM
Chevrolet Spark (USA)	PMSM	**BWM I3 (Germany)**	PMSM/IM
Ford Focus (USA)	PMSM	**Toyota Rav 4 (Japan)**	PMSM/IM
Daimler-Chrysler Durango (Germany, USA)	IM	**BWM X5 (Germany)**	IM
Tesla S (USA)	IM	**Chevrolet Silverado (USA)**	PMSM/IM
Renault Fluence Z.E. (France)	WRSM	**Renault ZOE (France)**	WRSM
Renault Kangoo Z.E. (France)	WRSM	**Renault Twizy (France)**	WRSM
Holden ECO (Australia)	SRM	**Peugeot-Citroen (France)**	DC
Toyota Crown (Japan)	Lundell		

Table 1.2. Machine types for different commercial vehicles [6, 22, 24, 32, 33].

Induction Machine (IM)

The cage induction machine is widely recognized as a strong candidate in EV and HEV traction applications owing to its mature technology, high reliability, low maintenance, low cost and

ability to operate in harsh conditions [24, 25, 28, 32-35].

A three-phase IM uses conventional AC inverter, which is inexpensive, reliable and widely applied in the automotive industry. The drive layout is shown in figure 1.8 (d). Vector control is commonly used for IM, where extended speed range for constant power operation is accomplished by flux weakening. The maximum CPSR is limited by breakdown torque, which commonly extends to 3 - 5 [25].

The major disadvantage of IM is the additional rotor copper loss. According to previous research, it makes the IM efficiency lower than an equivalently rated PM machine [22, 32] or SynRM [36], especially at high torque demand. Moreover, a low power factor is exhibited in IM under low load condition, and instability has been reported at high speed operation in ISGs application [35].

The advantages of the induction machine are summarised:

(1) Mature technology
(2) Low cost
(3) Robustness
(4) Able to work in a hostile environment

The disadvantages of the induction machine are summarised:

(1) High rotor copper loss
(2) Limited CPSR
(3) Low power factor under low load condition

Permanent Magnetic Synchronous Machine (PMSM)

PMSM is the major player in the EV and HEV market [17]. Its desirable characteristics include high efficiency, high torque density, high power density, good heat dissipation and a good CPSR.

The field excitation in a PM machine is provided by rare earth PMs like NdFeB, rather than coils or cage with flowing current as in the cases of the IM or the WRSM. The use of PM

eliminates the copper loss for field excitation and therefore increases efficiency. Rare earth PMs generate high flux density with low mass and volume compared with a coil [37], allowing an increase in torque and power density.

The conventional PMSM places PMs on the rotor, which can be sub-categorized into two types: surface mounted PMSM (SPMSM) and interior PMSMs (IPMSM). A typical IPMSM cross-section diagram is shown in figure 1.7 (a). IPMSM is favoured over SPMSM in HEV applications for the following reasons. First, the loss on the PM is much lower in IPMSM [38]. Second, despite that the SPMSM and IPMSM machine having comparable CPSR, the IPMSM machine has much higher overload capability at both low and high speed [39, 40]. Third, saliency in the IPMSM could further assist machine's overload ability [39]. Attempts to maximize the saliency leads to a combination of PM and SynRM, known as PM-assisted synchronous reluctance machine (PMaSynRM) [41].

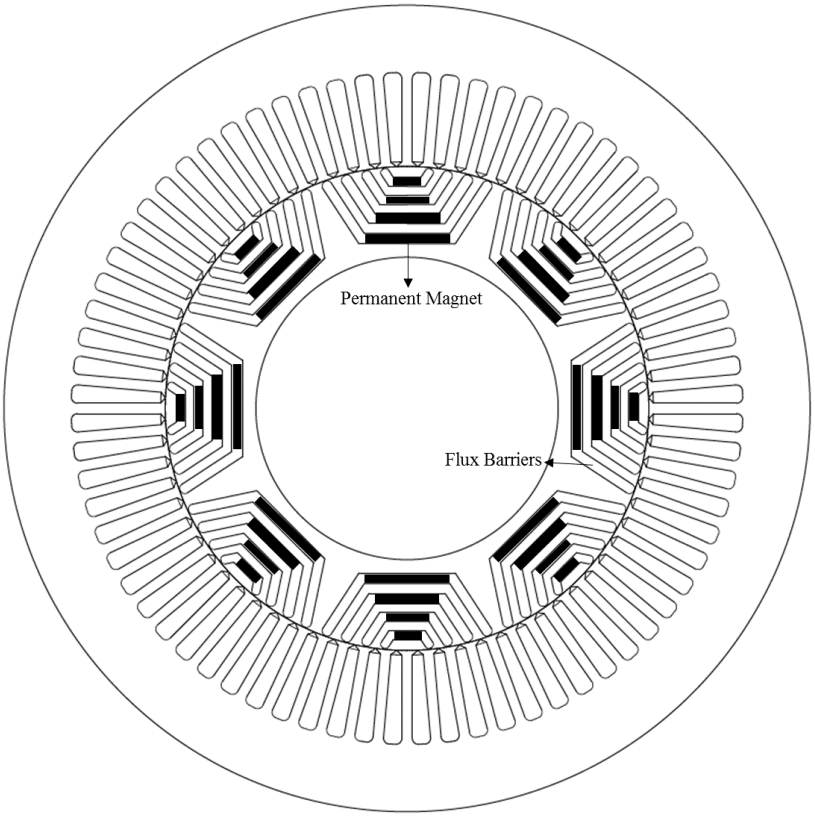

Figure 1.9. A typical PM-assisted synchronous reluctance machine (PMaSynRM) diagram for vehicle application

A typical PMaSynRM diagram is shown in figure 1.9. Owing to a high power factor, a large CPSR and a good overload ability, the PMaSynRM is suitable for vehicle traction applications [39, 42-45]. This machine also significantly reduces the requirement of PM material over SPMSM for the same power rating, resulting in a lower cost [37, 46]. The cost can be further reduced by replacing rare earth PMs with ferrites, as ferrites are ubiquitous and approximately one to two orders of magnitude less expensive than rare earth magnets. A compromise between good machine performance and cost can be found using carefully positioned ferrites [41, 43, 44].

Apart from PMaSynRM, newer geometries place PMs in the stator instead of the rotor [47]. These machines has been named doubly salient PM machine (DSPM) [48], flux reversal PM machine (FRPM) [49], and flux switching PM machine (FSPM) [50]. They have also attracted some attentions in EV industry [40]. Among them, a FSPM has been compared with a conventional IPMSM for EV application, where lower torque ripple, better rotor mechanical integrity, better thermal dissipation and lower copper loss is presented. However, this comes at a price of a much lower PM utilization [51]. A diagram of a typical 12/10 FSPM is shown in figure 1.10.

Like the IM, the conventional AC inverter is applied for a three-phase PMSM as shown in figure 1.8(d). Vector control is also readily applicable, allowing a simple field weakening operation [52].

Despite the merits of PM machines, there also have many drawbacks. Apart from the cost, the availability of rare earth magnet material and the sensitivity of PMs to temperature, another major problem is the difficulty in field weakening at high speed. To compensate for the PM magnetic field for field weakening, additional d-axis current is required. At high speed, this increasing demanding in current not only reduces machine efficiency and power factor, but also put PMs at risk of demagnetization [24]. Failure to provide such current result in high terminal voltage, where supplementary protection systems are required to disconnect the electrical machine to prevent damage to the vehicle and to ameliorate safety concerns. A low power factor

at high speed operation requires overrated power electronic components [53]. These problems restrict the field weakening capability of PMSM [24]. With proper design, an IPMSM can achieve a CPSR of 3 - 4 [33, 42].

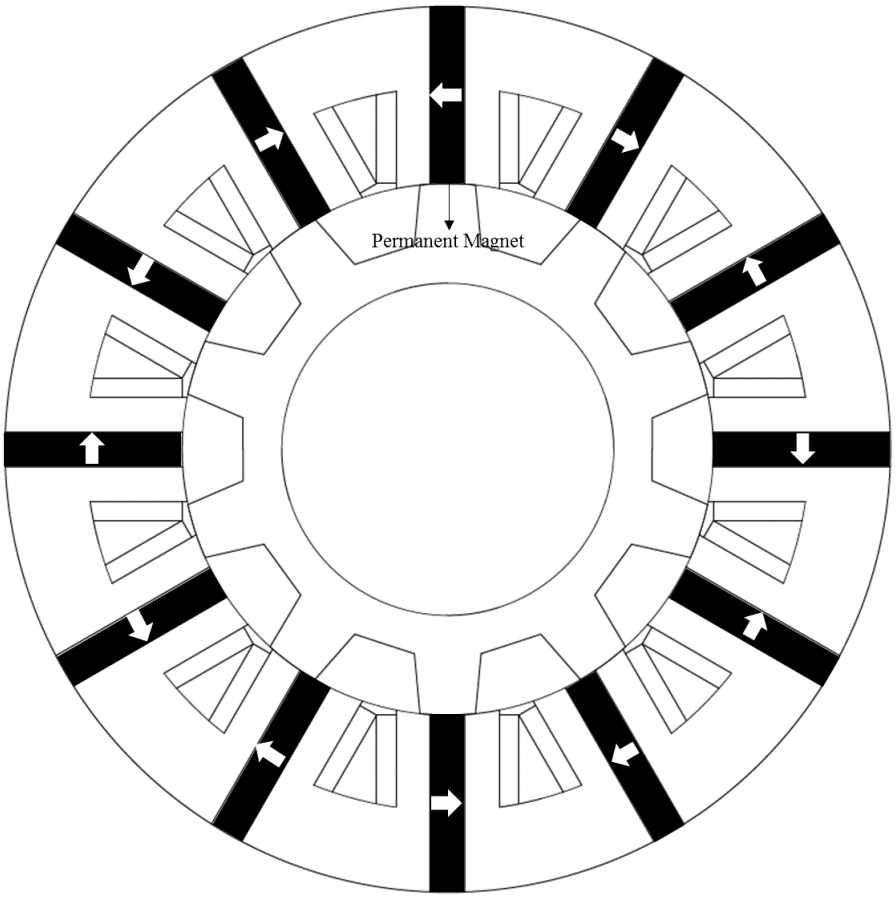

Figure 1.10. Diagram of a typical 12/10 flux switching PM machine (FSPM).

The advantages of PMSMs are:

(1) High power density

(2) High torque density

(3) High efficiency at low to medium speed

(4) Simple control

(5) Low maintenance

The disadvantages of PMSM are summarised:

(1) High cost

(2) Risk of demagnetization in flux weakening

(3) Sensitivity to temperature

(4) Difficulty in flux weakening in high speed operation

Switched Reluctance Machine (SRM)

The switched reluctance machine is a doubly salient machine with a concentrated short pitched winding. A cross-sectional diagram of a typical 12/8 SRM is shown in figure 1.7 (c), its winding configuration is shown in figure 1.11 (a).

The SRM is considered a strong potential contender in ISG applications [26, 27, 54-63], owing to its robustness, low rotor inertia, low cost, free from magnets and high reliability. From figure 1.7(c), salient structure is exhibited on both stator and rotor. Classical SRM (CSRM) uses concentrated winding with end winding span of a single tooth (short pitched) as illustrated in figure 1.11 (a) (b), as oppose to fractional pitched concentrated winding in figure 1.11(c), fully pitched concentrated in figure 1.11(d) and distributed winding in conventional IM, SynRM and PMSM.

According to previous research [22, 37, 46], the torque to volume ratio of the SRM is comparable to an IM, and significantly lower than PMSM. However, owing to the light weight of SRM from low consumption on winding and simple rotor structure, an excellent torque to mass ratio is presented.

With careful design and the use of a complicated control strategy based on a non-linear parameterization machine model, the classical SRM is able to deliver a much better field weakening performance than PMSM, IM and SynRM [62-64]. The simple robust rotor structure and low moment of inertia make it amenable to high rates of acceleration, high speeds and harsh environments [60]. The absence of magnets indicates a good capability to endure short time large currents, therefore a significant overload ability is possible. The classical SRM has separate windings and driving components, suggesting a magnetic separation between phases, so failure of one phase does not affect the performance of others. This feature increases the

reliability of SRM [31].

Despite all the merits, SRM has some inherent shortcomings. First, SRM suffers from a low power factor [65, 66]. This problem can be partially alleviated with carefully selected control strategies [67, 68]. Second, although the efficiency of SRM comparable to IM at low speed, major increase in iron loss compromised the SRM efficiency at high speed [22, 46]. Last, the SRM adopts highly complex control theory and drive, which is further elaborated below [62, 69-75].

Due to the highly nonlinear nature and the unipolar square current excitation, the theory of classical SRM is different from that of conventional AC machines. The general torque equation of SRM is shown in (1.5) as discussed later on in section 1.2.3. With independent phases, mutual inductances M_{xy} between phase x and y is close to zero. The phase x self-inductance, L_x is at its minimum when the stator and rotor poles are fully unaligned. With the rotor moves into alignment, inductance increases, $dL_x/d\zeta>0$. Phase x current, i_x is imposed as the rotor moves, producing positive torque. When L_x passes its maximum, $dL_x/d\zeta<0$, i_x should be reduced to 0 to avoid negative torque production. From the torque equation, the direction of torque is only related to $dL_x/d\zeta$, and not the direction of i_x.

To fully exploit the torque capability of the classical SRM, the excitation current is usually unipolar and rectangular in shape. The inverter for shaping this current with independent phases requires a minimum of two switches per phase, forming a half bridge as shown in figure 1.8 (a). Other possible inverter topologies have been extensively reviewed by R. Krishnan [76]. This requirement of a specially made inverter leads to a major problem in SRM applications, as there is a lack of a standardized power electronics modules that are readily available on the market [77]. This is in contrast with the AC drives market, where the standard three-phase voltage source inverter provides the standard solution. The lack of manufacturers offering SRM converter modules increases the cost of the drive system considerably, which erodes the low cost advantage of the SRM.

The operation of the SRM is regulated mainly by four parameters: switch turn on angle, switch turn off angle, current limit and voltage limit. Carefully selected turn on and off angles provide the machine with a wide speed range and a good efficiency. Below the base speed, the magnitude of current is restricted by power electronic components rating and machine thermal limitations. Above the base speed, due to the lack of DC voltage headroom, phase currents are naturally limited by phase voltage. To maintain a constant output power, the turn on angle should be advanced and the turn of angle should be adjusted accordingly so that a constant RMS current is fed into the machine phases. With the increasing speed, the advance angle also increases until the phase current enters continuous conduction mode, or single pulse mode.

From descriptions above, the classical SRM has an inherently complex control strategy, adding to the design difficulty and cost of the drive system. Moreover, an impulsive torque and a higher acoustic noise level are also presented compared with its competitors, which can only be mitigated by sophisticated design [27, 78, 79] or control strategies [80, 81].

To overcome the aforementioned challenges, prior researches suggests the implementation of different winding topologies on SRMs. The winding configurations can be categorized into two types.

(1) Changing the polarity of winding
(2) Including more teeth per coil

The first approach gives short pitched mutually coupled SRM (MCSRM) topology, which was first introduced by Li *et al* [82]. Compared with classical winding, the polarity of mutually coupled windings change alternately, as shown in figure 1.11(b). This winding topology is reported to produce a higher torque density and lower iron loss, resulting in an increase in overall efficiency [82, 83]. The MC winding also reduces the radial forces, so vibration and acoustic noise problem is mitigated [84]. Despite these merits, the MCSRM shows a larger torque ripple level than CSRM under AC sinusoidal current excitation. The problem can be relieved with an asymmetrical V-shape notch on rotor teeth. However, this approach only works

in unidirectional rotating application [85].

To achieve a better iron and coil utilisation, more than one stator tooth per coil is introduced as follows.

The fractional pitched SRM (FRSRM) was put forward by Y. Li and Y. Tang [86], where each coil is wound around two teeth, as shown in figure 1.11 (c). Compared with classical winding, this winding configuration significantly increases the machine torque under the same current density, at the price of a higher copper loss and a more expensive winding process.

The fully pitched SRM (FPSRM) topology was first introduced by B. Mecrow [87], where each coil is wound round three teeth, as shown in figure 1.11 (d). This winding produces a torque twice as great as classical SRM for the same current density. Despite the longest end winding of all configurations, an increase in torque per unit copper loss of between 30% and 90% can still be achieved [87].

The changes in winding configuration described above all utilises mutual inductance. From (1.5) in section 1.2.3, the direction of torque from mutual inductances is related to both direction and amplitude of the currents. This in principle allows the use of AC sinusoidal current excitation without large degradation in torque capability [88]. The implementation of the conventional machine drive and control theory has the potential to improve the performance of SRM in ISG applications in terms of noise level, system complexity and overall cost. However, there has been few literature focussing on using of new winding SRMs in EV applications [89]. To the author's knowledge, there appears no publications on the impact of the winding changes on other machine characteristics such as field weakening capability and power factor.

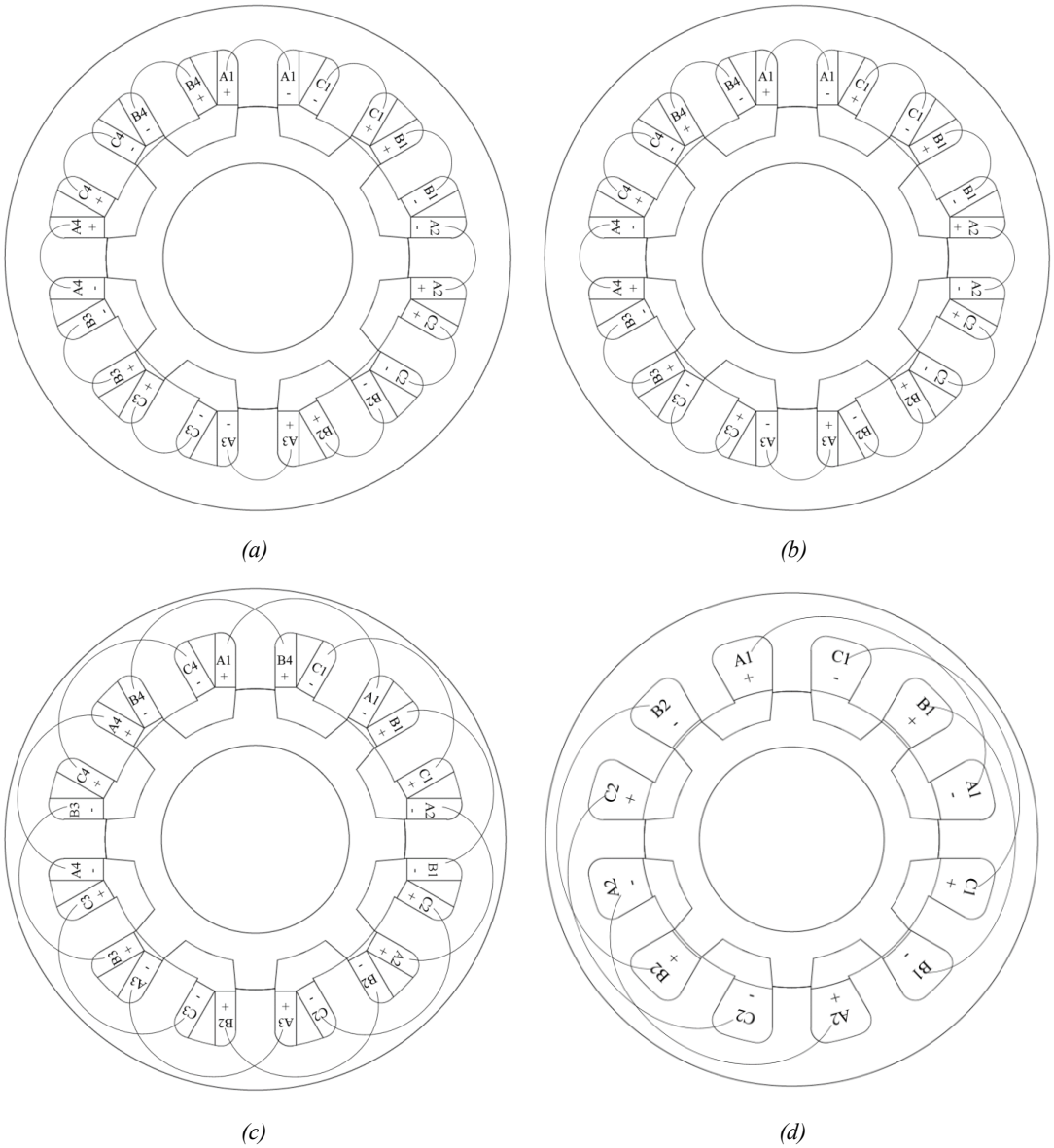

(a) *(b)*

(c) *(d)*

Figure 1.11. Winding layout of switched reluctance machine (a) Classical; (b) Short pitched mutually coupled (MC) [82] ; (c) Fractional pitched (FR) [86] ; (d) Fully pitched (FP) [90].

The advantages of the classical SRM are summarised:

(1) Low cost of machine

(2) Simple and robust structure

(3) Very high CPSR

(4) High speed operation ability

(5) Fast dynamic response

(6) Inherently fault tolerant operation

(7) Not sensitive to temperature

The disadvantages are summarised:

(1) High torque ripple
(2) Large acoustic noise
(3) Special and expensive inverter
(4) Complicated design and control theory
(5) Comparatively lower torque density than PMSM

Synchronous Reluctance Machine (SynRM)

The synchronous reluctance machine (SynRM) is considered another potential candidate for ISG applications [28, 33, 91, 92]. It has simple mechanical structure, no magnets, low cost, and subject to conventional AC machine theory.

Although the theoretical analysis of SynRM can be traced back to 1923 [93], the narrow stability region and low start up torque from the mains hampered its wide implementation. The situation was not changed until the availability of modern inverters and the advent of closed loop control [94]. Later studies investigated its performances under vector control and field weakening operation [95-98].

The SynRM has an operating principle similar to the traditional AC synchronous machine, but without the excitation windings on the rotor. Instead, the rotor is made highly anisotropic. The variation of reluctance produces a shifted flux that follows the direction of MMF in the airgap. As a result, the saliency of rotor is the key to torque production and field weakening operation [41, 95]. Influence of geometry on anisotropy has been extensively studied [99-101], where distributed stator winding with transverse laminated anisotropy (TLA) rotor of flux barriers (usually air) is most favourable due to its high anisotropy, simple structure and low rotor iron loss [102] [103]. The cross-sectional diagram of a typical transverse laminated rotor synchronous reluctance machine is shown in figure 1.7(d).

Compared with a SRM, the SynRM is less amenable to increases in torque to mass ratio by

design optimization, but the near sinusoidal MMF produced by the stator windings provides smooth torque with lower ripple. The rotor structure of the SynRM is not as mechanically strong as an equivalent SRM, limiting its operational speed. SynRM also has a simpler control algorithm and cheaper power electronics drive, reducing the cost and complexity of the overall system [91, 100, 104]. Compared with an IM, the SynRM is superior in torque density and efficiency due to lower losses on the rotor. The absence of rotor copper loss also means that heat dissipation in the rotor is less troublesome [34, 36, 105].

Despite the merits, the low power factor and limited field weakening capability of SynRM hampers its wide implementation in HEV applications [91]. The power factor of SynRM is inherently lower than the IM [36], and the CPSR of SynRM is usually reported less than 1.5 [34, 36, 91, 106]. Several attempts have been made to improve these shortcomings, including reintroducing PMs [41, 43, 44] and on-line reduction of stator winding turns [33].

The advantages of the SynRM are summarised:

(1) Low cost
(2) High efficiency
(3) Not sensitive to temperature
(4) Simple control theory
(5) Simple structure

The disadvantages of the SynRM are summarised:

(1) Low power factor
(2) Low CPSR

Wound Rotor Synchronous Machine (WRSM)

The wound rotor synchronous machine is another potential candidate for HEV applications. Previous simulations and experiments show promising performances in terms of efficiency, field weakening capability and power factor, where a theoretically unity power factor and unlimited CPSR is possible [46, 107-111]. The machine has been successfully implemented by

Renault on their EVs[112].

The WRSM uses well established technology [46]. A distinctive feature of the WRSM is the DC field winding on the rotor. To make room for rotor coils, the rotor usually has salient poles, where large pole shoes are presented to retain the coils and improve airgap flux distribution. A 3D drawing of the wound rotor is shown in figure 1.12 (a). The stator of conventional WRSM is similar to the IM. Like the PMSM, IM or SynRM, the WRSM adopts conventional AC machine theory and AC inverter. The absence of PMs means the WRSM has a low cost rotor, and is not sensitive to temperature. The cross-section diagram of a typical eight-pole WRSM is plotted in figure 1.7 (e).

To excite the machine, additional components are required, usually consists of carbon brushes, slip rings and a DC/DC chopper to regulate the excitation current. The inverter and DC/DC chopper layout is shown in figure 1.8 (c). Figure 1.12 (b) shows a 3D drawing of the slip rings and brushes. These components are based on mature and reliable technologies, which are commonly used in conventional ICEV alternator without major concerns of malfunction issues. It also does not represent an increase in the drive cost [107]. However, the introduction of slip rings and brushes could cause problems such as wearing and dust formation, affecting the life span and reliability of machine [113].

The WRSM is often compared with the IPMSM in EV propulsion applications. D. G. Dorrell conducted a detailed comparison between the WRSM and the IPMSM applied to the 2004 Toyota Prius [108]. The same rotor structure is used on both the IPMSM and the WRSM with modifications to accommodate rotor winding. At base speed, rotor winding produces four times higher copper loss than stator winding to provide the same excitation field as in the IPMSM, reducing the overall efficiency from 90.4% to 73.0%. By optimizing rotor current and geometries, an efficiency of 86.0% was achieved, which is comparable to an IM, but still lower than an IPMSM. Similar results have been reported by G. Friedrich [53, 111], where, at low speed, the WRSM suffers a significantly lower efficiency than an IPMSM.

Despite this, the WRSM delivers a comparable or even higher efficiency than IPMSM at high speed and low power. This advantage is brought by an extra controllable excitation flux, where active excitation flux weakening reduces stator and rotor copper losses in deep field weakening region. Another advantage brought by the controllable excitation is the near unity power factor [53, 107]. Compared with IPMSM, the power factor of WRSM is much higher under field weakening operation, so a reduction in the VA ratings of power electronic components is possible. With field oriented control, a fast dynamic response is achieved [111, 114], and by increasing current in both the stator and rotor, a good overload ability is realized [53, 107].

To access WRSM's high efficiency and wide speed range, the machine requires careful design and control. Research by D. G. Dorrell [108] shows the machine efficiency is affected by the balancing between rotor and stator current and rotor winding area, but this work focuses only on the rotor design. Other applications emphasize only on control strategies [53, 107, 109, 112]. There appears very limited report on the design procedure of the WRSM for optimum efficiency with consideration of both stator and rotor geometries, currents, pole pairs, etc.

Under the d-q frame, the WRSM operation is controlled by stator currents i_d, i_q, and an extra parameter, the rotor excitation current, i_f. Calculation of these parameters leads to different objectives such as maximum power factor [107, 115] or constant power operation [116] but, the most widely investigated objective is minimum loss operation.

Minimum loss operation has been successfully implemented in vehicle traction application [109, 111, 112], but limited details on the solution process were provided. A maximum torque per ampere (MTPA) algorithm was proposed with gradient decedent method [117], but the study did not consider field weakening operation. Ferrari's method has been applied by solving the intersections between voltage ellipse and torque hyperbola [115], but it only considers the circumstance where the machine operates on voltage constraints. The most extensively investigated approach is the Lagrangian method, which provides a promising solution to the minimum loss operation problem.

The accuracy of the Lagrangian method is dependent on the machine parameters such as λ_d, λ_q, L_d and L_q. Since the WRSM is susceptible to saturation and cross-saturation [118, 119], these parameters are highly dependent on i_d, i_q and i_r [115]. Failure to consider such effects adds to the complexity of the minimum loss control algorithm [120]. However, despite the widely reported Lagrangian method, the description of these parameters are either linear [121], or not clear [53, 111, 122-124].

To the author's knowledge, the only detailed description of accurate numerical models of λ_d and λ_q are proposed by Jeong, Kim, Nam and Kim based on least squares method (LSM) [125]. In this method, tables of pre-acquired flux data are obtained from either experiments or from finite element analysis. The numerical models are described in the form of a Vandermonde matrix, where the coefficients are evaluated using the least squares fitting procedure. This approach has two major drawbacks. Firstly, the resultant models are extremely complicated. Secondly, the approach inevitably introduces deviations between the models and the fitted data. A detailed analysis of the Lagrangian approach based on the aforementioned LSM is conducted later in section 5.1.

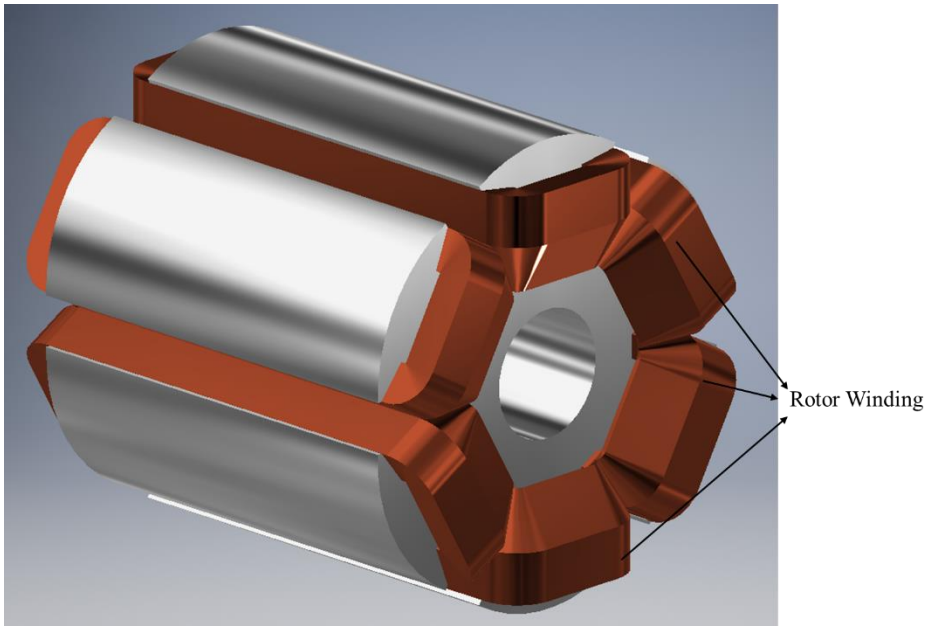

(a)

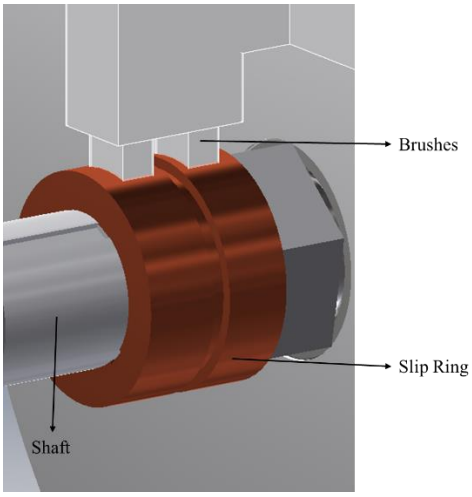

(b)

Figure 1.12. 3D diagram of (a) rotor structure and (b) brush and slip ring of wound rotor synchronous machine (WRSM).

To sum up, the advantages of the WRSM are:

(1) Low cost rotor

(2) High power density

(3) High efficiency at high speed

(4) Very high CPSR

(5) High power factor

(6) Simple field weakening

(7) Not sensitive to temperature

The disadvantages of the WRSM are:

(1) High rotor mass and rotor moment of inertia

(2) Sliding contacts reduces reliability and limits speed

(3) Low efficiency at low speed compared with PMSM

(4) Difficulty in optimum control criterion determination

Summary

Table 1.3 lists a comparison of each machine type discussed herein in terms of the key features from an B-ISG applications perspective. Since field weakening capability and power factor

outweigh the importance of other factors, they play more important role in the overall ranking of machine.

From the table, PMSM and WRSM has the most favourable features, followed by IM and SRM. SynRM is the least capable candidate. To be specific, the PMSM excels at torque density and efficiency, but there are major drawbacks in field weakening, cost and temperature sensitivity. The WRSM delivers a good overall performance, with some flaws in reliability. The IM uses highly mature and reliable technology, but has weakness in field weakening capability, power factor and efficiency. The SRM has high reliability and low environmental sensitivity, but suffers from power factor, noise, efficiency and cost issues. The SynRM delivers the poorest field weakening performance of all, but it has the lowest overall cost.

Item	IM	PMSM	SRM	SynRM	WRSM
Field Weakening Capability	o	+	++	-	++
Power Factor	o	+	-	-	++
Torque Density	-	++	+	o	+
Temperature Sensitivity	+	-	+	+	+
Reliability	+	o	++	+	-
Noise	+	+	-	+	+
Efficiency	o	++	+	-	+
Machine cost	+	-	++	++	o
Power Electronics Cost	++	+	-	++	o
Overall ranking	+	++	o	-	++

*'++': Very Good; '+': Good; 'o': Average; '-':Poor.

Table 1.3. Machine comparison for important features.

1.2.3 Machine Modelling

Classical Switched Reluctance Machine

To solve the electromagnetic problem in electrical machine, Maxwell's equations in the geometric region are applied with certain boundary conditions, where magnetic potential vector, A_n, is introduced. The equation between current density and magnetic field is:

$$\nabla^2 \overline{A} = -\mu \overline{J} \tag{1.1}$$

To solve (1.1) in for the case of an CSRM, several methods have been developed. An analytical method was introduced by A. V. Radun [126, 127], where, with complicated calculations, valid equations are derived for an analytical magnetic flux model linked by the rotor and stator at any position. Based on these flux equations, inductances, co-energy and torque are calculated.

This method shows major drawbacks, where the omission of saturation and leakage flux in an analytical model results in a large underestimation of the flux compared with finite element methods. Moreover, the calculation is very complicated even for a simple geometry, which requires evaluation with a computer.

Another common used way is the flux tubes method [128]. In this approach, the air between rotor and stator is divided into small imaginary tubes. Assuming the flux is evenly distributed in each tube, the tubes can be simplified as magnetic circuits. In a magnetic circuit, the MMF (1.2) is defined by number of turns, N, and current, i, which are balanced to magnetic reluctance, R_m and flux linkage, λ.

$$MMF = Ni = \lambda R_m \tag{1.2}$$

Magnetic reluctance, R_m is derived from the material B-H curve, length and cross section of flux path, as shown in (1.3).

$$R_m = \oint_l \frac{1}{\mu} \frac{dl}{S} \tag{1.3}$$

where μ is magnetic permeability, S is cross section of conductor and dl is an infinitesimal length in the parallel to the direction of the flux.

In flux tubes analysis, an initial stator pole flux density, B_{ini} is selected, from which the flux densities at each section of the circuit can be determined. Using the *B*-*H* curve, the magnetic field intensity *H* in all sections are calculated, giving the result on the right hand side of (1.2). It is then used to compared with the left hand side, forming an iterative process for *B* until certain precision is reached. Then all flux tubes are considered together and the magnetic flux distribution is determined. This method is more accurate than the analytical method but the flaws are still manifest. First, in each flux tube, variation in flux density and local saturation are neglected. Second, proper division of space into tubes is required in advance. Any irregular shaped rotor or stator pole can make tube division complicated. Last, mutual flux cannot be evaluated.

Compared with the approaches above, finite element (FE) analysis provides a more accurate prediction. In an FE model, the domain under investigation is divided into small areas, or 'meshes'. The density of each mesh can be adjusted for different accuracy requirements. Then (1.1) is solved on each mesh element based on finite difference method to achieve a predefined accuracy.

Altair Flux 2D/3D is a powerful FE analysis tool marketed by Altair. Altair Flux provides both magneto-static and transient analysis modes. In static analysis, each computation step is independent, where the electric field is considered static, and the magnetic field is considered constant. In transient analysis, step time is introduced, and the changing rate of electric and magnetic field between computation steps are considered, allowing the evaluation of voltage induction and iron loss, etc.

Altair Flux predicts torque using a virtual displacement method, where co-energy, W_c, is obtained in (1.4) from three phase currents, $\bar{i}$, and three phase inductances, $\bar{\bar{L}}$. Then using (1.5), torque is derived from the change of W_c with respect to rotor positon, ζ.

$$W_c = \int \bar{\bar{L}}\bar{i}d\bar{i} = \frac{1}{2}\bar{i}^T\bar{\bar{L}}\bar{i} \tag{1.4}$$

$$\bar{L} = \begin{bmatrix} L_a & M_{ab} & M_{ac} \\ M_{ab} & L_b & M_{bc} \\ M_{ac} & M_{bc} & L_c \end{bmatrix}$$

$$\bar{i} = \begin{pmatrix} i_a & i_b & i_c \end{pmatrix}^T$$

From (1.5), torque is generated from the three phase currents and the rate of change of self and mutual inductances with respect to rotor position.

$$T = \frac{\partial W_c}{\partial \zeta} = \frac{1}{2}\frac{dL_a}{d\zeta} i_a^{\,2} + \frac{1}{2}\frac{dL_b}{d\zeta} i_b^{\,2} + \frac{1}{2}\frac{dL_c}{d\zeta} i_c^{\,2} + i_a i_b \frac{dM_{ab}}{d\zeta} + i_b i_c \frac{dM_{bc}}{d\zeta} + i_c i_a \frac{dM_{ca}}{d\zeta} \qquad (1.5)$$

Synchronous Reluctance Machine

Doubly salient reluctance machines excited with sinusoidal current may be treated as a conventional synchronous reluctance machine (SynRM) [88, 129], where the stator current *i* and phase flux λ are decomposed to a dq axis frame fixed on the rotor. Figure 1.13 (a) illustrates a phasor diagram of a SynRM in steady-state and in the synchronous reference frame. Figure 1.13 (b) shows its equivalent circuit.

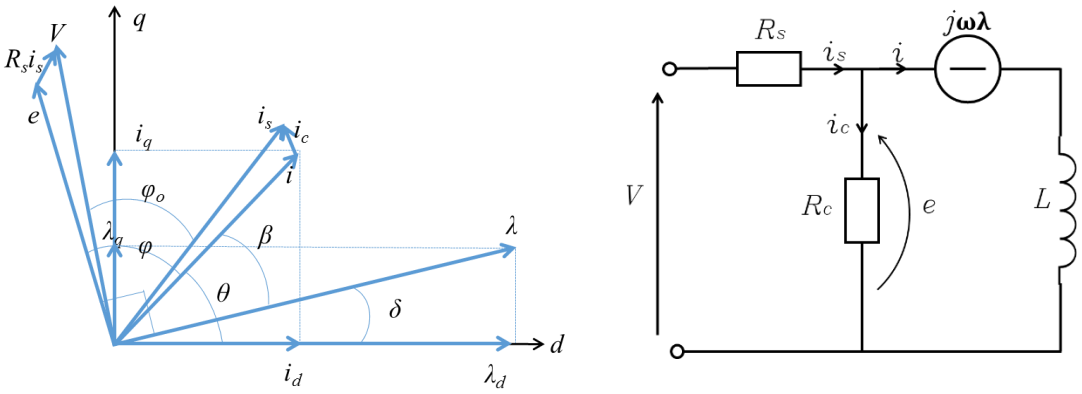

Figure 1.13. (a) Steady-state phasor diagram of synchronous reluctance machine in dq synchronous reference frame; (b) Equivalent circuit of synchronous reluctance machine including iron loss [41].

The symbols in figure 1.13 have the following meanings:

(1) i_s: stator current including iron loss;

(2) i_c: equivalent current induced by iron loss;

(3) φ: angle between stator current i and induced voltage e;

(4) φ_o: angle between stator current i_s and terminal voltage V;

(5) δ: angle between d-axis and net flux λ;

Neglecting copper loss, P_{cop} and iron losses, P_{ir}, internal power factor (IPF) is defined as $\cos(\varphi)$ [41]. IPF is usually smaller than power factor (PF), which is defined as $\cos(\varphi_o)$. Neglecting losses, the relationship between mechanical power, P_{mech}, phase voltage, V, stator current, i, and IPF is

$$P = T\omega = \frac{3p}{2} Vi \times IPF \tag{1.6}$$

IPF is derived as:

$$IPF = \cos(\varphi) = (\varepsilon - 1)\sqrt{\frac{\sin(2\theta)}{2(\tan\theta + \varepsilon^2 \cot\theta)}} \tag{1.7}$$

From (1.7), IPF is only related to current load angle, θ and saliency ratio, ε.

Derivation of (1.7) over θ gives maximum value of IPF as:

$$IPF_{\max} = \frac{\varepsilon - 1}{\varepsilon + 1} \tag{1.8}$$

Substitute IPF with IPF_{max} in (1.7), the corresponding load angles for IPF_{max} occurs at:

$$\theta_{\max IPF} = \tan^{-1}\left(\sqrt{\varepsilon}\right) \text{ (motoring)} \tag{1.9}$$

$$\theta_{\max IPF} = \tan^{-1}\left(-\sqrt{\varepsilon}\right) \text{ (generating)} \tag{1.10}$$

Figure 1.14 plots the IPF curves with different ε and θ. Clearly, IPF increases with ε over all θ, but the rate of change decreases as ε increases. (1.11) describes the torque, T versus θ for a constant i. Neglect saturation, the MTPA load angle, θ_{MTPA} is 45°.The θ_{MAXIPF} deviates from 45° as ε increases. This deviation provides field weakening ability, which will be elaborated as below.

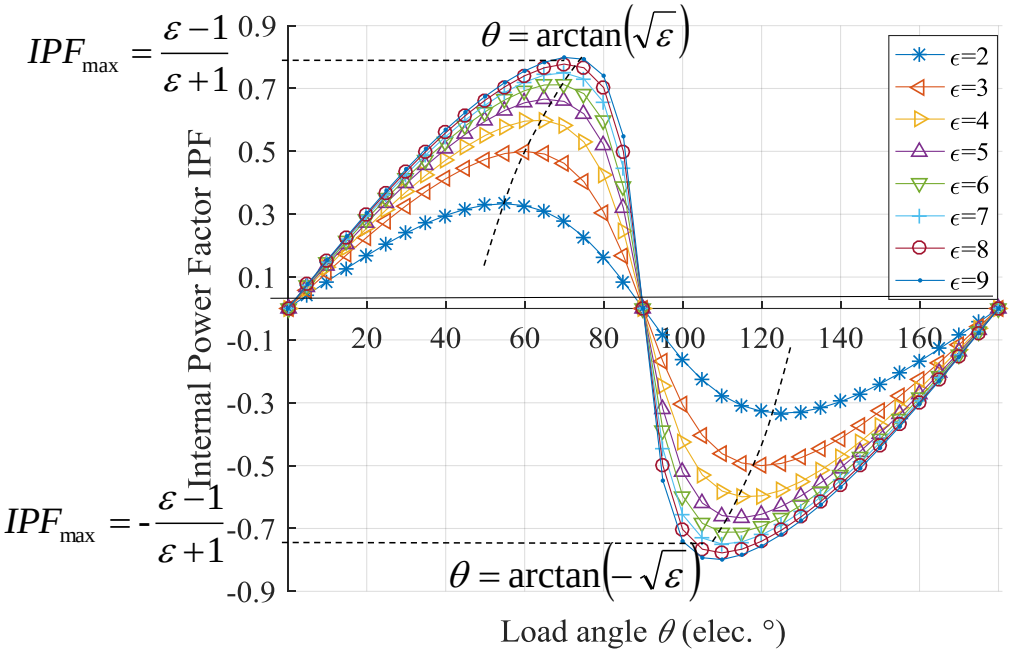

Figure 1.14. Internal power factor, IPF, vs. load angle θ and saliency ratio, ε.

For SynRM, neglecting losses, T is represented as a function of i and θ as:

$$T = \frac{3}{2}\frac{p}{2}\left(L_d - L_q\right)i^2 \sin\left(2\theta\right) \tag{1.11}$$

T is also represented as a function of e and δ as:

$$T = \frac{3}{2}\frac{p}{2}\left(\frac{1}{L_d} - \frac{1}{L_q}\right)\left(\frac{e}{\omega}\right)^2 \sin\left(2\delta\right) \tag{1.12}$$

(1.11) and (1.12) is sometimes referred to as the torque per ampere function and the torque per volt function. In figure 1.15, normalised (1.11) and (1.12) are plotted together with IPF from (1.7) in motoring mode.

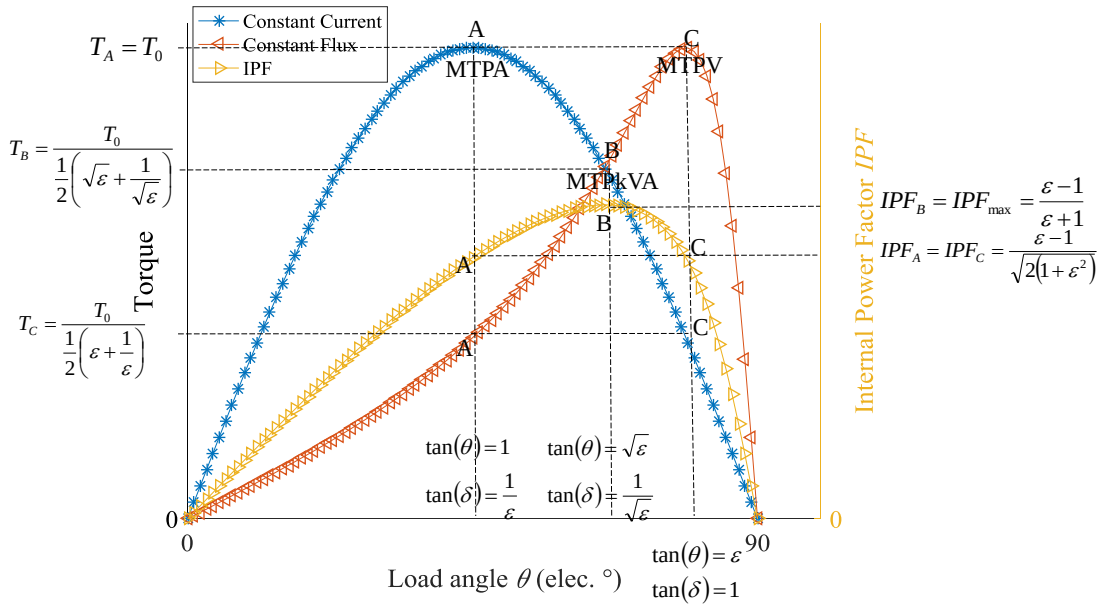

Figure 1.15. Normalized curve of torque vs load angle θ under constant current i and constant voltage V, with IPF vs load angle θ.

The MTPA point occurs at $\theta = 45°$ and $\delta = \tan^{-1}(1/\varepsilon)$, denoted as point A. The maximum torque per volt (MTPV) point occurs at $\theta = \tan^{-1}(\varepsilon)$ and $\delta = 45°$, denoted as point C. Substituting these values into (1.7) gives the IPF at point A and point C, where IPF is given by:

$$IPF_A = IPF_C = \frac{\varepsilon - 1}{\sqrt{2(1+\varepsilon^2)}} \tag{1.13}$$

With constant current, the flux weakening region starts from point A and ends at point C. Considering (1.6), (1.11), (1.12) and (1.13) together, the torque ratio between points A and C is the ratio between the base speed, ω_b and maximum possible speed for constant power, ω_{fw}. This ratio is defined as constant power speed ratio (CPSR), where

$$CPSR = 0.5\left(\varepsilon + \frac{1}{\varepsilon}\right) \tag{1.14}$$

The relationship between CPSR and ε is plotted in figure 1.16, where a ε of 20 is needed to achieve a desired CPSR of 10.

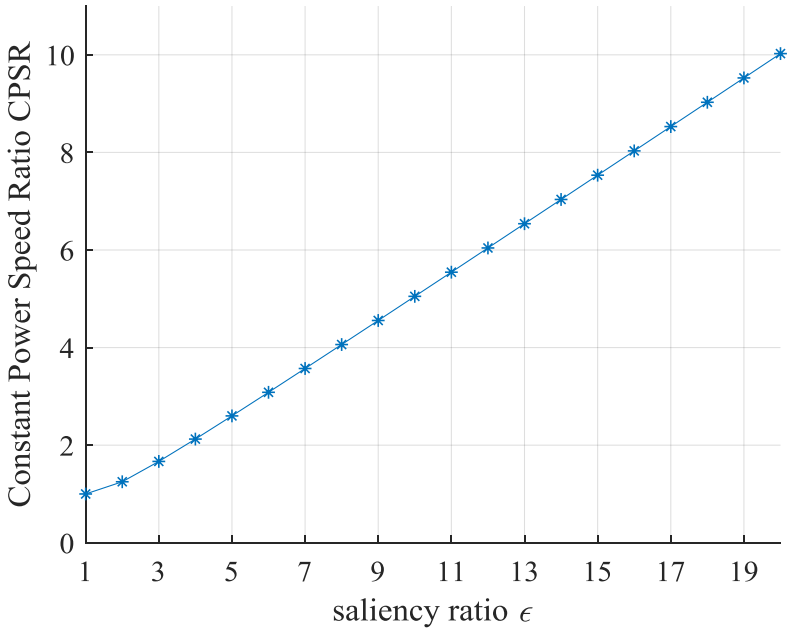

Figure 1.16. Constant power speed ratio, CPSR, vs. saliency ratio, ε.

Wound Rotor Synchronous Machine

The WRSM stator coils are sinusoidally distributed. With three-phase sinusoidal current excitation, a sinusoidal field is generated in the airgap. During operation, the rotor windings are fed with DC current, generating a rotating excitation field. The fundamental component of the rotor and stator fields rotate at same speed with a phase shift. Figure 1.17 shows the phasor diagram of the WRSM in steady state motoring mode. Compared with the phasor diagram of the SynRM in figure 1.13, a separate excitation field λ_r is introduced, providing an extra excitation source and a new dimension in the operation. The salient rotor structure also provides reluctance torque, so the torque of WRSM is a combination of rotor excitation torque and reluctance torque.

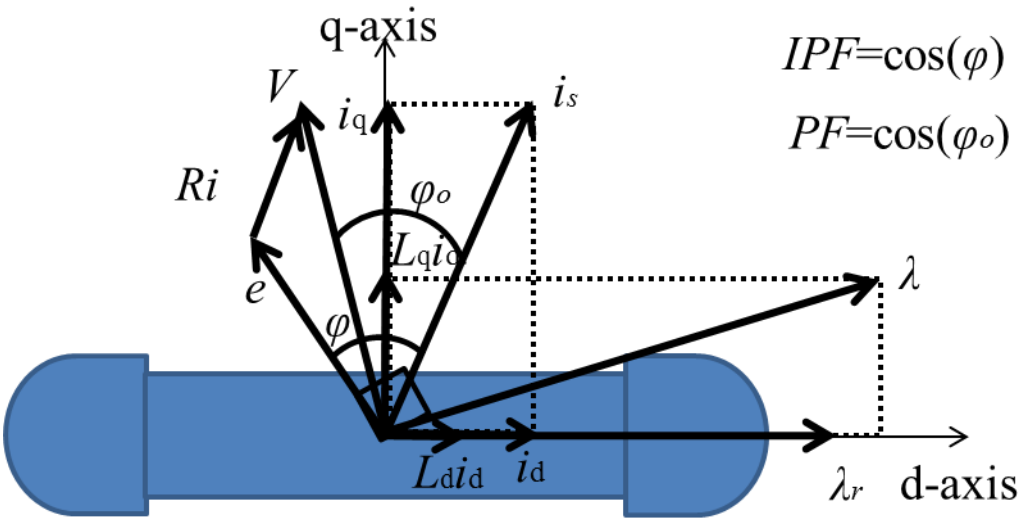

Figure 1.17. Motoring phasor diagram of the wound rotor synchronous machine.

From figure 1.17, the relationship between dq axis reluctances, L_d, L_q, and dq axis currents, i_d, i_q are shown in (1.15).

$$\boldsymbol{\lambda}_d = L_d \mathbf{i}_d \qquad (1.15)$$

$$\boldsymbol{\lambda}_q = L_q \mathbf{i}_q$$

The relationship between the amplitude of λ_d, λ_q, i_d, i_q and induced voltage, e is:

$$T = \frac{3}{2} p(\lambda_d i_q - \lambda_q i_d) = \frac{3}{2} p\left(\lambda_r i_q + L_d i_d i_q - L_q i_d i_q\right) = \underbrace{\frac{3}{2} p \lambda_r i_q}_{\text{Excitation Torque}} + \underbrace{\frac{3}{2} p\left(L_d - L_q\right) i_d i_q}_{\text{Reluctance Torque}} \qquad (1.16)$$

where the first item represents rotor excitation torque, T_{exc}, and second item represents reluctance torque, T_{re}.

The relationship between λ_d, λ_q, speed, ω, pole pair number, p and e is:

$$\mathbf{e} = p\omega\left(\boldsymbol{\lambda}_d + \boldsymbol{\lambda}_q\right) \qquad (1.17)$$

The relationship between p, e, stator net current, i_s, IPF and airgap power, P is:

$$P = \frac{3}{2} p(\mathbf{e} \bullet \mathbf{i}_s) = \frac{3}{2} p|\mathbf{e}||\mathbf{i}_s| IPF \tag{1.18}$$

where IPF=cos(φ).

Neglecting the iron loss, the angle between the stator current, i_s and the phase voltage, V is denoted as φ_o. The power factor PF= cos(φ_o). Compared with φ, φ_o is smaller, so the PF is larger than IPF.

1.2.4 Iron Loss Modelling

To evaluate efficiency of the machine, iron loss needs to be included, where Bertotti model [130] is applied in Altair Flux. The equation of instantaneous iron loss, $P_{ir,inst}$ is:

$$dP_{ir,inst}(t) = \underbrace{k_h B_p^{\alpha} f}_{\text{Hysteresis Loss}} + \underbrace{\sigma \frac{d^2}{12}\left(\frac{dB}{dt}(t)\right)^2}_{\text{Classic Loss}} + \underbrace{k_e\left(\frac{dB}{dt}(t)\right)^{1.5}}_{\text{Loss in Excess}} \tag{1.19}$$

where σ is the conductivity; α is the power coefficient of hysteresis loss item; f is the frequency of B. d is the thickness of the sheet; B_p is the peak flux density per cycle; k_h is the coefficient by hysteresis and k_e is the coefficient of losses in excess.

The Bertotti loss model under sinusoidal current excitation is written as [131]:

$$P_{l,ir,inst} = k_h B_p^{\alpha} f + \sigma \frac{\pi^2 d^2}{6}\left(B_p f\right)^2 + 8.67 k_e \left(B_p f\right)^{1.5} \tag{1.20}$$

With instantaneous iron loss, the volume density of the average loss over a period, $dP_{ir,ave}$ is:

$$dP_{ir,ave} = \frac{1}{T}\int_0^T dP_{ir,inst}(t)dt \tag{1.21}$$

Therefore, average power dissipated in a volume region is:

$$\iiint dP_{ir,ave} dV \tag{1.22}$$

The first term in (1.19) is the hysteresis loss, the second is the classical loss and the last is losses

in excess. In (1.19), coefficients of the classical loss and losses in excess are only related to characteristics of the material, and is irrelevant of flux wave shape. Therefore, they can be determined in a single data fitting. The hysteresis loss, however, is related to the pattern of excitation flux. If there is no minor loop in flux density hysteresis excursion, the coefficient k_h requires only a single determination like the other loss coefficients. If minor loops exist, a modification on hysteresis loss model is required, where a modified Bertotti loss model was proposed by J.D.Lavers *et al*. [132] as below:

$$W_h = W_h\Big|_{-Bp}^{+Bp} \times \left(1 + k\frac{1}{B_p}\sum_{i=1}^{n}\Delta B_i\right) \tag{1.23}$$

In this equation, $W_h\Big|_{-Bp}^{+Bp}$ represents conventional hysteresis loss model with symmetrical bipolar flux waveform and no minor loops. The loss with n minor loops of magnitude, ΔB per half cycle is given by a sum of conventional model and the minor loops losses. The basic principle of this method is the superposition of losses, which is more of an approximation as it fails to consider the inherent nonlinearity [133].

Since the flux on the classical SRM has unipolar pulsive patterns [134], to evaluate its hysteresis loss on classical SRM, the flux density pulses are recognised as minor loops. In the case of unidirectional pulse of between zero and a peak flux density, B_p, the hysteresis loss equation is modified from (1.23) as [133]:

$$W_h = W_h\Big|_{-Bp}^{+Bp} \times \frac{k}{2} \tag{1.24}$$

In (1.23) and (1.24), the accuracy of loss prediction is dependent on the correlation value of k. Lavers suggested a k value between 0.6 and 0.7 [132], but later research from Y. Hyashi *et al.* indicates that a k value of 0.8 is more suitable for some of the flux density patterns that is observed in classical switched reluctance machines [134].

1.3 Objective of Research

The objective of this research is to develop a non-PM electrical machine suitable for B-ISG applications. The performance of the developed machine is applied to compare with a benchmark classical SRM in terms of efficiency, torque, power and field weakening capability, with consideration for cost reduction.

1.3.1 Benchmark Machine Introduction

The benchmark machine is Federal Mogul Controlled Power (FMCP)'s Speedstart®, as shown in figure 1.18. It is a water cooled 12/8 three-phase classical switched reluctance motor/generator. The geometry and material specifications are listed in Table 1.4. The machine has a four quadrant operation capability with a normal speed range from 0 to 20000 rpm. The continuous generation power is 5 kW and the maximum power is 10 kW.

Figure 1.18. Picture of Federal Mogul Controlled Power Speedstart® B-ISG system.

The machine inverter consists of three H-bridges, powered by a 48 V battery. The terminal voltage is approximately 48 V during motoring mode and approximately 50 V during generation mode. The maximum phase current is 360 A.

A water cooling system is integrated with the machine, rendered by connection to the engine cooling loop that runs at approximately 85 – 115°C. The power electronics is integrated into the machine housing and is exposed to the cooling loop temperature. The operating temperature range is between approximately 110°C and 175°C, typical at 120°C.

Parameter	Value
Stator outer diameter	136 mm
Rotor outer diameter	93.4 mm
Airgap length	0.3 mm
Stator back iron thickness	8.03 mm
Rotor back iron thickness	21.75 mm
Machine axial length	80.5 mm
Winding area in slot	207.4 mm^2
Shaft diameter	23.5 mm
Rotor pole angle	21°
Stator pole angle	14°
Phase winding connection	Parallel
Number of turns per coil	41
Number of phases	3
Number of pole pairs	8
Rotor iron material	M400-50A
Stator iron material	M400-50A
Rated Power	5 kW
Rated Speed	2000 rpm
Speed Range	0-20000 rpm

Table 1.4. Specifications of FMCP Speedstart® switched reluctance machine.

The motoring power of the Speedstart B-ISG system versus speed curves under continuous and boost operating conditions are plotted in figure 1.19. The motoring and generating efficiency maps versus mechanical power and speed are shown in figure 1.20 (a) and (b). These data will be used as references to evaluate the performance of the designed machines as a part of this research.

From the figures and previous knowledge, there are three major drawbacks with the present system.

(1) The benchmark Speedstart B-ISG system suffers from a low efficiency. To be specific, the peak efficiency is 85 % for generation, and 78 % for motoring. At the rated mechanical power of 5 kW, the efficiency is between 76 % and 83 % for in generating mode, and 67 % to 74 % in motoring mode. To make things worse, the high efficiency speed and power regions are narrow, suggesting an even less satisfactory overall loss performance over a driving cycle.

(2) In the company's view, reducing the cost of the inverter could greatly decrease the price point of the machine, but the small operating temperature range requires significant overrating of the inverter to meet the current carrying capacity of the machine while maintaining an acceptable temperature rise in the switches. This significantly increases the cost of the power electronic components.

(3) A noise problem is also reported, especially at high speed.

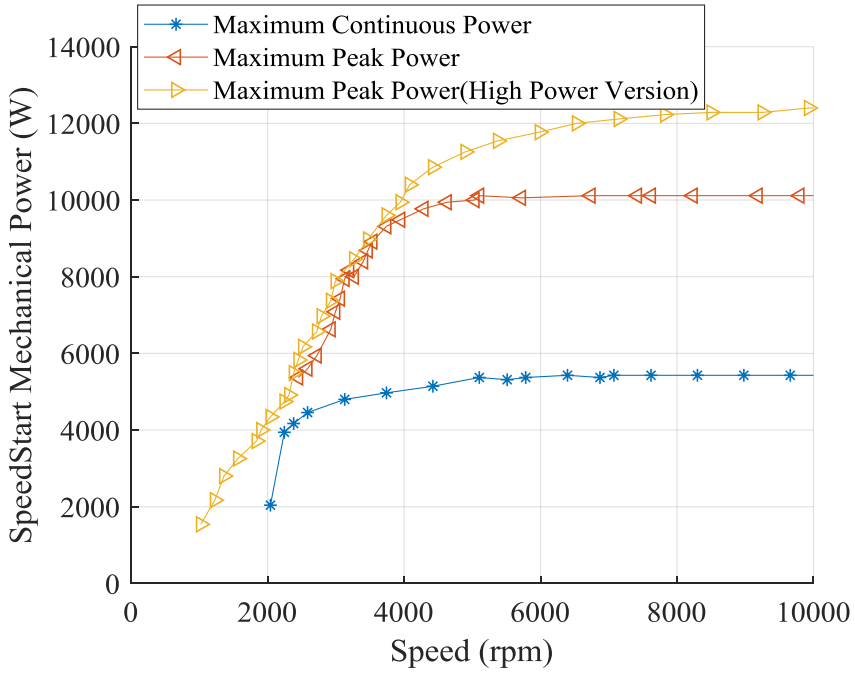

Figure 1.19. A continuous and maximum motoring power speed performance of FMCP Speedstart®.

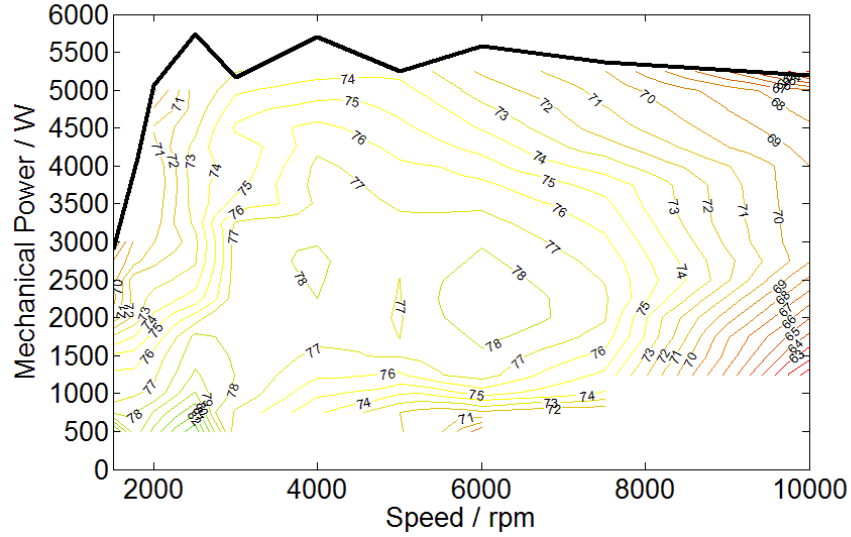

(a)

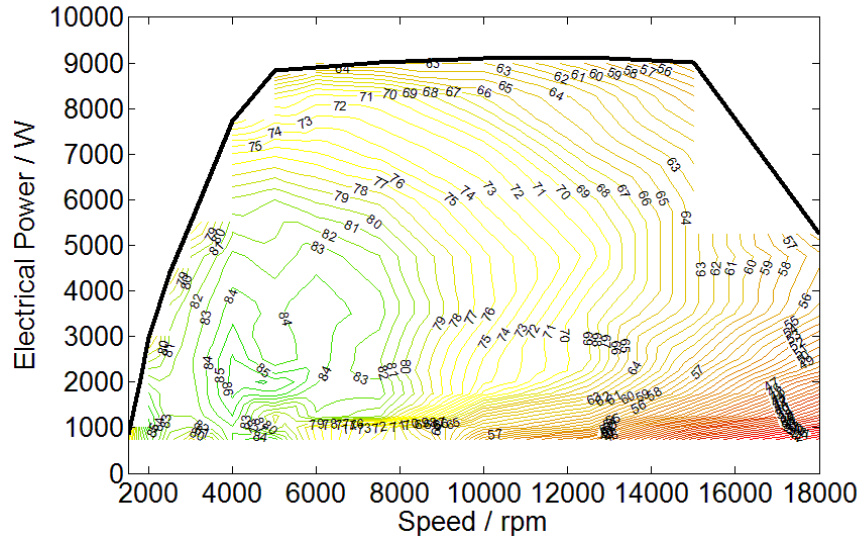

(b)

Figure 1.20. The efficiency map of FMCP Speedstart in (a) motoring mode(b) generation mode.

1.3.2 Selection of Machines

From the literature review in section 1.2.2, the advantages and disadvantages of the five machines types are analysed and compared for HEV application. Among them, the WRSM and the SRM with non-classical windings have a potential to outperform the benchmark classical SRM, so these machines are focused on in this research.

For the SRM, the study emphasize is on different winding topologies and its effects on machine

performances in terms of torque capability, efficiency and CPSR compared with the classical winding. The use of conventional AC machine theory to predict the behaviour of SRM is also investigated, where implementation of a simpler control strategy and a lower cost inverter is possible.

For the WRSM, at low speed, the research focuses on geometry optimization for lower loss. At high speed, it focuses on the optimum control strategy for optimum efficiency while maintaining a high CPSR.

1.3.3 Challenges

For SRM applications, the first challenge is to implement the low cost AC inverter and simple AC control theory without sacrificing the machine torque performance. The second challenge is to increase the machine efficiency over the benchmark SRM while keeping the good field weakening capability.

For the WRSM application, the first challenge is to design a high performance machine that shows improvement over the benchmark SRM in terms of efficiency, torque ripple, and control complexity. The second challenge is to develop a more efficient and more accurate approach over the existing Lagrange method for minimum loss operation.

1.4 Organization of the Thesis

This thesis consists of six chapters. Chapter 1 is the introduction. This chapter lays the background of the research. Chapters 2 and 3 focus on the SRM. Chapter 4, 5 and 6 discusses the WRSM.

In Chapter 2, different winding topologies are implemented on the benchmark Speedstart machine iron core, including the aforementioned fully pitched winding, fractional pitch classical winding, short pitched mutually coupled winding, as well as a proposed winding topology named fractional pitched mutually coupled winding. The performance of these windings are compared over different current excitations, where the power factor and field weakening capability under bipolar sinusoidal excitation are predicted using conventional AC

machine theory.

In Chapter 3, the mutually coupled SRM with bipolar sinusoidal current is further studied. First, a geometry optimization for copper loss is carried out. Then, the geometry influences on the power factor and CPSR are investigated. A Flux-Simulink co-simulation method is then developed to incorporate the inverter and control algorithm. The simulation results from the AC machine theory and co-simulation are compared, where some discrepancies are presented and discussed.

Chapter 4 focuses on the design aspects of the WRSM, where the machine is geometrically optimized for copper loss and torque ripple. First, a minimum loss optimization process is carried out on a four pole machine. The study emphasizes on the sensitivity of rotor pole shoe on copper loss. Then, comparisons are carried out between a four pole and a six pole machine. Last, a novel method of determination of eccentric rotor pole parameters to reduce torque ripple with minimum loss on average torque is introduced.

Chapter 5 emphasizes on the operation aspects of the WRSM, where a novel minimum loss searching algorithm is proposed. First, the proposed algorithm is introduced in comparison with the conventional Lagrange method. Then, the accuracy of the two methods is compared using finite element analysis. With the proposed algorithm, different designs are investigated over the entire speed range. This includes the poles numbers, eccentric rotor pole and lamination material. Lastly, the optimized WRSM is compared with the benchmark Speedstart SRM over a driving cycle.

Chapter 6 focuses on the multi-physical simulation and experiment of the WRSM. First, the mechanical limitations are evaluated using Autodesk Inventor to determine the safe operational speed. Second, a water cooling jacket is designed using motor-CAD, where a proposed approach to reduce rotor winding temperature by balancing stator and rotor copper loss is proposed. The experiments are then introduced, where the results are compared with FE analysis.

2. 12/8 Benchmark Switched Reluctance Machine

The classical SRM has some major drawbacks in efficiency, noise, control complexity and inverter cost, preventing a wide application in ISG applications. In this chapter, investigations are conducted to developing a more efficient machine with simpler control and a lower cost inverter by proposing a variety of winding configurations. A variety of current excitation strategies are imposed on the windings, where at least some of them uses AC sinusoidal current excitation. The simulation results are compared with the benchmark Speedstart SRM.

2.1 Classical Winding

A parametrized FE model of the Speedstart benchmark classical SRM is developed in Altair Flux for static electromagnetic FE analysis. The machine mesh is displayed in figure 2.1(a), the mesh near the airgap is shows in figure 2.1(b), the winding configuration is illustrated in figure 1.11 (a).

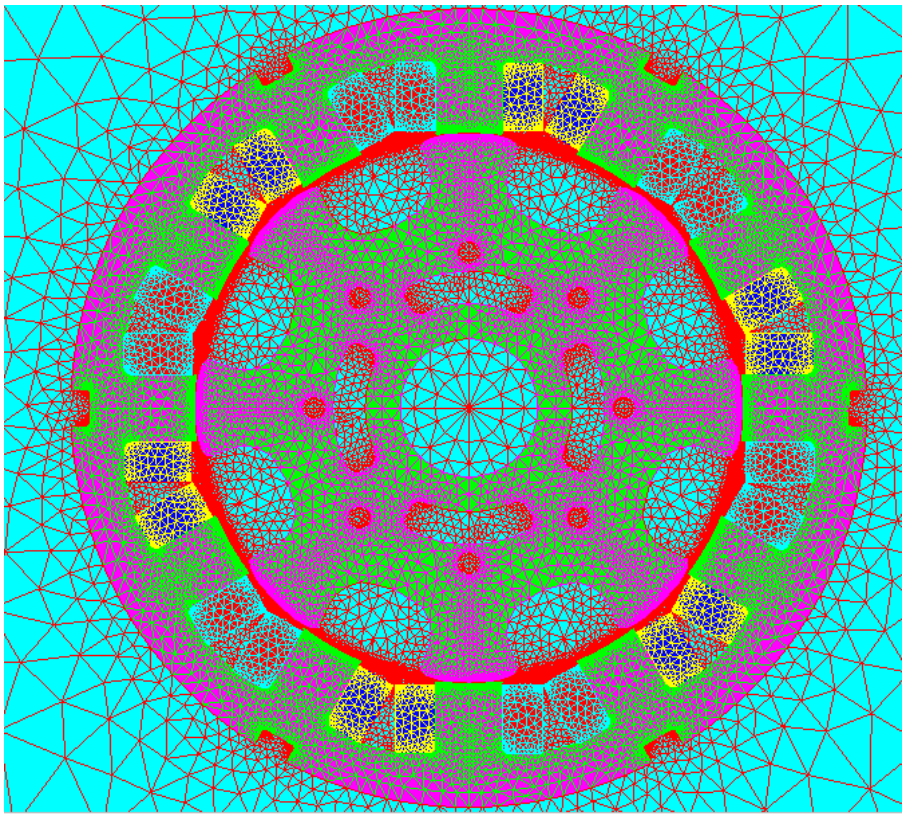

(a)

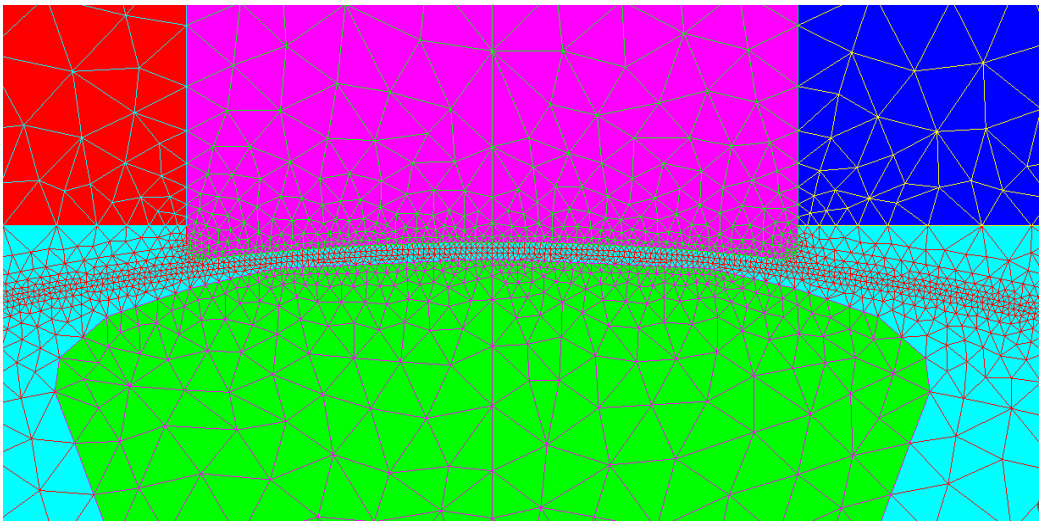

(b)

Figure 2.1. Mesh of FE model of the benchmark switched reluctance machine in FLUX 2D.

Since the machine has a pole pair number, p of eight under conventional excitation, an electrical cycle is equivalent to 45 mechanical degrees. Figure 2.2 (a) shows flux linkage, λ for the CSRM versus current density, J at various mechanical rotor positions, ζ_m, where $\zeta_m = 0°$ is the fully aligned position, and $\zeta_m = 22.5°$ is the fully unaligned position. Figure 2.2 (b) shows λ versus ζ at various J, where the five J levels represent stator current, i of 10, 30, 50, 70 and 90 A per coil, covering the current range in normal operation. The area enclosed by two λ (J) curves and a constant J value represent the co-energy, W_c, as described in (1.4).

Static torque waveforms of an electrical cycle verses mechanical angle, ζ_m, with phase-A energised at different J are shown in figure 2.3. The phase-B and phase-C torque can be derived by shifting the positive part or negative part of the torque curves by 120 and 240 electrical degrees. With negligible mutual inductances, the torque waveform of the machine is simply a sum the three phases torque waveforms.

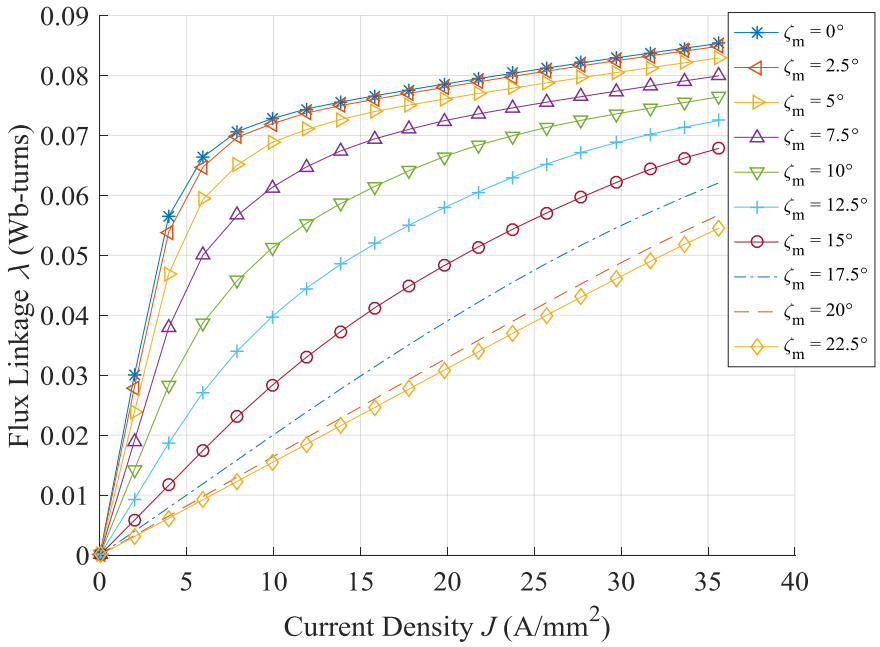

(a)

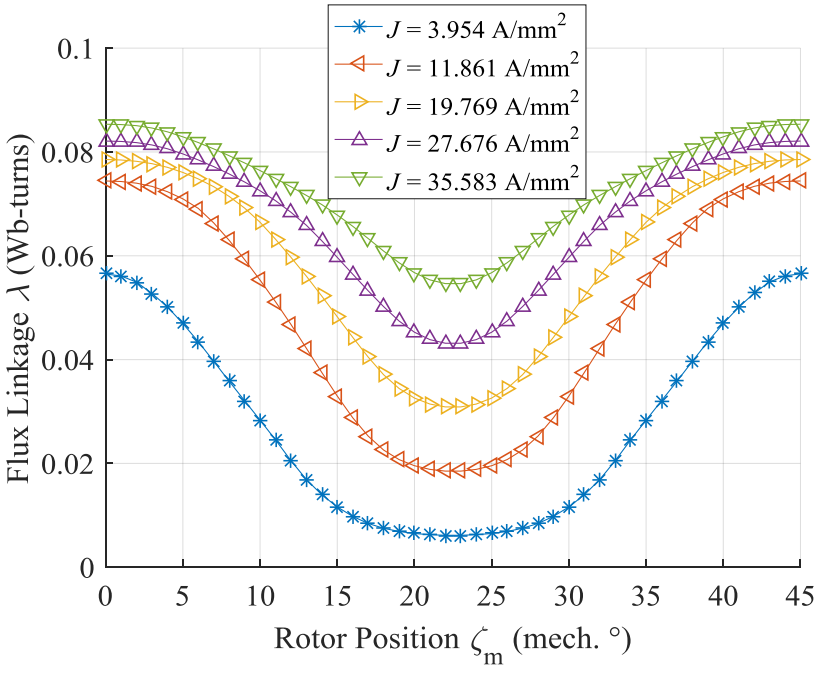

(b)

Figure 2.2. Classical SRM flux linkage, λ waveforms (a) at a rotor mechanical position, ζ_m of 0 – 22.5° in 2.5° steps vs. current density, J, (b) at various current densities, J vs. rotor position, ζ_m.

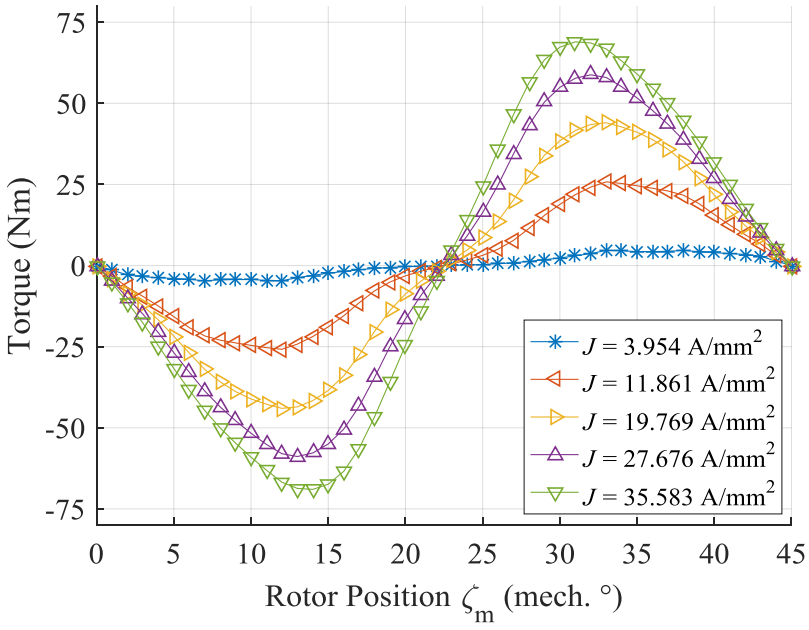

Figure 2.3. Classical SRM static torque at various current densities, J vs. rotor mechanical position, ζ_m.

2.2 Proposed Winding Configurations

In this section, five different windings topologies are applied to the iron core of the benchmark SRM. The topologies under investigation are listed in table 2.1 with acronyms and winding figures.

The classical winding is the most widely used SRM winding type in HEV applications. Compared with the classical winding, MC winding only changes the winding polarities, and no extra end winding is required. Apart from FRC winding, in this chapter, another fractional pitched winding is proposed by changing of winding polarity of FRC. This winding is named FRMC winding. In a fractional pitched winding, each coil is wound around two stator teeth, which increases the end winding length compared with classical winding. For FP winding, the winding area per coil on all winding topologies in this study are set the same for easy comparison, so double layer winding is applied on the FP winding, as opposed to the single layer winding described by Mecrow in figure 1.11(d). This change does not affect torque or loss characteristics.

Name	Acronym	Winding Configuration
Classical	C	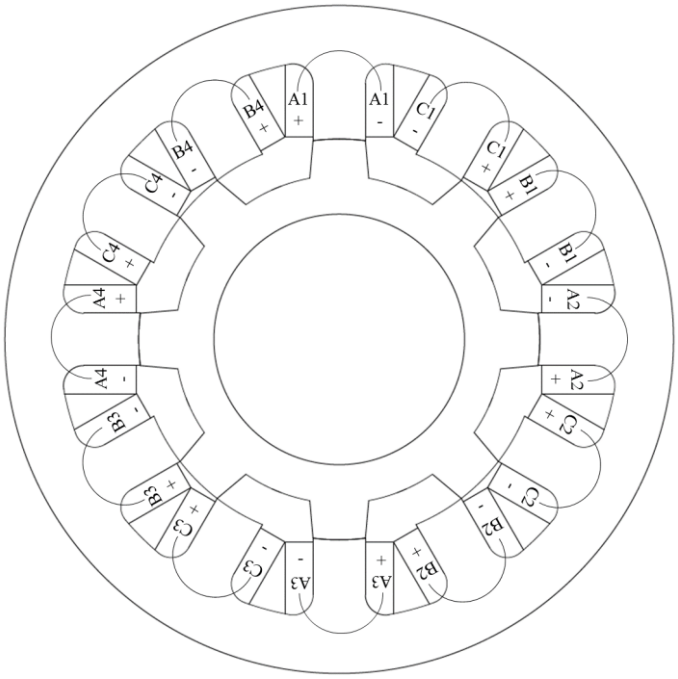
Short Pitched Mutually Coupled	MC	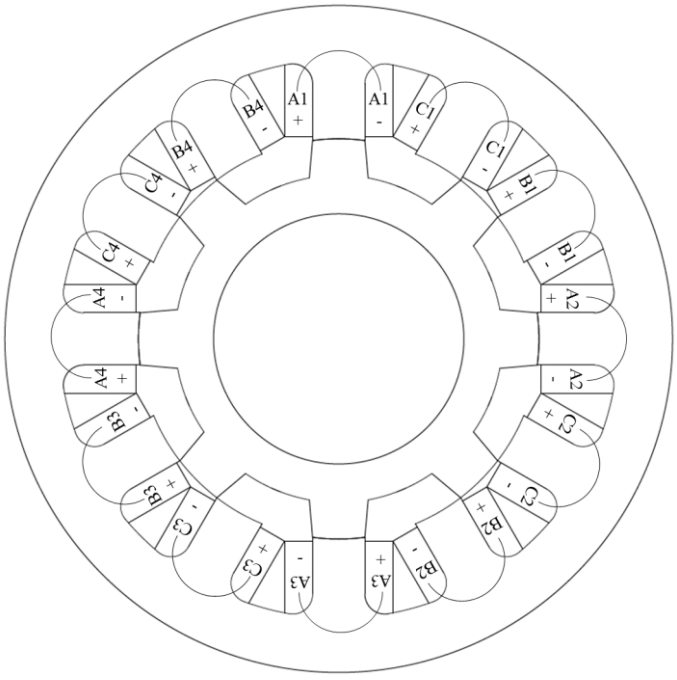

Fractional Pitched Classical	FRC	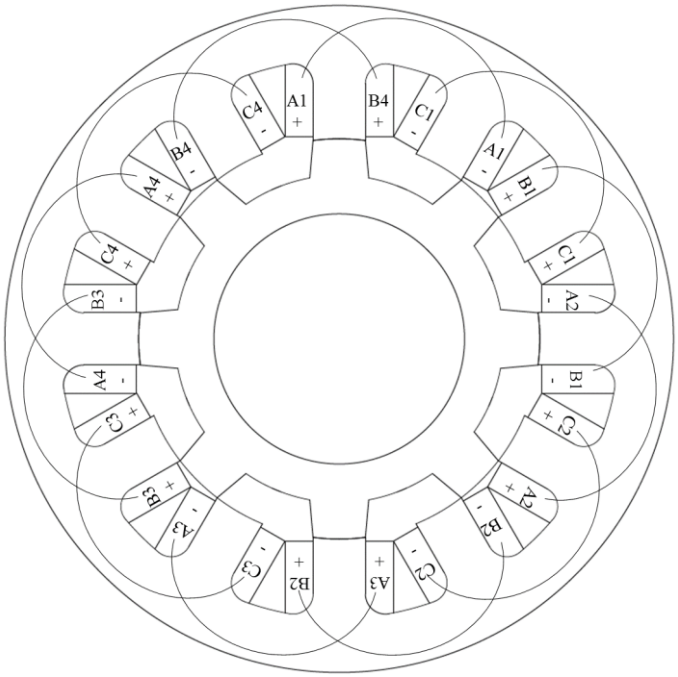
Fractional Pitched Mutually Coupled	FRMC	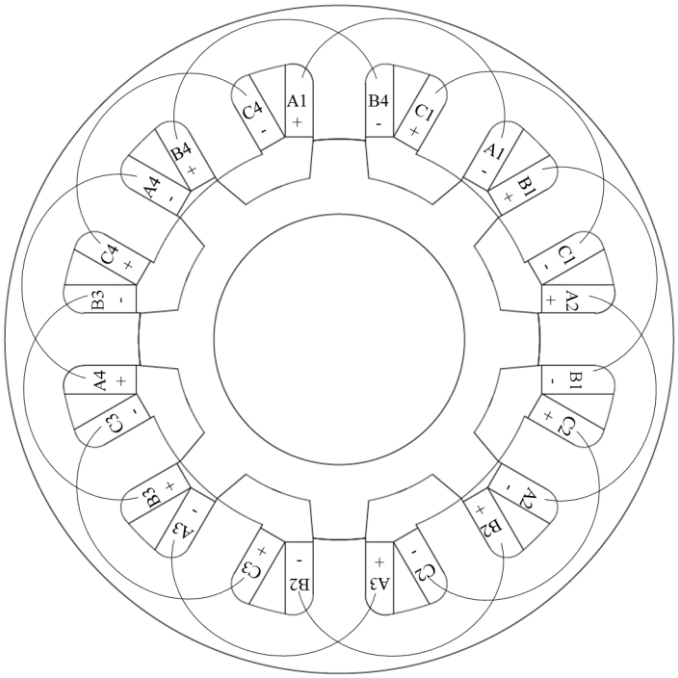

Fully Pitched	FP	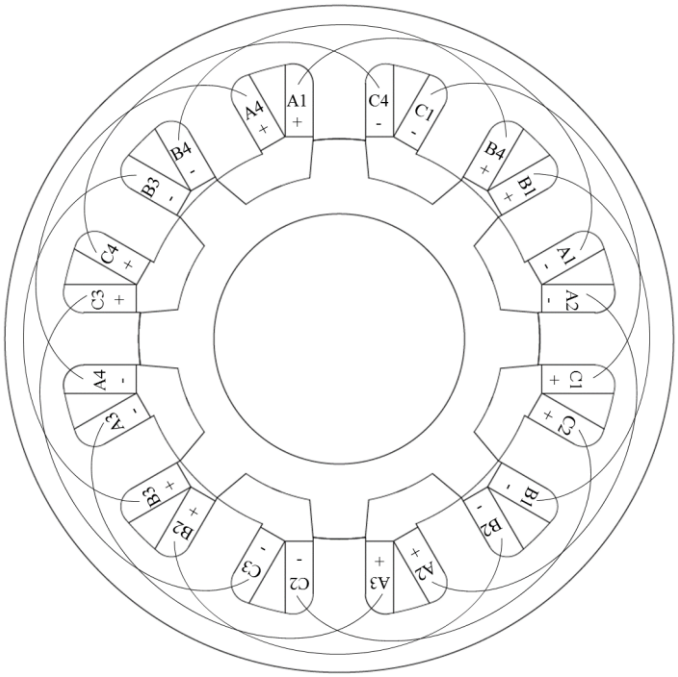

Table 2.1. Winding topologies under investigation

2.2.1 Inductances Comparison

The aligned and unaligned position with respect to phase - A of all winding topologies are defined in figure 2.4, where magnetic equipotential lines are displayed.

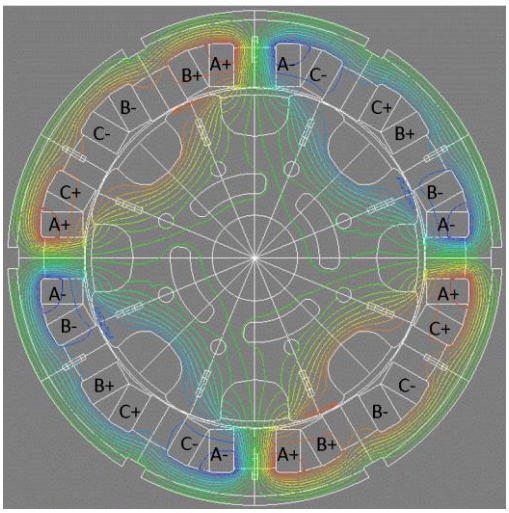

(a)

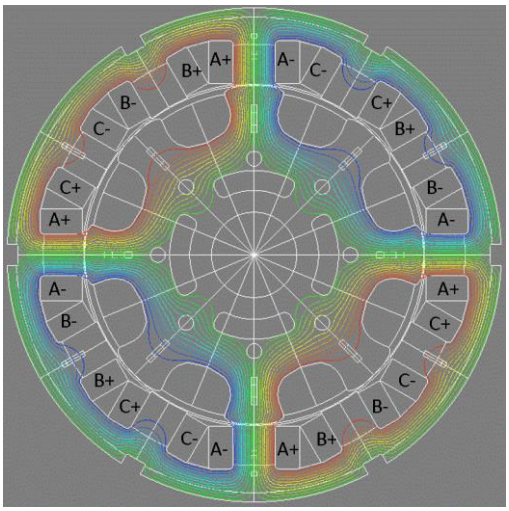

(b)

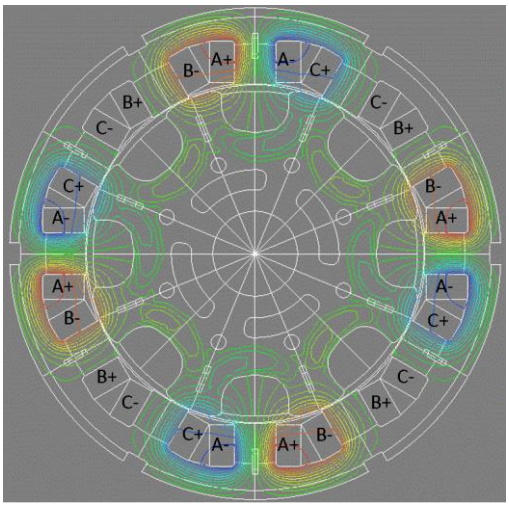
B- A+ A- C+ C- B+ B+ C- C+ A- B- A+ A+ B- A- C+ B+ C- C+ A- A+ B- B+ C- C- B+ C+ A- A+ B-

(c)

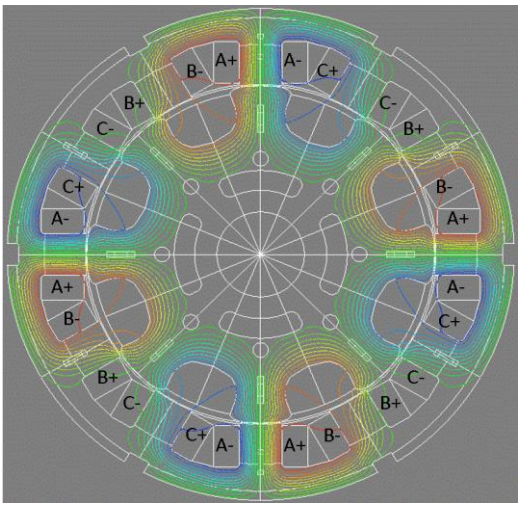
B- A+ A- C+ C- B+ B+ C- C+ A- B- A+ A+ B- A- C+ B+ C- C+ A- A+ B- B+ C- C- B+ C+ A- A+ B-

(d)

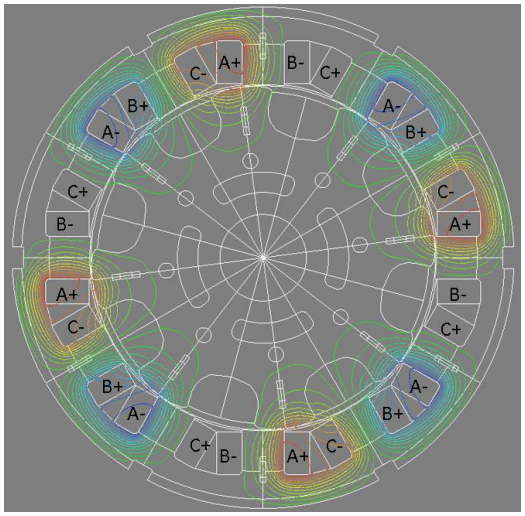
C- A+ B- C+ A- B+ B+ A- C+ C- A+ B- B- C+ A+ C- B+ A- A+ B- C+ A- C+ B- A+ C-

(e)

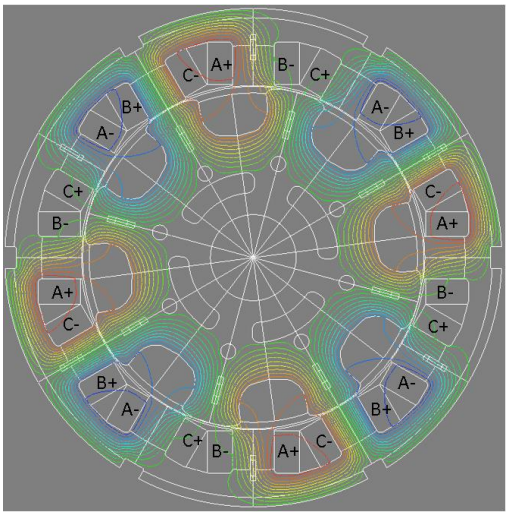
C- A+ B- C+ A- B+ B+ A- C+ C- A+ B- B- C+ A+ C- B+ A- A+ B- C+ A- C+ B- A+ C-

(f)

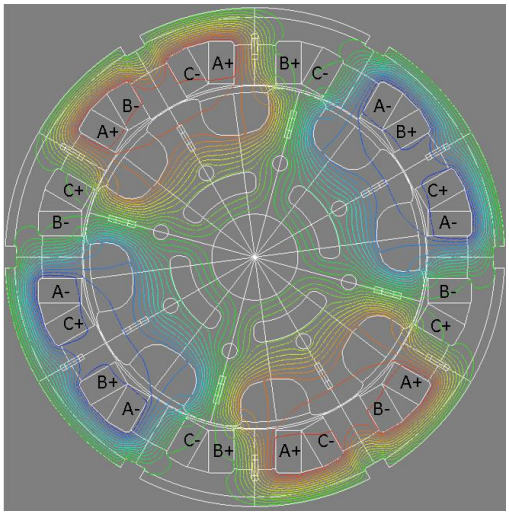
C- A+ B+ C- A- B- B+ A- A+ B- C+ C+ A- C+ B- B- C+ A- B+ A+ B- C+ A- C+ B- A+ C-

(g)

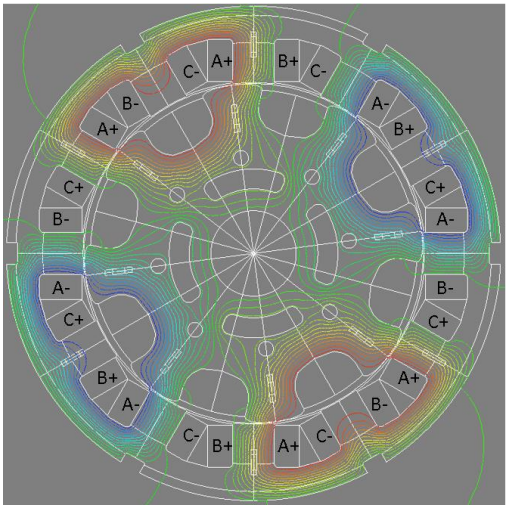
C- A+ B+ C- A- B- B+ A- A+ B- C+ C+ A- C+ B- B- C+ A- B+ A+ B- C+ A- C+ B- A+ C-

(h)

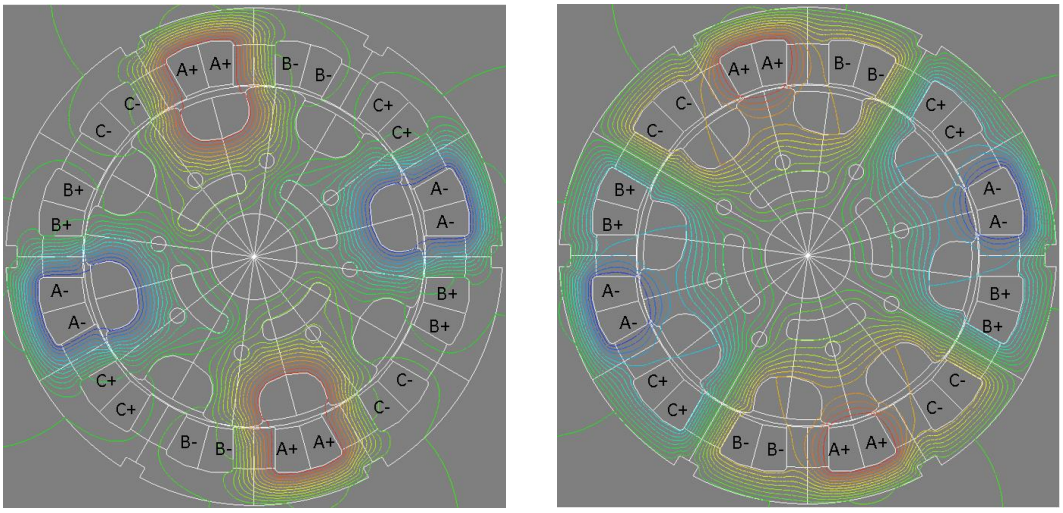

(i) *(j)*

Figure 2.4. Magnetic equipotential lines of CSRM at (a) unaligned position; (b) aligned position; of MCSRM in (c) unaligned position; (d) aligned position; of FRMCSRM at (e) unaligned position; (f) aligned position; of FRCSRM at (g) unaligned position; (h) aligned position and of FPSRM at (i) unaligned position; (j) aligned position. Current Density J is 19.769 A/mm^2.

According to (1.5) in section 1.2.3, torque is produced by current and inductance variation. Studying inductances helps to determine torque production capability, current excitation pattern and the switching angle of the current with respect to rotor position. Figure 2.5 displays the phase - A self-inductance, L_a and the mutual-inductances, M_{ab} of all winding topologies for comparison. Figure 2.6 shows their rate of change as a function of rotor position, ζ_m, at current density, J of 19.769 A/mm^2. The inductance of phase B and C can be obtained by a phase shifting of 120 and 240 electrical degrees from phase-A.

From figure 2.4, if flux leakage is neglected, almost all the flux generated by one phase in the classical winding passes through only itself, while in other winding configurations flux is forced to go through nearby phases. Consequently, a much larger mutual inductance and change in mutual inductance is observed in these windings. From the torque production point of view, the direction of torque produced by changes in mutual-inductance is determined by the direction of current in the related phases, while direction of torque produced by self-inductance change is irrelevant. This suggests bipolar current is more suitable than unipolar current for winding configurations that make use of mutual-inductance, and this is confirmed in prior reports [82,

90, 135].

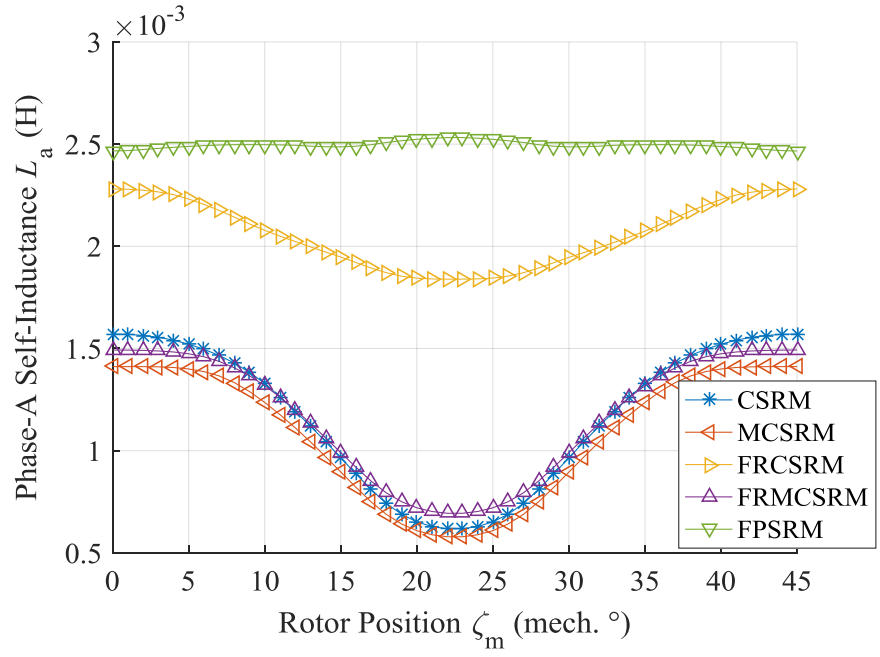

(a)

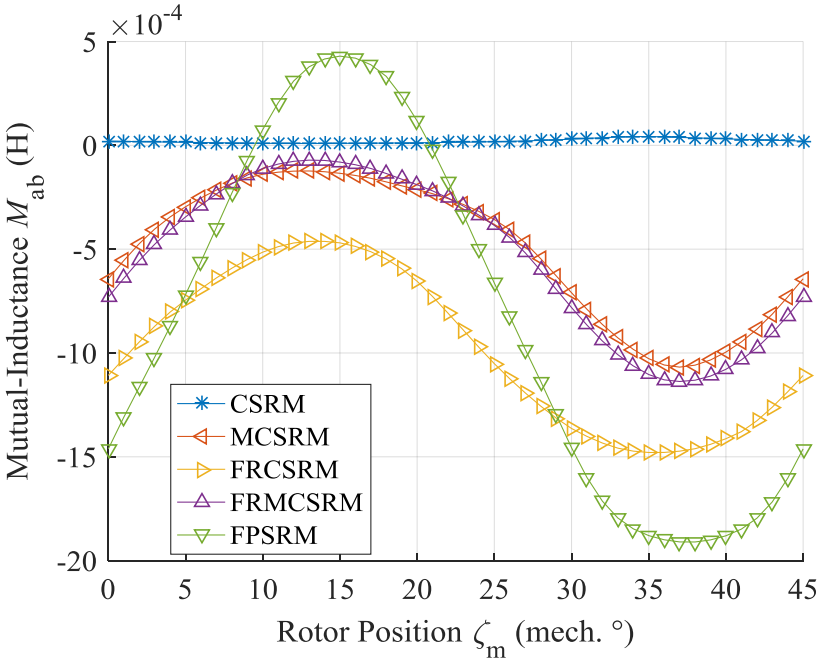

(b)

Figure 2.5. Phase-A self-inductance, L_a and (b) mutual inductance, M_{ab} between phase A and B vs rotor mechanical position, ζ_m of different winding topologies. Current Density, J is 19.769 A/mm^2.

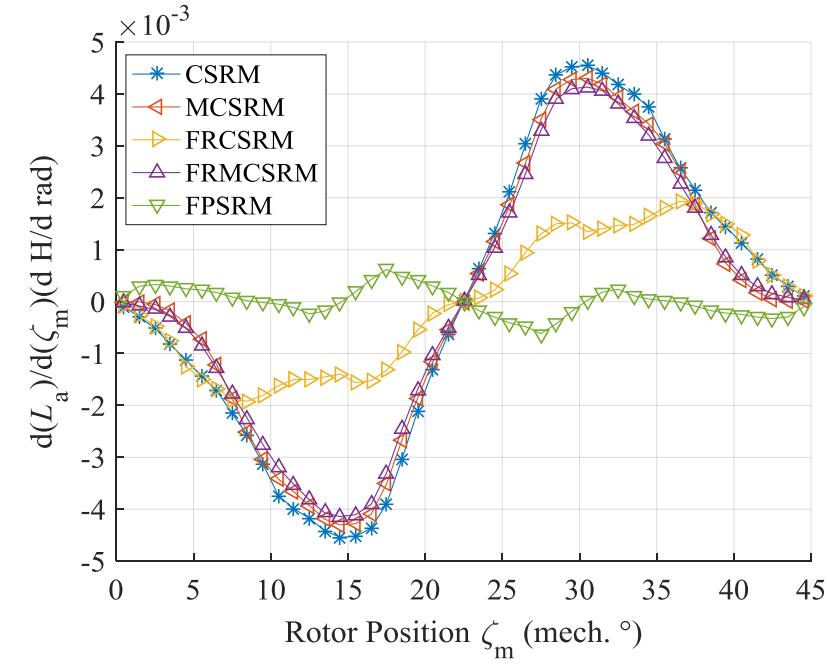

(a)

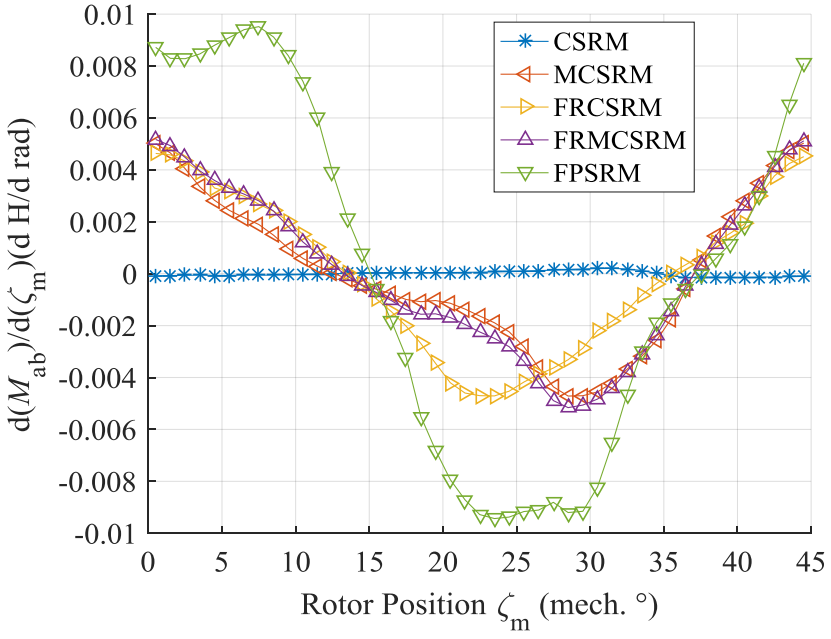

(b)

Figure 2.6. Variation of phase-A self-inductance, L_a and mutual inductance, M_{ab} between phase A and B over rotor mechanical position in radius vs rotor mechanical position, ζ_m of different winding topologies. Current Density, J is 19.769 A/mm^2.

From figure 2.5 - 2.6, the MC winding has a slightly smaller self-inductance and a much larger

mutual-inductance than classical winding. The amplitude of the mutual-inductances change is negligible in the classical winding compared with self-inductance change, whereas in the MC winding they are similar.

Compared with the FRC winding, the aligned and unaligned positions are switched in the FRMC winding. This is favourable because the large constant offset presented in the FRC self and mutual inductances are significantly reduced, so the FRMC is much less susceptible to saturation. Moreover, under sinusoidal current and conventional AC machine theory, power factor will be increased in the FRMC winding because less voltage is required to overcome the constant inductance without contributing to torque production.

In the FP winding, self-inductance is constant versus position, so the self-inductance will not contribute to torque production. All torque is produced by a mutual-inductance variation. The mutual-inductance variation is significantly larger in this winding configuration than in any of the others. Similar to the FRC, with a large self-inductance offset, the FP winding is easy to saturate and suffers from low power factor under AC sinusoidal current excitation.

2.2.2 Current Excitations

Since unipolar current is more suitable for the classical winding, and bipolar current is more suitable for other windings, to investigate the torque performance for all winding configurations, four different current waveforms with different conduction angles are investigated as shown in figure 2.7. The conduction angle, η, of excitation current in this literature is defined as the 'current on' angle of bipolar square current excitation. The current waveforms are:

(1) Unipolar square current waveform with a η of 180 electrical degrees, referred to as USQ. This current excitation is conventional for classical windings, so the torque performance of the CSRM under USQ is treated as reference for other machine windings and excitations.
(2) Bipolar sinusoidal current, referred to as SIN.
(3) Bipolar square waveform with two phases conducting simultaneously and a η of 120 electrical degrees, referred as SQ2.

(4) Bipolar square waveform with all three phases conducting simultaneously and a η of 180 electrical degrees, referred to as SQ3.

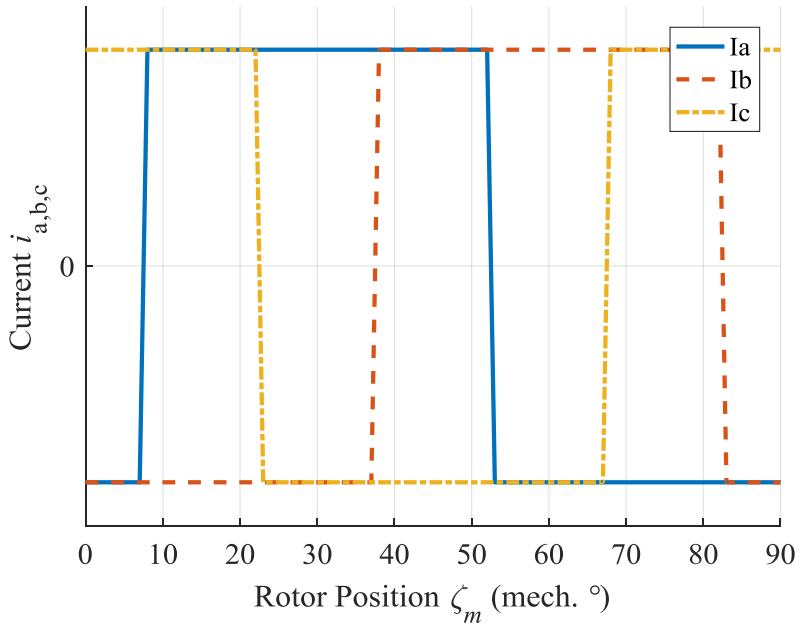

(a)

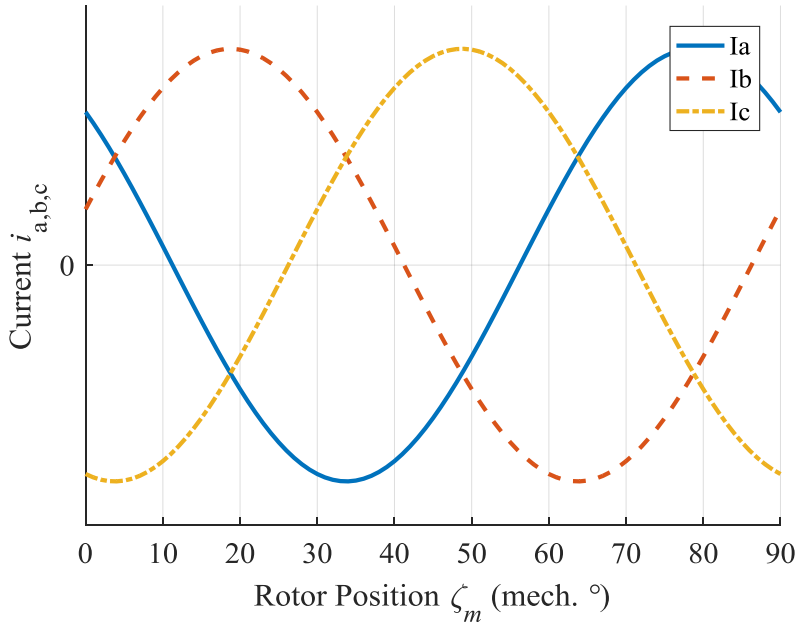

(b)

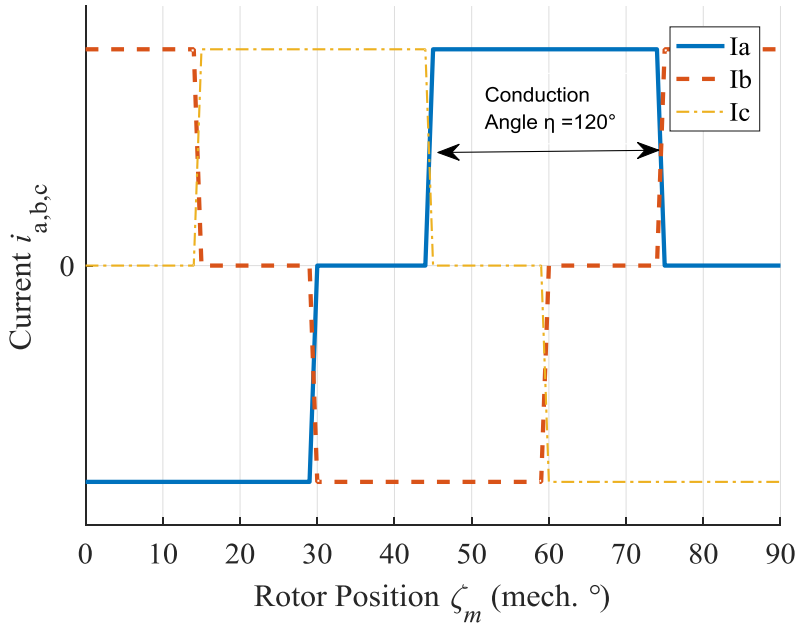

(c)

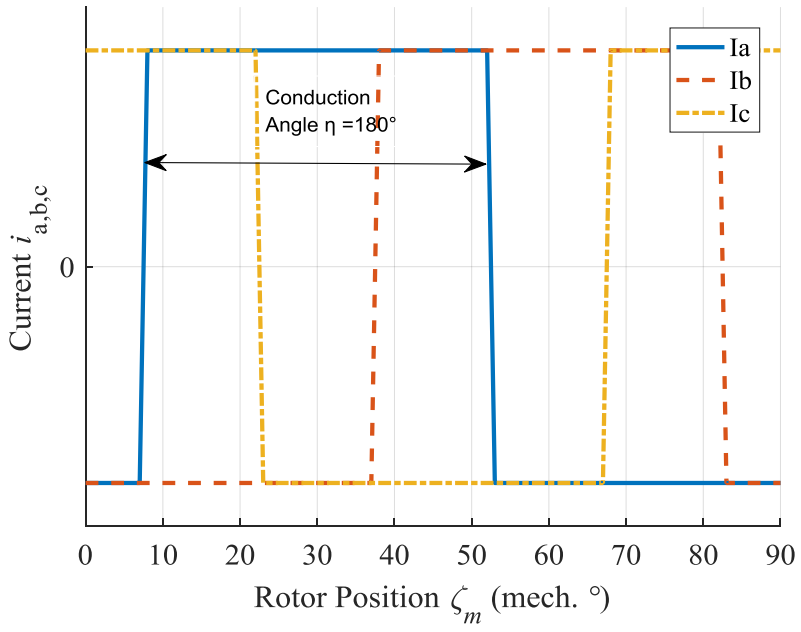

(d)

Figure 2.7. Excitation current waveforms (a) unipolar square waveform (USQ), (b) bipolar sinusoidal waveform, (c) bipolar square waveform, two phases conducting simultaneously (SQ2), (d) bipolar square waveform, three phases conducting simultaneously (SQ3).

For the half and full H-bridge inverters shown in figure 1.8 (a) and (b) in section 1.2.2, the DC-link voltage can both be fully utilized at any rotor position, and phase currents are independent. The difference is that for the H-bridge, the voltage on the windings are bi-directional, so generation of both unipolar and bipolar currents is possible, as illustrated in figure 2.7 (a) and (d). In the case of the half bridge, the voltage is unipolar, so only unipolar currents in figure 2.7 (a) can be generated.

For a conventional AC inverter shown in figure 1.8 (c) and (d), only bipolar current is possible. Moreover, current that passes though one phase must be shared by at least one other phase, so phase currents are not independent. If current in one phase is shared by both other phases, conventional switching strategy produces bipolar sinusoidal current (figure 2.7 (b)), where the six-step operation gives the best DC-link voltage utilization. If current in one phase is shared by only one other phase, a maximum η of 120 electrical degrees is realized, resulting in current waveform resemblance to figure 2.7 (c).

Apart from conduction angle, current commutation angle also affects the machine performance, and only the correct angle can give maximum torque per ampere (MTPA) performance. The principle of this angle selection is to compare current waveforms with inductance change waveforms in terms of direction and amplitude [86, 87, 135]. The result can be verified with FE simulation. In this research, the MTPA is always sought unless otherwise specified.

It is worth mentioning that, compared with unipolar excitation, the fundamental excitation frequency of bipolar current is halved [82], and so is the pole pair number. For this machine, poles pair reduces from eight to four with bipolar excitation.

The torque performance of machine is evaluated in terms of average torque, T_{ave} and torque ripple coefficient, T_{ripp}, where torque ripple coefficient is defined as:

$$T_{ripp} = T_{\max} - T_{\min} \tag{2.1}$$

T_{max} and T_{min} are highest and lowest instantaneous values of torque in one cycle.

2.2.3 Conduction Angle

From previous study, the conduction angle η affects the doubly salient machine torque performances [136]. For different windings, average torque, T_{ave} and torque ripple, T_{ripp} versus η at typical peak current density, J_p of 19.769 A/mm^2 are plotted in figure 2.8 (a) (b).

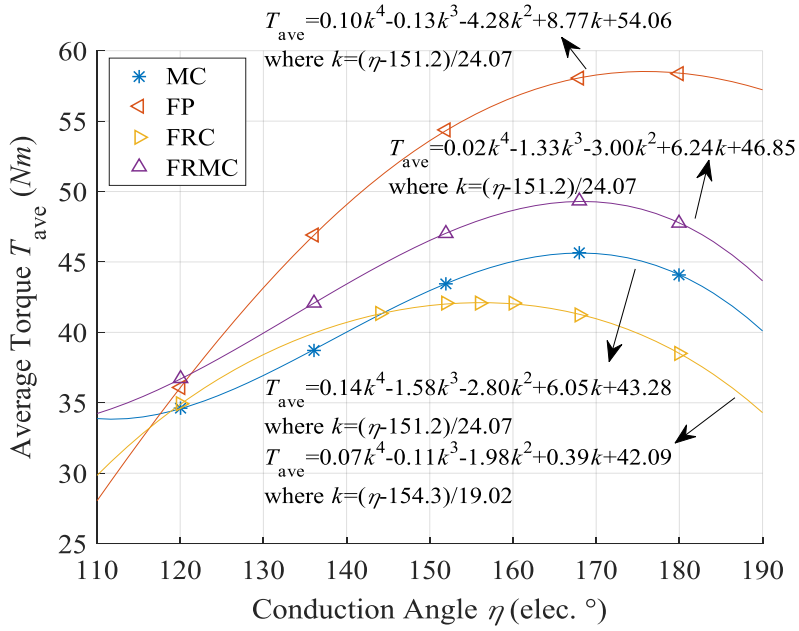

(a)

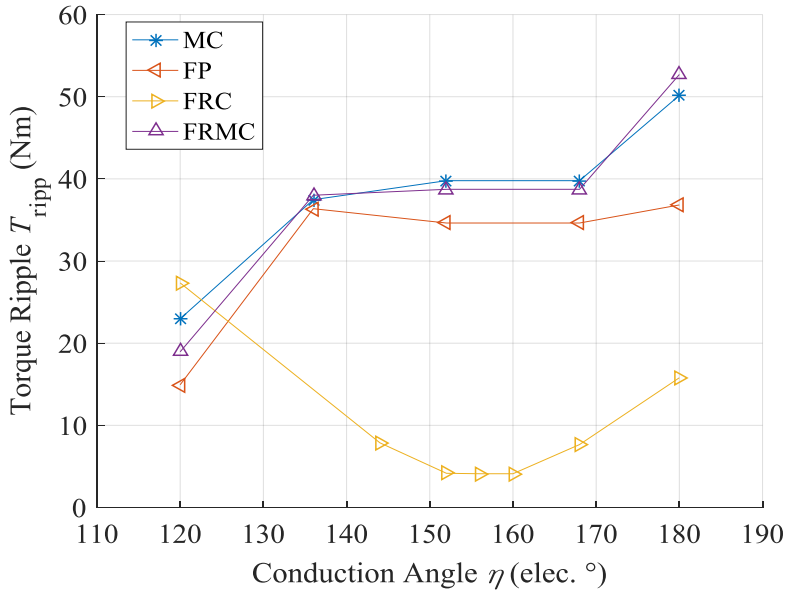

(b)

Figure 2.8. (a) Average torque, T_{ave} and (b) torque ripple, T_{ripp}, vs conduction angle, η, under SQ_η excitation at peak current density, J_p of 19.769 A/mm^2.

Noticeably, an optimum conduction angle, η_{opt} for maximum average torque exists for all windings. To symbolize the current waveform, bipolar square excitation with a conduction angle of x is referred to as SQ_x. To predict the η_{opt}, linear least square curve fitting method is applied using Matlab. The η_{opt} for the MCSRM, FPSRM, FRCSRM, FRMCSRM are derived as 168, 176, 156 and 168 electrical degrees. The T_{ripp} of the MCSRM, PRMCSRM and FPSRM all increase with η, while the T_{ripp} of the FRCSRM is greatly reduced at η_{opt}.

The role of η on torque production is more apparent in figure 2.9, where torque waveforms under SIN, SQ2, SQ3 and SQ_ η_{opt} are plotted over half cycle at J_p of 19.769 A/mm^2. From the figures, unsuitable η result in negative torque production, causing torque waveform dips between strokes, which increases T_{ripp} and reduces T_{ave}.

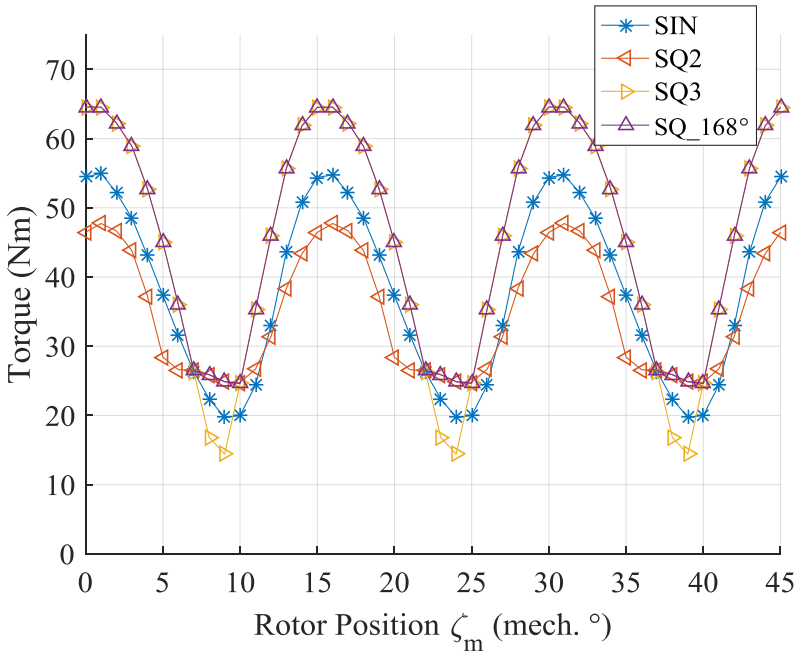

(a)

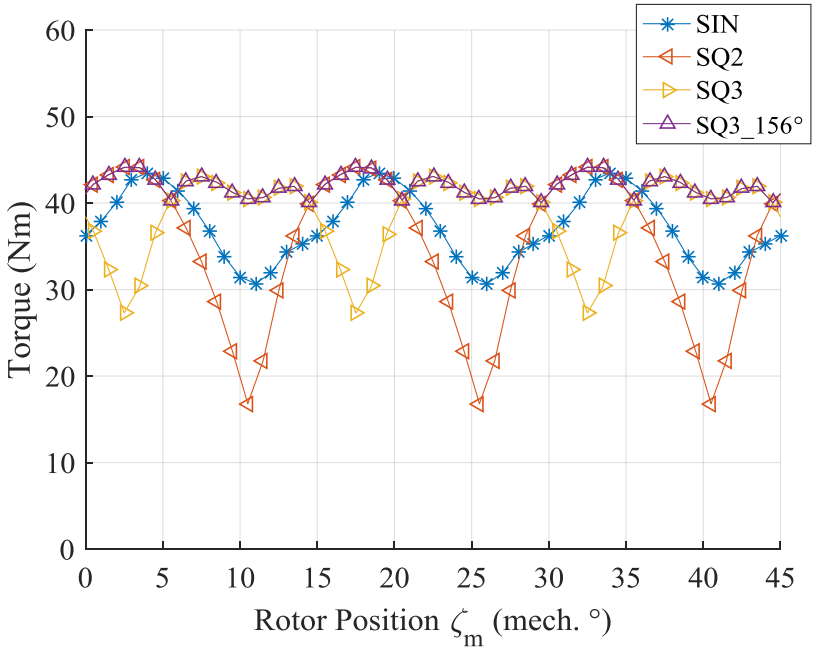
SIN
SQ2
SQ3
SQ3_156°
Torque (Nm)
Rotor Position ζ_m (mech. °)
0
10
20
30
40
50
60
0
5
10
15
20
25
30
35
40
45

(b)

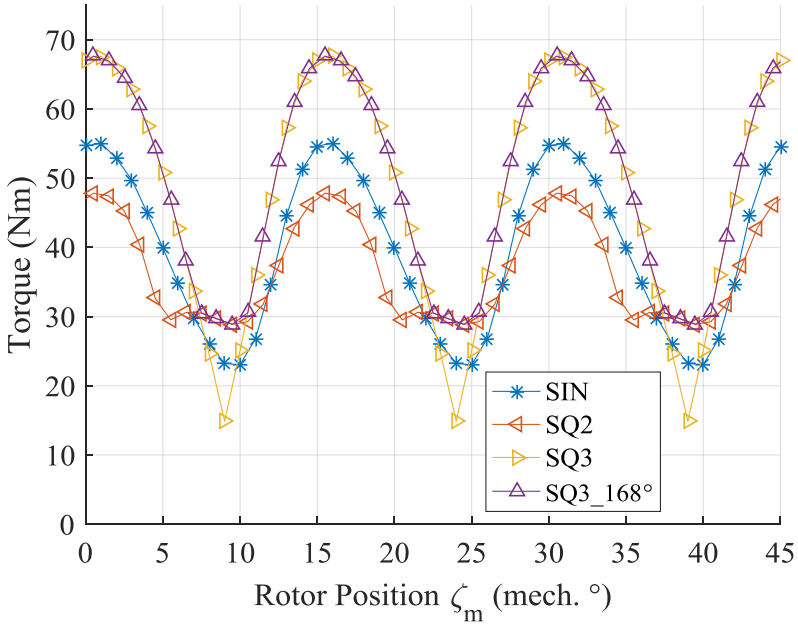
SIN
SQ2
SQ3
SQ3_168°
Torque (Nm)
Rotor Position ζ_m (mech. °)
0
10
20
30
40
50
60
70
0
5
10
15
20
25
30
35
40
45

(c)

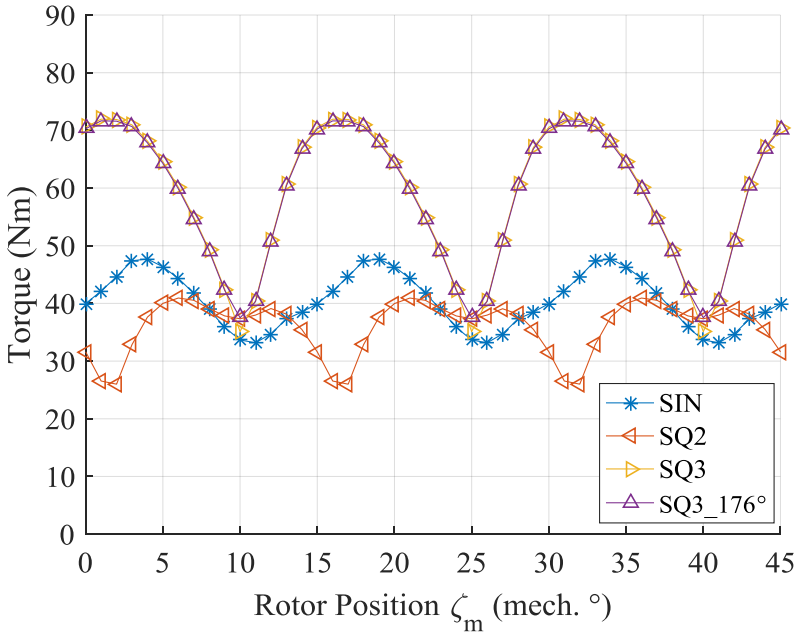

(d)

Figure 2.9. Torque waveform vs. rotor position, ζ_m, under SQ2, SQ3, SIN and SQ_η_{opt}. (a) MC Winding, (b) FRC Winding, (c) FRMC Winding and (d) FP Winding. Peak Current density, J_p is 19.769 A/mm^2.

2.2.4 Torque Comparisons

In the proposed winding configurations, the average torque, T_{ave} versus peak current density, J_p under SIN, SQ2 and SQ_η_{opt} excitations are plotted in figure 2.10 - 2.12, together with classical winding under USQ excitation as a reference.

Comparing all three figures, SQ_η_{opt} excitation produces the highest T_{ave}, followed by SQ2 and SIN who delivers similar performance. Under SQ_η_{opt}, the FP winding generates the highest T_{ave} while the classical winding gives the lowest throughout the entire current density range. The FRC winding produces higher T_{ave} than the MC and the classical windings below J_p of 12.5 A/mm^2, but quickly saturates as J_p increases. The FRMC winding generates higher T_{ave} than the MC and the FRC windings at high J_p. In terms of T_{ripp}, the MC and FRMC windings produce the highest T_{ripp}, followed by the FP winding. The classical and the FRC windings yield the lowest T_{ripp} level.

Under SIN excitation, the classical winding delivers the lowest T_{ave} of all. Below J_p of around 20 A/mm^2, the FP winding generates the highest T_{ave}, followed by the FRC and the FRMC

windings. With increasing J_p, the FP and FRC windings saturate much more readily, while the FRMC winding outperforms all others. In terms of T_{ripp}, the MC and the FRMC windings produce much higher T_{ripp} than the classical, the FP and the FRC windings, especially at high J_p.

Compared with SIN, the SQ2 excitation generally produces slightly higher T_{ave} below 15 A/mm^2, and lower T_{ave} above 15 A/mm^2. Though both SIN and SQ2 current waveforms are possible using a conventional AC inverter, only the sinusoidal current facilitates the implementation of conventional AC machine theory and vector control methods. Therefore, the SIN excitation is considered more favourable than SQ2 excitation.

The analysis above indicates that the bipolar square current excitation with optimum conduction angle and FP winding is the best combination, as it produces the highest torque with low torque ripple.

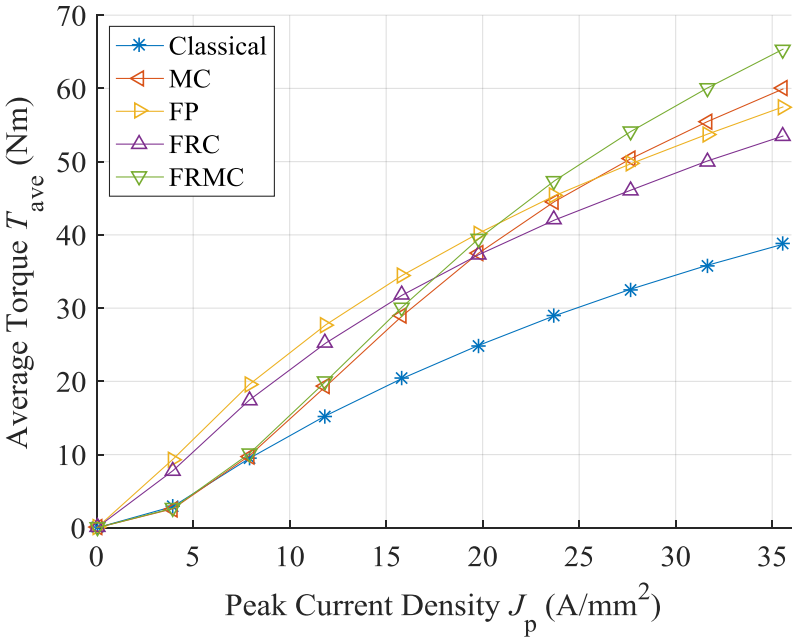

(a)

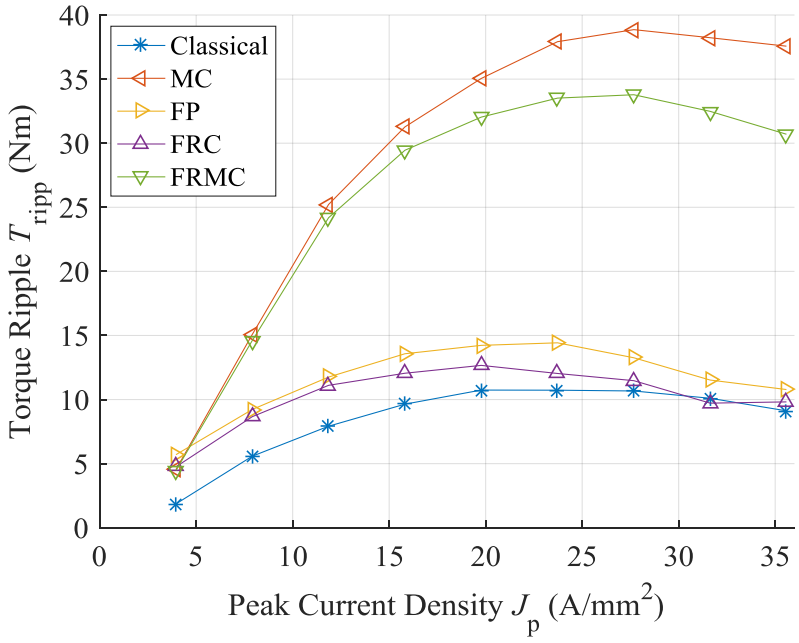

(b)

Figure 2.10. Classical, MC, FR, FRC and FRMC winding performances under SIN current excitation vs. peak current density, J_p. (a) average torque, T_{ave}, (b) torque ripple, T_{ripp} comparison.

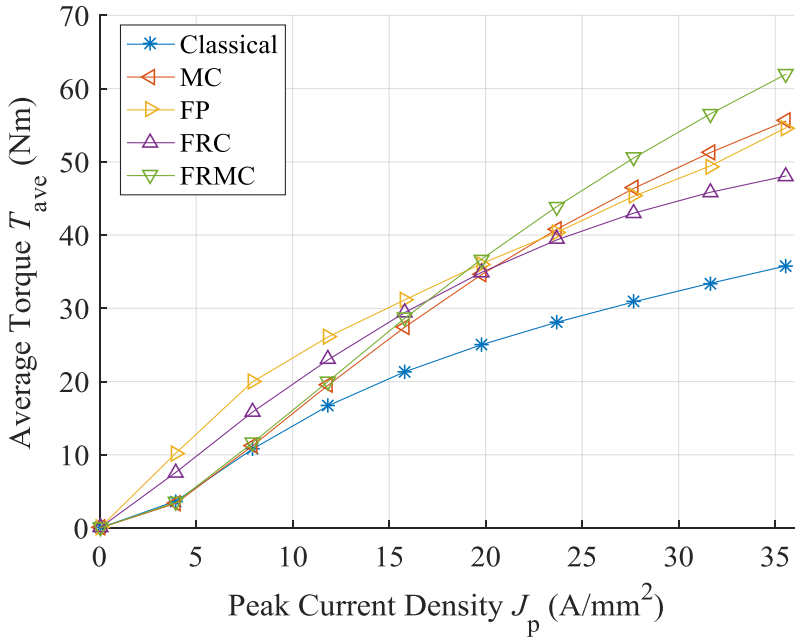

(a)

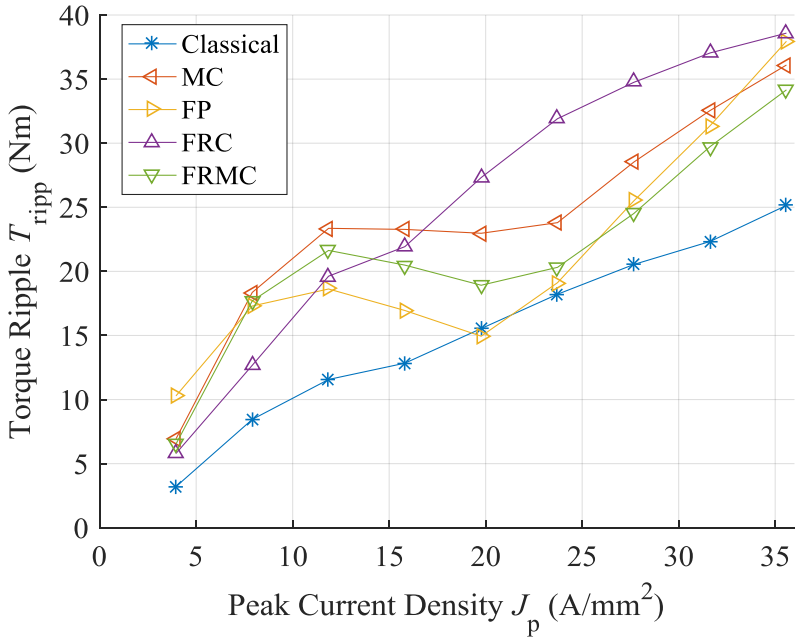

(b)

Figure 2.11. Classical, MC, FR, FRC and FRMC winding performances under SQ2 current excitation vs. peak current density, J_p. (a) Average torque, T_{ave}, (b) torque ripple, T_{ripp} comparison.

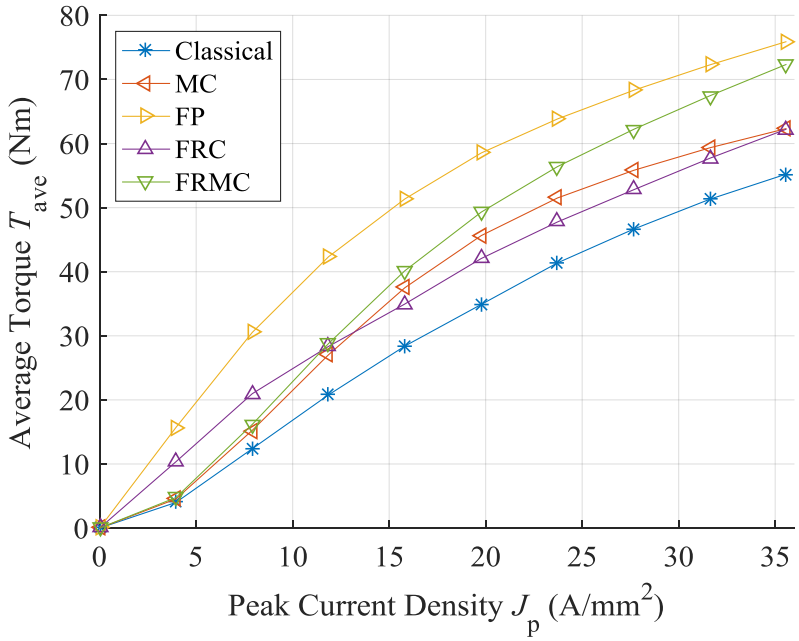

(a)

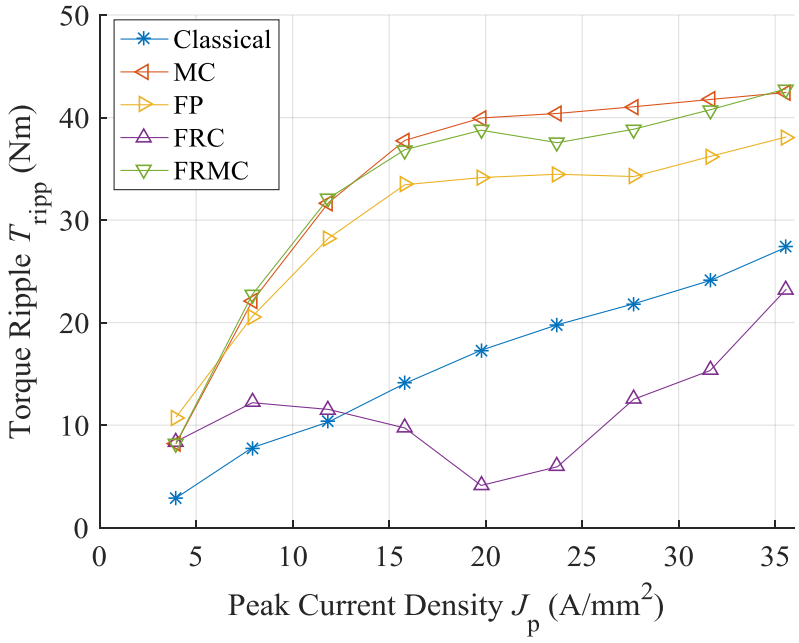

(b)

Figure 2.12. Torque performance under USQ excitation for Classical SRM and SQ_η_{opt} excitation for MC, FR, FRC, FRMC vs. peak current density, J_p. (a) average torque, T_{ave}, (b) torque ripple, T_{ripp} comparison. The conduction angle, η_{opt} are 168, 176, 156 and 168 electrical degrees for MC, FR, FRC and FRMC, respectively.

2.2.5 Torque versus Copper Loss

Since copper loss is the dominant loss under most operating condition, torque normalised for copper loss is are compared on all windings to evaluate their efficiency.

Different winding configurations have different end winding lengths and resistances for the same number of turns per coil, N, and different excitation waveforms have different RMS values for the same peak value, J_p. As a result, the copper losses, P_{cop} under the same J_p are often different.

A schematic drawing of winding is shown in figure 2.13. The winding lengths and resistances are listed in table 2.2.

Winding	*R*	*L*	*S*	*W*	*C*	*E*	Ave. Length per turn	*R* (Ω)
Classical/MC	6.895	91.9	5.415	11.46	0	201.33	228.38	0.1649
FRC/FRMC	6.895	114.82	5.415	11.46	17.90	183.43	327.48	0.2346
FP	6.895	114.82	5.415	11.46	43.382	121.55	384.07	0.2735

Table 2.2. Lengths and resistance of one coil in the classical, MC, FR and FP windings. Unit: mm; Number of Turns, N = 41; Copper resistivity, ρ = 0.02359 Ω mm²/m (at 120°C); Copper winding cross sectional area, S = 1.368 mm².

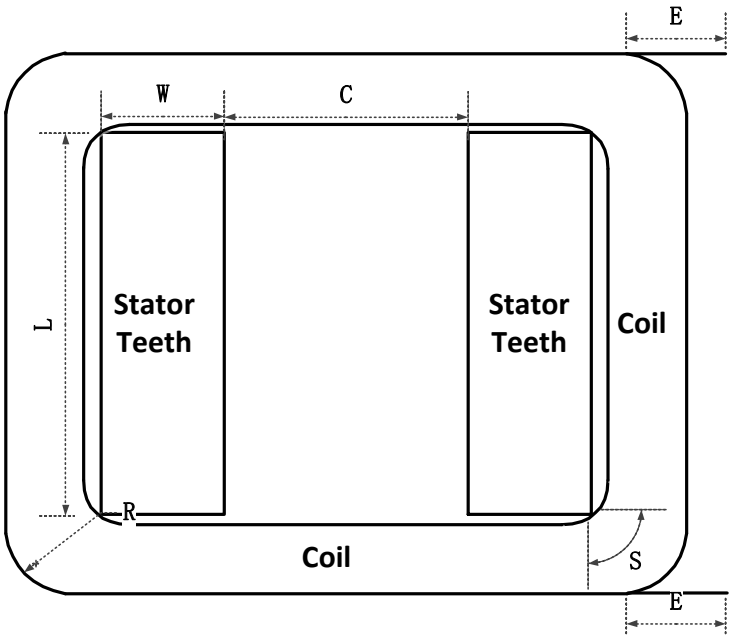

Figure 2.13. Diagram of one coil on the stator.

Figure 2.14 (a) (b) and (c) displays the average torque, T_{ave} of the proposed windings under SIN, SQ2 and SQ_η_{opt} current excitation versus copper loss, P_{cop}, respectively. The classical winding is plotted as a reference. For SIN excitation, the MC winding gives the highest T_{ave} to P_{cop} ratio, followed by the FRMC, while the classical winding has the worst performance. Compared with the MC, FRC and FP windings perform slightly better at low P_{cop}, but saturate much faster.

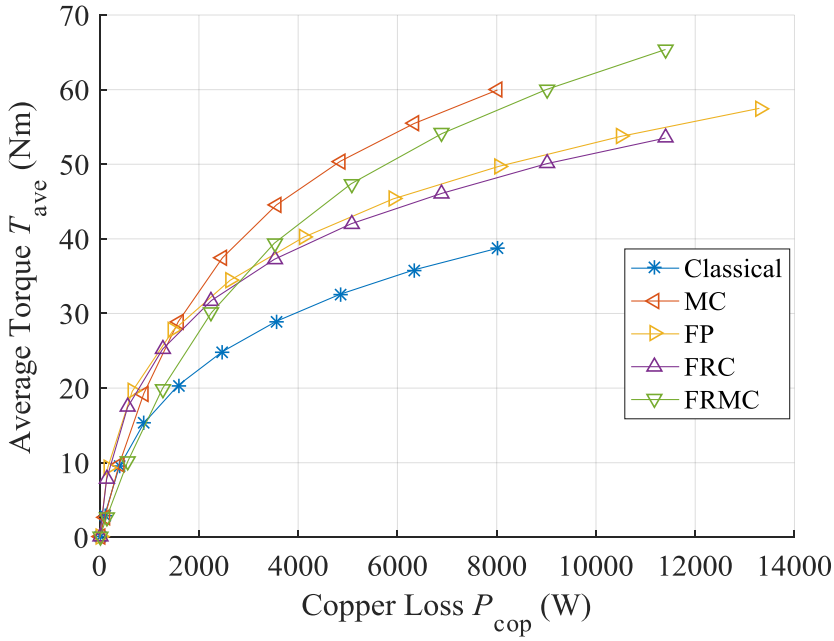
Average Torque T_{ave} (Nm)
Copper Loss P_{cop} (W)
0
10
20
30
40
50
60
70
0
2000
4000
6000
8000
10000
12000
14000
Classical
MC
FP
FRC
FRMC

(a)

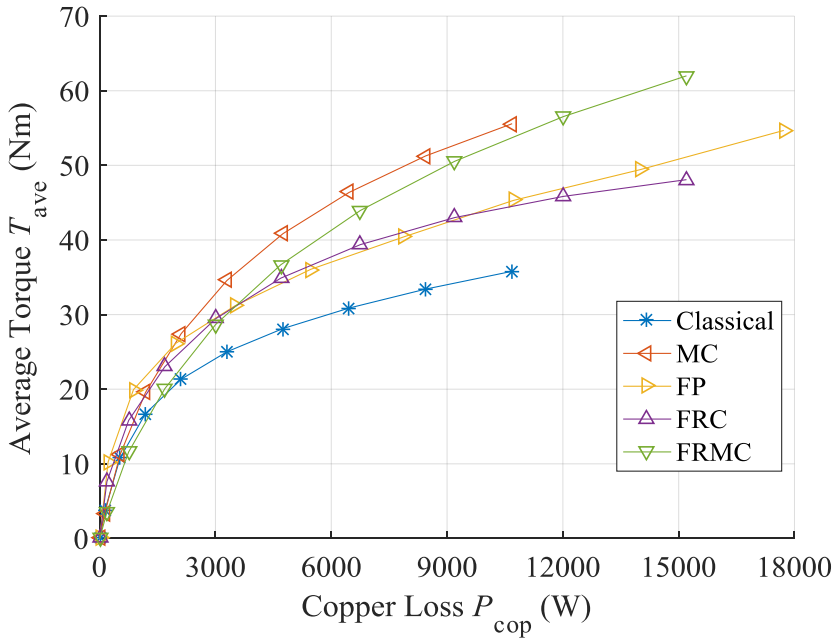
Average Torque T_{ave} (Nm)
Copper Loss P_{cop} (W)
0
10
20
30
40
50
60
70
0
3000
6000
9000
12000
15000
18000
Classical
MC
FP
FRC
FRMC

(b)

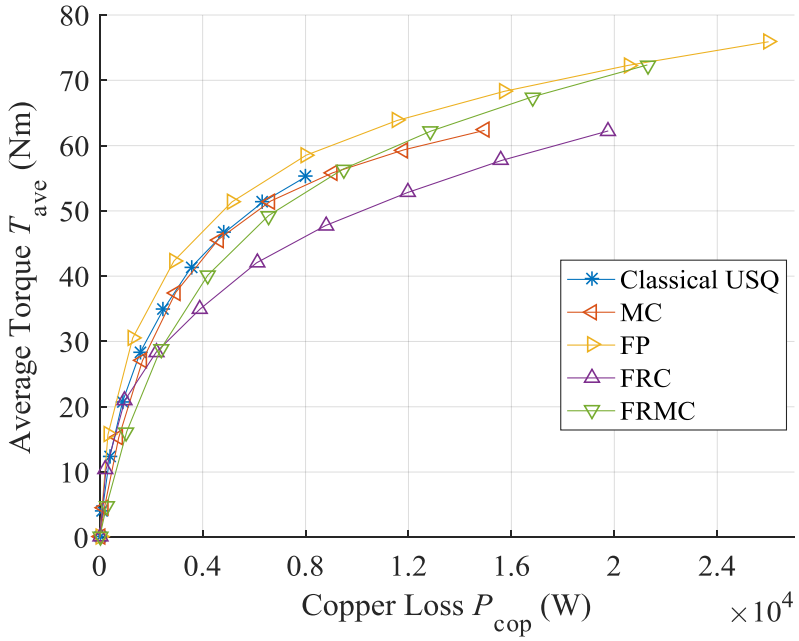

(c)

Figure 2.14. Average torque, T_{ave}, to copper loss, P_{cop}, ratio of Classical, MC, FR and FP windings vs. copper loss, P_{cop}, with (a) SIN; (b) SQ2; (c) SQ_η_{opt} current excitations.

Comparison of figure 2.14 (a) and (b) shows that SQ2 excitation has lower T_{ave} to P_{cop} ratio than SIN excitation at all copper loss levels and therefore will not be discussed further.

For the SQ_η_{opt} excitation in figure 2.14 (c), the FP winding produces the highest T_{ave} to P_{cop} ratio. The MC and classical windings with USQ excitation have similar performance. The FRMC winding only shows advantage at high copper loss and the FRC winding has the most unfavourable feature of all.

In figure 2.15, the most promising winding and excitation combinations are plotted on the same graph. Compared with the classical winding under USQ excitation, improvement in T_{ave} to P_{cop} ratio is found by SIN excitation with the MC winding at medium to high copper loss level, or by using SQ_η_{opt} excitation on an FP winding at low to medium copper loss level.

From this study, compared with the classical winding, similar or even better torque and loss performance can be achieved by using an MC winding and a bipolar sinusoidal current excitation, where conventional AC machine theory and a low cost AC inverter can be used. This

is expected to considerably reduce the price point of the SRM drive by reducing the non-recurring engineering costs and part count in the power electronics.

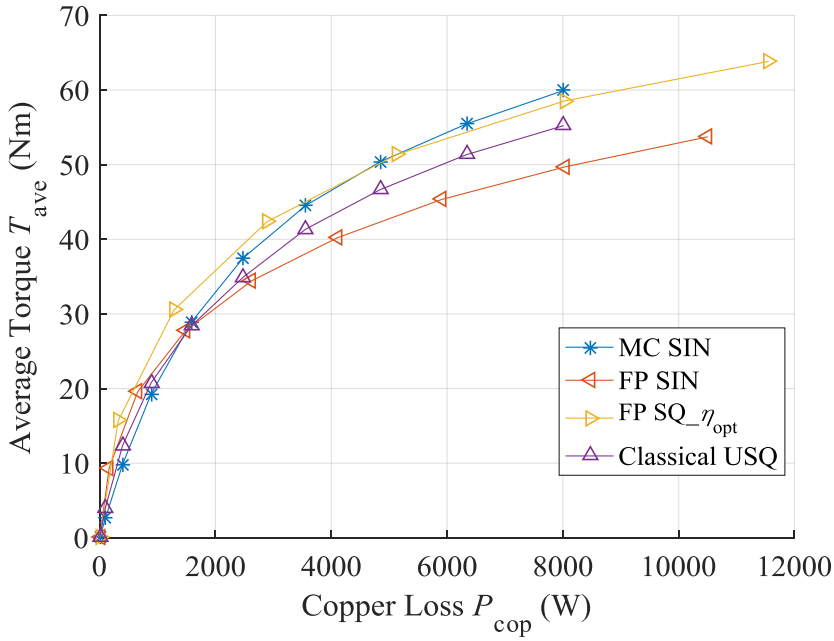

Figure 2.15. Average torque, T_{ave}, to copper loss, P_{cop}, ratio of the CSRM under USQ; the MCSRM under SIN; the FPSRM SIN and the FPSRM under SQ_η_{opt} current excitations windings vs. copper loss, P_{cop}.

2.3 Application of AC Machine Theory

The ISG is a voltage sensitive application, so apart from high efficiency and high torque density, a suitable machine also requires a wide field weakening region. This helps to reduce the size of the machine and increase the power density. Moreover, a high power factor (PF) is favoured to reduce the VA ratings of power electronic components.

The previous section focused on the torque capability and copper loss characteristics of the SRM. In this section, AC sinusoidal current excitation is implemented on all winding topologies, where doubly salient reluctance machines excited with sinusoidal AC current is treated as a conventional synchronous reluctance machine (SynRM) [88, 129]. With the help of SynRM theory, the machine's power factor and field weakening capabilities are considered.

2.3.1 Inductances Comparison

The d-axis inductance, L_d and q-axis inductance, L_q of different windings versus peak current

density, J_p are plotted in figure 2.16. The saliency ratio, ε under MTPA operation versus J_p for all windings is plotted in figure 2.17.

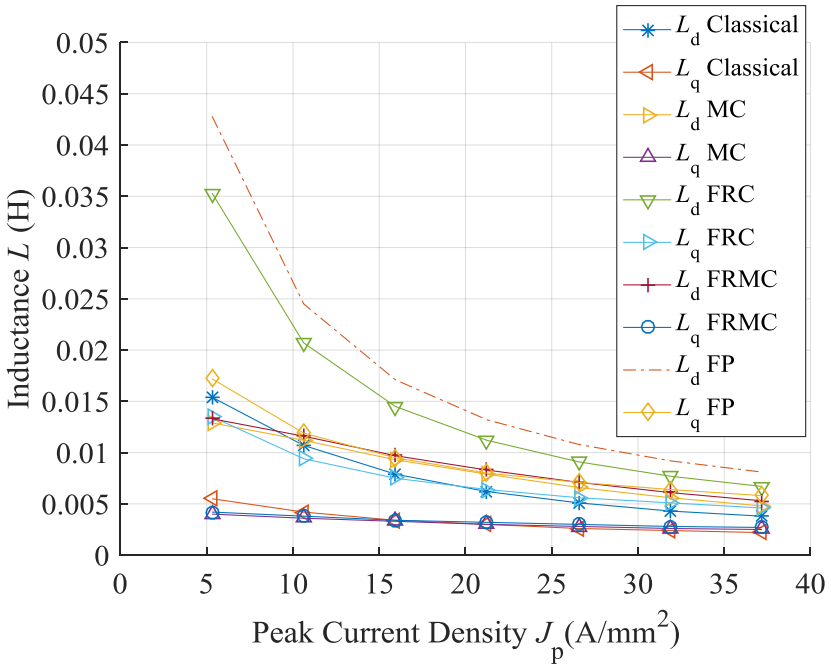

Figure 2.16. d and q axis inductances, L_d, L_q, vs. peak current density, J_p for Classical, MC, FRC, FRMC and FP winding.

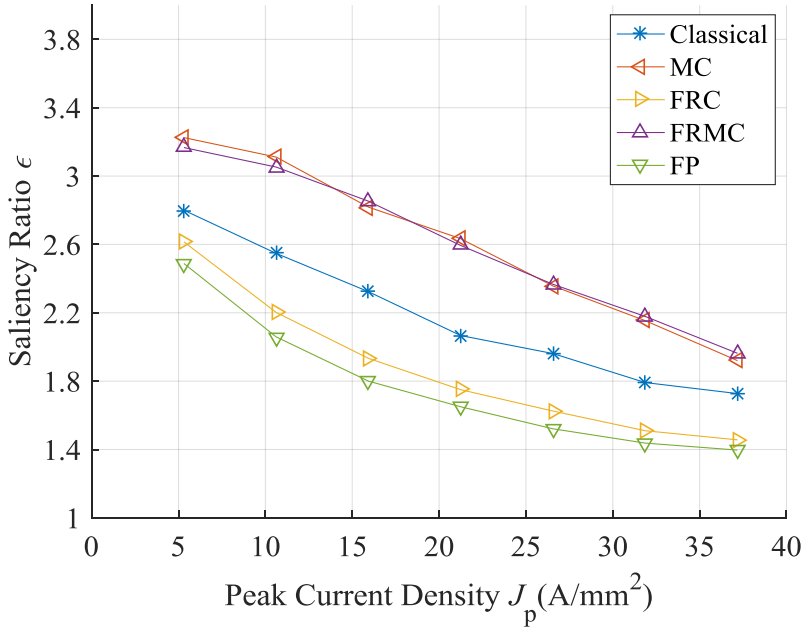

Figure 2.17. Saliency ratio, ε, vs. peak current density, J_p for Classical, MC, FRC, FRMC and FP winding.

From the figures, ε drops with increasing J_p due to saturation effects. In all winding types, ε are lower than 3.4. According to the AC machine theory described in section 1.2.3, this suggests a low IPF and CPSR. Among them, the MC and FRMC windings have comparatively better performance than other types.

2.3.2 Field Weakening Capability

From table 1.4 in section 1.3.1, the benchmark Speedstart machine has a rated mechanical power, P_{mech} of 5 kW and the base speed, ω_b of 2000 rpm. From section 1.2.3, at constant current, flux decreases with the increasing load angle from 45°, so induced voltage, e is limited with the increase of speed and field weakening is achieved. The machine operating at the rated power and base speed under MTPA condition is considered as a reference, the rated current and voltage is denoted as i_{rtd} and e_{rtd}. At operational speed, ω, the corresponding IPF and e to e_{rtd} ratio versus ω to ω_b ratio in the classical and MC windings are plotted in figure 2.18 (a) (b), respectively.

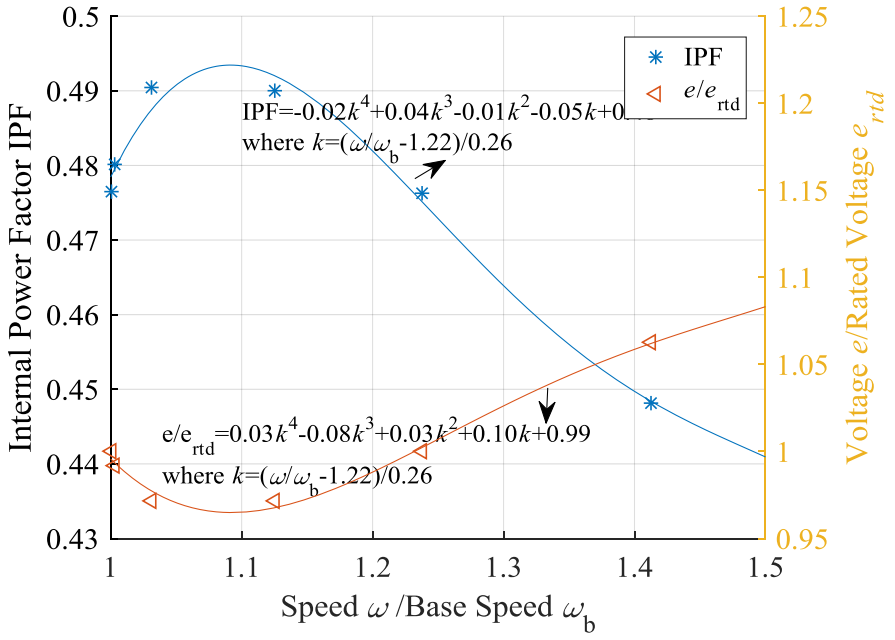

(a)

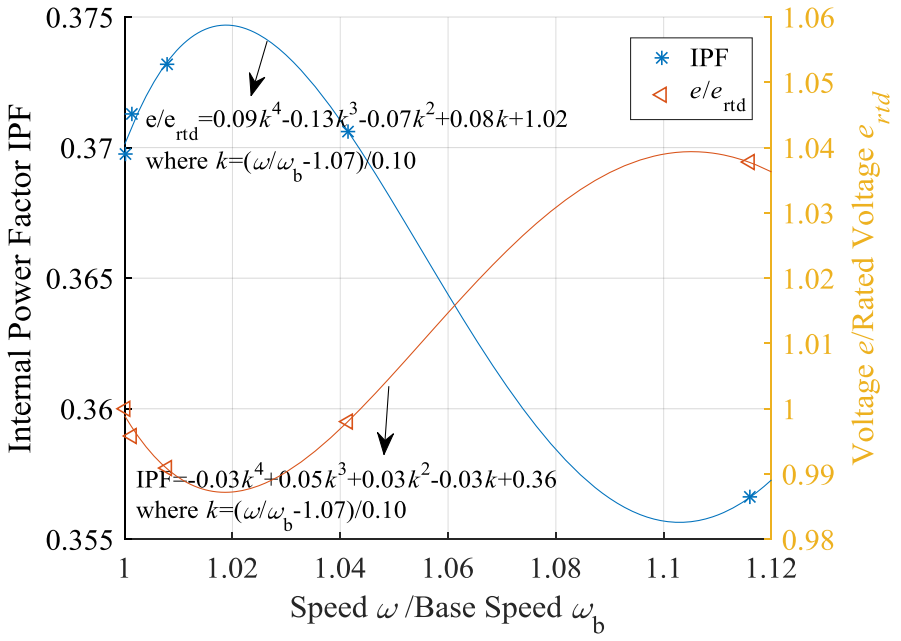

(b)

Figure 2.18. Internal power factor, IPF and induced voltage, e, to rated induced voltage, e_{rtd}, ratio vs. speed, ω, to base speed, ω_b, ratio for (a) MCSRM and (b) CSRM.

From the figures, each ω in field weakening region corresponds to a IPF value, and the maximum speed for constant power, ω_{fw}, should have a IPF value same as base speed. Since ω_{fw} to ω_b ratio is CPSR, using curve fitting method, CPSR of different windings can be derived from the figures. For the MC winding, CPSR is 1.230, so ω_{fw} for MC winding is 2460 rpm. For the classical winding, CPSR is 1.045, so ω_{fw} for classical winding is 2090 rpm. The IPF at ω_{fw} is 0.476 for the MC winding, and 0.370 for classical winding.

Using the method described above, the IPF and CPSR for all windings are plotted against J_p in figures 2.19, and against average torque, T_{ave} in figure 2.20.

From figure 2.19, with an increasing current, all IPF and CPSR decrease due to the saturation influence on saliency ratio. Among them, the IPF of the MC and FRMC windings are the highest, followed by the classical winding, the FRC, and the FP winding yield lowest values.

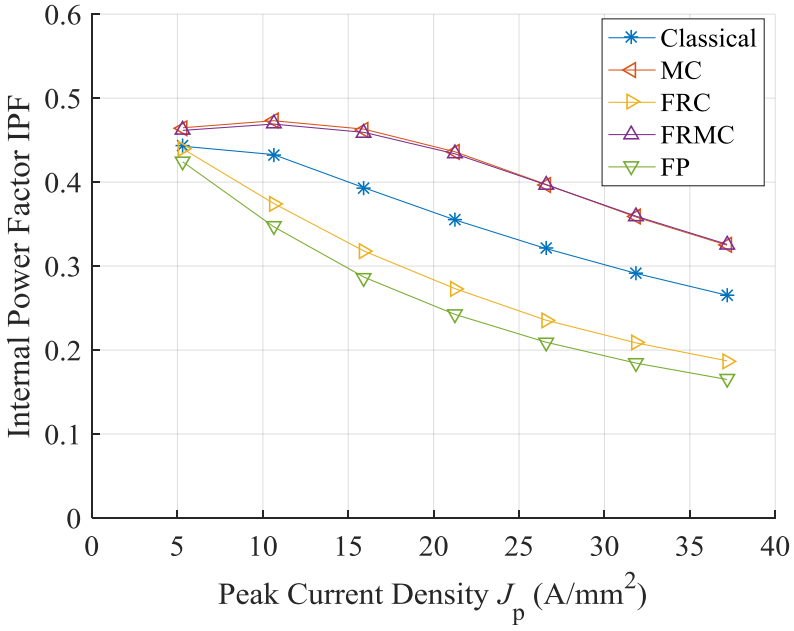

(a)

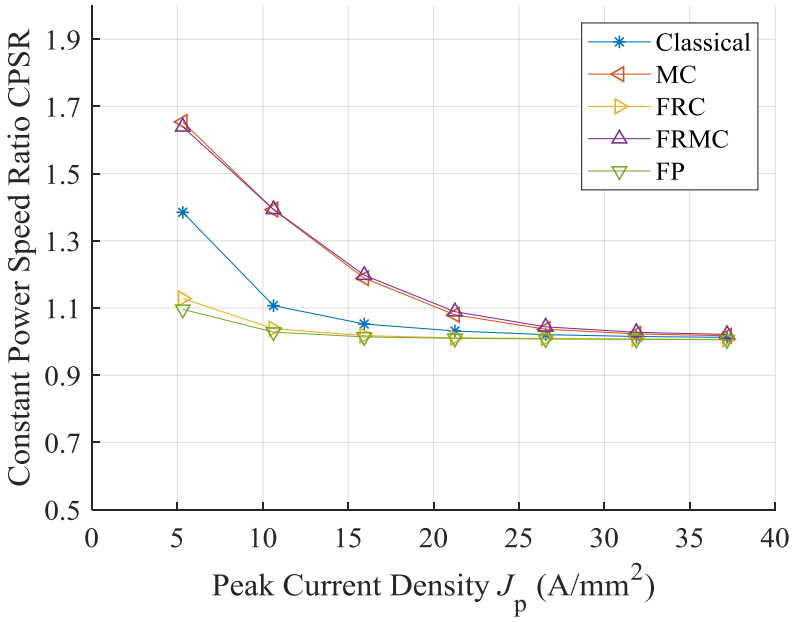

(b)

Figure 2.19. (a) Internal power factor, IPF and (b) Constant power speed ratio, CPSR, of classical, MC, FRC, FRMC and FP under SIN excitation vs. peak current density, J_p.

From figure 2.20, both IPF and CPSR versus T_{ave} provide two distinctive sets of values, where the MC and FRMC windings form one group. The classical, FRC and FP windings form the other group. The first group provides significantly higher values than the second.

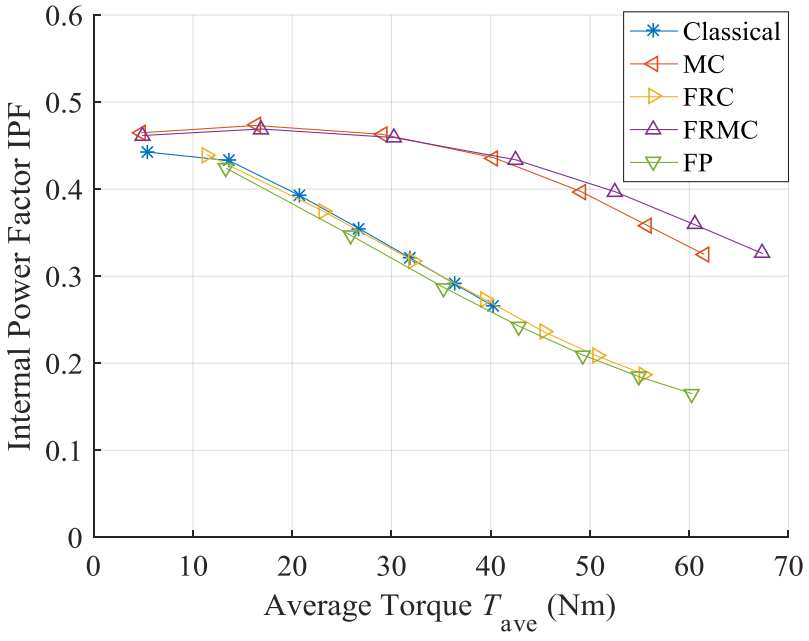

(a)

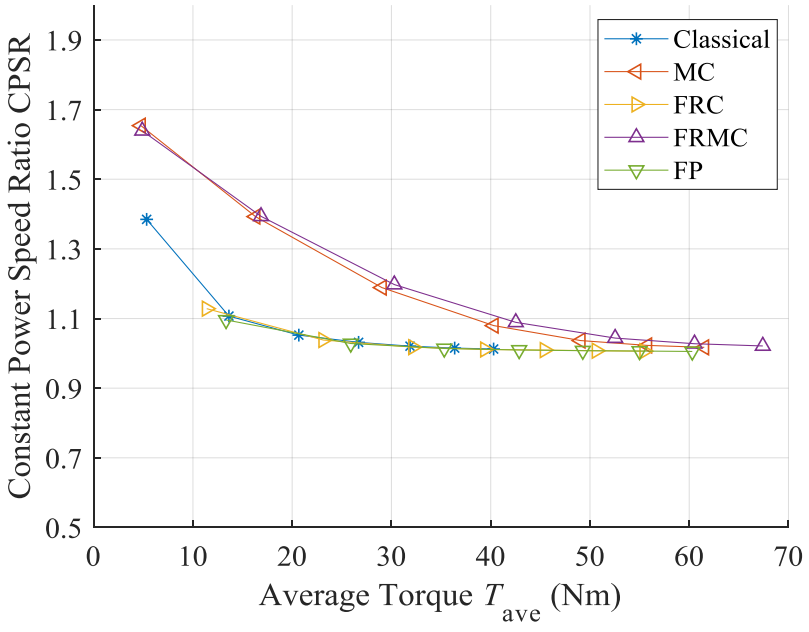

(b)

Figure 2.20. (a) Internal power factor, IPF and (b) Constant power speed ratio, CPSR of the classical, MC, FRC, FRMC and FP under SIN excitation vs. torque.

2.4 Summary

This chapter investigates the influences of winding topologies and excitation on the

performance of the SRM. The contributions are threefold. First, a novel winding topology named fractional pitched mutually coupled (FRMC) winding is proposed. Second, bipolar current excitation with both square and sinusoidal shapes are compared on different winding configurations including short pitched mutually coupled, full pitched, fractional pitched mutually coupled and fractional pitched classic. Last, the machine features under AC sinusoidal current are investigated, where conventional AC machine theory is applied for power factor and CPSR prediction. From the analysis in this chapter, several conclusions have been reached.

(1) Compared with the classical winding, the introduction of short pitched mutually coupled, fully pitched, fractional pitched mutually coupled and fractional pitched conventional windings allows an improvement in torque production capability for the same current density or copper loss.
(2) To achieve a high torque, bipolar current excitation is applied, where square current with optimum conduction angle generates a higher torque density than AC sinusoidal current. However, the sinusoidal current is favoured over the square current as it facilitates the application of conventional AC machine theory and a standard inverter topology. The short pitched mutually coupled winding works better for AC sinusoidal currents, and the fully pitched winding works better for bipolar square currents.
(3) Implementation of an AC sinusoidal current brings problems of low power factor and low field weakening capability. Among all the windings, the short pitched mutually coupled and fractional pitched mutually coupled windings perform best, but the internal power factor is still smaller than 0.5, and the CPSR is lower than 1.7.

Overall, in all windings investigated the short pitched mutually coupled winding performs best under AC sinusoidal current in terms of torque, power factor and field weakening ability.

3. Mutually Coupled Switched Reluctance Machine

In the last chapter, different winding topologies and current excitations waveforms were studied on the benchmark Speedstart 12/8 switched reluctance machine iron core to evaluate the performance in terms of torque capability and possibility of using conventional AC inverter. By implementing the mutually coupled winding and AC sinusoidal excitation, the same machine iron core produces comparable, even higher average torque than a unipolar square current excited classical winding for the same copper loss. The disadvantage of the mutually coupled winding is the larger torque ripple, low power factor and very limited field weakening capability.

In this chapter, the influence of geometry on sinusoidal AC excited mutually coupled switched reluctance machine performance of efficiency, power factor, and constant power speed ratio is investigated and discussed.

3.1 Geometry Optimization

In this section, the machine geometries are optimized for minimum copper loss. The geometry parameters under investigation are illustrated in figure 3.1 and listed in table 3.1.

The optimization process is carried out at base speed and rated mechanical power. The outer radius, l_{sr} and axial length, l_{al} are fixed due to application restrictions. It is assumed that the machine performance changes continuously with geometry, so least square curve fitting is applied to determine the optimum point in geometry change.

3.1.1 Iron Loss Determination

In the case of benchmark Speedstart machine, the three phases current waveforms versus rotor mechanical position, ζ_m are shown in figure 3.2. The radial direction (RD) and tangential direction (TD) flux density waveforms at four typical positions is illustrated in figure 3.1 and plotted in figure 3.3.

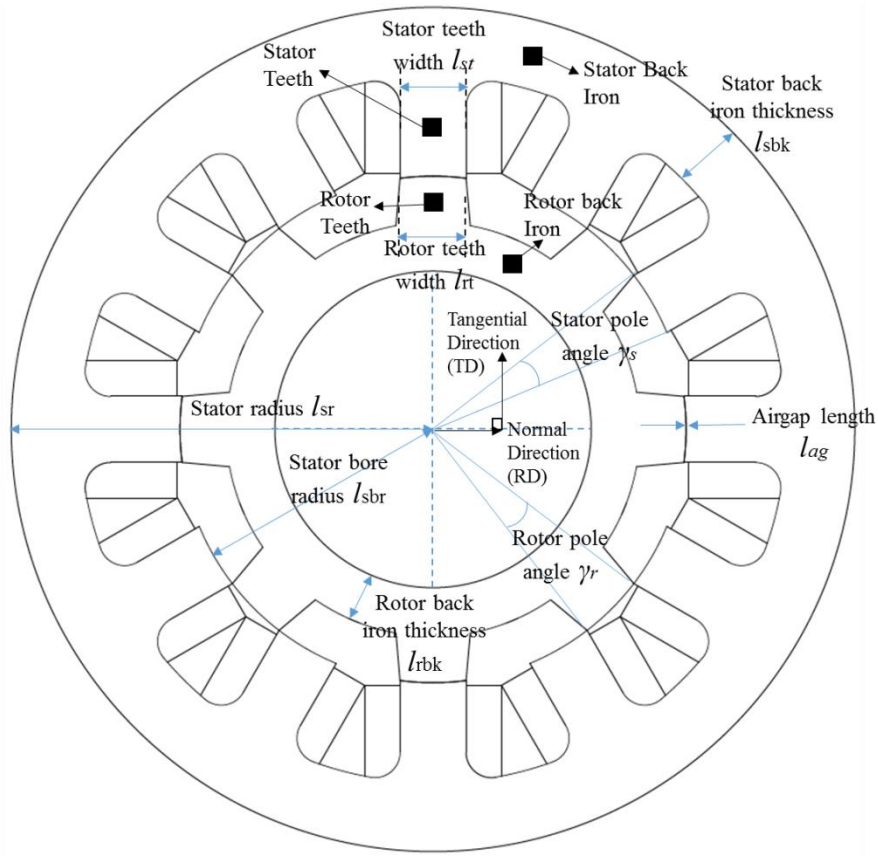

Figure 3.1. Geometry parameters in the machine optimized process.

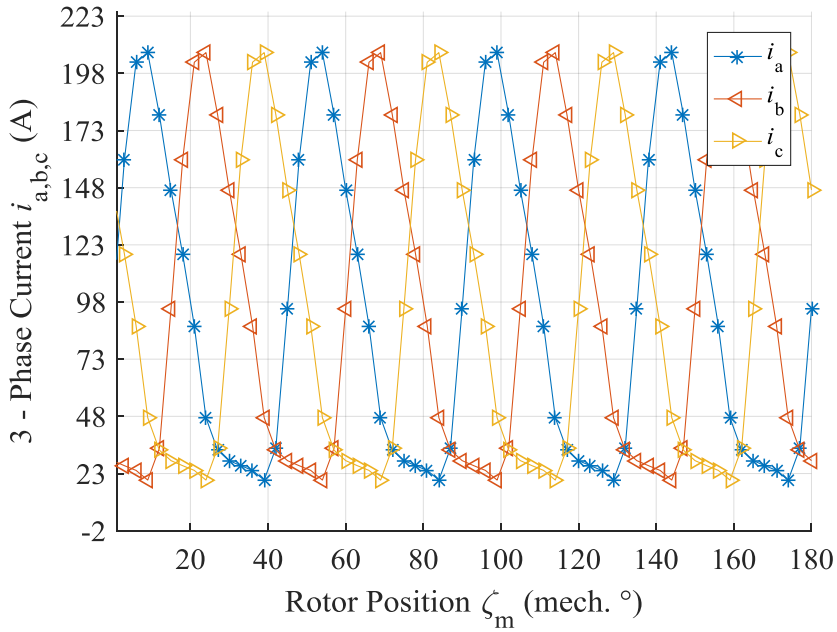

Figure 3.2. Three - Phase current, i_a, i_b, i_c of classical switched reluctance machine (CSRM) vs. rotor position, ζ_m.

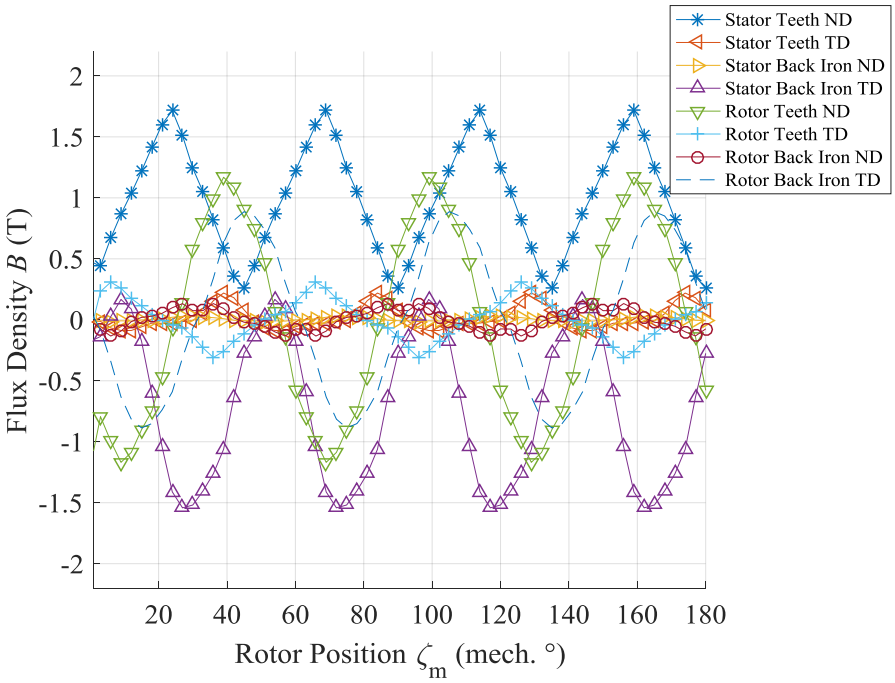

Figure 3.3. Normal direction (ND) and tangential direction (TD) flux density, B, at various positions on iron core displayed in figure 3.1 vs. rotor position, ζ_m of classical switched reluctance machine (CSRM) under unipolar current excitation (USQ) as shown in figure 3.2.

The flux density on the rotor is bipolar, at a fundamental frequency 3/4 times of the excitation current. Neglecting minor loops, conventional hysteresis model in (1.19) from section 1.2.4 can be directly applied. Unlike rotor, stator flux density waveforms has unipolar pulsive pattern, which has the same frequency as the excitation current. To evaluate its hysteresis loss, the flux density pulses are recognised as minor loops, where a modification of the hysteresis item is applied according to (1.24).

In the case of CSRM and MCSRM under SIN excitation, RD and TD flux density waveforms at the four positions in figure 3.1 are plotted in figure 3.4 (a) and (b).

For CSRM, bipolar flux density pattern is observed on both stator and rotor. On the stator, the flux density has a fundamental frequency same as the excitation current. On the rotor, the frequency is 3/2 times larger. For MCSRM, on the stator, bipolar flux density waveforms pulse at same the frequency as excitation current. On the rotor, a DC bias is exhibit where small fluctuations are present. From the flux patterns, conventional hysteresis model in (1.19) can be directly applied to CSRM and MCSRM stator, as minor loops are small compared with the

major bipolar flux density excursion. On MCSRM rotor, flux fluctuation is small compared with DC bias, so minor loops are neglected, hysteresis loss is therefore considered zero.

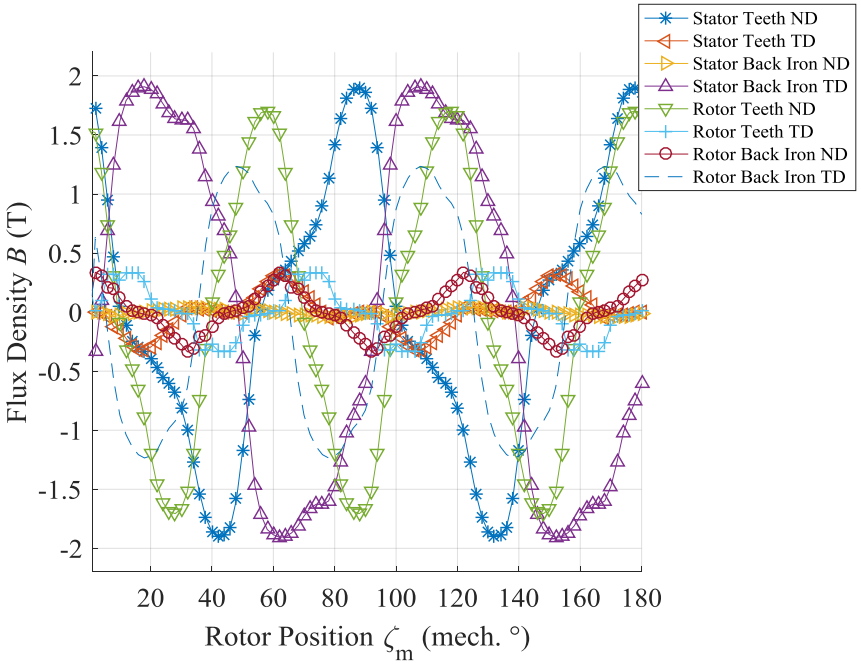

(a)

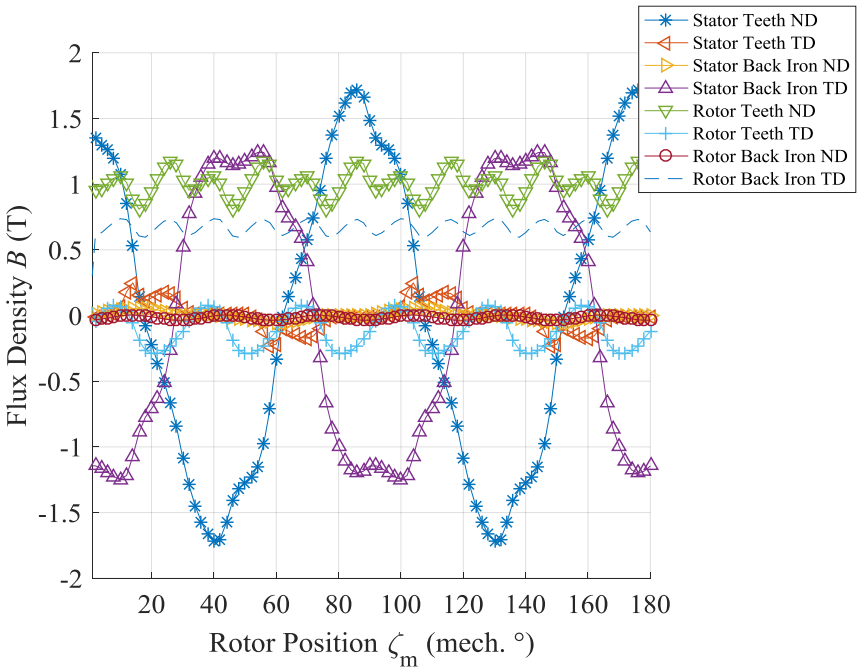

(b)

Figure 3.4. Normal direction (ND) and tangential direction (TD) flux density, B at various positions displayed in figure 3.1 vs. rotor position, ζ_m of (a) classical and (b) mutually coupled switched reluctance machine under sinusoidal AC (SIN) excitation at 5 kW and 2000 rpm.

The coefficients in the Bertotti equation shown in (1.20) from section 1.2.4 can be obtained either from the material datasheet or by surface fitting of loss data provided by manufacture. For M400-50A laminated steel, 2D curve fitting of peak flux density from 0.5 T to 1.5 T and frequency from 50 Hz to 1000 Hz is shown in figure 3.5. The coefficients from surface fitting are listed in table 3.1.

Symbol	Value (Unit)
k_h	110.2 ($WsT^{-2}m^{-3}$)
σ	2380952.4 (S/m)
k_e	1.27626 ($W(Ts^{-1})^{-3/2}m^{-3}$)
α	2.5

Table 3.1. Bertotti loss coefficients of M400-50A in (1.19).

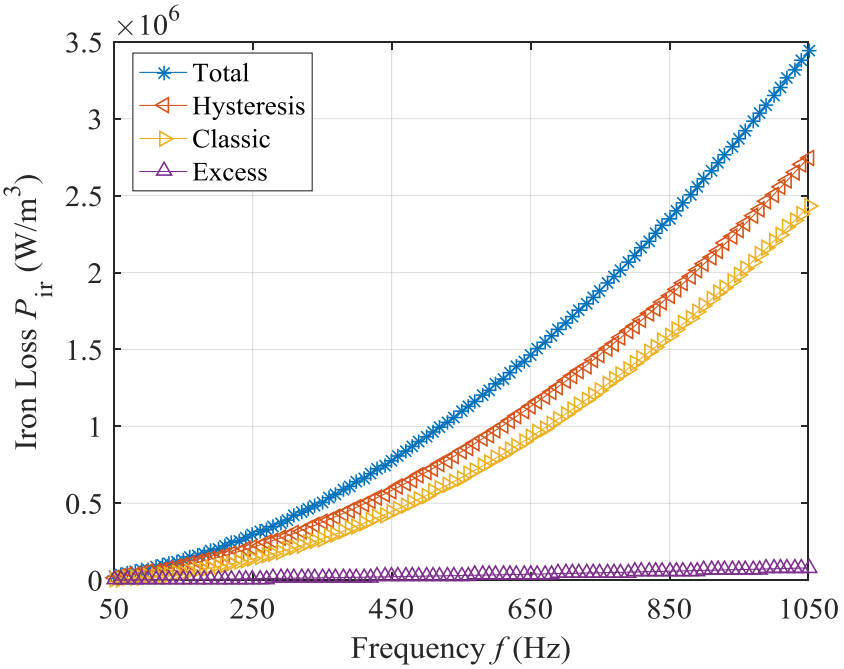

Figure 3.5. Iron loss, P_{ir}, components vs. frequency, f at peak flux density, B_p of 1.5 T.

3.1.2 Optimization Procedure

In previous investigation of the winding topologies, original machine dimensions from Speedstart are implemented. This section discusses the influences of crucial parameters in torque, IPF and CPSR. The dimensions under investigation are marked in figure 3.1.

Stator back iron thickness, l_{sbk} is a crucial parameter in torque performance. If the stator back iron is too thick, it occupies winding area, causing increases in copper loss. If it is too thin, large saturation is presented, limiting the flux in poles.

Figure 3.6 plots the total loss, P_l versus l_{sbk} and the fitting equation. Derivative of the equation gives the minimum P_l of 1042 W at l_{sbk} of 6.408 mm. The optimum l_{st} to l_{sbk} ratio is 1.79.

The rotor and stator pole widths plays an important part in machine performance. In the MCSRM, the rotor pole angle, γ_r should be slightly larger than that of the CSRM to provide a wider path for the mutual flux [85]. The stator pole angle, γ_s selection is a trade-off between coil flux and winding area, where, for every γ_r, an γ_s for minimum loss exists.

The P_l versus γ_r and γ_s is plotted in figure 3.7 with the 2D surface fitting equation. Taking partial derivative of the equation yields a minimum loss stator pole angle of 13.83° and a rotor pole angle of 21.04°. The minimum loss is 941.2 W.

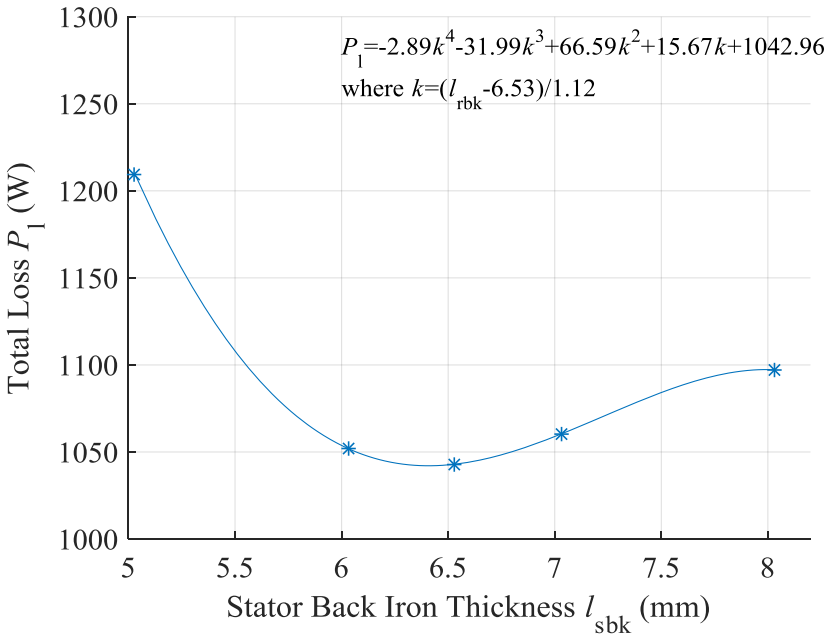

Figure 3.6. Loss, P_l vs. stator back iron thickness, l_{sbk}.

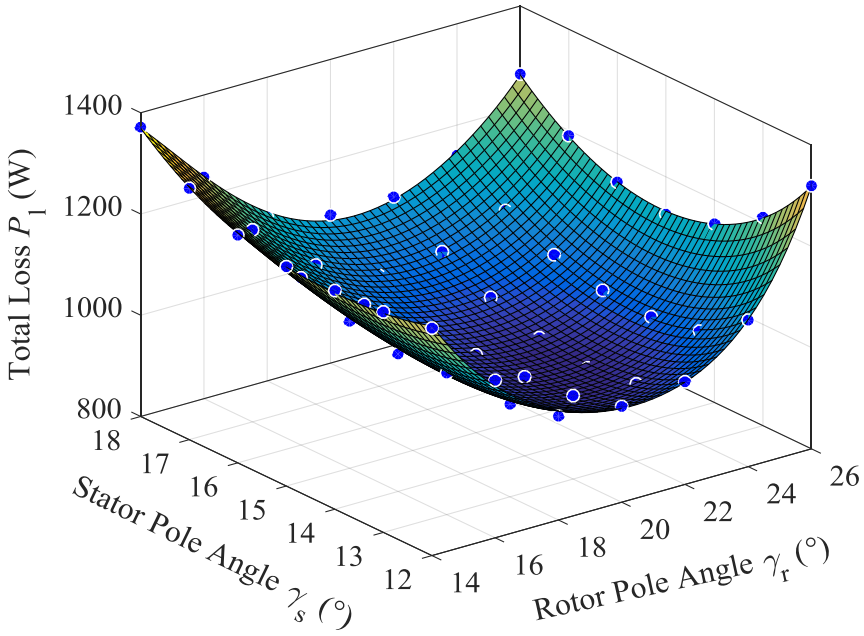

Figure 3.7. Loss vs. stator pole angle, γ_s and rotor pole angle, γ_r. The fitted polynomial is Loss=959.7-49.02k + 38.68h + 85.88k² - 1.563kh + 28.04h² - 2.081k³ + 6.414k²h + 7.166kh² + 0.1919h³ + 6.871k⁴ - 4.42k³h + 9.37k²h² - 3.681kh³ + 2.466h⁴ + 4.074k⁵ - 9.017k⁴h + 1.831k³h² + 1.479k²h³ + 0.4745kh⁴ - 1.351h⁵ where k = (γ_r - 20) / 4.41 and h = (γ_s - 15) / 2.021.

The split ratio is defined as the ratio between stator bore radius, l_{sbr} and stator radius, l_{sr}. With an increasing split ratio, torque is increased for the same tangential airgap force at the price of a reduction in stator winding area. The total loss, P_l versus split ratio is plotted in figure 3.8. Derivative of the curve fitting equation gives an optimum l_{sbr} of 45.557 mm, where the minimum loss is 937.22 W. The optimum split ratio is 45.557/68.1 = 0.669.

The machine's axial length, l_{al} is fixed at 80.5 mm due to application restrictions, but it is interesting to see how the change in l_{al} affects loss production. Figure 3.9 (a) (b) plots the P_l versus l_{al} and peak current density, J_p. Noticeably, significant reduction in P_l is observed with an increasing of l_{al}, especially when l_{al} < 180 mm. At l_{al} of 230 mm, P_l is about 615 W. Further increase does not affect total loss very much. J_p also drops as l_{al} increases, and the rate of reduction decreases as l_{al} increases.

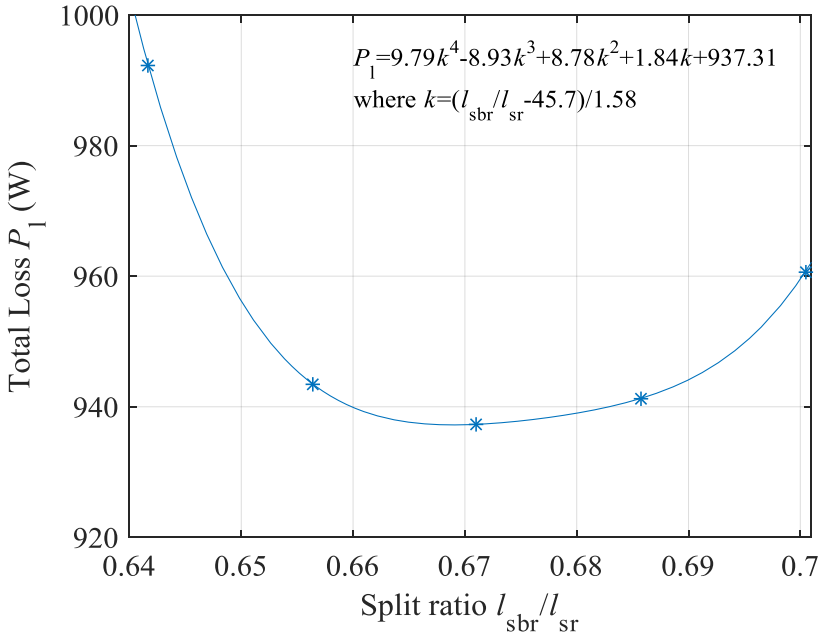

Figure 3.8. Loss, P_l vs. split ratio, l_{sbr} / l_{sr}.

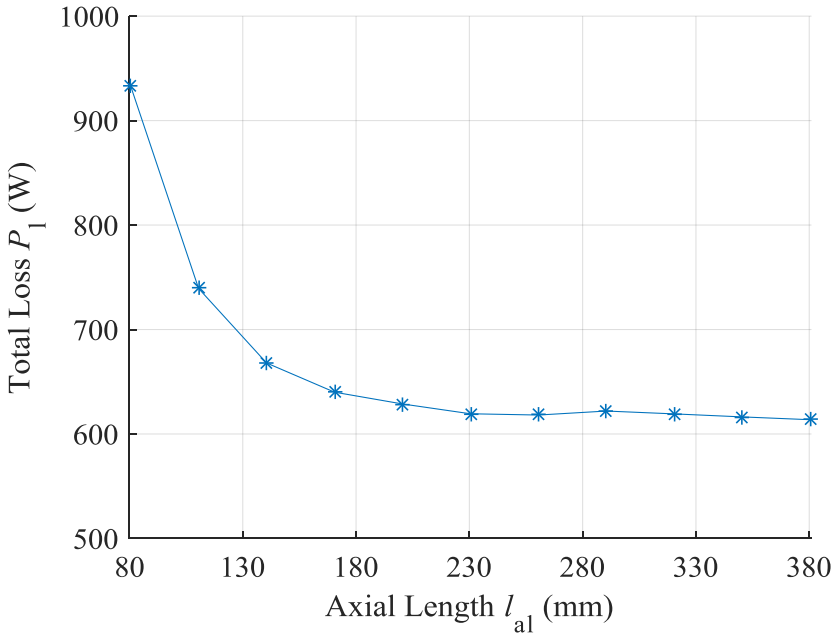

(a)

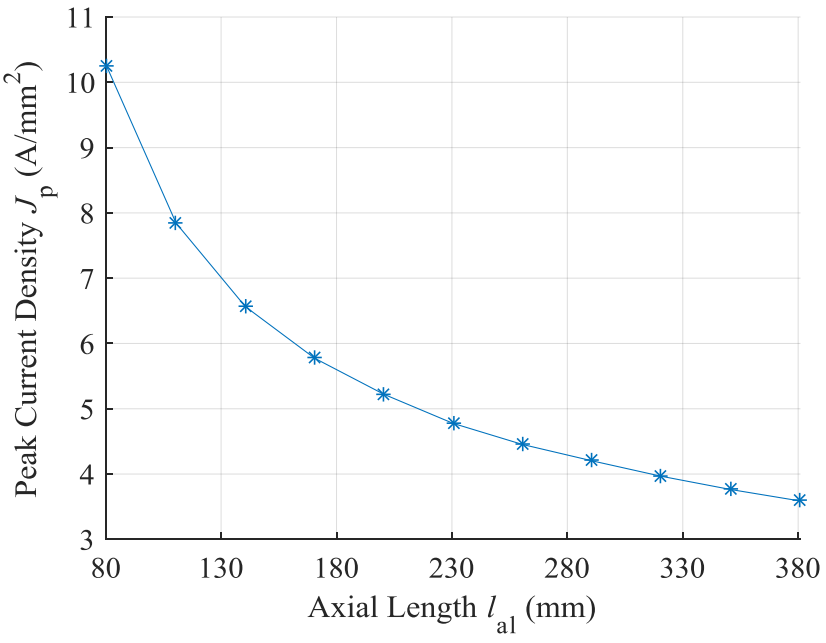

(b)

Figure 3.9. (a) Loss, P_l vs. axial length, l_{al} and (b) peak current density, J_p vs. axial length, l_{al}.

The comparison of the studied geometries before and after optimization is shown in table 3.2. The comparison of different losses is listed in table 3.3. After optimization, the stator iron loss, P_{sir} and rotor iron loss, P_{rir} both increase, and the copper loss, P_{cop} decreases. Since the iron loss only accounts for a small proportion of total loss at rated speed, the decrease in P_{cop} outweighs the increase in P_{ir}. After optimisation, the total loss, P_l is reduced from 1254.6 W to 933.2 W at a l_{al} of 80.5 mm, and 619.3 W at a l_{al} of 230.5 mm. The efficiency increases from 79.9% to 84.1% at a l_{al} of 80.5 mm, and 88.6% at a l_{al} of 230.5 mm.

	γ_s (°)	γ_r (°)	l_{sbk} (mm)	l_{sbr} (mm)	l_{sr} (mm)	l_{al} (mm)
Benchmark	14	21	8.03	46.7	68.1	80.5
Optimum	14.18	21.58	6.33	45.56	68.1	80.5

Table 3.2. Geometries of the MCSRM before and after optimization.

	P_{cop} (W)	P_{sir} (W)	P_{rir} (W)	P_l (W)	Efficiency (%)
Benchmark	1189.0	47.0	18.5	1254.6	79.9
Optimum l_{al} = 80.5 mm	841.9	69.0	22.2	933.2	84.1
Optimum l_{al} =230.5 mm	424.9	140.9	53.5	619.3	88.6

Table 3.3. Loss information at 5 kW and 2000 rpm of the MCSRM before and after optimization.

The average torque, T_{ave} before and after optimization versus P_l is plotted in comparison with the benchmark Speedstart machine in figure 3.10, where the Speedstart is driven by a half bridge inverter as shown in figure 1.8 (a), with a DC link voltage of 48 V. The switching angles are provided by FMPT. Compared with Speedstart, AC sinusoidal current generates lower loss above 30 Nm, and higher loss below 30 Nm. This result agrees with the conclusion drawn in section 2.2. Moreover, further loss reduction can be achieved with optimized geometry especially at low to medium torque levels, so compared with the Speedstart, the optimized MCSRM produces less loss at all torque level.

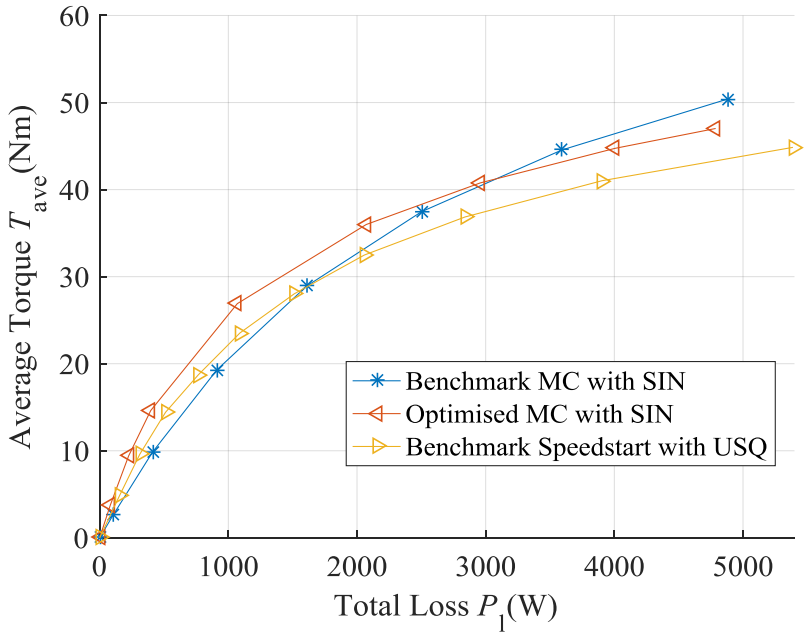

Figure 3.10. Average torque, T_{ave} vs. total loss, P_l for benchmark MCSRM with SIN excitation, optimized MCSRM machine with SIN excitation and Speedstart with USQ excitation.

3.2 Prediction of Power Factor and Field Weakening Capability

With fixed split ratio and stator teeth to stator back iron thickness ratio, in this section, the role of rotor pole angle, stator pole angle and axial length on internal power factor, power factor and constant power speed ratio (CPSR) is studied.

In section 2.3, the CPSR was prediction without loss. In this section, a prediction method that considers copper loss is introduced. Using this method, the performance of the machine is evaluated in terms of torque, field weakening capability and efficiency.

3.2.1 Geometric Influences

Rotor pole angle, γ_r and stator pole angle, γ_s play an important role in determining the power factor and CPSR. Figure 3.11 shows the IPF versus γ_r and γ_s with 2D surface fitting equation. In the majority of the region of interest, the IPF increases as γ_s increases and γ_r decreases, but this trend gradually diminishes, giving an optimum γ_s of 15.5° and γ_r of 16.6°. The maximum IPF is 0.506, compared with 0.469 in the benchmark machine. For the minimum total loss geometry, the IPF is 0.467.

The CPSR without losses versus γ_r and γ_s is plotted in figure 3.12. Like IPF, with the increase of γ_s and decrease of γ_r, CPSR also increase and plateaus. The CPSR of the minimum total loss geometry is 1.17, and the highest CPSR is around 1.37.

Figure 3.13 plots the relationship between CPSR and axial length, l_{al}, where the increase in l_{al} also increases the CPSR at a descending rate. If l_{al} increases to 230 mm, CPSR increases from 1.17 to 1.56.

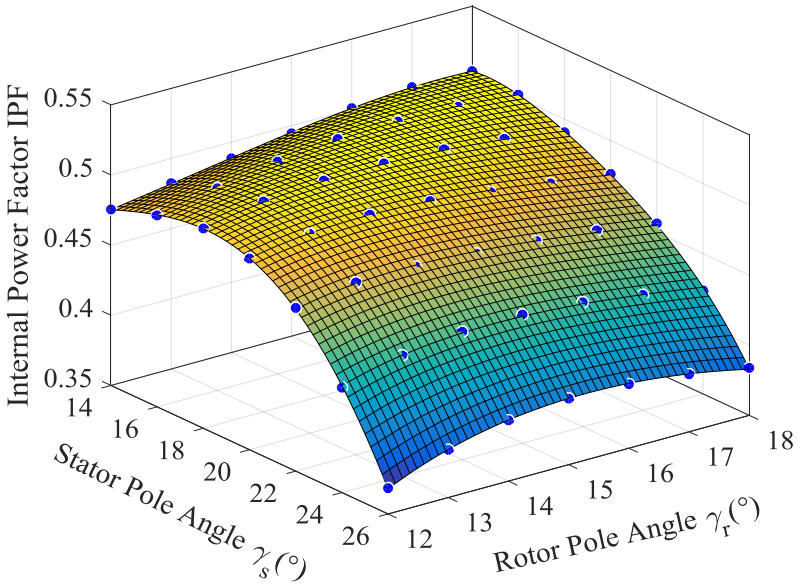

Figure 3.11. Internal power factor, IPF, vs. stator pole angle, γ_s and rotor pole angle, γ_r under rated operating condition. The fitted polynomial is IPF = 0.49 - 3.18×10^{-2}k - 6.15×10^{-3} h - 1.92×10^{-2}k^2 - 5.31×10^{-3}kh - 4.62×10^{-3}h^2 - 8.88×10^{-4}k^3 + 8.62×10^{-3}k^{2}h + 3.43×10^{-4}kh^2 + 1.02×10^{-3}h^3 - 7.49×10^{-4}k^4 + 9.00×10^{-4}k^{3}h - 5.55×10^{-4}k^{2}h^2 + 8.23×10^{-4}kh^3 - 1.87×10^{-4}h^4 + 1.50×10^{-4}k^5 - 1.109×10^{-3}k^{4}h - 1.25×10^{-3}k^{3}h^2 - 5.47×10^{-4}k^{2}h^3 - 1.74×10^{-5}kh^4 + 5.8×10^{-5}h^5 , where k = (γ_r - 20) / 4.041 and h = (γ_s - 15) / 2.021.

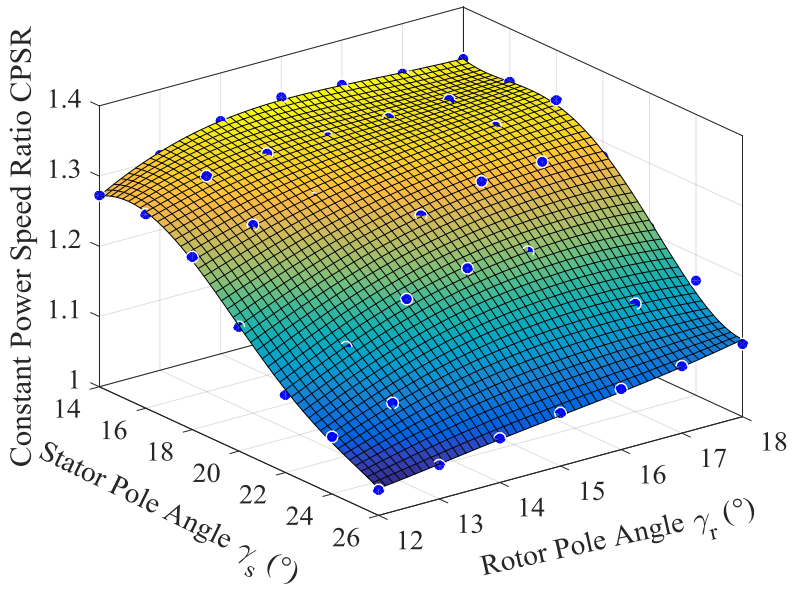

Figure 3.12. Constant power speed ratio, CPSR, without losses, vs. stator pole angle, γ_s and rotor pole angle, γ_r. The fitted polynomial is β=1.26 - 9.34×10^{-2}k + 3.43×10^{-2}h - 3.84×10^{-2}k^2 + 1.15×10^{-2}kh -1.50×10^{-2}h^2 + 7.58×10^{-3}k^3 - 2.86×10^{-2}k^{2}h - 1.28×10^{-2}kh^2 + 2.16×10^{-3}h^3 + 5.36×10^{-3}k^4 - 2.39×10^{-3}k^{3}h + 2.65×10^{-3}k^{2}h^2- 1.97×10^{-3}kh^3 + 3.81×10^{-4}h^4 - 2.67×10^{-3}k^5 + 8.18×10^{-3}k^{4}h + 8.39×10^{-3}k^{3}h^2 + 1.68×10^{-3}k^{2}h^3 + 2.81×10^{-4}kh^4 - 5.55×10^{-4}h^5, where k = (γ_r - 20)/4.041 and h=(γ_s - 15)/2.021.

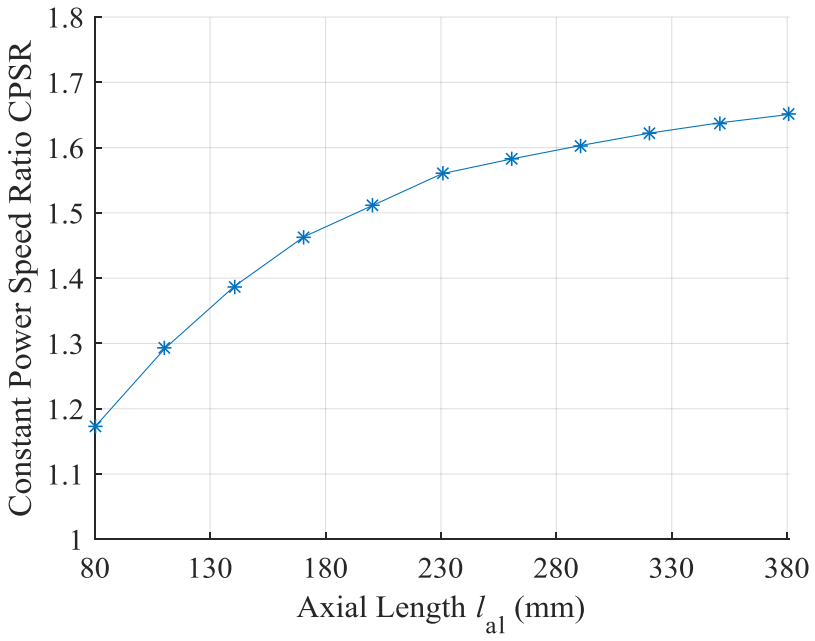

Figure 3.13. Constant power speed ratio, CPSR without losses, vs. axial length, l_{al}.

To study the effect of losses on the PF, the iron loss is incorporated by introducing a resistor to the equivalent machine circuit as shown in figure 1.13 (b) as discussed in section 1.2.3 [137]. The PF including both copper and iron loss is plotted in figure 3.14, where a significant increase is presented compared to the IPF. The larger the loss is, the higher increase there is in power factor.

The voltage include copper loss is presented as V. V at base speed and rated power is denoted as V_{rtd}. Figure 3.15 plots the PF, IPF, V to V_{rtd} ratio and e to e_{rtd} ratio on the same graph against ω to ω_b ratio. According to section 1.2.3, neglecting all losses, machine at the speed of ω_{fw} has the same IPF as the base speed, ω_b. However, figure 3.15 indicates that this relationship no longer holds for PF, so the method of CPSR prediction used in section 2.3.2 is obsolete.

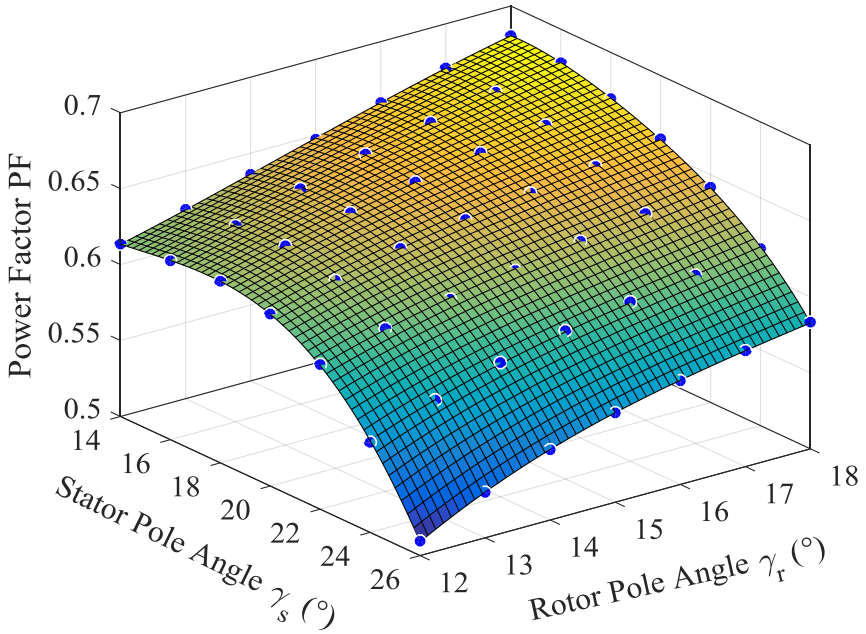

Figure 3.14. Power factor PF vs. stator pole angle, γ_s and rotor pole angle, γ_r. The fitted polynomial is PF = 0.6404 - 0.02613k + 0.01347h - 0.01588k² - 0.00295kh - 0.002282h² -0.001963k³ + 0.005963k²h + 2.553×10⁻⁵kh² + 0.0008047h³ -0.0003732k⁴ + 0.001025k³h -0.0004508k²h² + 0.0006713kh³ +2.927×10⁻⁵h⁴ + 8.819×10⁻⁵k⁵ -0.0007305k⁴h -0.0008086k³h² -0.0001878k²h³ - 2.066×10⁻⁵kh⁴ - 4.458×10⁻⁵h⁵, where k = (γ_r - 20)/4.041 and h=(γ_s - 15)/2.021.

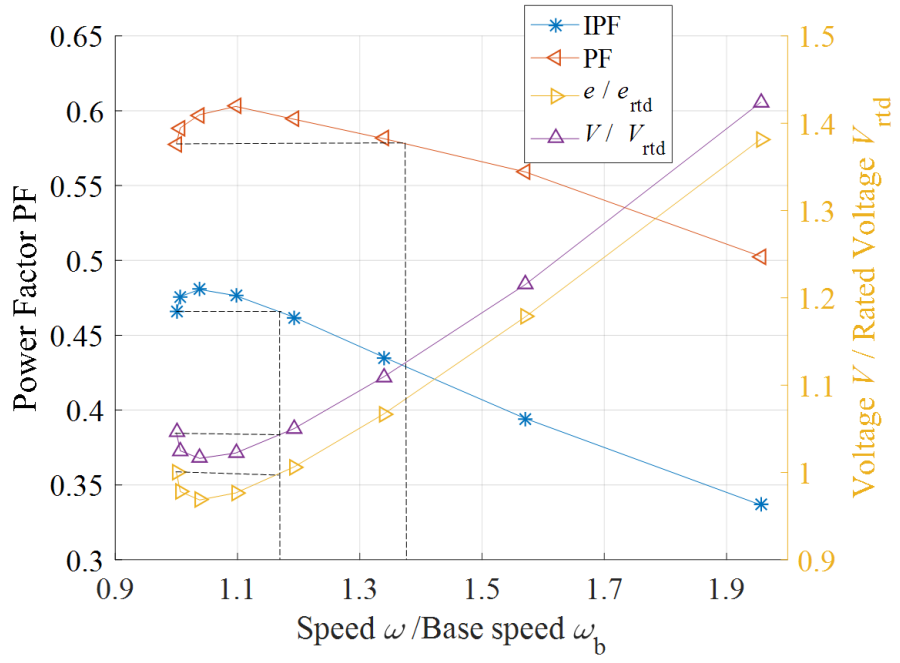

Figure 3.15. Power factor, PF, internal power factor, IPF, V to V_{rtd} ratio and e to e_{rtd} ratio vs. speed ω to base speed ω_b ratio at rated mechanical power, P_{mech}.

3.2.2 Interpolation Method

In vector control, iron loss is usually neglected, leaving copper loss as the only loss under consideration [137]. Previous sections predict field weakening capability of machine using the method described in section 1.2.3, but this method does not take copper loss into account.

The problem of predicting machine torque and voltage in the field weakening region with consideration of copper loss can be achieved by solving the following equation set:

$$\begin{cases} V_0 = \sqrt{V_d^2(i,\theta) + V_q^2(i,\theta)} = \sqrt{\left(-\omega\lambda_q(i,\theta) + R_s i_d(i,\theta)\right)^2 + \left(\omega\lambda_d(i,\theta) + R_s i_q(i,\theta)\right)^2} \\ T_0 = \max\left(\frac{3}{2} p\left(\lambda_d(i,\theta) i_q(i,\theta) - \lambda_q(i,\theta)(i,\theta) i_d\right)\right) \end{cases} \quad (3.1)$$

where V_0 is the objective voltage. T_0 is the objective torque under the V_0 and speed ω. R_s is the phase resistance. The objective power $P_0 = p\omega T_0$, where p is the number of pole pair.

To solve (3.1), a procedure that involves look-up table (LUT) and piecewise interpolation is developed. The ideal of using LUT and interpolation method to predict torque performance is proposed by J.M. Stephenson [138]. With pre-acquired LUTs of machine parameters from either simulations or measurements, accurate and rapid prediction of machine performance under different operating conditions is possible. To obtain the data between pre-acquired points, cubic spline polynomial functions interpolation is usually applied [139].

For the LUT method, the procedure is described below:

(1) Set the reference voltage V_0 and torque T_0. The current, i and load angle, θ are to be determined.

(2) Using Altair Flux, a surface of voltage, V and torque, T over current, i and load angle, θ, with interval of, Δi and, $\Delta\theta$ is generated, written as $V(i, \theta)$ and $T(i, \theta)$. Figure 3.16, 3.17 shows $V(i, \theta)$ and $T(i, \theta)$ for the benchmark machine with MC winding.

(3) Apply a 2D spline interpolation method to make the points on the surfaces denser, where the interpolation interval, $\Delta_{int}\, i$ and $\Delta_{int}\, \theta$ is smaller than Δi and $\Delta\theta$.

(4) Set maximum allowed percentage of error or deviation of V and T as V_e and T_e. Find

all T and V points on interpolated surface that locate within the error range, where these discrete points form a belt, as shown in figure 3.18. Any point on the belt satisfies the desired accuracy.

(5) If there exist any points where the V and T belts shares a common value. This common value point (i_{res}, θ_{res}) is the field weakening point that satisfies both V_0 and T_0. If a common value exists but the two belts are not tangentially intersecting as shown in figure 3.18, T_0 should be increased for MTPV operation.

(6) If there are no common points because the two belts do not intersect, T_0 should be reduced, as the machine reaches its field weakening limit. If there are no common points because the points in the belt are to sparse, Δ_{int} θ and Δ_{int} i should be reduced and surface should be re-interpolated.

(7) To validate the results, i_{res} and θ_{res} is then applied to the FE model to generate torque and voltage, written as V_{res} and T_{res}. If V_{res} and T_{res} are within the error range of (V_0 - V_0 V_e, V_0 + V_0 V_e) and (T_0 - T_0 T_e, T_0 + T_0 T_e), the procedure is finished. If not, reduce Δi and $\Delta\theta$ and repeat the procedure from (2).

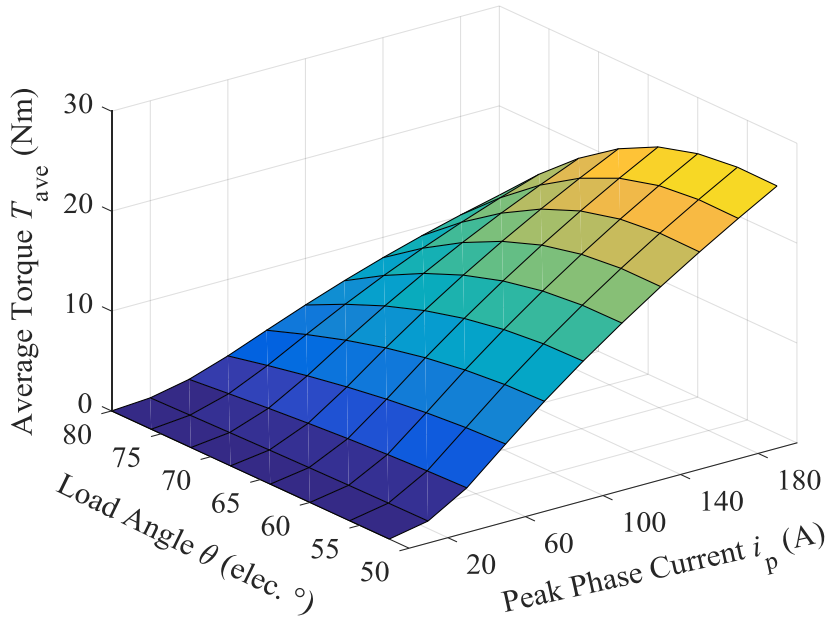

Figure 3.16. Average torque, T_{ave} vs. peak phase current, i_p and load angle, θ for the benchmark machine under AC sinusoidal current excitation.

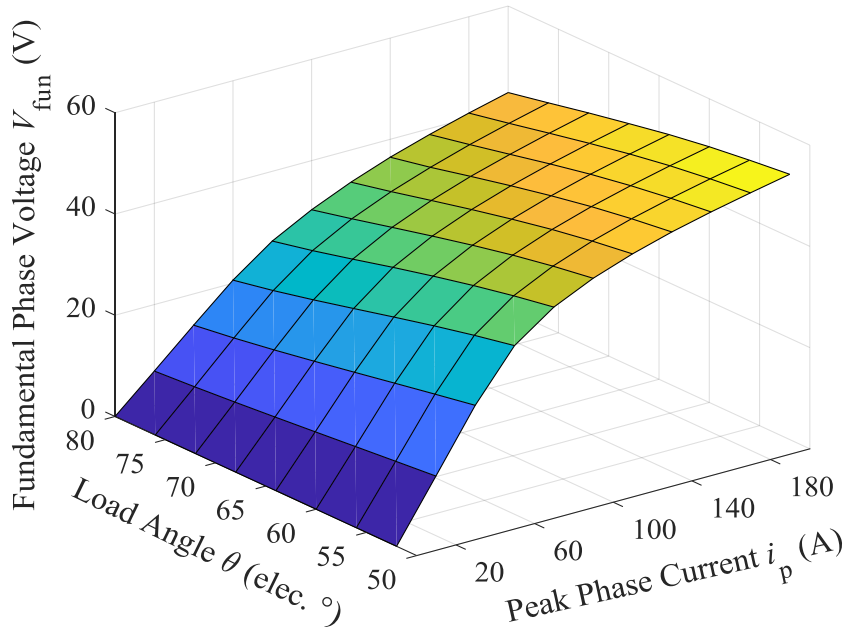

Figure 3.17. Fundumantal phase voltage, V_{fun}, vs. peak phase current, i_p and load angle, θ for the benchmark machine under AC sinusoidal current excitation.

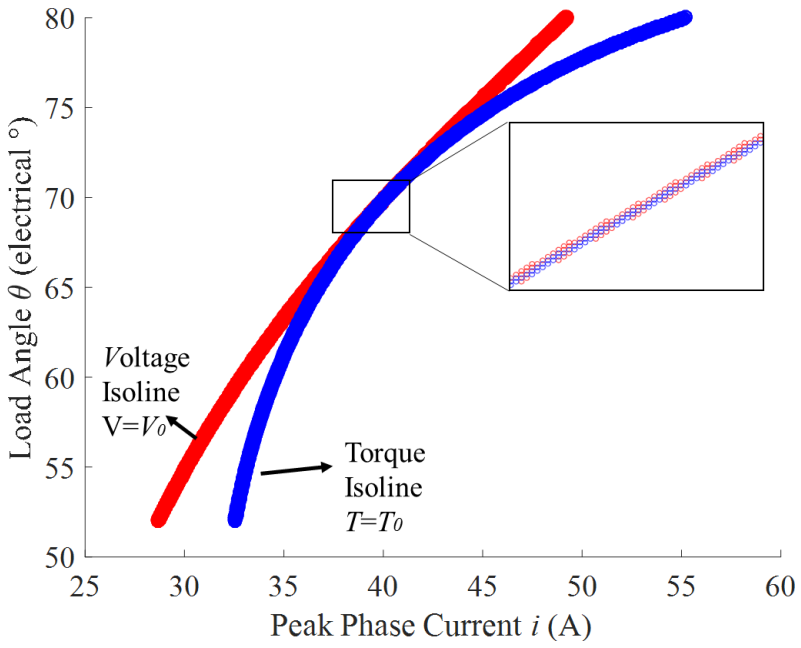

Figure 3.18. Torque, $T = T_0$ and voltage, $V = V_0$ isolines vs. current, i and load angle, θ.

A detailed flowchart of this procedure is shown in figure 3.19.

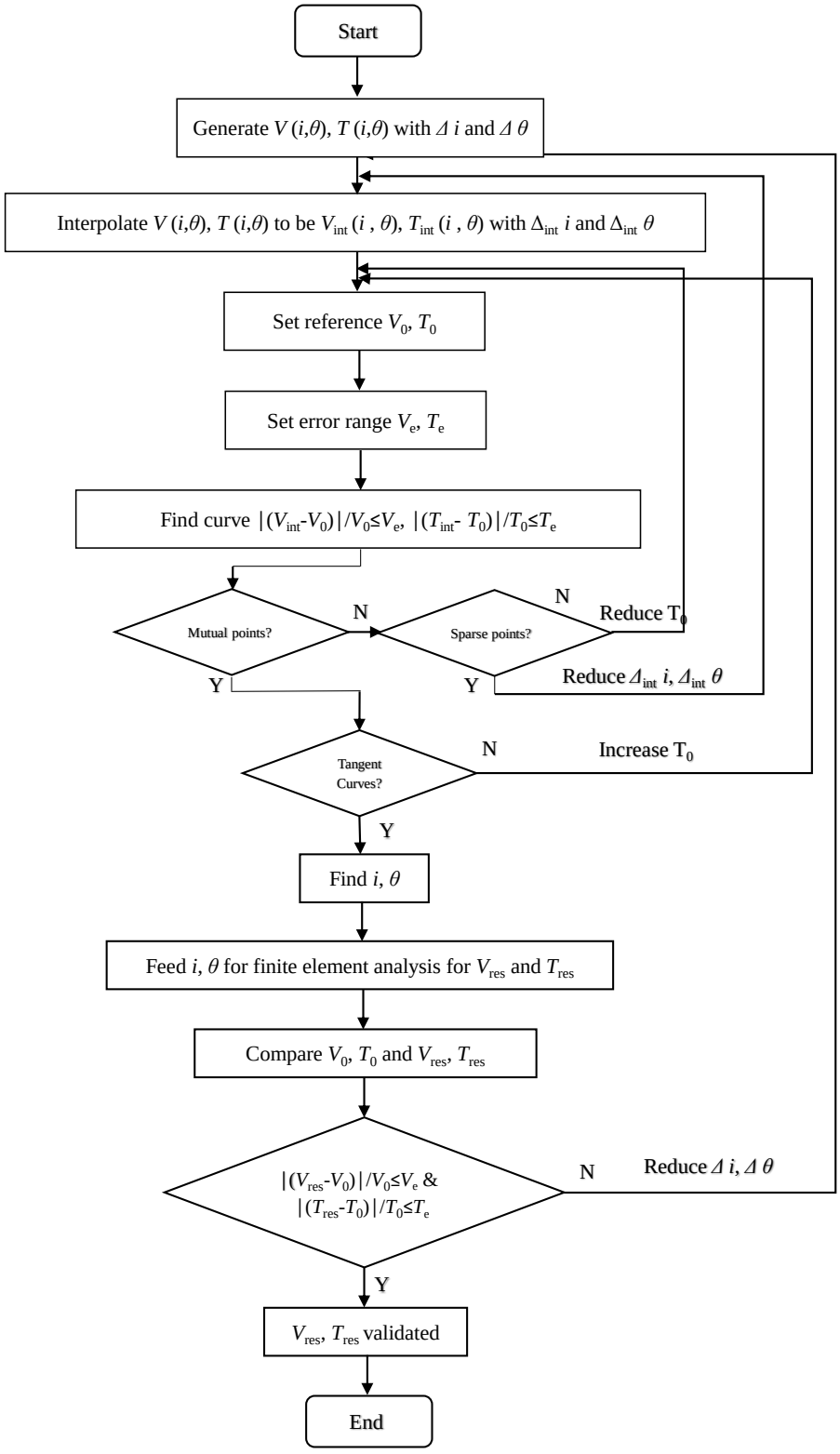

Figure 3.19. Flowchart of LUT interpolation procedure.

The aforementioned procedure is performed on three different machine windings and dimensions; they are (1) CSRM with benchmark dimensions; (2) MCSRM with benchmark

dimensions; (3) MCSRM with optimized geometry as described in section 3.1. These results are all obtained under AC sinusoidal excitation. For comparison, benchmark CSRM with 48V DC voltage half bridge excitation is also plotted.

Average torque, T_{ave} and mechanical power, P_{mech} versus speed, ω is plotted in figure 3.20 and 3.21. Figure 3.22 and 3.23 display the fundamental phase voltage, V_{fun} and PF as a function of ω. The copper loss, P_{cop}, iron loss, P_{ir} and efficiency comparisons are shown in figure 3.24 and 3.25.

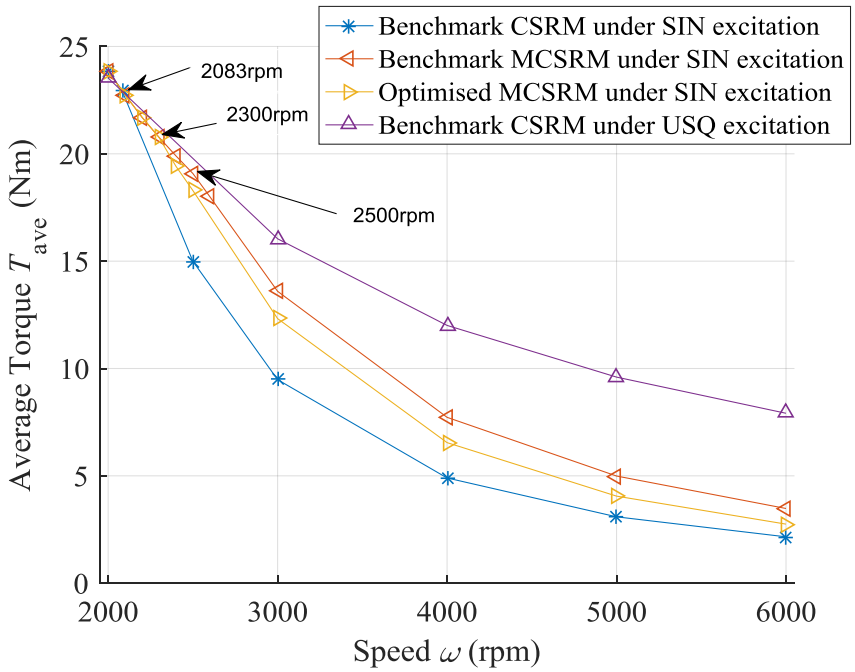

Figure 3.20. Average torque, T_{ave}, vs. speed, ω for the benchmark CSRM under SIN excitation, the benchmark MCSRM under SIN excitation, the geometry optimized MCSRM under SIN excitation, and the benchmark CSRM under USQ excitation.

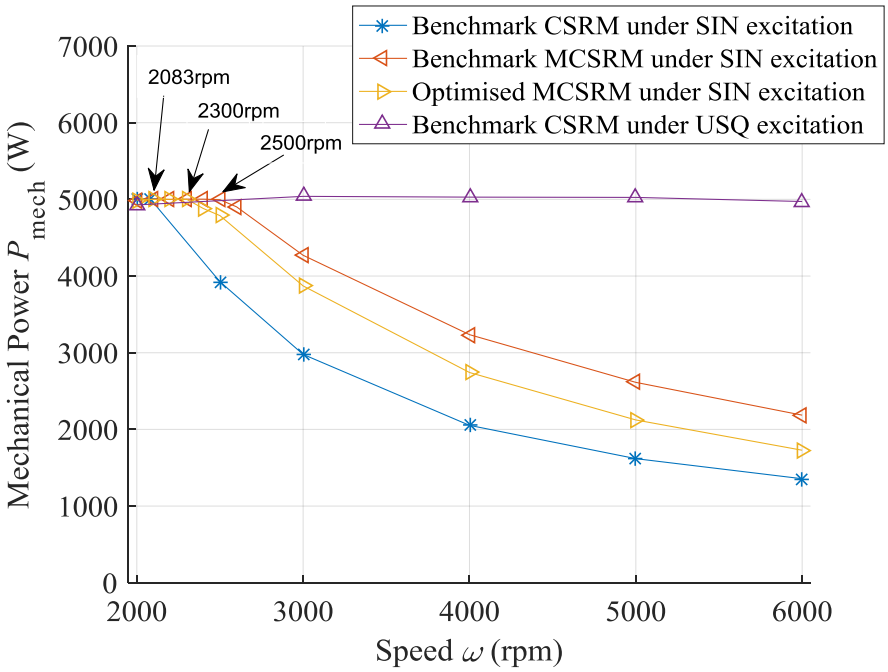

Figure 3.21. Mechanical power, P_{mech}, under AC sinusoidal current excitation vs. speed, ω for the benchmark CSRM under SIN excitation, the benchmark MCSRM under SIN excitation, the geometry optimized MCSRM under SIN excitation, and the benchmark CSRM under USQ excitation.

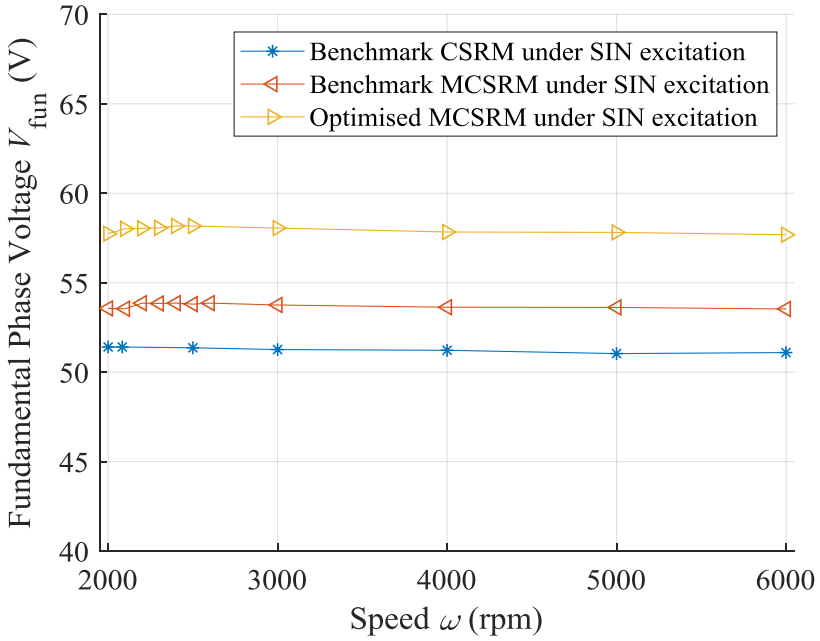

Figure 3.22. Fundamental phase voltage, V_{fun}, under AC sinusoidal current excitation vs. speed, ω, for the benchmark CSRM under SIN excitation, the benchmark MCSRM under SIN excitation, the geometry optimized MCSRM under SIN excitation, and the benchmark CSRM under USQ excitation.

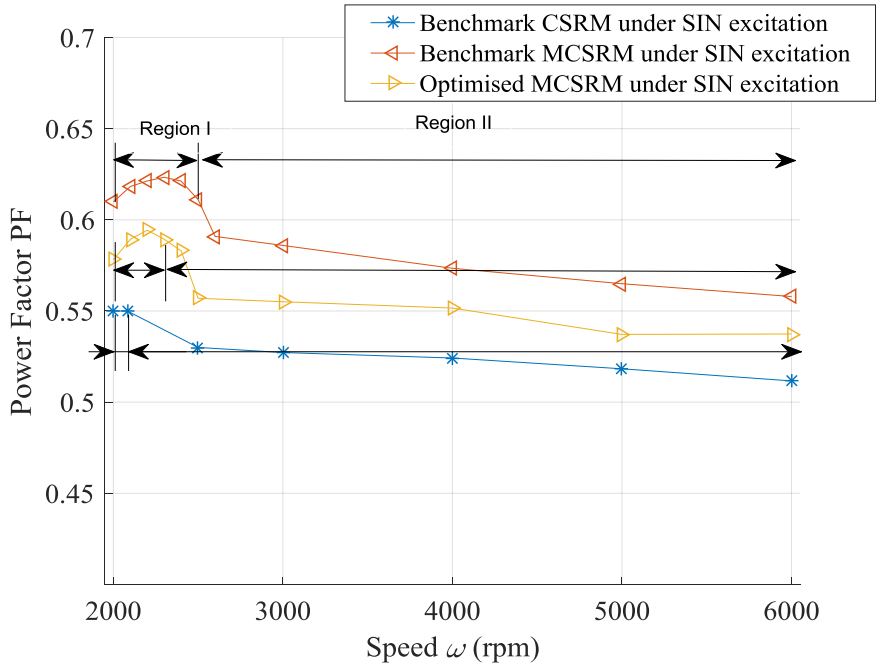

Figure 3.23. Power factor, PF, under AC sinusoidal current excitation vs. speed, ω for the benchmark CSRM under SIN excitation, the benchmark MCSRM under SIN excitation and the geometry optimized MCSRM under SIN excitation.

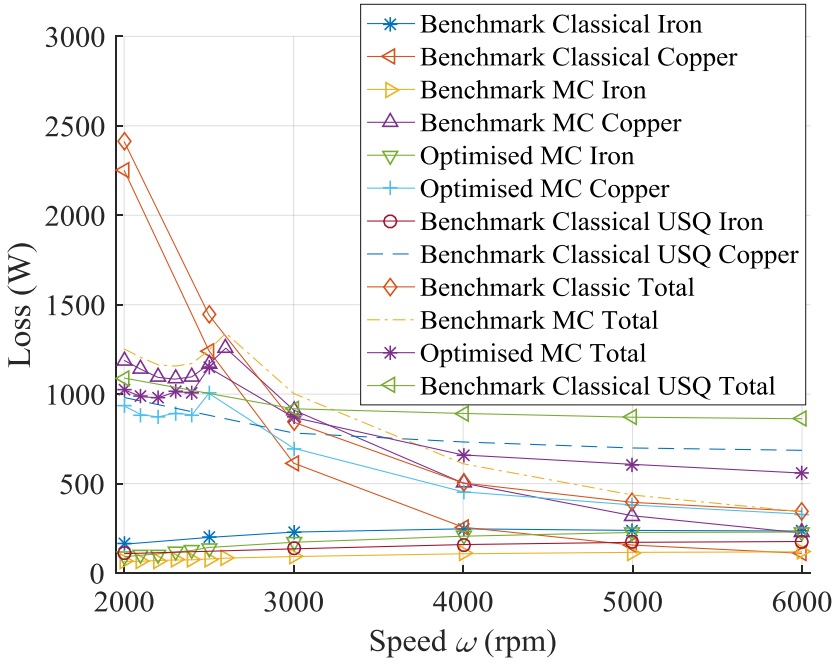

Figure 3.24. Iron loss, P_{ir}, copper loss, P_{cop} and total loss, P_l, vs. speed, ω for the benchmark CSRM under SIN excitation, the benchmark MCSRM under SIN excitation, the geometry optimized MCSRM under SIN excitation, and the benchmark CSRM under USQ excitation.

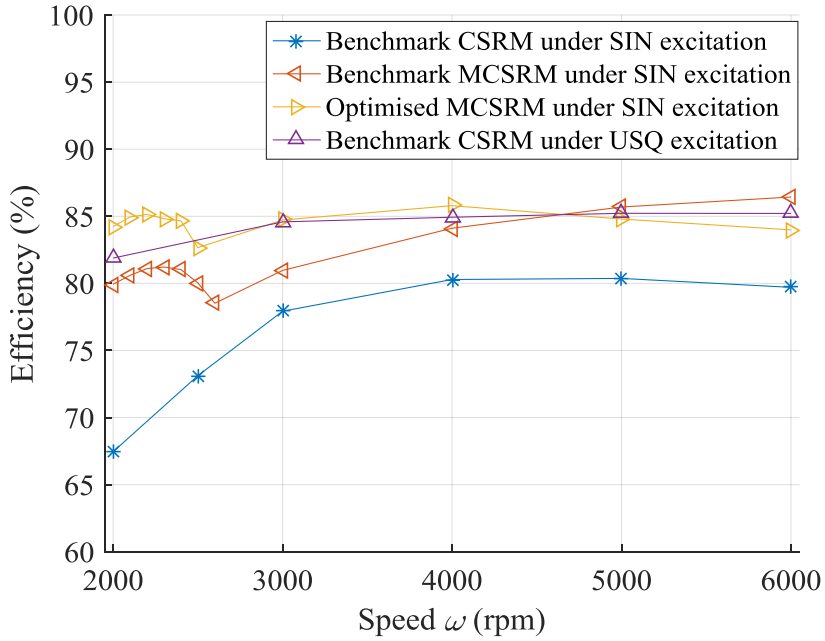

Figure 3.25. Efficiency vs. speed, ω for the benchmark CSRM under SIN excitation, the benchmark MCSRM under SIN excitation, the geometry optimized MCSRM under SIN excitation, and the benchmark CSRM under USQ excitation..

From figure 3.20 and 3.21, the ω_{fw} of MC winding is 2500 rpm while the ω_{fw} of classical winding is only 2083 rpm. This result is very similar to the CPSR derived in section 2.3.2 where no loss is considered. The larger ω_{fw} allows the MC winding to deliver a higher mechanical power in all field weakening speed. Also, minimum loss optimisation of geometry reduces ω_{fw} to about 2300 rpm.

From figure 3.22, with the same number of turns in phase coil, the AC sinusoidal excited machines have a fundamental phase voltage requirement between 50 V to 60 V. Driven with three-phase conventional inverter, a DC link voltage of at least π/2 times higher than the phase voltage is required when the machine operates under six-step operation. As a result, compared with classical winding and half bridge inverter, AC sinusoidal current excitation strategy with conventional AC inverter greatly increases the DC link voltage requirements.

The PF versus ω is displayed in figure 3.23, where the MC winding has a higher PF than the classical winding. This increase in PF is also compromised by minimum loss optimization of geometry. As a result, the classical winding requires a higher VA requirement for inverter.

Moreover, operation can be categorized into two regions from base speed up. In region I, there is sufficient voltage to maintain the required phase current, so a constant power is possible. In this region, increase of speed sees a slight increase in power factor, then drops back to base speed level. The phase current shows the opposite behaviour, which first decreases, then increases to base speed level. This phenomenon can be easily explained by (1.6) in section 1.2.3. With further increase in speed, machine enters region II, where constant current cannot be maintained, and the power reduces monotonously. The speed where region one ends is ω_{fw} and region one is called the field weakening region.

The losses and efficiencies of different windings under AC sinusoidal excitation are plotted in figure 3.24 and 3.25. From figure 3.24, iron loss of all machines are generally small compared with copper loss, especially at low speed. From figure 3.24, the current requirement for the classical winding is larger than the MC winding, resulting in a higher copper loss. The classical winding also exhibits a higher iron loss. The high losses on the classical winding reduces the efficiency compared with MC winding at all speed. For the MC winding, the optimized geometry significantly decreases the copper loss, so efficiency sees an improvement at low to medium speed despite of the reduction in mechanical power.

Compared with CSRM and MCSRM under AC sinusoidal current excitation, the benchmark Speedstart (CSRM) with half bridge excitation provides a much better field weakening capability with a comparable efficiency.

3.3 Altair Flux-Simulink Co-simulation

Sections 3.1 and 3.2 focus on the performance of the stand-alone machine only. In this section, a co-simulation approach is introduced, where the effect of the inverter and control strategy can be taken into consideration.

Co-simulation of machine with driving system usually takes two approaches. The first approach uses LUT and interpolation method. With pre-acquired LUTs of flux with respect to rotor position and currents, accurate and rapid prediction of torque and current under certain terminal

voltage and speed is possible. The second approach integrates FE model into the analysis, where the machine inputs and outputs are simulated at reach iterative time step.

Both methods have their benefits and drawbacks. The FE method provides accurate calculation with consideration of geometry and harmonics [140], but it is computationally extensive [141-144]. The LUT method provides a computationally efficient solution with the same accuracy of FE model [145], but it is not capable of simulate space harmonics without introduction of highly complicated multi-dimensional LUTs. To be specific, the LUT method can be divided into two categories. The first category uses dq0 model [146, 147]. The advantage of this model is that the LUTs are usually 1D (linear) [145] or 2D (with saturation) [148-150], so they are computationally fast and easy to obtain. The drawback of this approach is that the space harmonics are usually neglected, making the model incapable in torque ripple or voltage harmonics simulation. The second category uses abc model. This model can incorporate space harmonics, but the LUTs are usually N-dimensional (*N*-D) [140, 145, 151]. The complicated LUTs takes longer time to be generated, and increases simulation time.

It is worth mentioning that, the aforementioned methods have not only been applied in the PMSM, IM or SynRM, but also validated in the classical SRM with half bridge driver [152, 153]. In spite of that, there has been no report on the influence of AC inverter and space harmonics on the performance prediction of mutually coupled SRM. In this section, both FE and LUT co-simulation methods are introduced. The FE method is then performed to predict the field weakening performance of the benchmark MCSRM, where the simulation results are compared with stand-alone machine from section 3.2.2.

3.3.1 Introduction

The switched reluctance machine co-simulation system can take advantage of both FE analysis and dynamic modelling software, achieving flexible and high accuracy simulation. Using Altair Flux and Matlab Simulink, both the LUT and the FE co-simulation methods can be realised.

For LUT method, LUTs are extracted from Altair Flux and imported into Simulink where the

inverter and control system models runs. In LUT co-simulation, only Simulink is running, Altair Flux is used once to produce the LUTs and then plays no further part. Therefore, fast simulation speed is achieved. A control structure diagram of the LUT co-simulation method is shown in figure 3.26 (a).

For the FE co-simulation method, directly links between control and inverter models are developed in Simulink to the magnetic models in Altair Flux. Using a specifically designed interface block from an Altair proprietary Simulink library, the data is exchanged between models in the two software programs in every iteration and at a controllable rate. A control structure diagram of the FE co-simulation method is shown in figure 3.26 (b).

From figure 3.26, both co-simulation systems consist of three parts: a FE model in Altair Flux, a Simulink model, and link mechanism between the software packages. The only difference between them is the different way in which the machine model is involved. It means that once the control system and inverter model are built, they are communal for both systems.

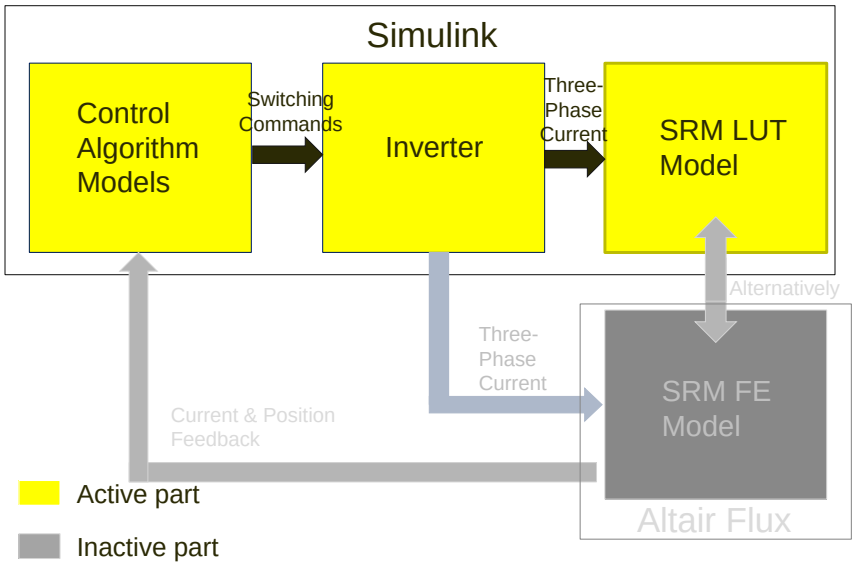

(a)

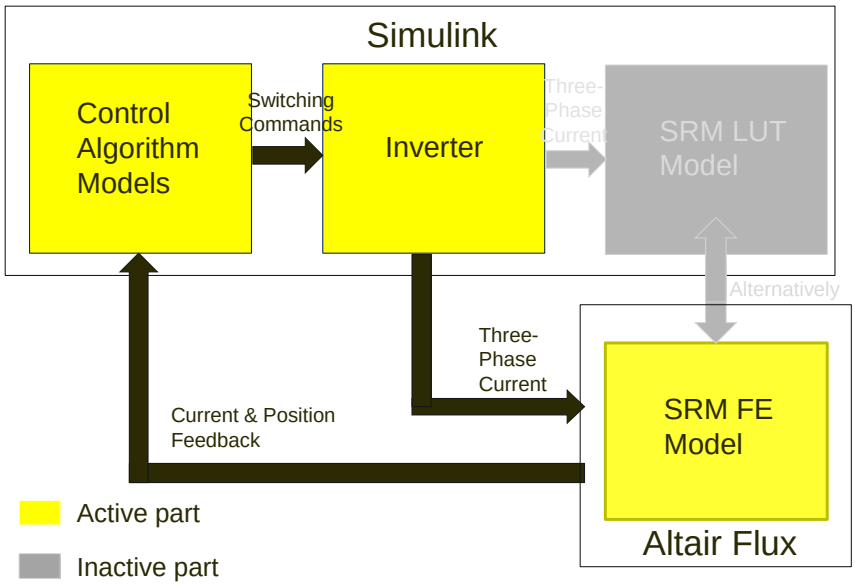

(b)

Figure 3.26. Simulation system structure diagram of (a) look-up table co-simulation method, (a) finite element co-simulation method.

Altair Flux software 10.4.1 and later versions provide a built-in interface (a bespoke Simulink block) that allows data exchange between Simulink and Altair Flux at a controllable time step defined by Simulink. This function greatly facilitates the proposed co-simulation method.

In Altair Flux, a magnetic transient target model is defined. A conventional three-phase AC inverter circuit model is built and coupled with machine coils. The switches are ideal with an off resistance of 1×10^{8} Ω and an on resistance of 1×10^{-8} Ω. The ideal inverter and the FE model is shown in figure 3.27. Then the input and output values are defined. In this case, the input values are regarded as the input from Simulink to Altair Flux, which incorporate switching signals and DC link voltage. The output values are the parameters passed from Altair Flux to Simulink, including all values of interest for control and monitoring, usually rotor position, speed, phase current, coil flux and back-EMF. After the input/output parameter configuration, Altair Flux provides a function that automatically links between Altair Flux and Simulink.

In the Simulink library, a ‘Flux link’ module is available, where the input and output ports appear on the block are related to the linked FE model. The ‘Flux link’ block for the MCSRM and inverter is shown in figure 3.28.

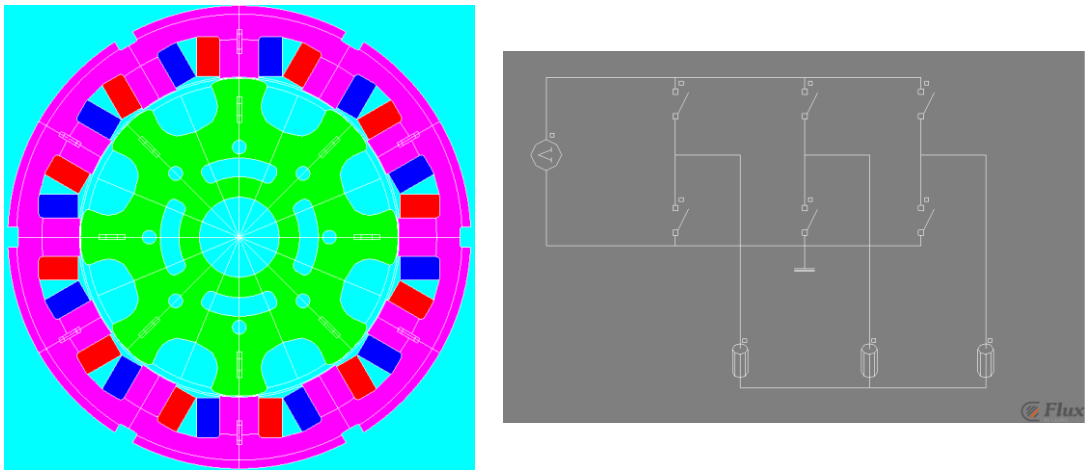

(a) (b)

Figure 3.27. Altair Flux Model of the mutually coupled SRM in (a) FE Domain and (b) Electrical Domain.

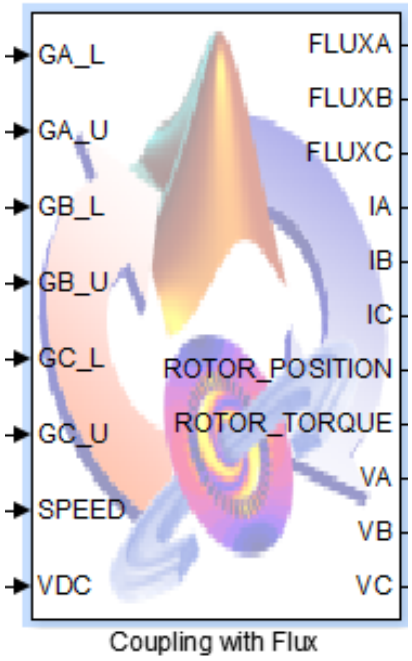

Figure 3.28. Co-simulation model of SRM in Simulink 'Flux link' module.

3.3.2 Control System

In Simulink, a simple current PI controller with anti-windup is applied, as shown in figure 3.29. The output of the PI controller is connected to a sinusoidal PWM (SPWM) block, which is shown in figure 3.30. As only field weakening operation is of interest, the control will be carried out using six step operation. The gate signal from the SPWM is feed into FE model in Altair Flux to induce current and produce torque. The three-phase current signal, i_{abc} generated in

Altair Flux is converted to i_d and i_q and feedback to a PI module. With speed, DC link voltage and load angle inputs, current and torque are obtained.

With all subsystems created, a machine and drive co-simulation system is realized. The diagram of the Altair Flux Simulink co-simulation system is shown in figure 3.31.

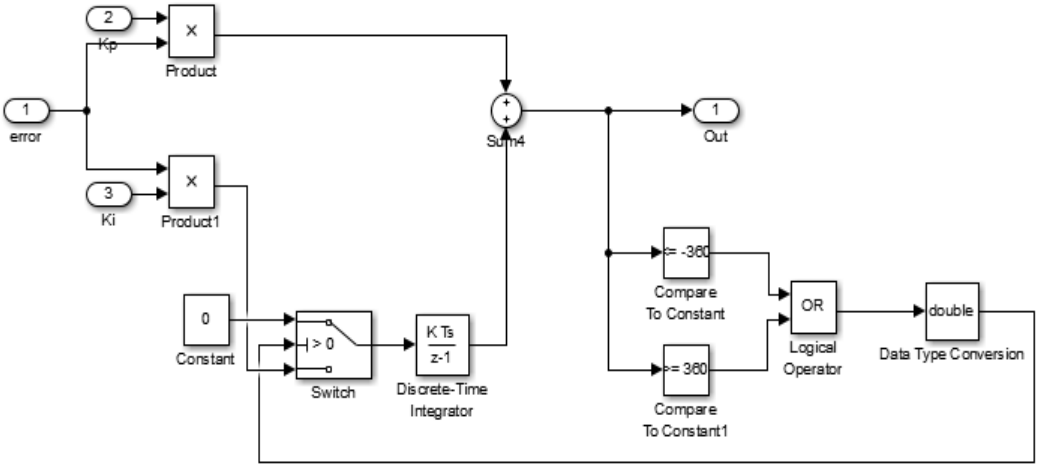

Figure 3.29. A Simple PI control model with anti-windup in Simulink.

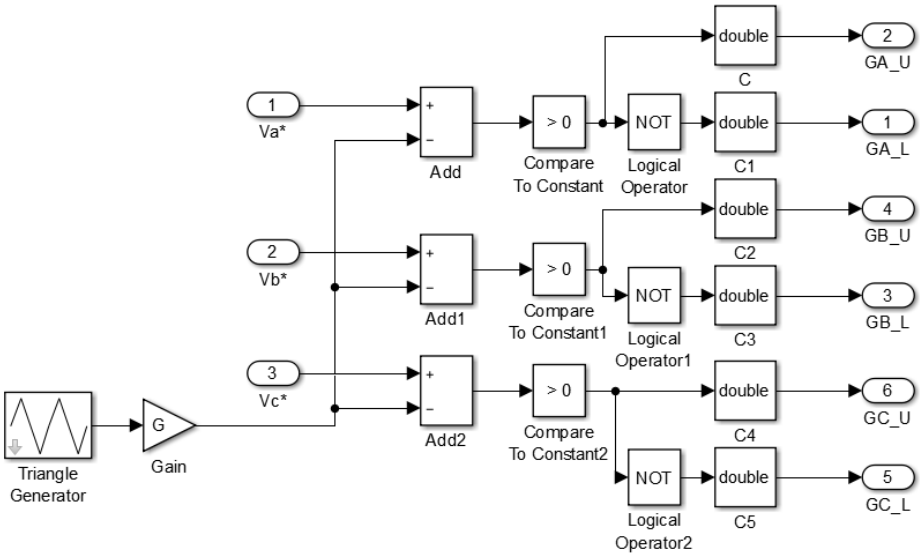

Figure 3.30. A simple SPWM model in Simulink.

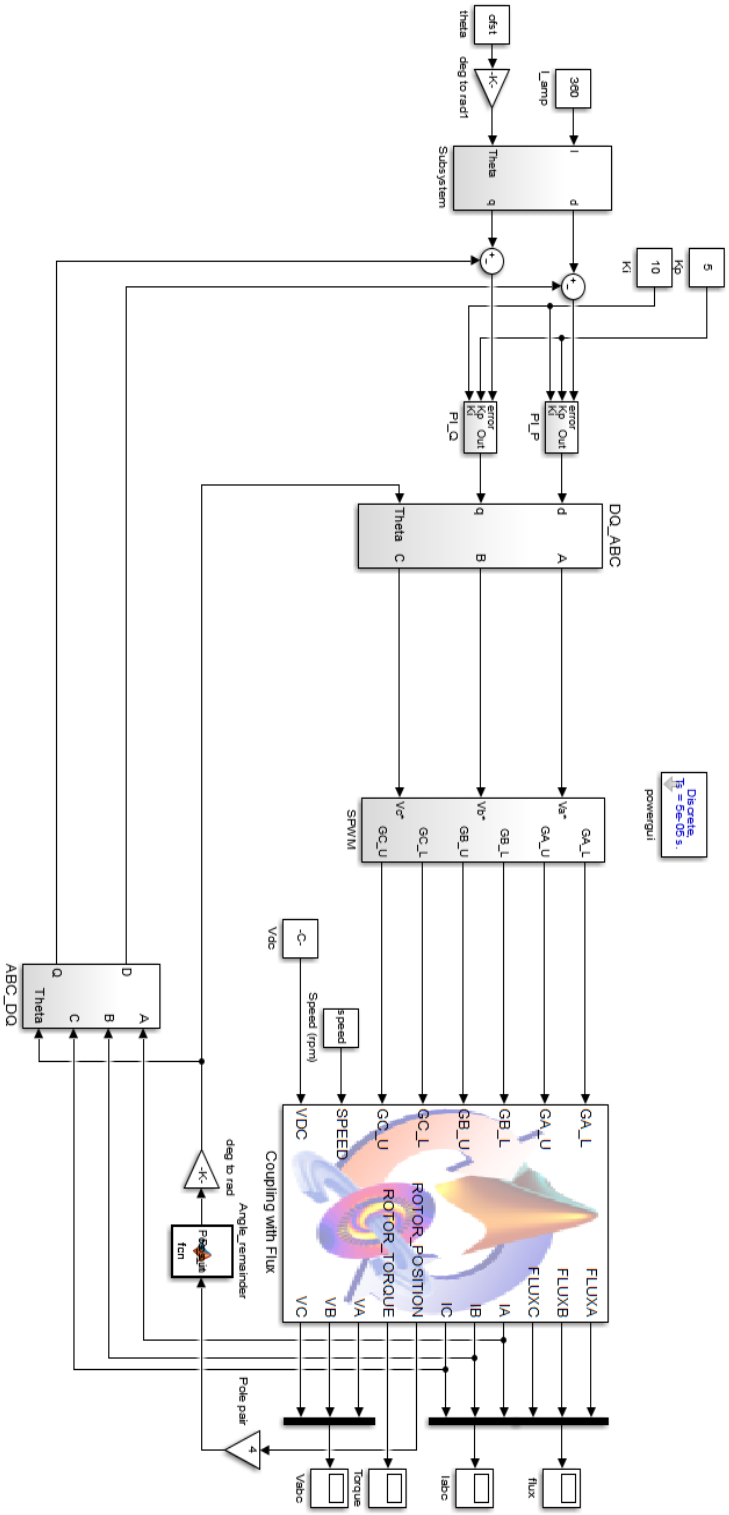

Figure 3.31. An Altair Flux Simulink Co-simulation model of a switched reluctance machine and drive system using sinusoidal AC current excitation.

3.3.3 Comparative Study

In this section, the FE co-simulation results of the benchmark MCSRM is generated and compared with that from the LUT interpolation method described in section 3.2.2.

The main differences between the proposed FE co-simulation method compared with the stand-alone machine operation in section 3.2.2 is that, the former method uses purely sinusoidal current excitation regardless if there is sufficient voltage headroom to enable that current to flow. The co-simulation method allows a more realistic simulation with consideration of AC inverter, where at field weakening region, six-step operation is adopted. Phase currents are induced by this voltage so a purely sinusoidal current is not guaranteed.

To conduct a co-simulation that is comparable with the LUT interpolation method, in Simulink, the DC link voltage is set so the two methods have the same fundamental phase voltage amplitude, in this case a DC link voltage of 84.1 V is applied. At base speed of 2000 rpm and rated power of 5 kW, the current phase in co-simulation is changed until the average torque is the same as the LUT interpolation method. In the field weakening region, the load angle in co-simulation is changed until a maximum average torque is produced.

Simulation results from the two methods at 2000 rpm are plotted in comparison. Figures 3.32 and 3.33 show the phase-A current, i_a and voltage, V_a waveforms together with their FFT analysis. From the figures, six-step operation and AC sinusoidal current both produce even order harmonics other than the multiples of three in the phase voltage. The difference is that the six-step voltage waveform contains lower 5^{th} and 7^{th} order harmonics, and higher harmonics of high order. The phase current generated by six-step operation is slightly larger in fundamental. It also contains harmonics mainly of 5^{th} and 7^{th} order. The torque waveforms are plotted in figure 3.34, where a 3% lower average torque and smaller ripple is exhibited in six-step operation.

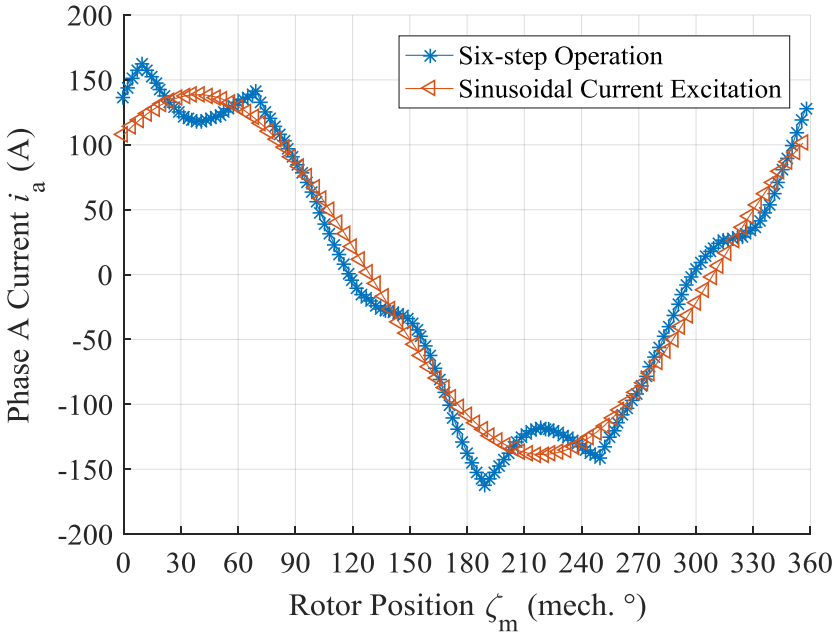

(a)

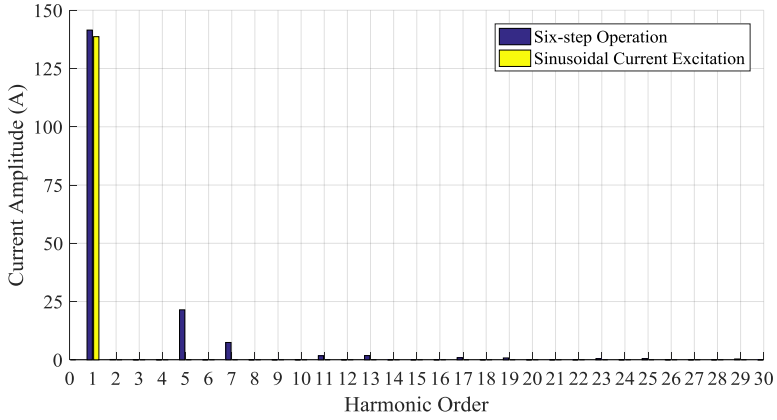

(b)

Figure 3.32. Comparison of phase current of sinusoidal current excitation and six-step operation at 5 kW and 2000 rpm.(a) current waveform vs. rotor position, ζ_m; (b) harmonic analysis.

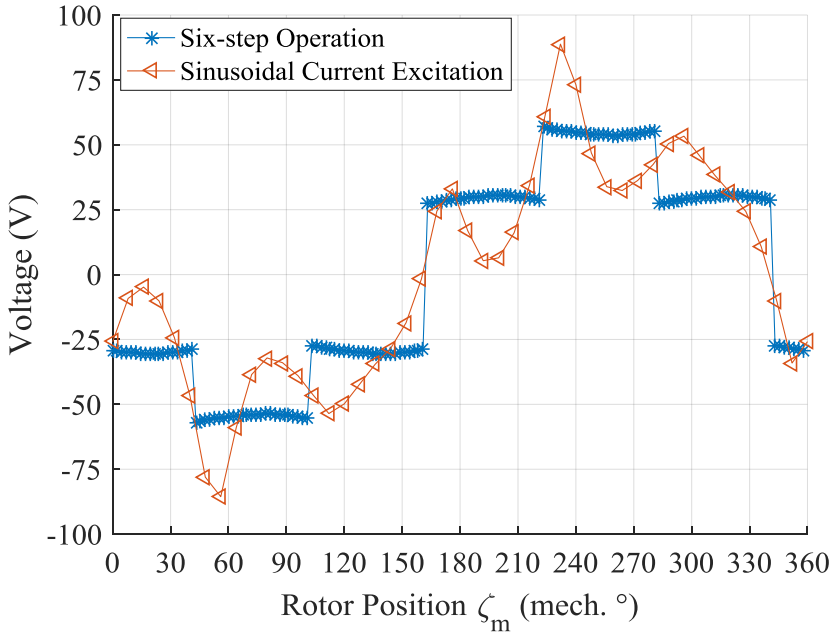

(a)

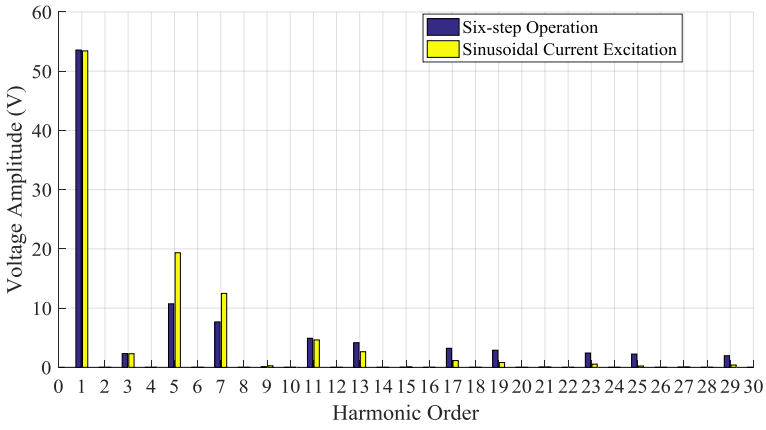

(b)

Figure 3.33. Comparison of phase voltage of sinusoidal current excitation and six-step operation at 5 kW and 2000 rpm. (a) voltage waveform vs. rotor position, ζ_m; (b) harmonic analysis.

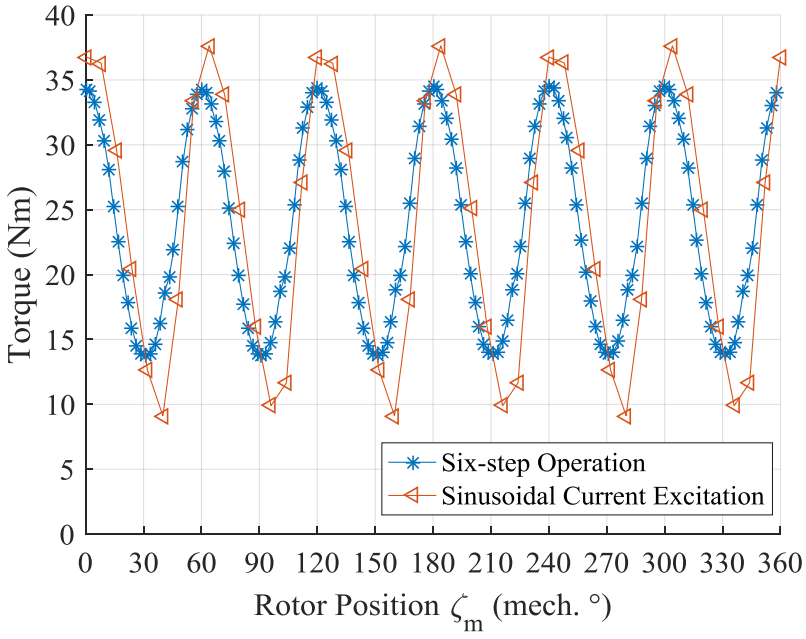

Figure 3.34. Comparison of torque waveforms vs. rotor position, ζ_m of sinusoidal current excitation and six-step operation at 5kW and 2000 rpm.

In the field weakening region, the average torque, T_{ave}, fundamental component of phase-A current, i_{afun}, power factor and fundamental component of phase-A voltage, V_{afun} are plotted in figure 3.35 to 3.38, respectively. From the figures, average torque of six-step operation is slightly lower than a pure sinusoidal current excitation in region one, and identical in region two. A 5% to 12% larger fundamental current and a 7% to 10% lower PF is presented in six-step operation. From the comparisons, the prediction of the MCSRM performance with pure sinusoidal current tends to overestimate the power factor and underestimate the current requirements. Since the current harmonic components will increase the iron and copper losses, the efficiency calculated by the sinusoidal current is also an underestimate. Despite of that, the average torque and voltage predictions are similar from both methods, indicating that the CPSR of the machine is correctly predicted.

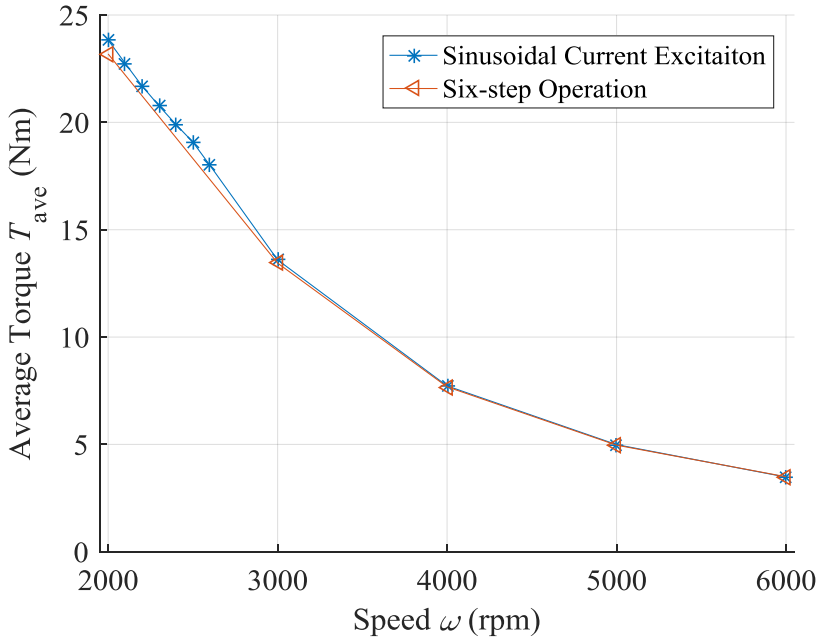

Figure 3.35. Comparison of average torque, T_{ave}, vs. speed, ω of sinusoidal current excitation and six-step operation in field weakening region.

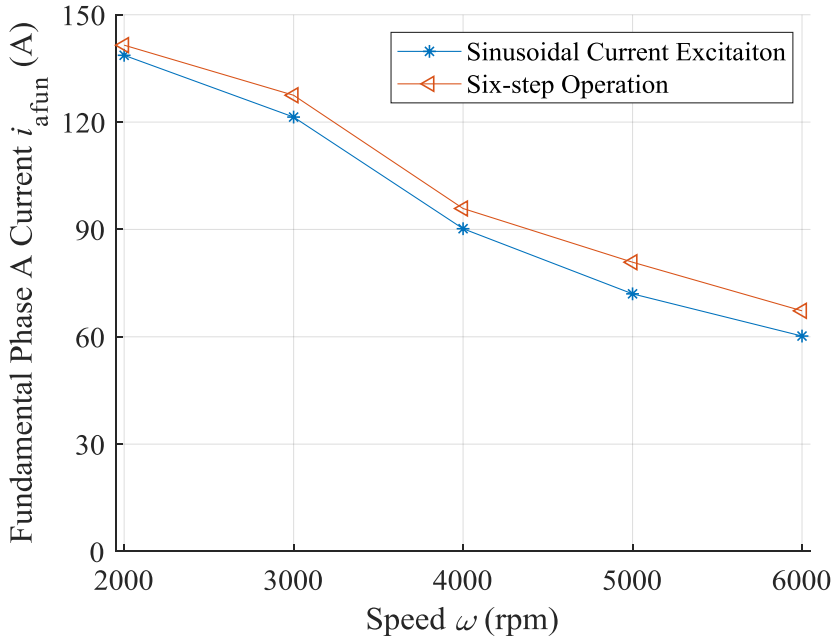

Figure 3.36. Comparison of phase-A fundamental current, i_{afun}, vs. speed, ω of sinusoidal current excitation and six-step operation in field weakening region.

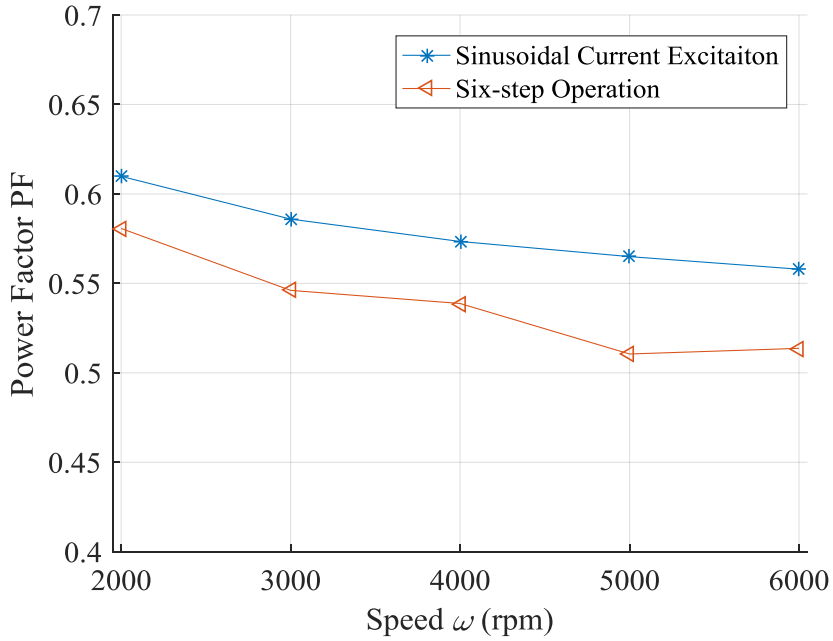

Figure 3.37. Comparison of power factor, PF, vs. speed, ω of sinusoidal current excitation and six-step operation in field weakening region.

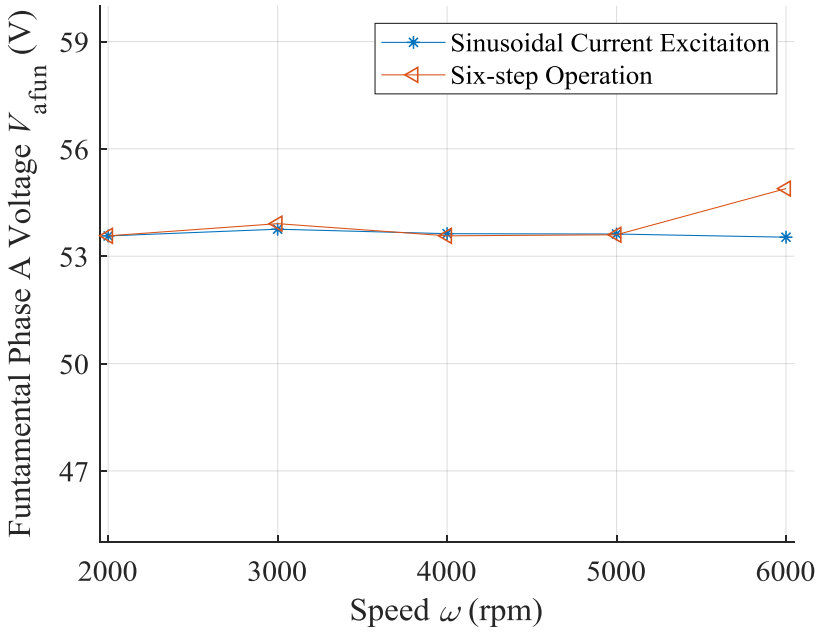

Figure 3.38. Comparison of phase-A fundamental voltage, V_{afun}, vs. speed, ω of sinusoidal current excitation and six-step operation in field weakening region.

3.4 Summary

This chapter focuses on the dimensions, power factor and constant power speed ratio (CPSR)

of the mutually coupled switched reluctance machine (MCSRM) under AC sinusoidal excitation, where the major contributions are listed below. First, this study proposed using AC machine theory to investigate the influence of dimensions on MCSRM including loss, power factor and field weakening capability. Second, a FE co-simulation method between the machine and drive is introduced to validate the application of AC machine theory on MCSRM, where the influence of six-step operation in field weakening region is emphasized.

From the analysis in this chapter, the following conclusions have been reached.

(1) Loss optimisation of MCSRM dimensions comes at a price of power factor and CPSR reduction;
(2) Application of AC machine theory with sinusoidal current and neglecting inverter does not affect torque prediction, but leads to overestimation of power factor and underestimation of phase currents in field weakening operation.
(3) Compared with the benchmark Speedstart CSRM driven with a half bridge inverter, a low power factor and poor field weakening capability in MCSRM limit its utility in B-ISG applications.

The main reason why the MCSRM cannot maintain a desirable CPSR is that the AC sinusoidal excitation turns the SRM into a synchronous reluctance machine (SynRM). From the literature review in section 1.2.2, this type of machine has an intrinsic low power factor and poor field weakening capability. Consequently, the investigation will change focus to the other plausible candidate reviewed in section 1.2.2, which is the wound rotor synchronous machine.

4. Design of Wound Rotor Synchronous Machine

The wound rotor synchronous machine (WRSM) is regard as a new candidate in hybrid vehicle applications. There are a limited number of reports of its application in vehicle propulsion system. In this chapter, an investigation is conducted on the geometry design of a wound rotor synchronous machine for a belt driven integrated starter-generator system. The performance of which is compared with the benchmark Speedstart switched reluctance machine.

4.1 Geometric Study

To study the feature of WRSM, a simple four pole machine structure is applied. The torque and efficiency performances are emphasized, and their relationship with geometry parameters are studied. An optimum efficiency geometry is then selected at the rated operational speed and power.

4.1.1 Initial Geometry

A four pole wound rotor machine with salient rotor pole is modelled in Altair Flux, as shown in figure 4.1. The geometry parameters under investigation and the windings arrangement are labelled. The initial dimensions are selected from general machine theory [154] and traditional design of induction motor [155-157]. The winding configurations, geometry parameters and their initial values are listed in table 4.1.

From figure 4.1, there are eighteen coils on the stator, and four coils on the rotor. Each phase is split into three coils. To calculate copper loss, the average length of distributed coil, l_{coil} is given by[158]:

$$l_{coil} = 1.6\frac{2\pi l_{ew}}{p} + l_{al} \tag{4.1}$$

where l_{ew} is average radius of the end winding.

Parameter	Value	Parameter	Value
Pole pair p	2	**Stator back iron thickness l_{sbk} (mm)**	12.43
Phase number m	3	**Rotor back iron thickness l_{rbk} (mm)**	12.25
Winding type	distributed	**Rotor pole shoe thickness l_{rss} (mm)**	7.64
Number of slots Q	36	**Axial active length l_{al} (mm)**	80.5
Slot Angle $\gamma_{sl}=2\pi p/Q$	$\pi/9$	**Stator teeth angle γ_s (°)**	5
Number of slots per pole and phase $q=Q/2pm$	3	**Rotor teeth angle γ_r (°)**	30
Stator bore radius l_{sbr} (mm)	40.83	**Pole shoe angle γ_{rs} (°)**	70
Stator shaft radius l_{sfr} (mm)	11.75	**Stator fill factor (c_s)**	0.3
Stator radius l_{sr} (mm)	68.1	**Rotor fill factor (c_r)**	0.4
Airgap Length l_{ag} (mm)	0.3	**Number of turns per phase N**	15
Rotor teeth width l_{rt} (mm)	20.98	**Iron core material**	M400-50A
Rotor pole shoe width l_{rs} (mm)	46.49	**Rated speed (rpm)**	2000
Stator teeth width l_{st} (mm)	3.57	**Maximum speed (rpm)**	20000

Table 4.1. Initial configurations and geometry parameters of a four pole wound rotor synchronous machine.

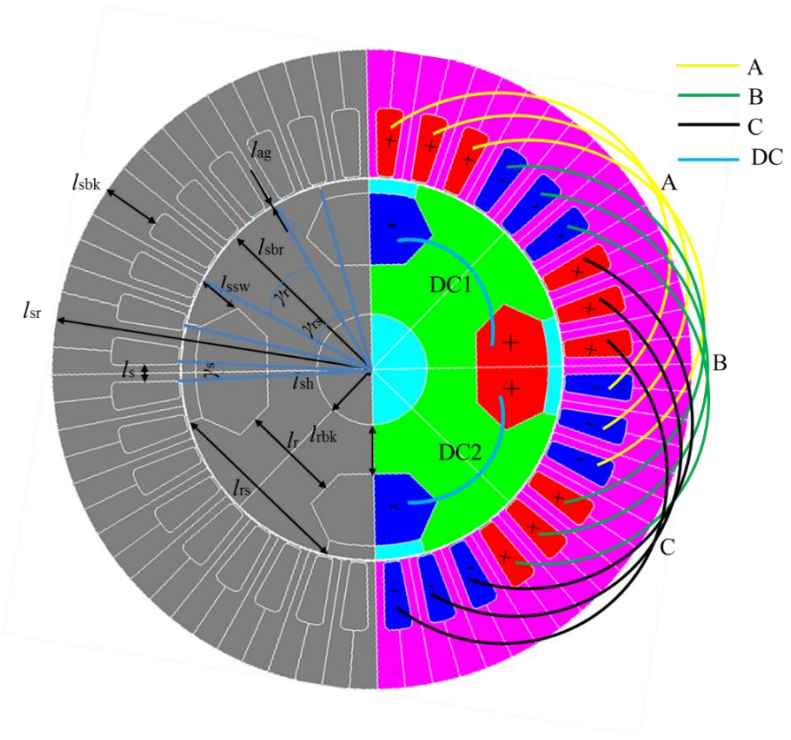

Figure 4.1. A four pole wound rotor synchronous machine model in Altair Flux. The windings arrangement are labelled.

4.1.2 Influence of Rotor Pole Shoe

Wound rotor synchronous machine usually has pole shoes on the rotor poles. In this section, the role of pole shoes on machine performance is investigated.

As described in section 1.2.3, the phasor diagram of WRSM is shown in figure 1.17. The d-axis flux, λ_d, and q-axis flux, λ_q, are derived from (1.15). The rotor MMF per coil is represented by i_f, and the flux linkage induced by i_f is denoted as λ_r.

The open circuit λ_d equipotential lines due to i_f is shown in figure 4.2(a). The open circuit i_f versus average flux density, B_{ave} at various geometric positions of interest are indicated in figure 4.2 (a) and these are plotted in figure 4.2 (b). The rated λ_r is chosen so that open circuit rotor tooth flux density is 1.5 T. From figure 4.2 (b), at the rated λ_r, the flux density through the stator teeth and stator back irons lays within typical values for IM design [159]. This indicates the thickness of stator teeth and stator back iron are properly configured.

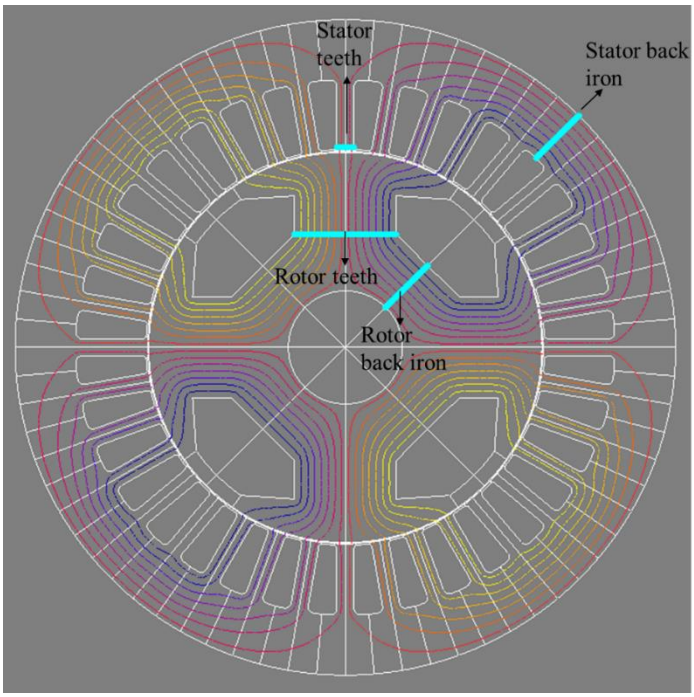

(a)

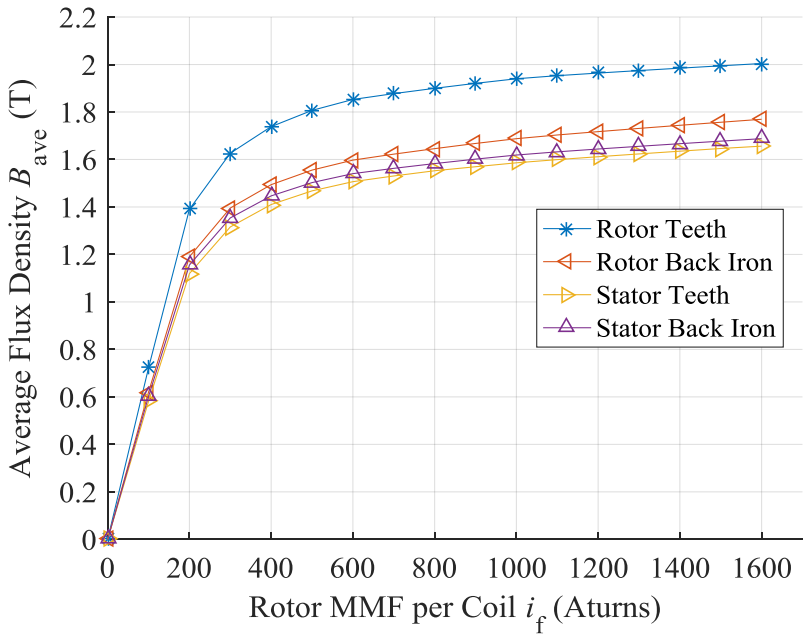

(b)

Figure 4.2. Open circuit magnetic equipotential lines of a four pole wound rotor synchronous machine. (a) d-axis flux pattern and (b) average flux density, B_{ave} vs. rotor magnetic motive force per coil, i_f for various position on iron core.

At i_f and i_d of 0, the λ_q distribution pattern is shown in figure 4.3 (a). The stator peak current density, J_{sp} versus average flux density, B_{ave} at various geometric positions is indicated in figure 4.3 (a) and are plotted in figure 4.3 (b). The figure shows a significant saturation occurs on the stator teeth, rotor pole shoes and stator back iron even at low peak current densities. This cross saturation will adversely affect the machine performance.

To evaluate the influence of cross saturation on machine torque, both stator and rotor windings are excited. Set i_d to 0 and increase i_q, λ_d and λ_q versus J_{sp} at various values of i_f are plotted in figure 4.4, and the corresponding torque is shown in figure 4.5. The i_f values are selected so the resultant open circuit rotor teeth flux densities are 1.5 T, 1.6 T, 1.7 T, 1.8 T and 1.9 T. From the figures, cross saturation hampers the build of λ_d and produces excessive λ_d, which deteriorates torque ability.

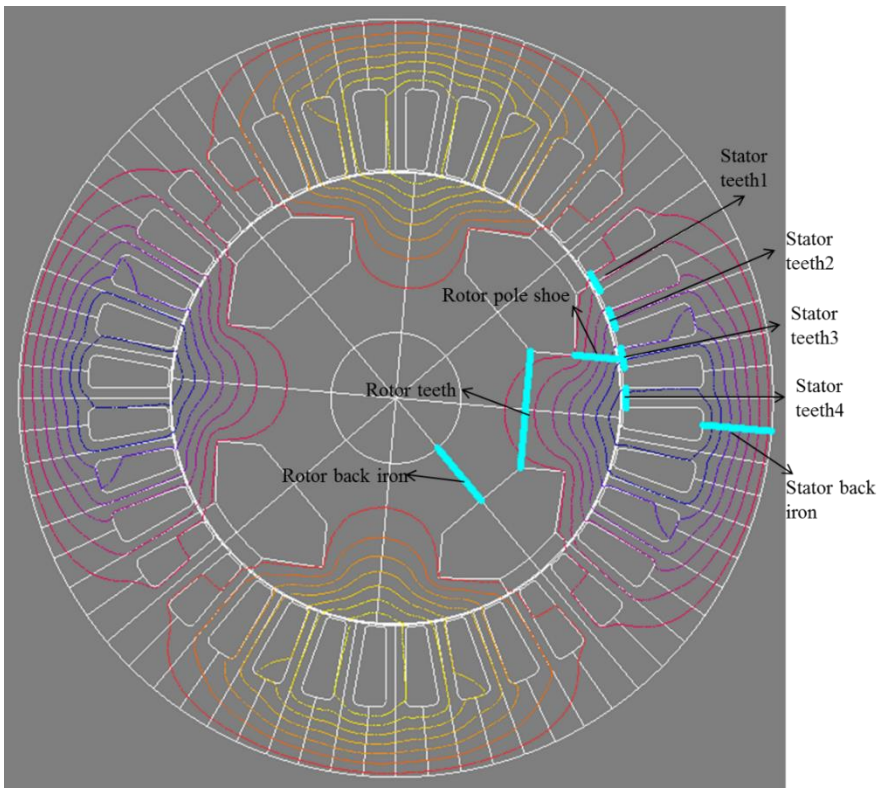

(a)

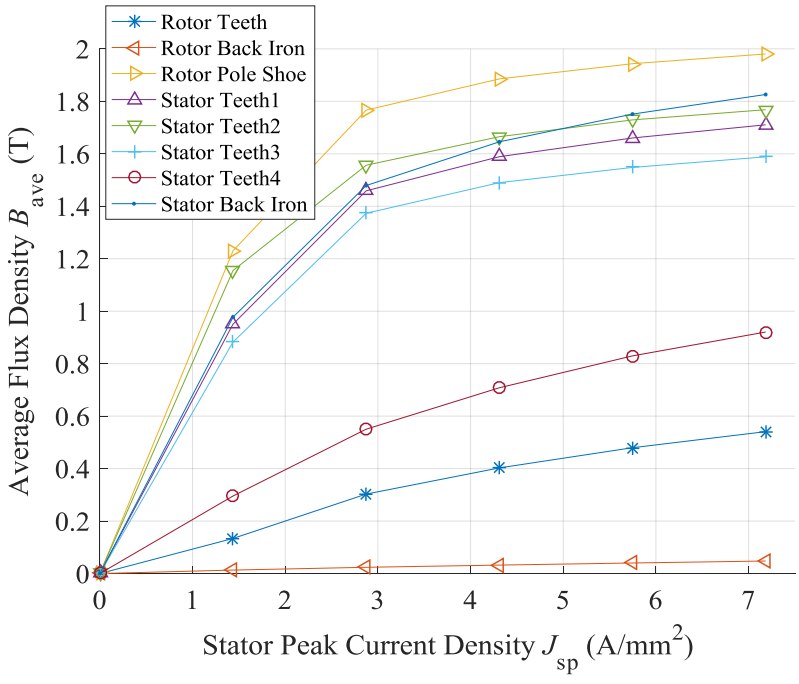

(b)

Figure 4.3. Magnetic equipotential lines of a four pole wound rotor synchronous machine. (a) q-axis flux pattern and (b) average flux density, B_{ave}, vs. stator peak current density, J_{sp} for various position on iron core.

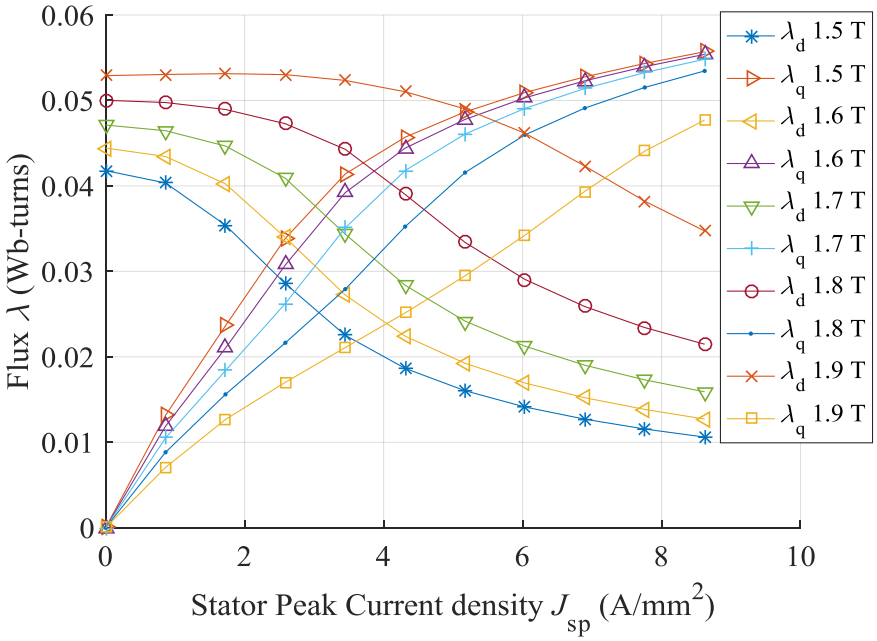

Figure 4.4. d-axis flux, λ_d and q-axis flux, λ_q, vs. peak stator current density, J_{sp} for various open circuit rotor teeth flux densities. $i_d = 0$, rotor teeth open circuit flux density is 1.5 T, 1.6 T, 1.7 T, 1.8 T and 1.9 T.

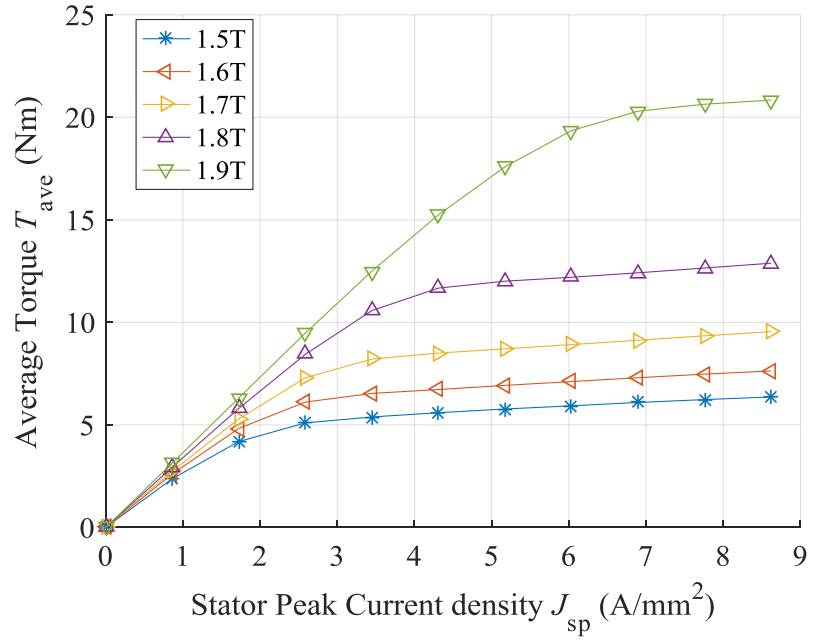

Figure 4.5. Average torque, T_{ave}, vs. peak stator current density, J_{sp} for various open circuit rotor teeth flux densities. $i_d = 0$, rotor teeth open circuit flux density is 1.5 T, 1.6 T, 1.7 T, 1.8 T and 1.9 T.

To overcome this problem, three approaches are suggested.

(1) Increase the l_{sbk}, l_{rbk} and l_{ssw} to accommodate more flux.

(2) Maintain λ_r by raising i_f to overcome the increase of magnetic reluctance caused by cross saturation.

(3) Increase q-axis magnetic reluctance and reduce L_q.

Since the open circuit flux densities at stator teeth and back irons are within normal range at a rotor teeth flux density of 1.5 T, the first approach is not adopted.

For the second approach, at i_d of 0, with increase of i_f, λ_d increases and λ_q decreases at the same i_q as shown in figure 4.4, so the torque also increases as plotted in figure 4.5. Alternatively, for same torque, stator current drops with increase of i_f. Since copper loss is produced from both stator and rotor, for each torque value, a stator and rotor current combination for minimum total copper loss exists.

For the third approach, from λ_q distribution pattern in figure 4.3 (a), a wide rotor pole shoe provides an easy path for q-axis flux, so reduction in l_{rs} helps to reduce L_q and alleviates cross saturation. From λ_d distribution pattern in figure 4.2 (a), a reduction in l_{rs} also narrows the path for d-axis flux, so a reduction in λ_r for same i_f value is expected as a side effect.

From generalisation purposes, with the same l_{sbr}, l_{rs} is represented by the pole shoe angle γ_{rs}. Figure 4.6 and figure 4.7 show λ_d and λ_q versus J_{sp} at various γ_{rs}, where i_d is set as 0 and λ_r as rated. From the figures, at open circuit, an optimum γ_{rs} of around 40° exists for maximum λ_d. Moreover, the cross saturation effect is greatly alleviated with reduction of γ_{rs} under the same i_q as expected. The reduction in cross saturation helps to maintain a higher torque with the increase of i_q, as illustrated in figure 4.8.

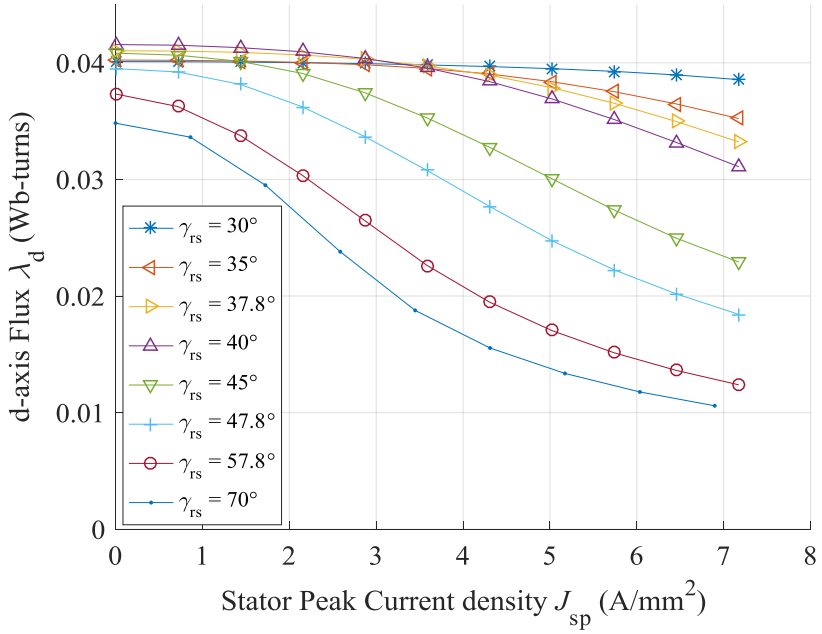

Figure 4.6. d-axis flux, λ_d, vs. stator peak current density, J_{sp} for various rotor pole shoe angle, γ_{rs}. i_d = 0, rotor teeth open circuit flux density is 1.5T.

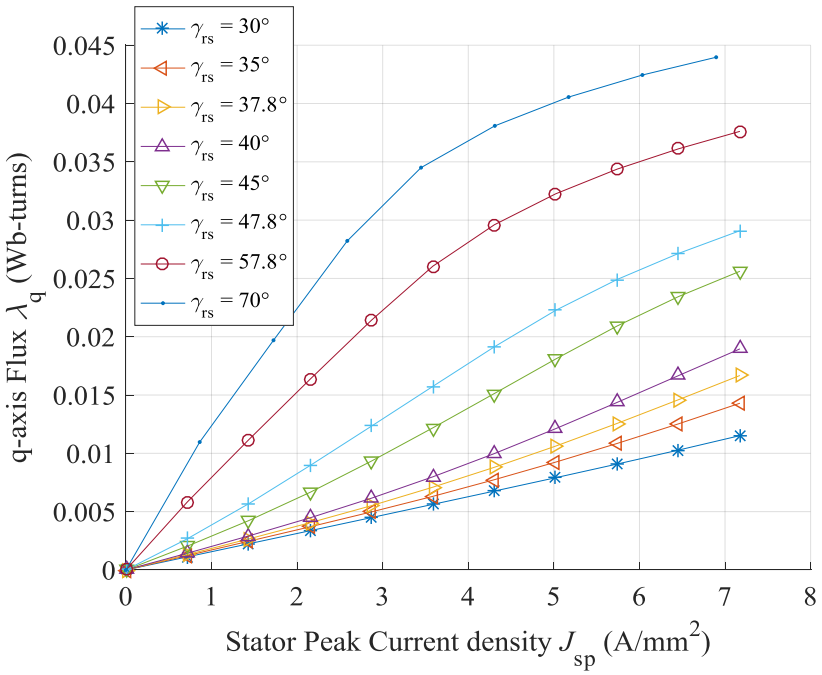

Figure 4.7. q-axis flux, λ_q, vs. peak stator current density, J_{sp} for various rotor pole shoe angle, γ_{rs}. i_d = 0, rotor teeth open circuit flux density is 1.5 T.

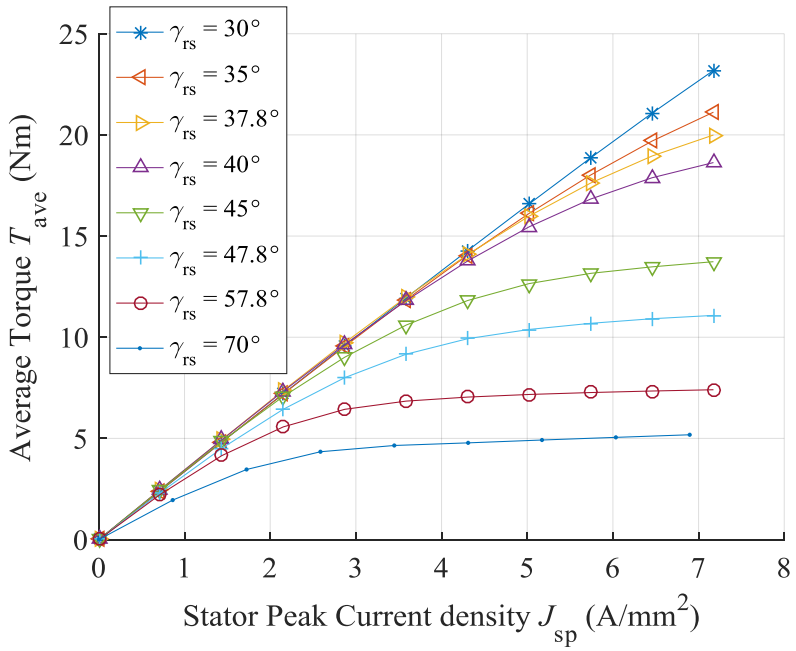

Figure 4.8. Torque vs. peak stator current density, J_{sp} for various rotor pole shoe angle, γ_{rs}. i_d = 0, rotor teeth open circuit flux density is 1.5 T.

Figure 4.9 plots the relationship between γ_{rs} and required i_f to produce the rated λ_r. The figure shows the decrease of γ_{rs} increases the requirement of i_f for same λ_r, as equivalent magnetic reluctance on d-axis increases with γ_{rs} reduction.

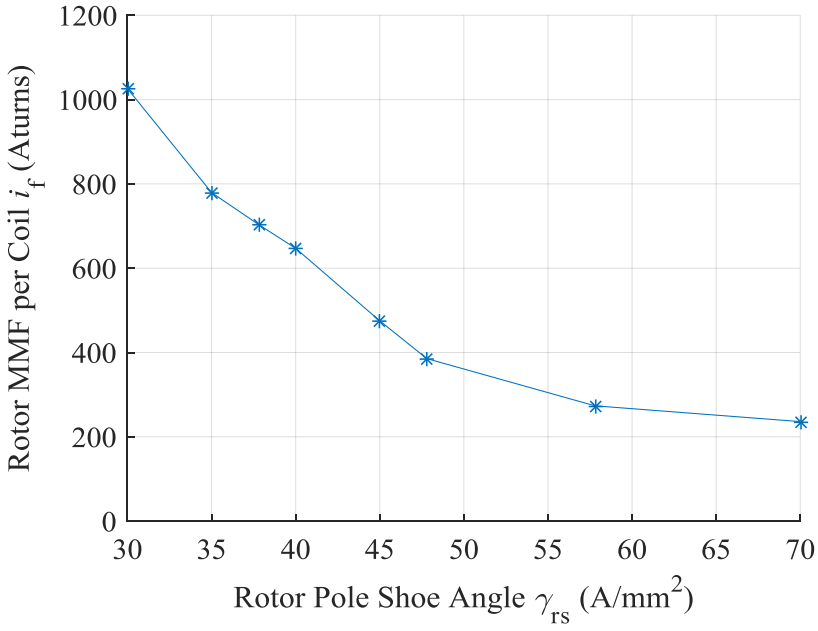

Figure 4.9. Rotor magnetic motive force per coil, i_f, required for open circuit rotor teeth average flux density of 1.5 T vs. rotor pole shoe angle, γ_{rs}.

The aforementioned description suggests the existence of a copper loss optimum rotor pole shoe angle for any torque value. Figure 4.10 plots the copper loss, P_{cop} versus average torque, T_{ave} at rated λ_r. On one hand, the minimum copper loss reduces as pole shoe width increases, and on the other hand, narrower rotor pole shoes gives a much wider high torque range, where machine torque drops slower with copper loss.

In conclusion, rotor pole shoes play an important part in machine torque and copper loss performances. To design a machine with low torque density, a wide rotor pole shoe is favourable for the lower copper loss, and to design a machine with high torque density, pole shoe width should be reduced to avoid cross saturation.

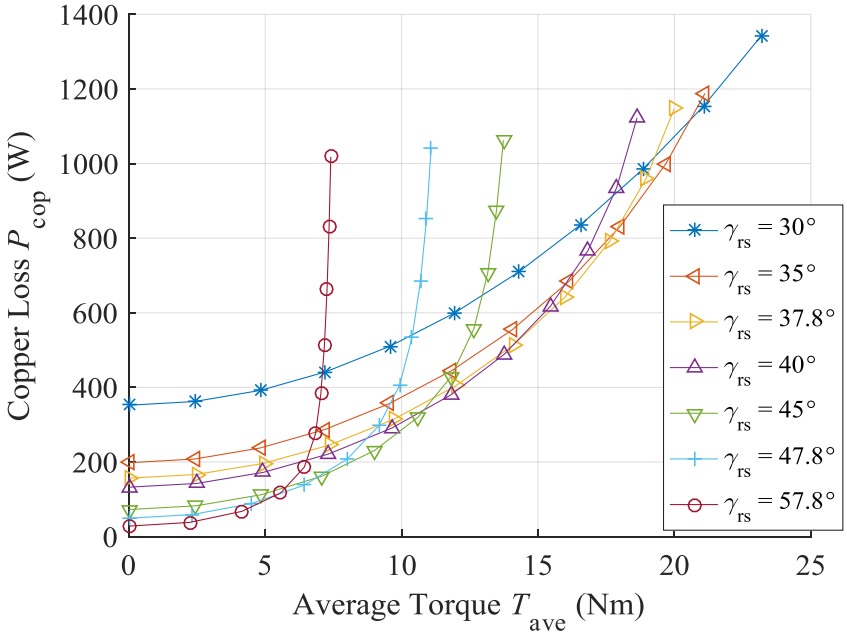

Figure 4.10. Copper loss, P_{cop}, vs. torque for various rotor pole shoe angle, γ_{rs} at open circuit rotor teeth flux density of 1.5 T.

4.1.3 Optimized Geometry

In this chapter, the machine geometry is optimized for minimum loss at base operation speed ω_b of 2000 rpm and rated mechanical power, P_{mech} of 5 kW. Both iron loss and copper loss are considered.

The geometry parameters for optimization are:

(1) Rotor pole shoe angle γ_{rs};

(2) Rotor pole angle γ_r;

(3) Stator teeth width s;

(4) Stator back iron thickness l_{sbk};

(5) Rotor back iron thickness l_{rbk};

(6) Split ratio l_{sbr}/l_{sr};

(7) Axial length l_{al}.

The prior section indicates that rotor pole shoe angle, γ_{rs} is an important factor in WRSM design for high efficiency. In figure 4.11, for different γ_r, the minimum loss is plotted against γ_{rs}. To obtain the minimum loss, stator and rotor losses are balanced. A lowest loss of 1205W is presented at an optimum combination of 35° for γ_r and 50° for γ_{rs}.

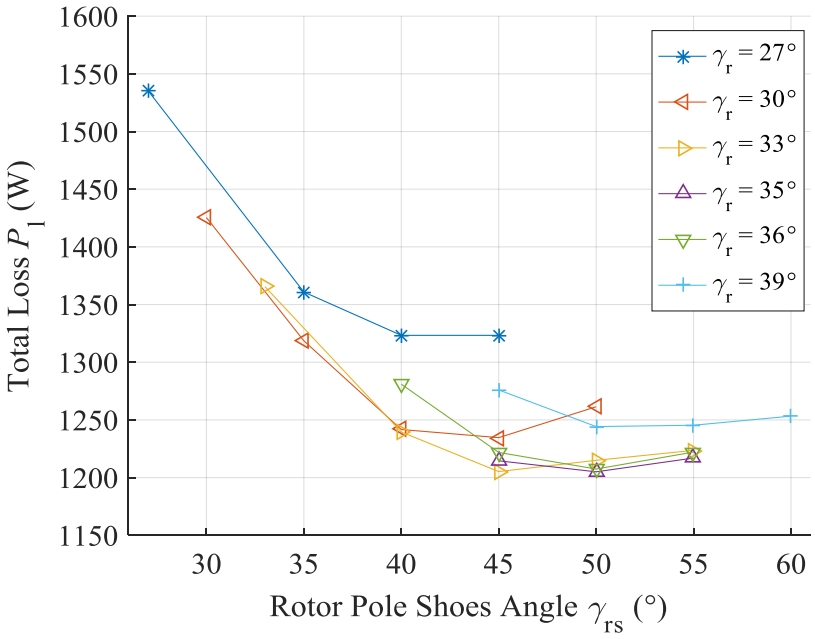

Figure 4.11. Total loss, P_l vs. rotor pole shoe angle, γ_{rs} for various rotor pole angle, γ_r .

The stator teeth width, l_s is a crucial factor in machine design. A wide tooth on one hand reduces equivalent airgap length and stator teeth saturation level, and on the other hand reduces stator winding area. These competing factors give rise to an optimum width for loss production. From optimization, l_s increase from 3.57 to 4.07 mm, and loss slightly reduces from 1205 W to 1185

W, as shown in figure 4.12.

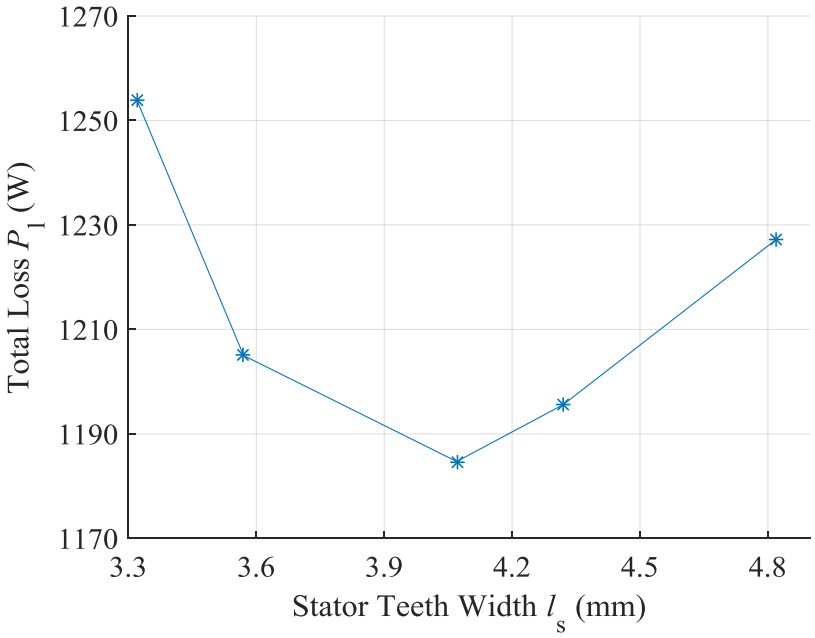

Figure 4.12. Total loss, P_l vs. stator teeth width, l_s.

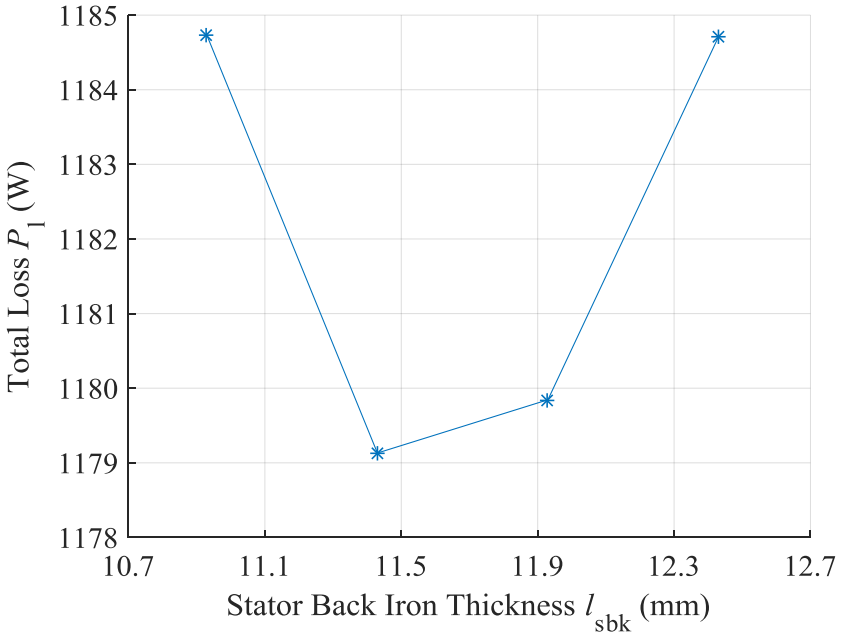

Figure 4.13. Total loss, P_l vs. stator back iron thickness, l_{sbk}.

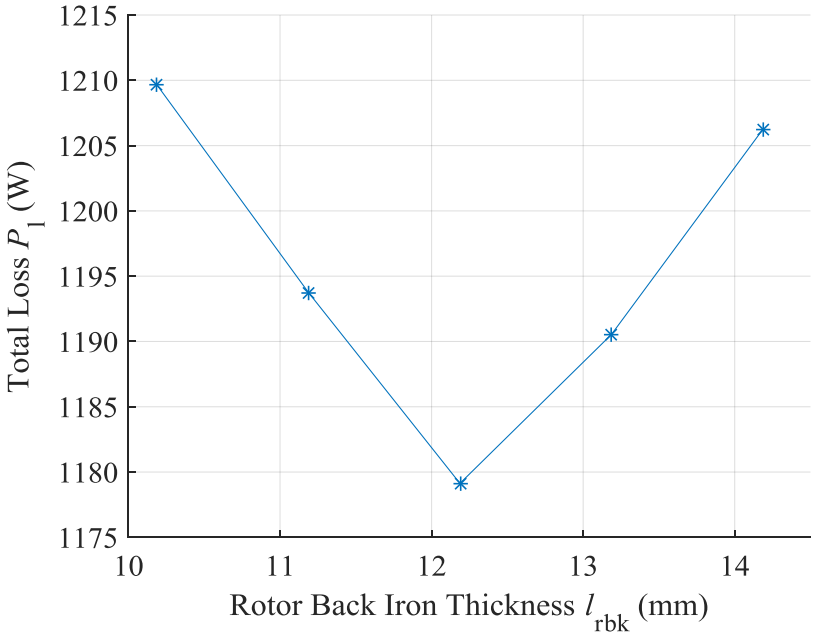

Figure 4.14. Total loss, P_l, vs. rotor backiron thickness, l_{rbk}.

Optimization of stator back iron thickness, l_{sbk} and rotor back iron thickness, l_{rbk} are shown in figure 4.13 and 4.14, where an optimum l_{sbk} of 11.4 mm and l_{rbk} of 12.2 mm reduces total loss to 1179 W.

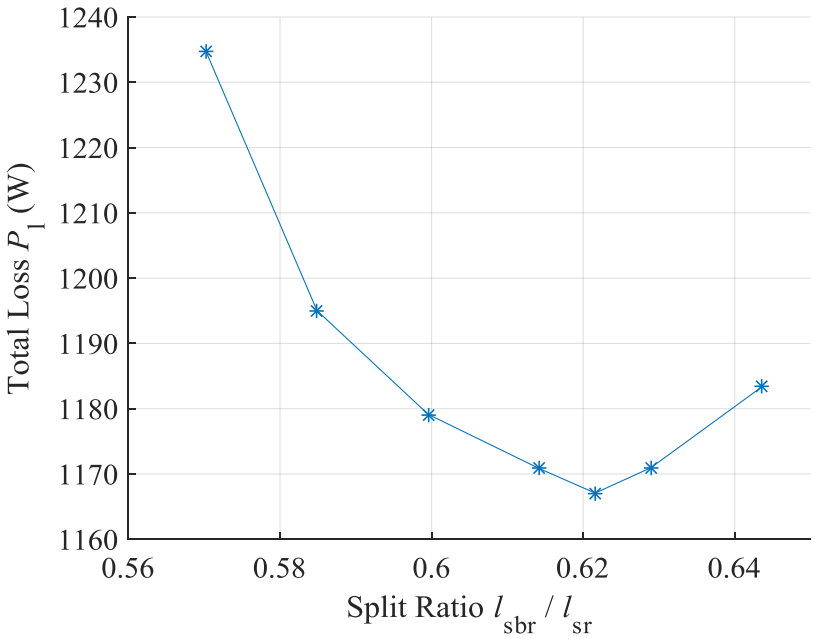

Figure 4.15. Total loss, P_l vs. split ratio, l_{sbr} / l_{sr}.

With a fixed l_{sr} of 68.1 mm and a changeable l_{sbr}, the split ratio, l_{sr} / l_{sbr}, is plotted against total loss in figure 4.15, where an optimum split ratio of 0.622 is presented. The optimum l_{sbr} is 42.63 mm.

With geometrical optimization, under rated operating condition, J_{sp} is 6.65 A/mm^2, the fundamental stator current i_{sfun} is 171.3 A, i_f is 962.5 Aturns and the rotor current density J_r is 5.71 A/mm^2. Total loss, P_l is 1167 W and the efficiency is 81.1%.

Despite a limitation of 80.5 mm in axial length, it is intriguing to investigate the role of axial length in loss production. This follows the previous geometric optimization process, the stator copper loss, P_{scop}, stator iron loss, P_{sir}, rotor copper loss, P_{rcop} and rotor iron loss, P_{rir} versus l_{al} is plotted in figure 4.16. Stator peak current density, J_{sp} and rotor current density, J_r are plotted in figure 4.17, and the efficiency in figure 4.18.

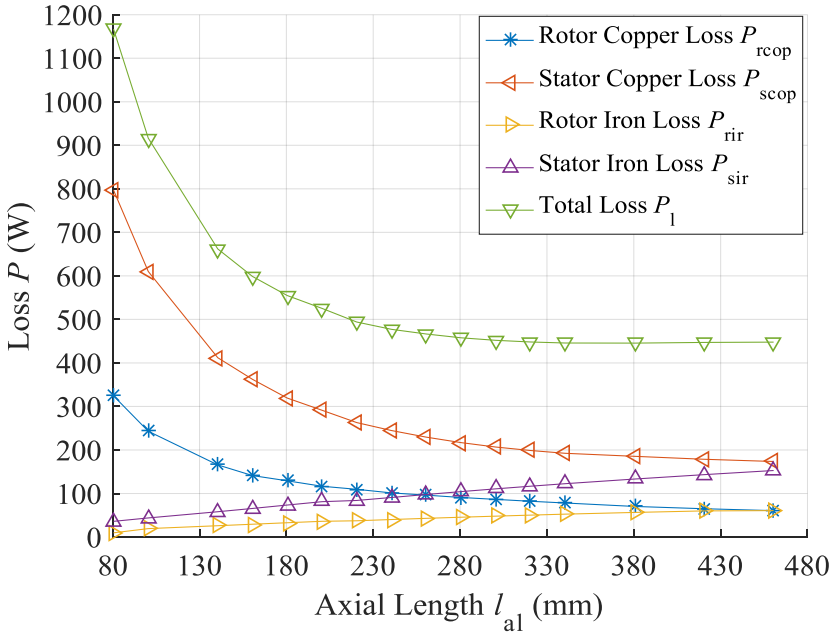

Figure 4.16. Iron and copper losses vs. axial length, l_{al}.

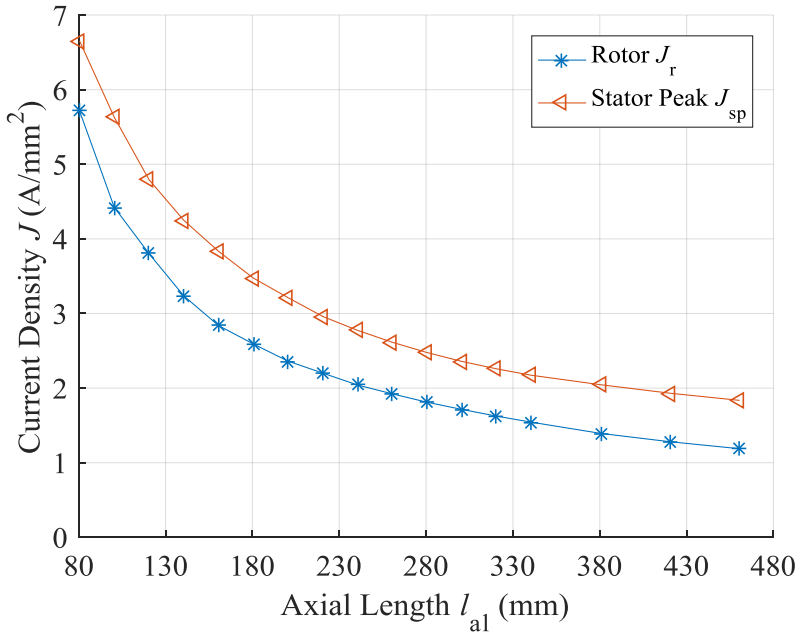

Figure 4.17. Stator peak current density, J_{sp} and rotor current density, J_r, vs. axial length, l_{al}.

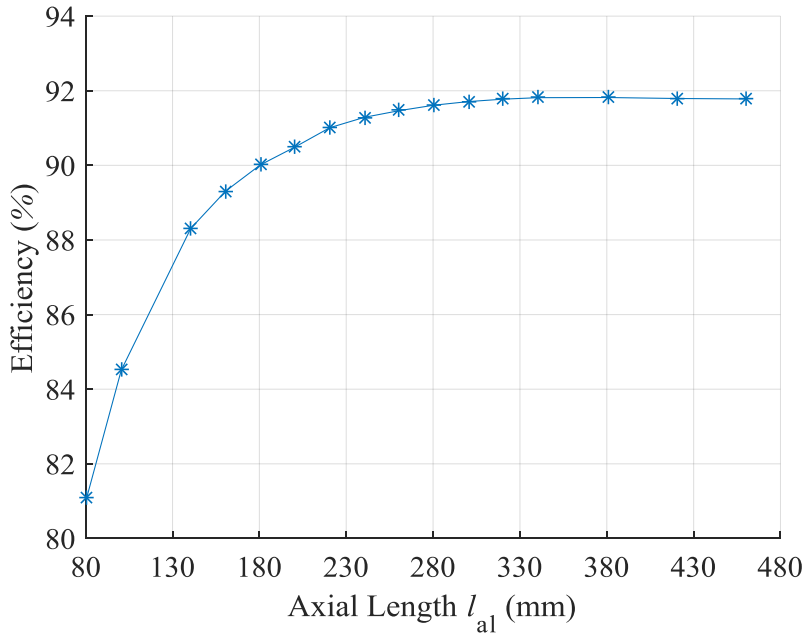

Figure 4.18. Efficiency vs. axial length, l_{al}.

From the figures, with increase of axial length, a rise in iron loss is exhibited, but this is overtaken by a significant reduction in copper loss, which allows a major reduction in total loss. An optimum axial length of 320.5 mm is selected, where total loss drops from 1167 W to 446 W, and the efficiency increases from 81.1% to 91.8%. The optimum peak stator current density

reduces from 6.65 A/mm^2 to 2.26 A/mm^2, and rotor current density from 5.71 A/mm^2 to 1.63 A/mm^2. This reduction in current densities allows a decrease in both stator and rotor copper loss despite an increase in rotor winding resistance.

In conclusion, this section investigates the torque and efficiency performance of a four pole WRSM. From the study, the machine is susceptible to cross saturation, which requires careful design of rotor pole angle. For the rated operation requirement, the efficiency of the machine can only be greatly improved with increase in axial length.

4.2 Comparison Between Four and Six Poles

In this section, the influence of pole number on the wound rotor synchronous machine performance is investigated.

Generally speaking, changing the pole number affects machine performances in many ways [154]. Firstly, increasing the pole number allows a reduction in back iron thickness and therefore a lower machine iron volume. As iron loss is roughly proportional to the square of the electrical frequency, higher pole number increases iron loss, but this is partially offset by reduction in machine iron volume.

Secondly, inductance of the windings changes with the pole number, which may affect WSRM performances. In the case of IPM, the reluctance torque is inversely proportional to the square of pole number, so increase in pole number diminishes reluctance torque [154]. The reluctance torque in the case of WRSM is unclear, and therefore will be studied in this chapter.

Lastly, the pole number affects copper losses. Increasing the pole number have opposite effects on stator and rotor copper loss. On one hand, it decreases stator end winding span and therefore reduces stator phase resistance and copper loss. On the other hand, it reduces rotor winding area per coil, so for the same rotor excitation MMF, a higher copper loss is generated. This decrease in rotor winding area can be partially offset by reduction in rotor machine back iron thickness.

This section investigates the performance of WRSM with six pole. A six pole structure is

adopted over higher pole number due to inverter requirement. Further increase of pole number in high speed design increases switching frequency, which posts challenges on the applied switching devices, including switching loss and inverter cost problems.

4.2.1 Optimized Geometry

In Altair Flux, a six pole wound rotor synchronous machine model is constructed as below in figure 4.19. By applying the geometric optimization process at based speed, ω_b, and mechanical power, P_{mech}, the efficiency optimized geometry parameters are listed below in table 4.2.

After optimization, at base speed and rated power, the stator peak current density, J_{sp} is 5.74 A/mm^2. The rotor MMF per coil, i_f is 665.5 Aturns and the rotor current density, J_r is 4.21 A/mm^2. Compared with the stator and rotor current densities of 6.65 A/mm^2 and 5.71 A/mm^2 on the four pole machine, both current densities are reduced.

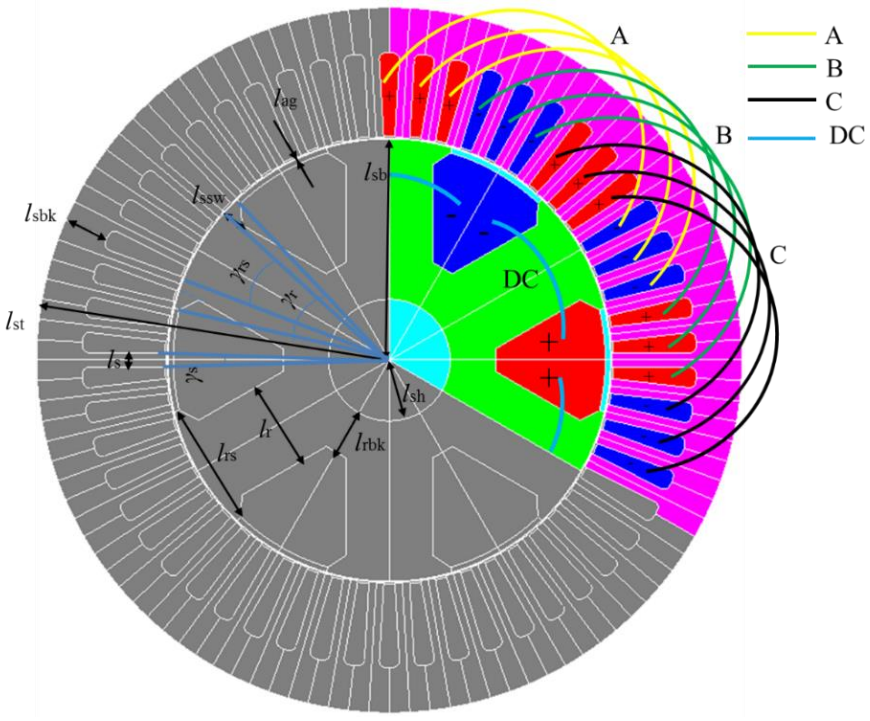

Figure 4.19. A six pole wound rotor synchronous machine model in Altair Flux.

Parameter	Value	Parameter	Value
Pole pair p	3	**Stator back iron thickness l_{sbk} (mm)**	8.67
Phase number m	3	**Rotor back iron thickness l_{rbk} (mm)**	8.79
Winding type	distributed	**Rotor pole shoe thickness l_{rss} (mm)**	4.40
Number of slots Q	54	**Axial active length l_{al} (mm)**	80.5
Slot Angle $\gamma_{sl}=2\pi p/Q$	$\pi/9$	**Stator teeth angle γ_s (°)**	3.78
Number of slots per pole and phase $q=Q/2pm$	3	**Rotor teeth angle γ_r (°)**	22.56
Stator bore radius l_{sbr} (mm)	43.02	**Pole shoe angle γ_{rs} (°)**	33
Stator shaft radius l_{sfr} (mm)	11.75	**Stator fill factor (c_s)**	0.3
Stator radius l_{sr} (mm)	68.1	**Rotor fill factor (c_r)**	0.4
Airgap Length l_{ag} (mm)	0.3	**Number of turns per phase N**	15
Rotor teeth width l_{rt} (mm)	16.71	**Iron core material**	M400-50A
Rotor pole shoe width l_{rs} (mm)	24.26	**Rated speed (rpm)**	2000
Stator teeth width l_{st} (mm)	2.84	**Maximum speed (rpm)**	20000

Table 4.2. Optimized geometric parameters of a six pole wound rotor synchronous machine.

4.2.2 Open Circuit Comparison

According to (1.16) - (1.18) in section 1.2.3, in order to take pole pair difference into consideration, a factor of 1.5 is applied on the flux of six pole machine in comparison with four pole machine,

At open circuit, $\lambda_d = \lambda_r$, flux distribution diagrams of four and six pole machine are shown in figure 4.20. Figure 4.21 illustrates the relation between λ_d and i_f of four and six pole machines in comparison. Notably, the six pole machine produces an approximate 1.7×10^{-3} to 3.1×10^{-3} Wb-turns higher flux linkage for same i_f. This can be explained with magnetic circuit equation (4.2) and figure 4.20. From figure 4.20, the excitation flux path on d-axis of six pole machine is shorter than that of four pole machine, results in a lower magnetic reluctance R_m.

$$\frac{MMF}{\lambda} = \frac{l}{\mu S} = R_m \tag{4.2}$$

S is the cross section of path, l is the equivalent length of path, λ is flux through the circuit and μ is magnetic permeability.

R_m of two machines versus i_f are plotted for comparison in figure 4.22, where S and λ are measured on the rotor teeth. With increasing i_f, the iron core gradually saturates so the R_m for both machine increases, but the six pole machine maintains a 1.7×10^4 to 2.2×10^4 Aturns / Wb lower R_m than four pole machine.

The rotor radius l_{rr} is 42.72 mm on six pole machine, and 42.03 mm on four pole machine. With the same l_{al}, the rotor volume on six pole machine is 3.2% larger. From previous research [154], machine torque can be represented as:

$$T = 2V_l BJ \tag{4.3}$$

where V_l is the rotor volume, B is the flux density or magnetic loading, J is the current density or electric loading. From (4.3), with same electric and magnetic loading, six pole machine produces 3.2% higher torque.

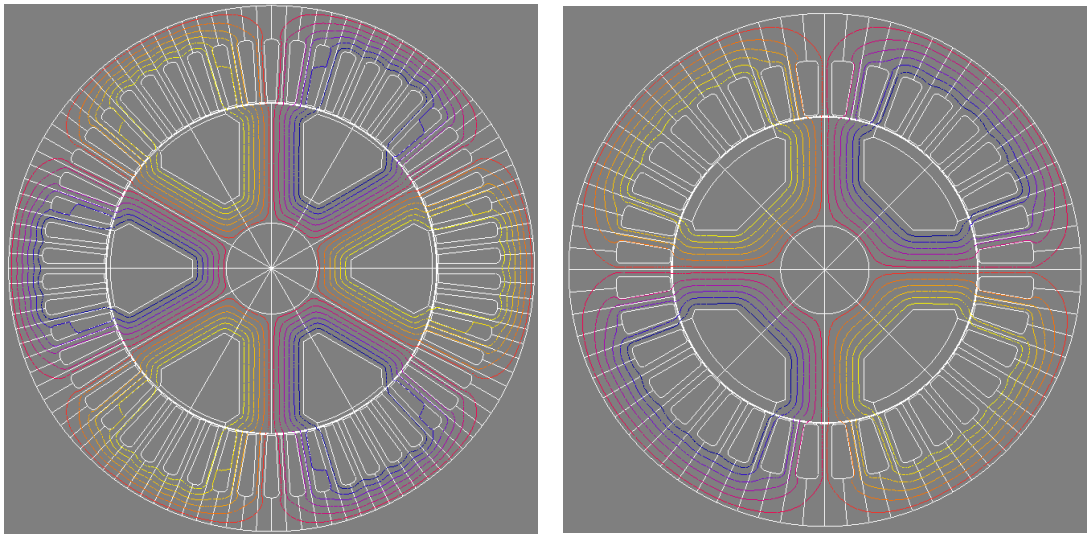

(a) *(b)*

Figure 4.20. Open circuit magnetic equipotential lines of wound rotor synchronous machine (a) four pole and (b) six pole.

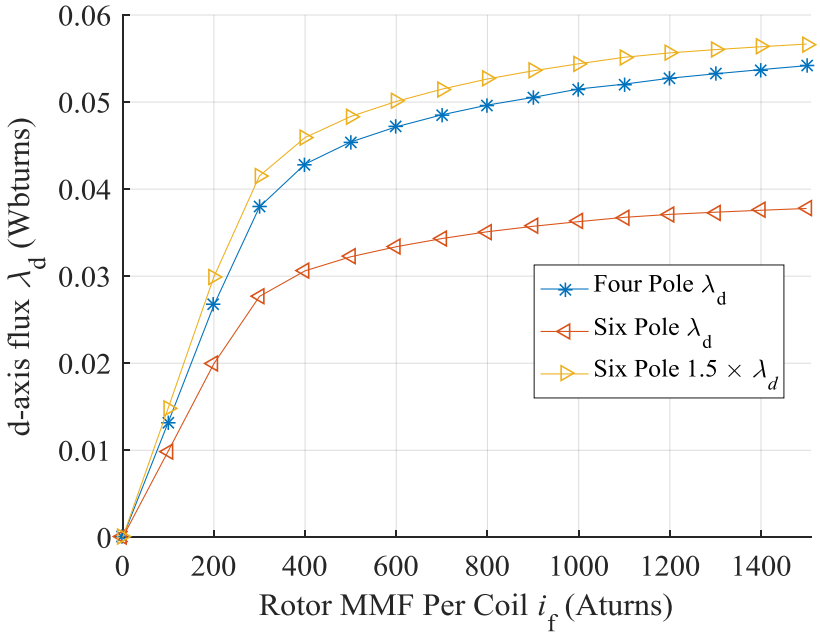

Figure 4.21. Open circuit d-axis flux, λ_d, vs. rotor MMF per coil, i_f, comparisons for four pole and six pole wound rotor synchronous machine.

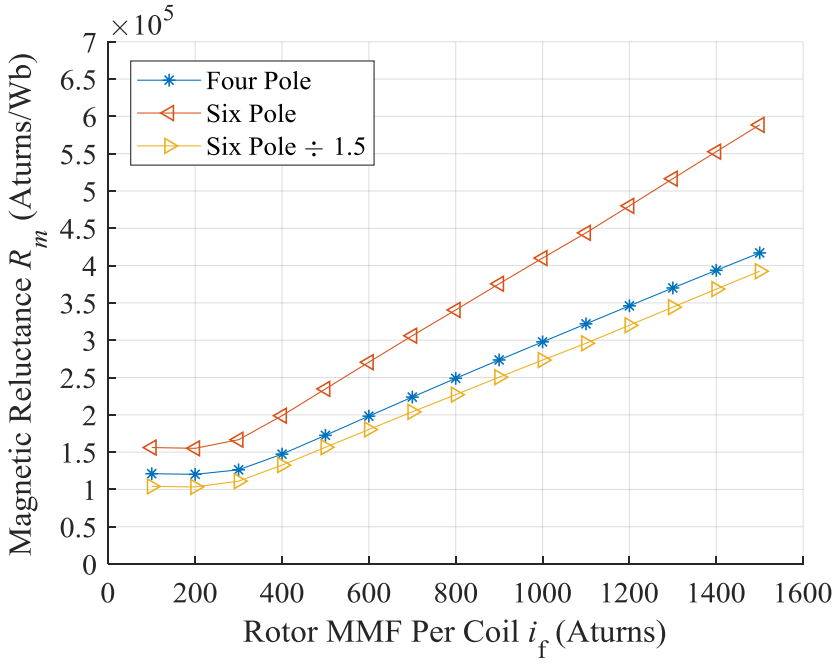

Figure 4.22. Open circuit magnetic reluctance, R_m, vs. rotor MMF per coil, i_f, comparisons for four pole and six pole wound rotor synchronous machine.

4.2.3 Inductance Torque Comparison

With $i_f = 0$, the reluctance torque, T_{re} at MTPA load angle, θ_{MTPA} of both four and six pole

machines are investigated. L_d, L_q and T_{re} versus peak stator current density, J_{sp} are plotted in figure 4.23 and 4.24, respectively. From figure 4.23, L_d and L_q of four pole machine are significantly higher than six pole machine. However, if the factor of 1.5 is applied, L_d of six pole machine is much closer to four pole, especially at high J_{sp}, and L_q are similar in both machines. This results in an only slightly larger reluctance torque in four pole machine, as shown in figure 4.24. Compared with an IPM, increasing pole number in the WRSM only slightly affects reluctance torque performance. Regardless of saturation due to rotor current, at the rated J_{sp}, the reluctance torque is around 10 Nm, which is more than 40% of total torque.

With $i_f \neq 0$, at the rated stator and rotor current, the torque and their components from rotor excitation, T_{exc} and reluctance, T_{re}, can be derived from (1.16). In figure 4.25, T_{exc} and T_{re} are plotted against load angle, θ. From the figure, T_{re} of the four and six pole machine are similar in amplitude and distribution pattern. At $\theta < 90°$, T_{re} diminishes due to saturation. At $\theta > 90°$, T_{re} reappears, but is much smaller than when $i_f = 0$. The minimum T_{re} is around -3 Nm for both machines. The θ_{MTPA} in four pole machine is 87.8° and in six pole machine is 88.6°. From the figure, reluctance torque does not contribute much under rated operating conditions.

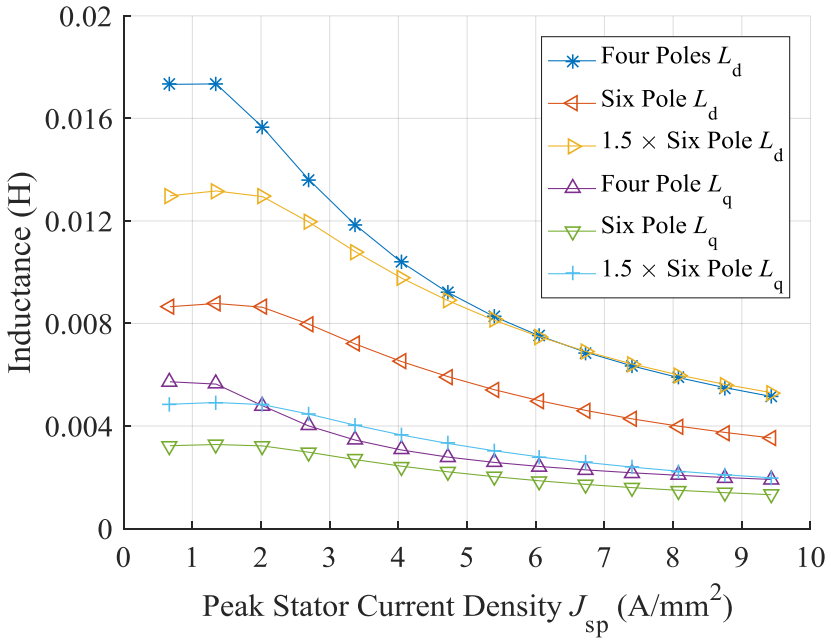

Figure 4.23. d-axis flux, λ_d and q-axis flux, λ_q, vs. peak stator current density, J_{sp} of four pole and six pole

wound rotor synchronous machine in comparison.

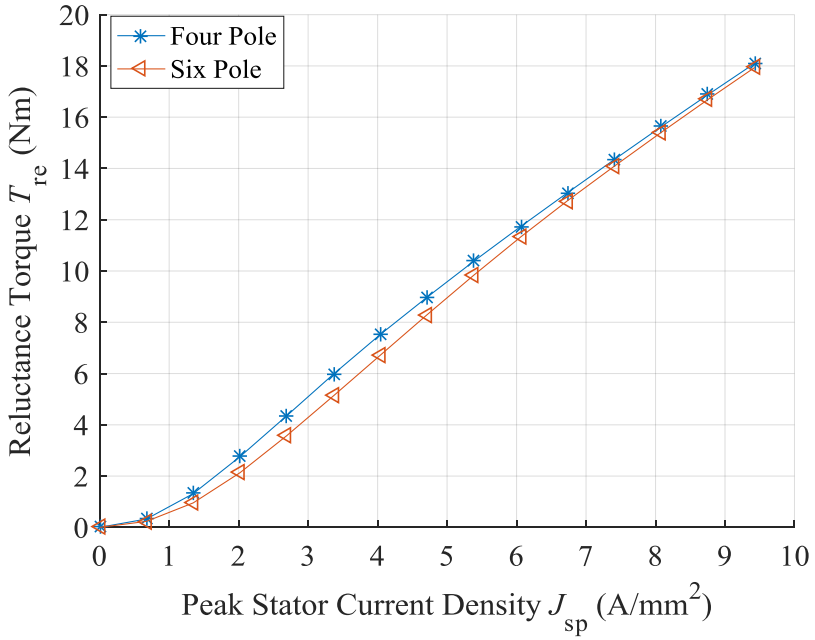

Figure 4.24. Reluctance torque, T_{re}, vs. peak stator current density, J_{sp} of four pole and six pole wound rotor synchronous machine in comparison.

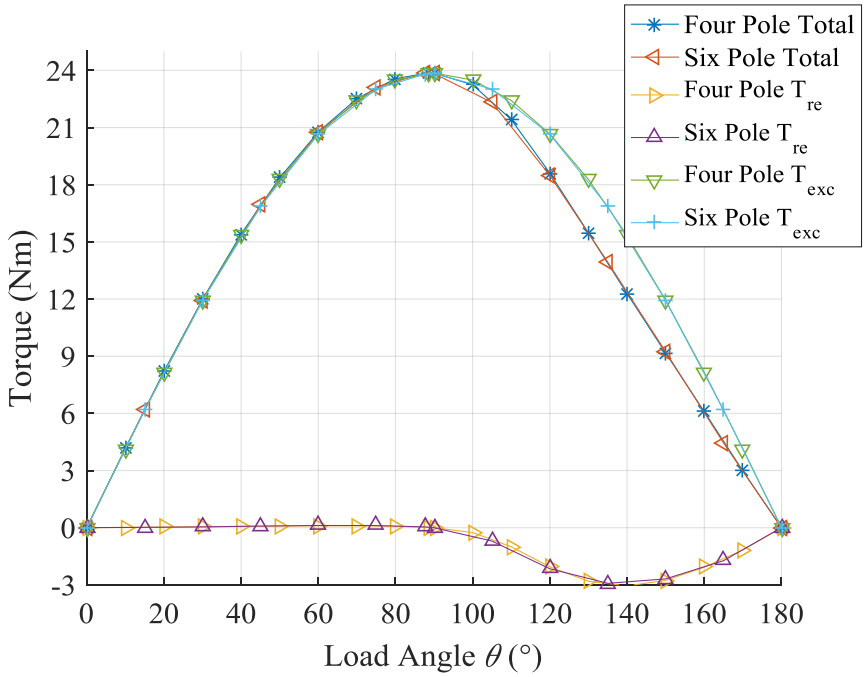

Figure 4.25. Reluctance torque, T_{re}, excitation torque, T_{exc} and their sum vs. load angle, θ of four pole and six pole wound rotor synchronous machine in comparison.

4.2.4 Loss Comparison

Generally speaking, compared with a four pole rotor, a six pole rotor has about 0.6 times winding area per coil, therefore for same rotor outer dimensions, coil number and fill factor, an increase of 1.5 times the rotor winding resistance of the four pole machine may be expected. For the same i_f, the six pole rotor should produce about 1.5 times higher copper loss. On the stator, the four and six pole machines share a similar total winding area while the six pole stator has 0.6 times shorter end winding, so a reduction in stator copper resistance and stator copper loss is expected.

In this study, with geometric optimization for efficiency, the copper losses are offset by the following factors. First, from section 4.2.2, a lower i_f is required in six pole machine for same λ_r. Second, from section 4.1.3 and table 4.2, l_{rbk} of the six pole rotor reduces from 12.19 mm of four pole rotor to 8.79 mm, allowing expansion in winding area per coil to 158 mm^2, which is only 10% smaller than four pole rotor of 176 mm^2. With the same number of turns per coil, the rotor resistance of the six pole machine is 45% higher than the four pole. Similar to l_{rbk}, the l_{sbk} of six pole stator reduces from 11.43 mm of four pole to 8.67 mm, and winding area per phase increases from 760.8 mm^2 to 891.0 mm^2. Larger winding area and shorter end winding length reduces phase resistance by a significant 25%.

With balanced stator and rotor current for minimum loss and MTPA operating conditions, figure 4.26 (a) and (b) illustrate the stator peak current density, J_{sp} and rotor current density, J_r versus average torque, T_{ave}. Notably, a decrease in both current densities are achieved in six pole machine compare with four pole, where the reduction is more manifest at high average torque.

The comparisons between stator copper loss, P_{scop}, rotor copper loss, P_{rcop}, stator iron loss, P_{sir} and rotor iron loss, P_{rir} versus average torque, T_{ave} are plotted in figure 4.27. The comparison between efficiency versus T_{ave} are shown in figure 4.28. From the figures, except for low torque conditions under 7 Nm, copper losses are lower in six pole structure on both stator and rotor. The six pole machine shows a higher iron loss level, but since iron loss is much smaller

compared with copper loss at base speed, the total loss on six pole machine is much smaller than four pole, leading to a significant improvement in efficiency over most of the operational power region.

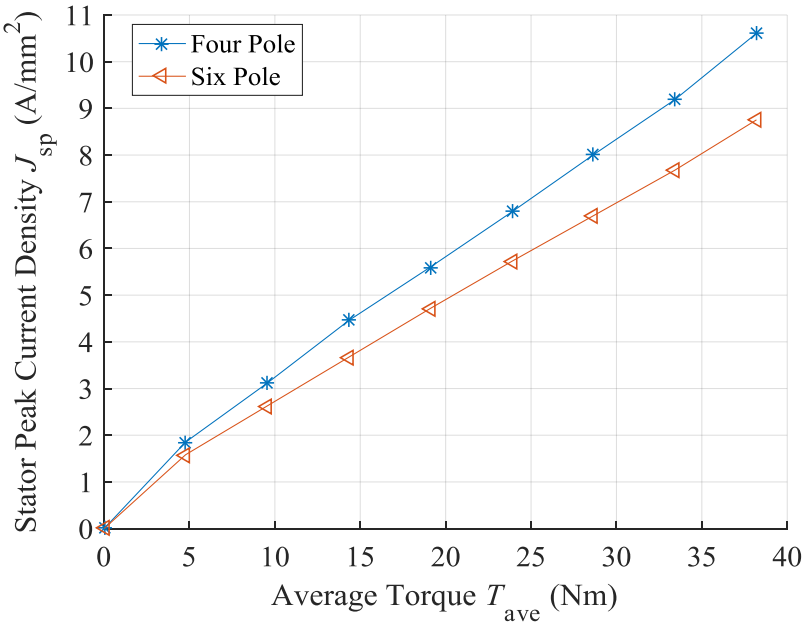

(a)

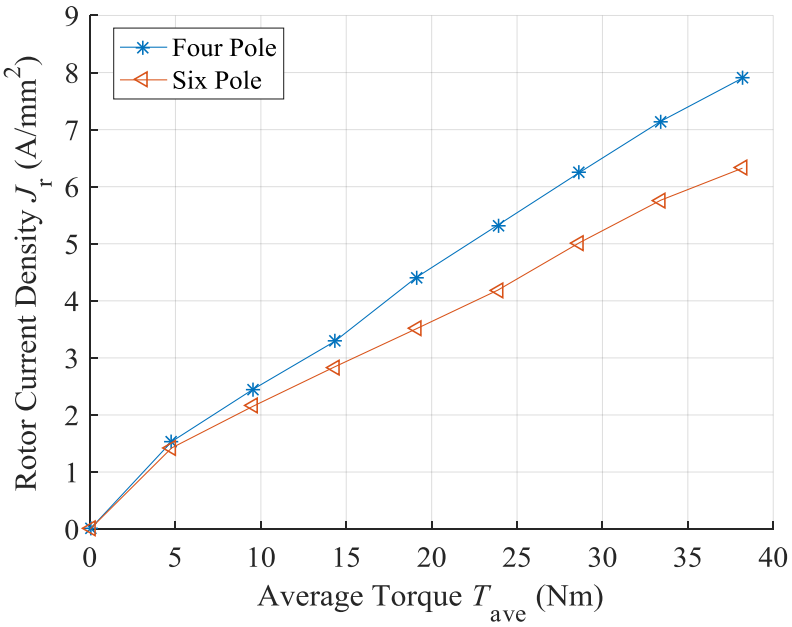

(b)

Figure 4.26. (a) Stator peak current density, J_{sp} and (b) rotor current density, J_r, vs. average torque, T_{ave} for four pole and six pole wound rotor synchronous machine.

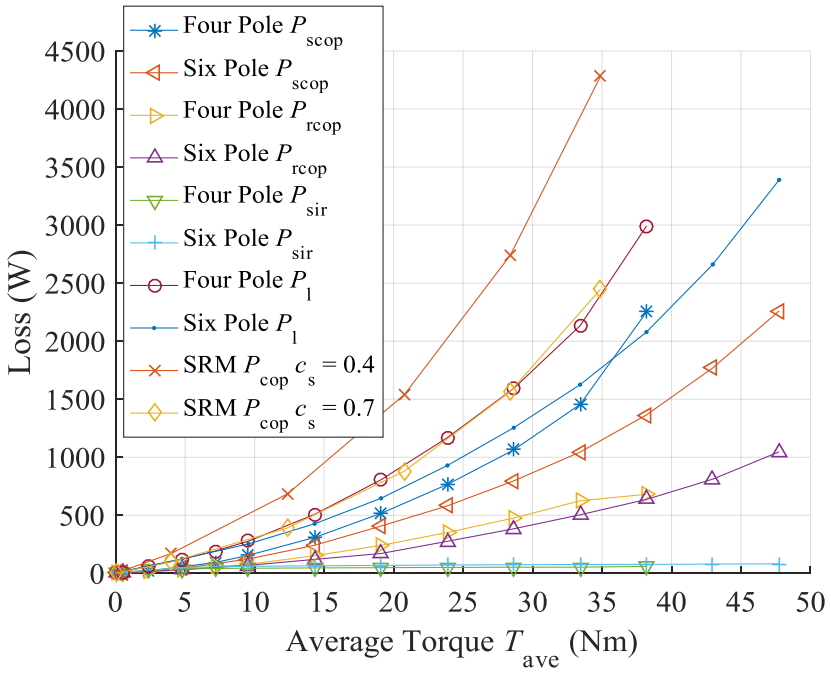

Figure 4.27. Stator copper loss, P_{scop}, rotor copper loss, P_{rcop}, stator iron loss, P_{sir} and rotor iron loss, P_{rir}, vs. average torque, T_{ave} for four pole and six pole wound rotor synchronous machine under rated speed, and copper loss, P_{cop} of the benchmark 12/8 classical SRM with fill factor, c_s of 0.4 and 0.7, under unipolar square current excitation.

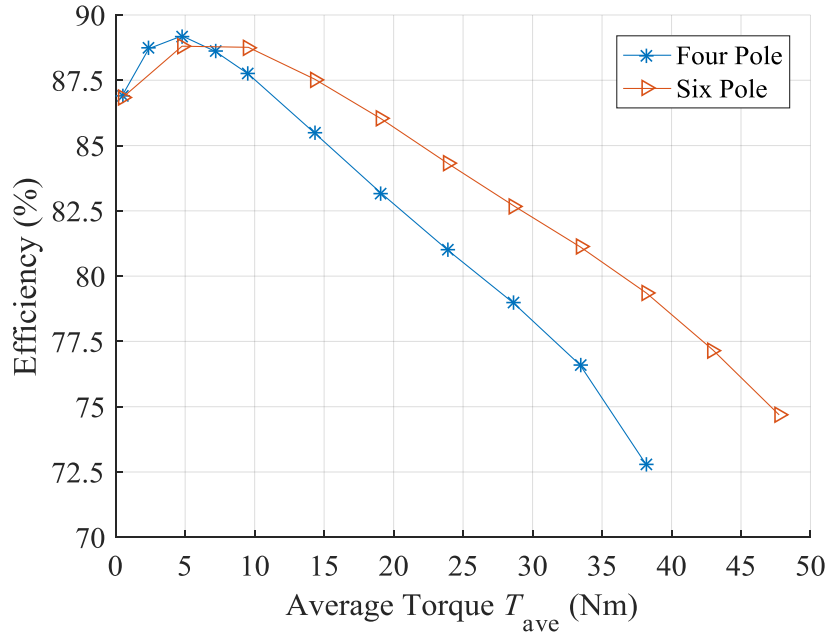

Figure 4.28. Efficiency vs. torque for four pole and six pole wound rotor synchronous machine under rated speed.

Comparing current densities in figure 4.26 with benchmark classical SRM under USQ

excitation in figure 2.13 (a), for the same torque, the peak current density on the SRM stator coil is about twice as that in WRSM stator coil. Set stator fill factor, c_s of 0.4 to the SRM concentrated winding, the resultant copper loss in SRM is plotted in figure 4.27 for comparison. Clearly, SRM under USQ excitation naturally produces significantly higher copper loss than WRSM under AC sinusoidal current excitation. If the copper loss of classical SRM is set to be equivalent to six pole WRSM with c_s of 0.3 and c_r of 0.4, c_s of classical SRM need to reach 0.7.

4.3 Torque Ripple Reduction

The six pole wound rotor synchronous machine developed in previous sections exhibit a significant torque ripple. To quantize the goodness of torque ripple harmonic level, the harmonic coefficient, f_n is introduced as:

$$f_n = \frac{A_1}{\sum_{i=1\cdots n} A_n} \tag{4.4}$$

where A_n is the amplitude of n^{th} harmonics. A_1 is the amplitude of fundamental component. A coefficient closer to one represents a lower torque ripple harmonic level.

Figure 4.29 (a) shows the torque waveform of one electrical cycle under rated operating condition. The average torque, T_{ave} is 23.87 Nm, and torque ripple coefficient, T_{ripp} is 11.45. Figure 4.29 (b) displays the harmonics of (a), where a multiple of six order of harmonics are presented. The 6^{th}, 18^{th}, 36^{th} and 54^{th} harmonics are more manifest than others, and the 18^{th} has the highest amplitude.

To reduce the torque ripple, the problem is discussed in three parts. In the first part, the source of the ripple is determined. In the second part, a torque reduction method by implementing eccentric magnetic pole is proposed. To minimize torque ripple while keeping maximum average torque, a systematic approach is developed under same rotor excitation. Extra benefits in reduction of iron loss is also exhibited.

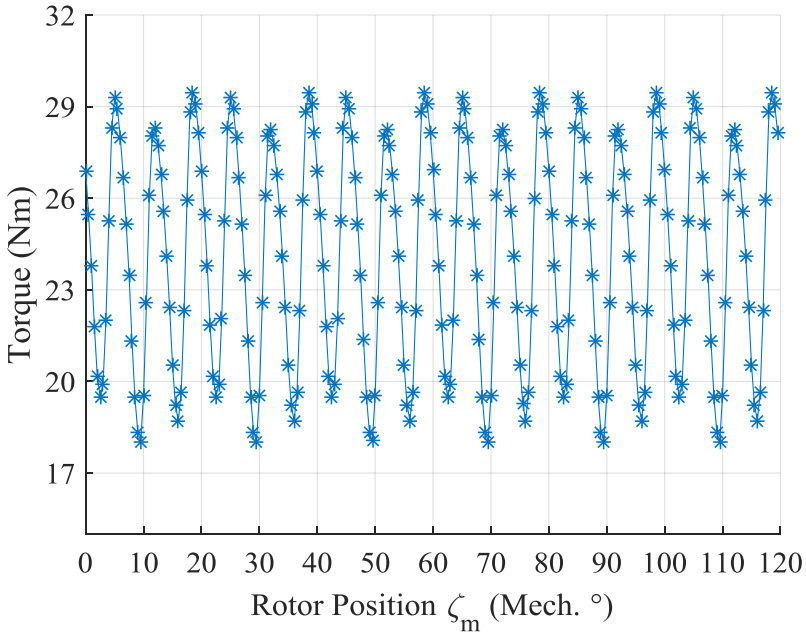

(a)

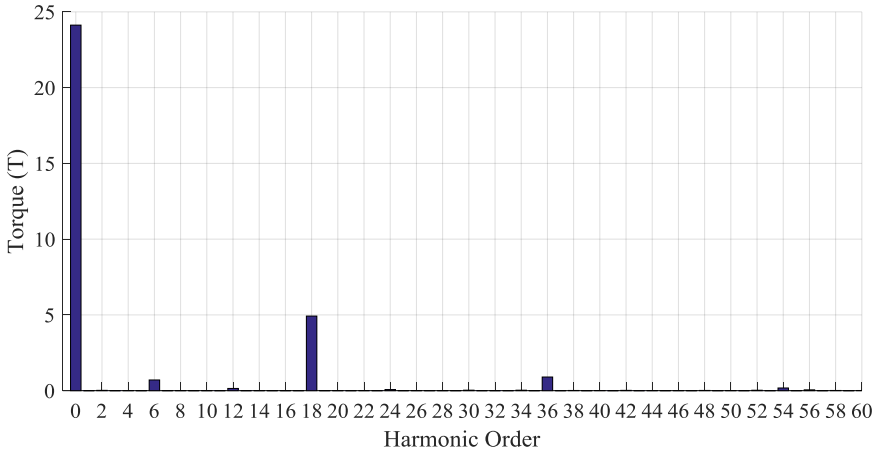

(b)

Figure 4.29. Normal rotor pole torque performance of (a) instantaneous torque vs. rotor position, ζ_m and (b) harmonics analysis. Average torque, T_{ave} is 23.87 Nm.

4.3.1 Source of Torque Ripple

To determine the source of torque ripple, conventional theory in PM machine is adopted. From previous study, the machine total torque in abc model is [160] :

$$T = p\left(\frac{1}{2}\mathbf{i}_{abc}^{T}\frac{d\mathbf{L}_{abc}}{d\zeta}\mathbf{i}_{abc} + \mathbf{i}_{abc}^{T}\frac{d\boldsymbol{\lambda}_{rabc}}{d\zeta}\right) + T_{cog} \tag{4.5}$$

where p is pole pair, T_{cog} is cogging torque, ζ is rotor position in electrical degree. $\boldsymbol{\lambda}_{rabc}$ is the phase abc flux linkage generated by rotor coil. $\boldsymbol{\lambda}_{rabc}$ is given with:

$$\boldsymbol{\lambda}_{rabc} = \sum_{n=1}^{\infty} N\lambda_{2n-1} \begin{bmatrix} \cos\left[(2n-1)(\omega t + \varphi_{2n-1})\right] \\ \cos\left[(2n-1)\left(\omega t + \varphi_{2n-1} - \frac{2\pi}{3}\right)\right] \\ \cos\left[(2n-1)\left(\omega t + \varphi_{2n-1} + \frac{2\pi}{3}\right)\right] \end{bmatrix} \tag{4.6}$$

where λ_{2n-1} are the $(2n-1)^{th}$ flux harmonics magnitude induced in phase coil. N is phase number of turns. ω is the fundamental flux angular speed, φ_{2n-1} is the $(2n-1)^{th}$ flux harmonics phase angle with respect to currents.The flux harmonics are generated by non-sinusoidal winding and rotor excitation flux distribution. The item that contains $\boldsymbol{\lambda}_{rabc}$ in (4.5) represents the torque from rotor flux excitation.

$\boldsymbol{i}_{abc}$ is the phase current vector that takes the following form:

$$\mathbf{i}_{abc} = i\left[\cos(\omega t) \quad \cos\left(\omega t - \frac{2\pi}{3}\right) \quad \cos\left(\omega t + \frac{2\pi}{3}\right)\right] \tag{4.7}$$

where i is the amplitude of phase current.

$\boldsymbol{L}_{abc}$ is the stator inductance matrix, which is given with:

$$\mathbf{L}_{abc} = \begin{bmatrix} L(\zeta) & M\left(\zeta, \frac{2\pi}{3}\right) & M\left(\zeta, -\frac{2\pi}{3}\right) \\ M\left(\zeta - \frac{2\pi}{3}, -\frac{2\pi}{3}\right) & L\left(\zeta - \frac{2\pi}{3}\right) & M\left(\zeta - \frac{2\pi}{3}, \frac{2\pi}{3}\right) \\ M\left(\zeta + \frac{2\pi}{3}, \frac{2\pi}{3}\right) & M\left(\zeta + \frac{2\pi}{3}, -\frac{2\pi}{3}\right) & L\left(\zeta + \frac{2\pi}{3}\right) \end{bmatrix} \tag{4.8}$$

where

$$L(\zeta) = \sum_{k=0}^{\infty} L_k \cos(2k\zeta)$$

and

$$M(\zeta,\alpha)=\sum_{\substack{k=0\\k\neq 3,6,\cdots}}^{\infty} M_k\cos(2k\zeta-k\alpha)$$

where k is the harmonic order and α is the phase angle with respect to rotor position.

$\boldsymbol{L}$ and $\boldsymbol{M}$ are self and mutual inductances of the stator phases. The inductances are dependent on winding distribution, saturation and rotor saliency, where harmonics are presented. The item that contains $\boldsymbol{L}_{\text{rabc}}$ in (4.5) represents the torque from reluctance variation.

Expand (4.5) with (4.6), (4.7) and (4.8), the torque from rotor excitation flux T_{exc} is:

$$\begin{aligned}
T_{exc} &= \frac{pi}{\omega}\left[\cos(\omega t)\quad \cos\left(\omega t-\frac{2\pi}{3}\right)\quad \cos\left(\omega t+\frac{2\pi}{3}\right)\right]\frac{dN}{dt}\left\{\begin{bmatrix}\lambda_1\cos(\omega t+\varphi_1)\\ \lambda_1\cos\left(\omega t-\frac{2\pi}{3}+\varphi_1\right)\\ \lambda_1\cos\left(\omega t+\frac{2\pi}{3}+\varphi_1\right)\end{bmatrix}+\right.\\
&\left.\begin{bmatrix}\lambda_3\cos(3(\omega t+\varphi_3))\\ \lambda_3\cos\left(3\left(\omega t-\frac{2\pi}{3}+\varphi_3\right)\right)\\ \lambda_3\cos\left(3\left(\omega t+\frac{2\pi}{3}+\varphi_3\right)\right)\end{bmatrix}+\begin{bmatrix}\lambda_5\cos(5(\omega t+\varphi_5))\\ \lambda_5\cos\left(5\left(\omega t-\frac{2\pi}{3}+\varphi_5\right)\right)\\ \lambda_5\cos\left(5\left(\omega t+\frac{2\pi}{3}+\varphi_5\right)\right)\end{bmatrix}\cdots\right\}\\
&=\frac{3}{2}\frac{pi}{\omega}\left\{e_1\sin(\varphi_1)+\sum_{n=6N^+}^{\infty}(e_{n-1}\sin(n\omega t+(n-1)\varphi_{n-1})-\right.\\
&\left.e_{n+1}\sin(-n\omega t-(n+1)\varphi_{n+1}))\right\}
\end{aligned}\tag{4.9}$$

where

$$\mathbf{e}_n=N\frac{d\boldsymbol{\lambda}_n}{dt}=N\frac{d(\lambda_n\cos(n(\omega t+\varphi_n)))}{dt}$$

e_n is the induced EMF from n^{th} order harmonics of rotor flux. N^+ is positive integer.

From (4.9), the excitation flux contains fundamental component and even order harmonics components. The fundamental component only produces average torque, and the harmonics only contribute to torque ripple. For maximum unidirectional torque production, $\varphi_1=\pm 90°$, so the current phase should be leading or lagging the rotor position by 90° for MTPA operation. The harmonic components with the order of $(6N^+ + 1)^{\text{th}}$ and $(6N^+ - 1)^{\text{th}}$ produce ripple that

fluctuates at a frequency of $6N^{+}\omega/2\pi$. When $n=3N^{+}$, the harmonics does not contribute to torque or torque ripple. If no saturation is involved, e is equal to the open-circuit back-EMF, so reduction in back-EMF harmonics helps to alleviate torque ripple. However, torque ripple may still be reintroduced by saturation.

The torque from inductances, T_{i} is separated into two parts. The first part is the torque from self-inductance, T_{is}:

$$T_{is} = pk\frac{i^2}{4}\sum_{k=0}^{\infty} L_k \left\{ \left[2\cos\left(\frac{4\pi}{3}(k+1)\right)+1 \right] \sin\left(-2k\zeta - 2\omega t\right) + \left[2\cos\left(\frac{4\pi}{3}(k-1)\right)+1 \right] \sin\left(-2k\zeta + 2\omega t\right) \right\} \tag{4.10}$$

The second part is the torque from mutual-inductance, T_{im}:

$$T_{im} = p\frac{ki^2}{2}\sum_{\substack{k=0 \\ k\neq 3N^{+}}}^{\infty} M_k \left\{ \left[2\cos\left(\frac{2\pi}{3}(k+1)\right)+1 \right] \sin\left(-2k\zeta - 2\omega t\right) + \left[2\cos\left(\frac{2\pi}{3}(k-1)\right)+1 \right] \sin\left(-2k\zeta + 2\omega t\right) \right\} \tag{4.11}$$

The equations (4.10) and (4.11) are composed of two items, representing torque produced by forward and reverse rotational flux. In both equations, when $k = 0$, no torque or torque ripple is produced. $k = 1$, torque is produced by both self and mutual inductances, where $\omega t \pm k = 45°$ gives the maximum unidirectional torque production. $k > 1$, harmonics only contribute to torque ripples. At $k = 3N^{+} + 1$, torque ripple is created from forward rotational flux, at $k = 3N^{+} - 1$, torque ripple is created from reversed rotational flux. The frequency of ripple is $2 \times 3N^{+}\omega / 2\pi$. At $k = 3N^{+}$, no torque ripple is presented.

From (4.5)-(4.11) and a previous study [161], the sources of ripple torque in sinusoidally excited machines arises from:

(1) Permeance variations in the airgap due to the slotting effect (cogging) and local saturation;

(2) Harmonics variations in the airgap due to the inductance harmonics;

(3) Harmonics in the excitation flux induced EMF.

(4) Bulk saturation in the machine iron core;

(5) Harmonics in the current induced by the inverter.

To reduce torque ripple on wound rotor synchronous machine, this section proposed a systematic procedure by introducing eccentric magnetic pole surface. The torque ripple mitigation effects are evaluated according to item (1) (2) (3).

4.3.2 Proposed Method

Rotor pole shaping has been extensively applied in machine design, where the airgap length is usually described as an inverse cosine function. Centre offset arc pole shoe has also been used to approximate inverse cosine function, with the advantage that they can be defined as a single arc [162]. In this thesis, the centre offset pole shoe is named ‘eccentric rotor pole’.

Eccentric magnetic pole surface shapes have been extensively investigated for PM machine design, where reduction is exhibited in the open circuit airgap flux harmonics [162], back-EMF harmonics [163], cogging torque and torque ripple [164-166]. It is also a common method for reduction of harmonics, torque ripple, iron loss and acoustic noise in wound rotor synchronous machine [167, 168]. Despite this, to the author’s knowledge, there are few literatures on the study of optimal pole shape for torque ripple minimisation with maximum average torque.

To control the shape of rotor pole, figure 4.30 shows the defined parameters, where l_{rr} is radius of rotor, l_{rp} is radius of eccentric rotor pole, γ_{rs} is rotor pole shoe angle. To avoid physical breach, the following conditions are satisfied.

(1) To make sure the minimum distance between rotor and stator occurs at centre line, radius of rotor, $l_{rr} \geq$ radius of eccentric circle, l_{rp}.

(2) Large circle with radius of l_{rr} and small circle with radius of l_{rp} intersects at centre line, where distance between rotor and stator reach its minimum of 0.3 mm;

The relationship between l_{rp}, γ_{rs} and T_{ave}, T_{ripp} are obtained from Altair Flux as shown in

figure 4.31 (a) (b). In this procedure, both l_{rp} and γ_{rs} varies while keeping l_{rr} constant. The rated stator and rotor currents are applied. From figure 4.31, T_{ave} and T_{ripp} are functions of l_{rp} and γ_{rs}. In general, both T_{ave} and T_{ripp} reduce with increasing γ_{rs} and decreasing l_{rp}. Therefore, there exist an optimum l_{rp} and γ_{rs} for each T_{ave}, where T_{ripp} is minimised. The nature of this problem is described as:

$$\begin{cases} \tau_{ave} = T_{ave}(l_{rp}, \gamma_{rs}) \\ \tau_{ripp} = \min(T_{ripp}(l_{rp}, \gamma_{rs})) \end{cases} \tag{4.12}$$

where τ_{ave} is the required torque, τ_{ripp} is the minimum torque ripple coefficient at τ_{ave}.

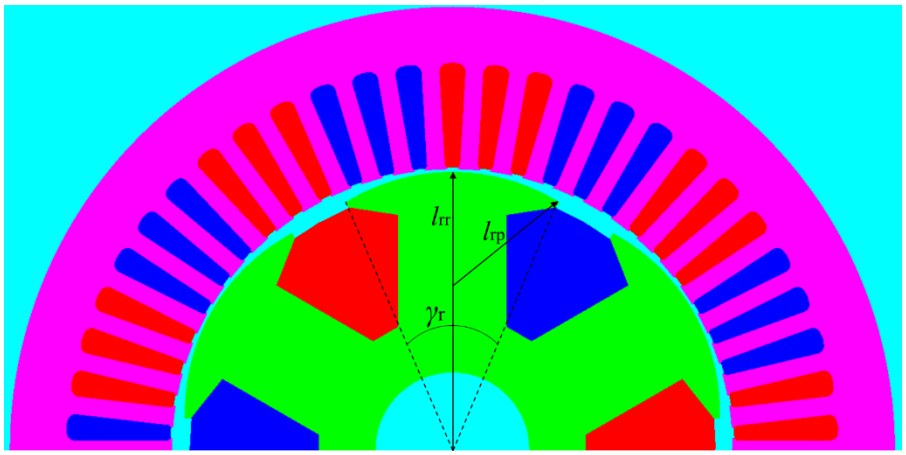

Figure 4.30. Controlled parameters in an eccentric rotor pole. l_{rr} is radius of rotor, l_{rp} is radius of rotor pole, γ_{rs} is rotor pole shoe angle.

To solve (4.12), the look-up table with a piecewise interpolation algorithm described in section 3.2.2 is applied, where the LUTs are obtained from Altair Flux. Figure 4.32 illustrates the interpolated contour map of T_{ripp} and T_{ave}, where the intersection of T_{ripp} and T_{ave} isolines gives corresponding l_{rp} and γ_{rs} values. For certain τ_{ave}, τ_{ripp} exists where the T_{ripp} isoline barely intercept T_{ave} isoline. The common point is marked as ($l_{rp,com}$, $\gamma_{rs,com}$). At different points, τ_{ave} versus τ_{ripp} are plotted in figure 4.33.

From figure 4.32 and 4.33, with small sacrifices in average torque, significant reduction in torque ripple coefficient can be achieved. In this process, eccentric pole radius increases and pole shoe angle decreases.

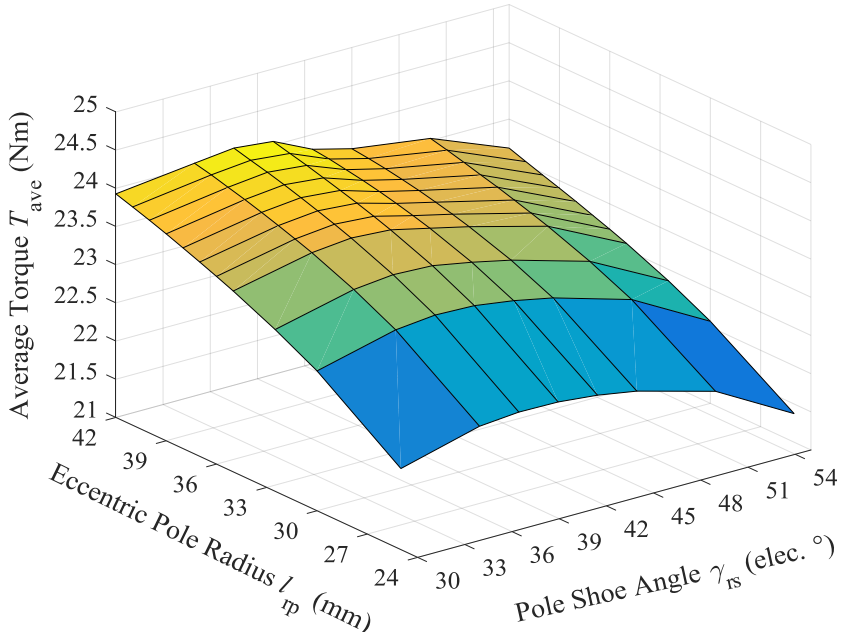

(a)

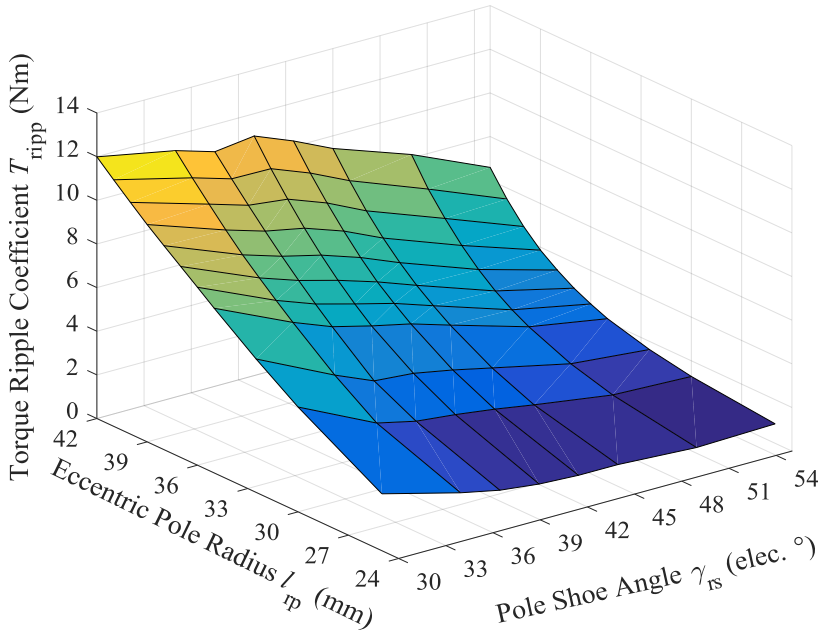

(b)

Figure 4.31. Torque performances vs. rotor eccentric pole radius, l_{rp} and rotor pole shoe angle, γ_{rs} of (a) average torque, T_{ave} and (b) torque ripple coefficient, T_{ripp}.

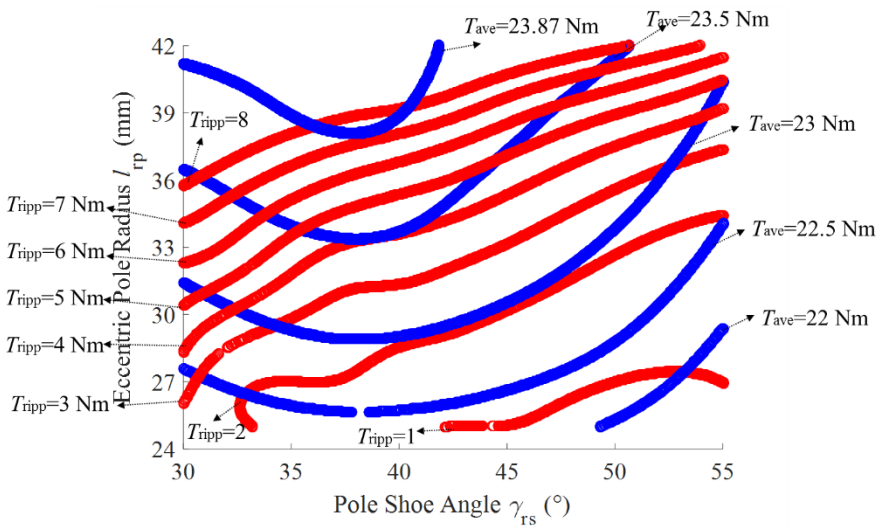

Figure 4.32. Isolines of average torque, T_{ave} and torque ripple coefficient, T_{ripp}, vs. rotor eccentric pole radius l_{rp} and rotor pole shoe angle γ_{rs}.

To validate this interpolation method, ($l_{rp,com}$, $\gamma_{rs,com}$) from LUT are implemented back on Altair Flux model. The T_{ripp} and T_{ave} from FE analysis are plotted in comparison with its expected values obtained from LUT interpolation method in figure 4.33. From the figure, a good agreement between the two results are observed, so the LUT interpolation method is validated.

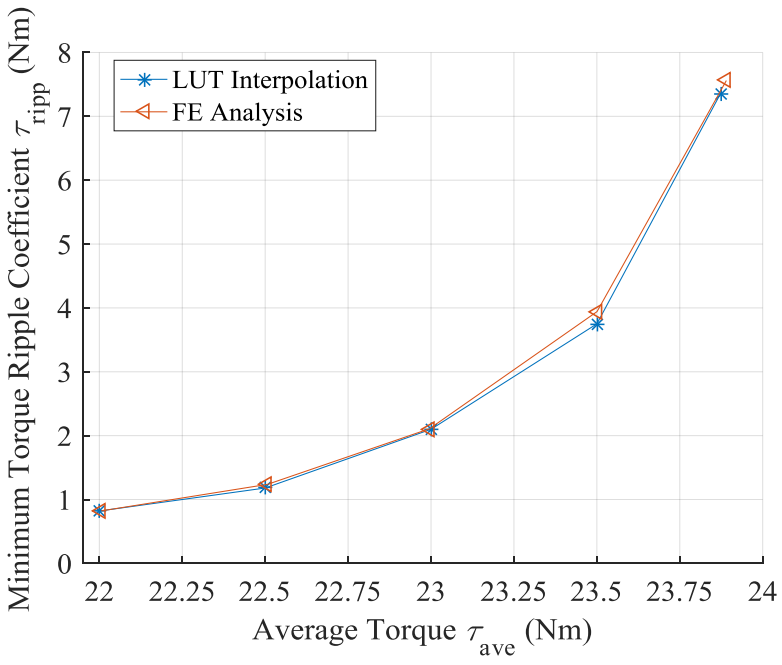

Figure 4.33. Minimum torque ripple coefficient, τ_{ripp}, vs. average torque, τ_{ave}, comparisons between LUT interpolation and FE analysis.

Compared with normal geometry, eccentric pole surface at a common point of (38.51, 38.21) reduces torque ripple coefficient from 11.45 Nm to 7.36 Nm without sacrificing average torque. At a common point of (31.34, 47.02), average torque is 23 Nm, torque ripple coefficient is further decreased to 2.10 Nm. In this research, the geometry with an eccentric pole radius of 31.34 mm and a pole shoe angle of 47.02° is adopted as optimized rotor eccentric pole surface.

4.3.3 Analysis of Eccentric Rotor Effects

In this section, the effects of eccentric rotor pole on torque ripple are analysed and compared with the original rotor surface. The applied eccentric pole has a rotor pole radius, l_{rp} of 31.34 mm and rotor pole shoe angle, γ_{rs} of 47.02°.

From section 4.31, the non-sinusoidal winding displacement induces harmonics in the airgap flux, which modulates with the rotor permeance, causing high speed harmonics in the airgap. This phenomenon also distorts phase voltage and cause torque ripple. The relationship between harmonic distortion in stator phase inductances and torque ripple are specified in (4.10) and (4.11).

From (4.10) and (4.11), the reluctance DC offset does not contribute to torque or torque ripple. Reluctance torque is generated from 2nd harmonic, and torque ripples are from harmonics higher than the 2nd order. To generate torque ripple, the harmonic order should satisfy $n = 2k$. Among them, the $(6N^{+})^{th}$ torque ripple harmonic component is contributed from reluctance harmonic order of $6N^{+} - 2$ and $6N^{+} + 2$.

With zero i_f and phase A stator current, i_s of 170 A DC, the phase-A self-inductance, L_a and mutual - inductances, M_{ax} are plotted below in figure 4.34 (a) and 4.35(a). Their harmonics comparisons are plotted in figure 4.34 (b) and 4.35(b). Compared with a normal rotor pole, the inductances of the eccentric rotor pole contain harmonics higher than 2nd order at much lower amplitudes, indicating smaller reluctance torque ripple. A slightly lower 2nd order harmonic is also displayed. From section 4.2.3, reluctance torque contributes little to overall torque production under rated operational condition, so this decrease in 2nd harmonic does not affect the average torque performance.

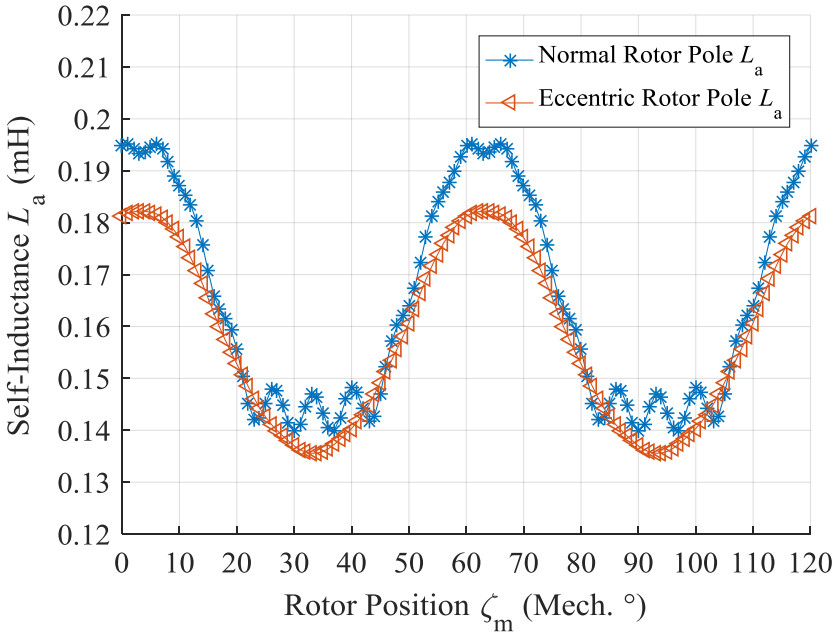

(a)

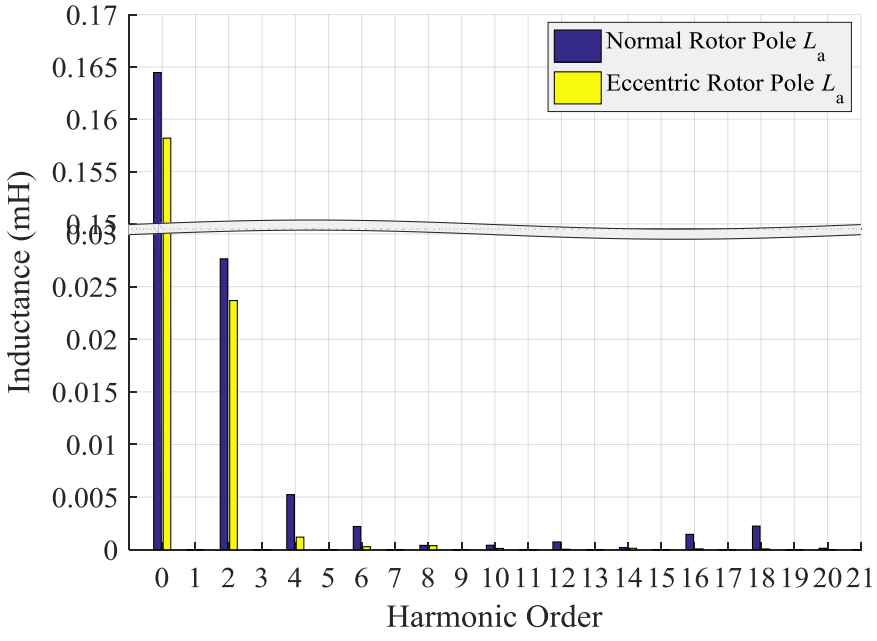

(b)

Figure 4.34. Phase A self-inductance, L_a, comparison between normal rotor pole and eccentric rotor pole at stator rotor current, i_s of 170 A DC (a) inductances vs. rotor position, ζ_m (b) harmonics analysis.

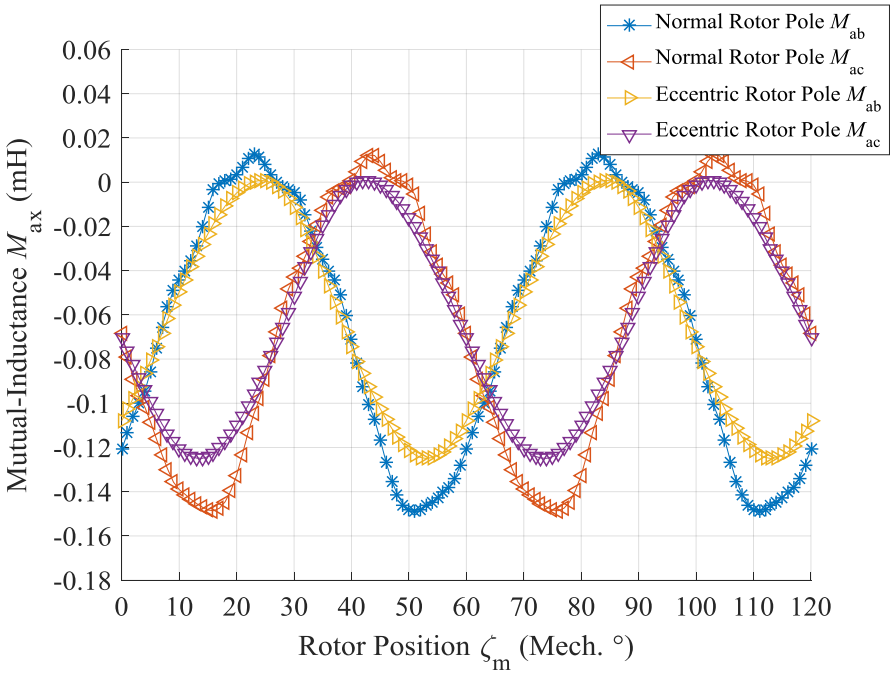

(a)

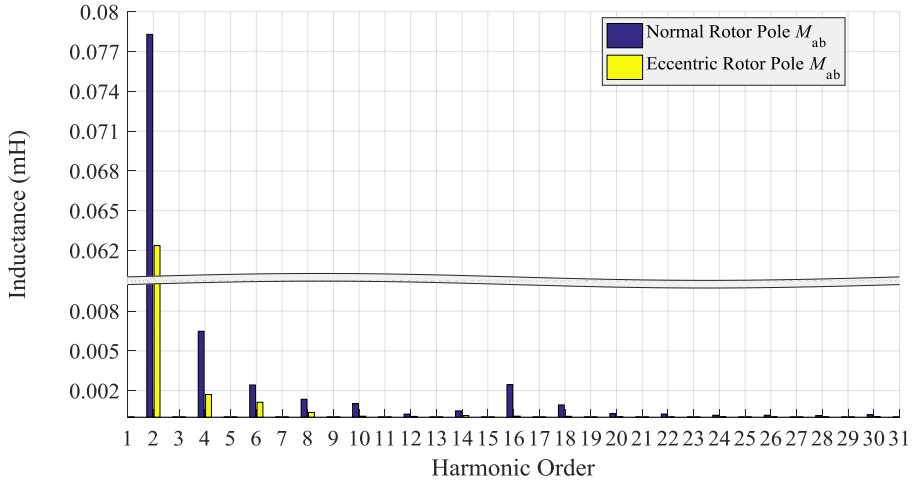

(b)

Figure 4.35. Phase A mutual inductance, M_{ax}, comparison between normal rotor pole and eccentric rotor pole at stator rotor current, i_s of 170 A DC (a) inductances vs. rotor position, ζ_m (b) harmonics analysis.

The pure reluctance torque T_{re} at a load angle θ of 45° and 90° of the normal and eccentric rotor poles are plotted in figure 4.36 (a). This is achieved by setting i_f at zero and i_s at the rated value. The harmonic analysis is displayed in figure 4.36 (b). Compared with normal rotor pole, at $\theta =$ 45°, T_{re} of eccentric rotor pole is reduced by 27%. The harmonics other than the 6th order are all greatly reduced in the eccentric rotor pole. At $\theta = 90°$, the 6th order harmonic is increased

with an eccentric pole, but other higher order harmonics are all reduced.

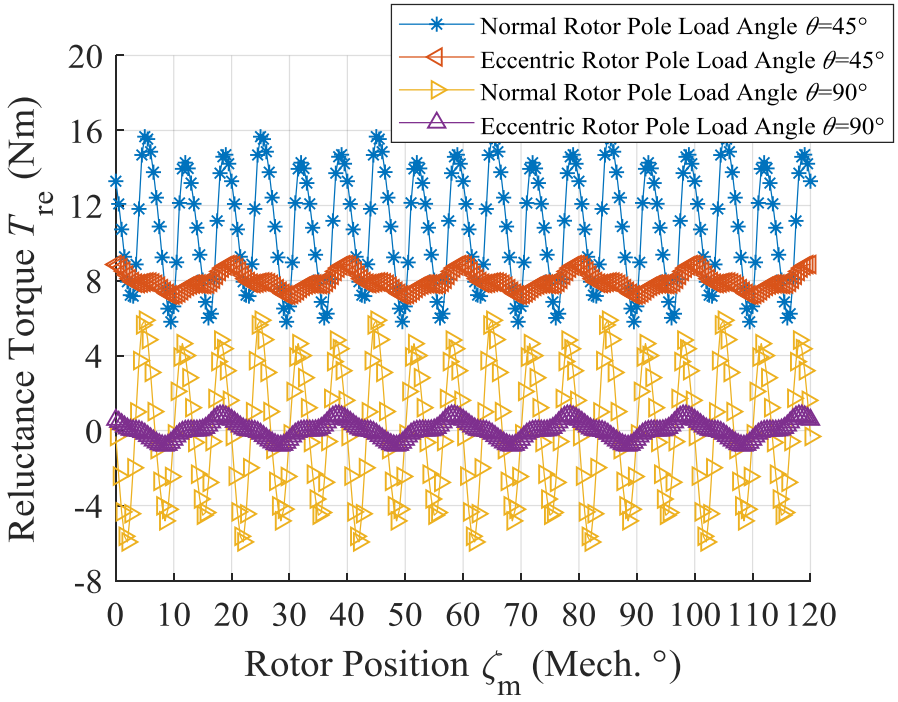

(a)

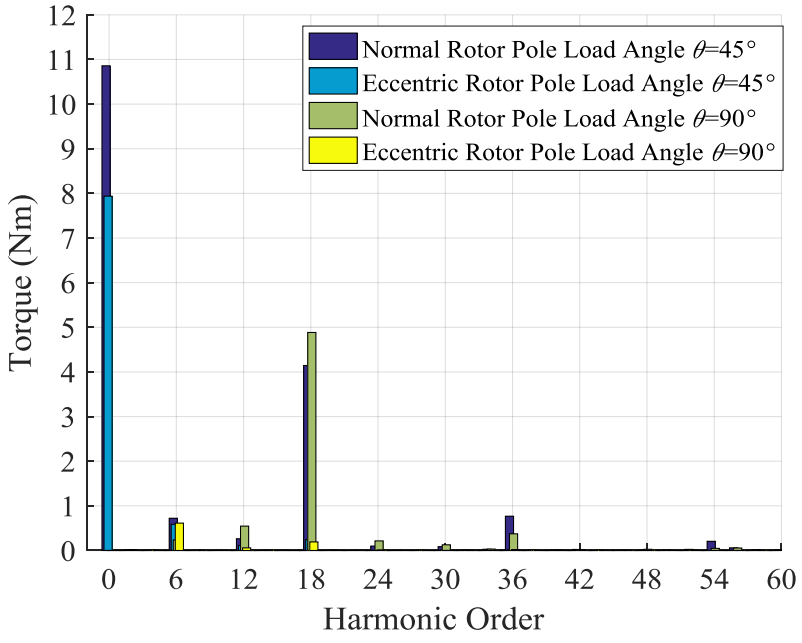

(b)

Figure 4.36. Reluctance torque, T_{re}, comparison between normal rotor pole and eccentric rotor pole at a load angle, θ of 45° and 90° (a) torque vs. rotor position, ζ_m (b) harmonics analysis.

The open circuit comparison of airgap flux density between normal and eccentric rotor poles

are shown below in figure 4.37, where figure 4.37 (a) plots flux density distribution over one pole pair span and figure 4.37 (b) illustrates its harmonics analysis. The open circuit comparison is implemented by setting i_s to zero and i_f to the rated value. From the graphs, the eccentric rotor pole increases equivalent airgap length, causing a slight reduction of fundamental flux density component from 1.06 T to 0.98 T. The gain is a great reduction in harmonics, where the harmonic coefficient, f_n, increases from 0.385 to 0.574. Low order harmonics like 5^{th}, 7^{th},9^{th} see a great reduction while the harmonics modulated by stator teeth like 17^{th} and 19^{th} are largely unaffected in amplitude.

The flux density near to the airgap at zero i_s and rated i_f are displayed in figure 4.38, where the upper plot is from the eccentric rotor pole and lower plot shows the normal rotor pole. Notably, local saturation is presented mainly on edge of rotor pole shoe and the adjacent stator teeth, where eccentric pole geometry shows a much lower local saturation.

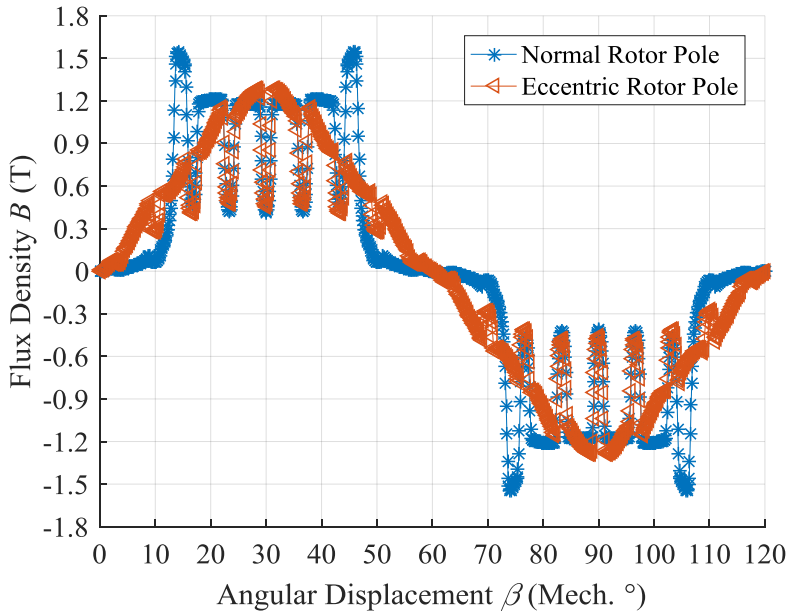

(a)

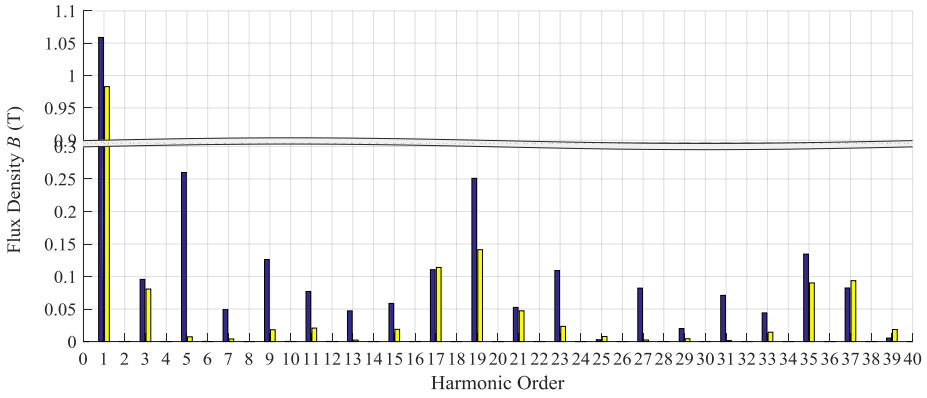

(b)

Figure 4.37. Open circuit airgap flux density comparison between normal rotor pole and eccentric rotor pole at rated rotor MMF per coil, i_f (a) flux density, B vs. angular displacement, β, (b) harmonics analysis.

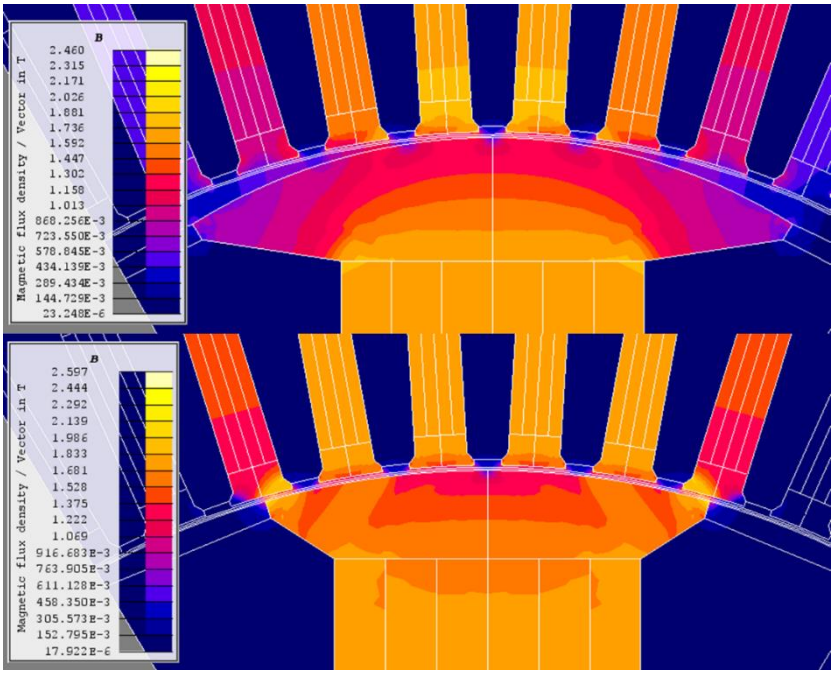

Figure 4.38. Plot of local flux density distribution on stator and rotor near airgap. Upper picture: eccentric rotor pole. Lower picture: normal rotor pole.

From the discussion above, the eccentric rotor pole produces a more sinusoidal airgap flux distribution with lower local saturation than normal rotor pole, so an alleviation in slotting effects and permeance variation is achieved, leading to a reduction in cogging torque. This is confirmed in figure 4.39 (a), where the cogging torque of eccentric rotor pole and normal rotor pole are plotted in comparison. The FFT analysis in figure 4.39 (b) indicates that the cogging torque has harmonics mainly of 18^{th}, 36^{th} and 54^{th} order, and the eccentric rotor pole reduces all

harmonics tremendously.

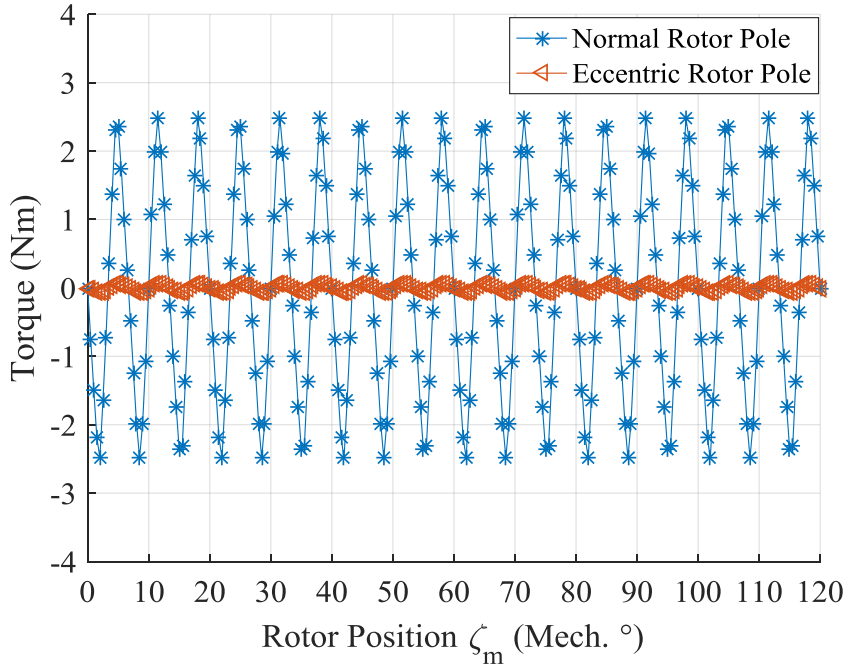

(a)

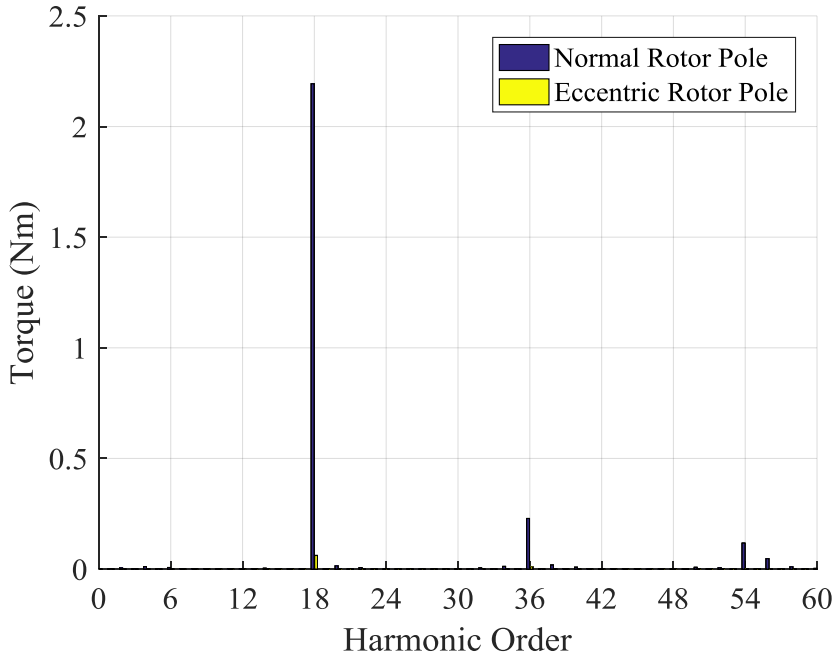

(b)

Figure 4.39. Cogging torque comparison between eccentric rotor pole and normal rotor pole (a) torque waveform vs. rotor positon, ζ_m, (b) harmonics analysis.

The phase-A back-EMF of both rotors are plotted in figure 4.40. Compared with normal rotor, a slight decrease in fundamental component of back-EMF from 21.6 to 20.3 is exhibited in the eccentric pole. In return, the harmonic coefficient sees a significant increase from 0.656 to 0.928, where all harmonic components are effectively reduced.

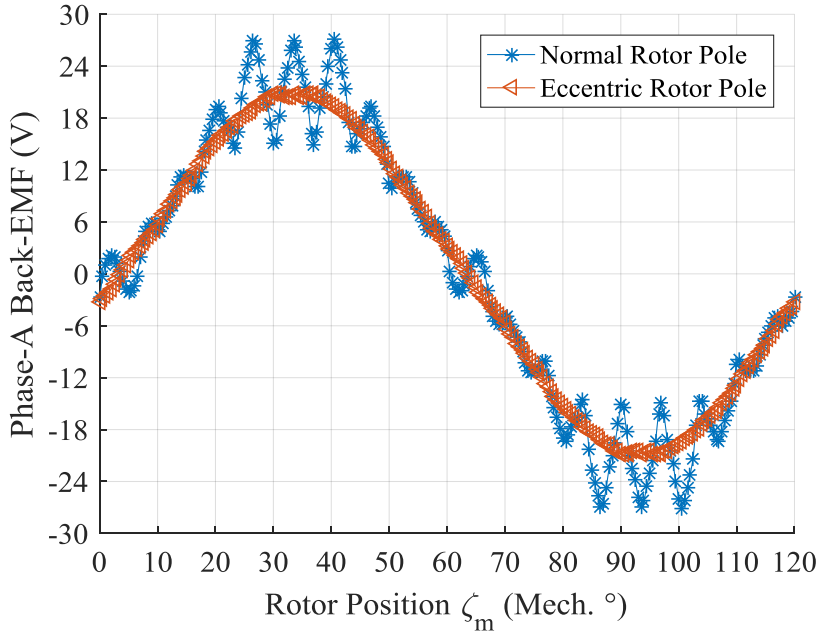

(a)

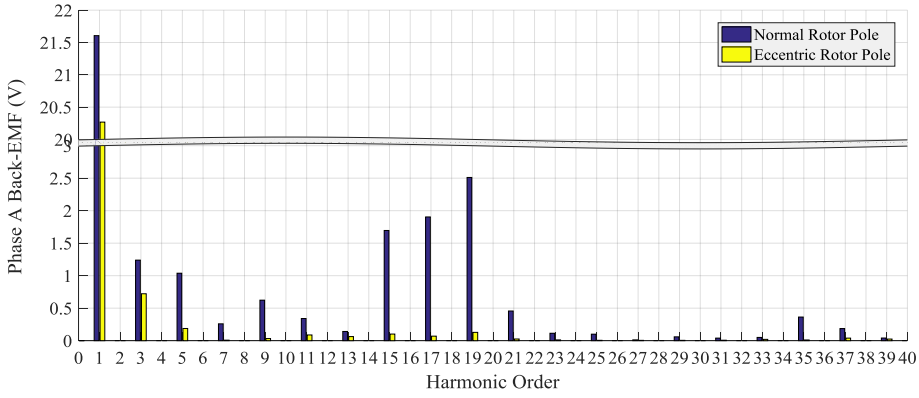

(b)

Figure 4.40. Phase-A open circuit back-EMF comparison between normal rotor pole and eccentric rotor pole at rated rotor MMF per coil, i_f (a) back-EMF vs. rotor position, ζ_m (b) harmonics analysis.

When i_f and i_s are both non zero, the torque waveforms from normal and eccentric geometries are plotted against rotor position, ζ_m in figure 4.41 (a). The FFT analysis is displayed in

figure 4.41 (b). In the simulation, i_f is set to the rated value. i_s is set at both 20% rated and rated values. At 20% rated i_s, the normal rotor produces torque harmonic components similar to cogging as shown in figure 4.39, but all harmonics amplitudes are slightly increased. With the eccentric pole, the torque has nearly no harmonics, but fundamental component is reduced by 6.3%. At rated i_s, all harmonics components of normal rotor are further increased from cogging. The application of the eccentric pole still greatly reduces high order harmonic components in torque ripple such as 18th, 36th and 54th, but low order components such as 6th and 12th are reintroduced, and total harmonics see an increase compared with 20% rated i_s. Compared with normal rotor pole, the fundamental torque component is decreased by 4.6% with the eccentric pole.

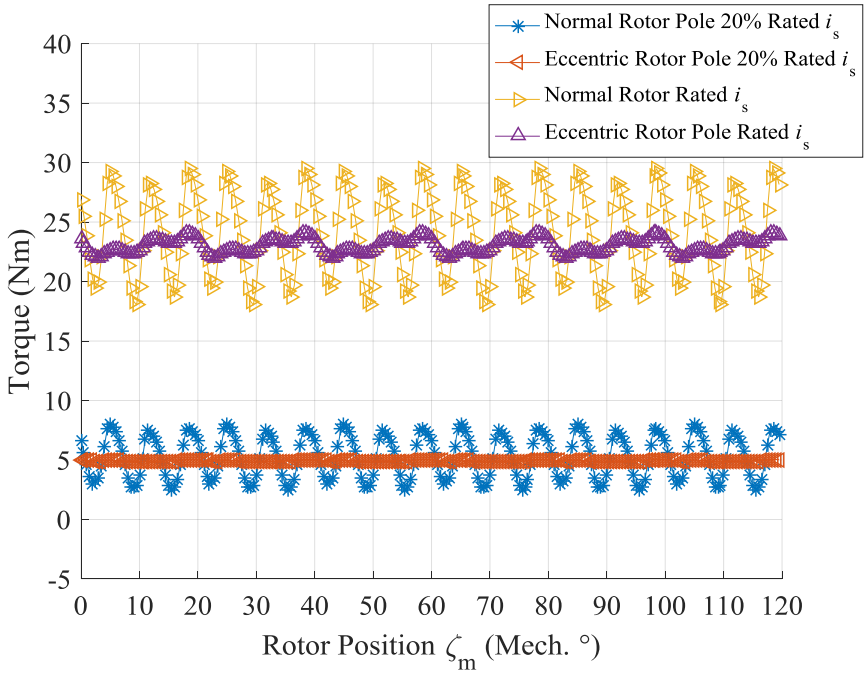

(a)

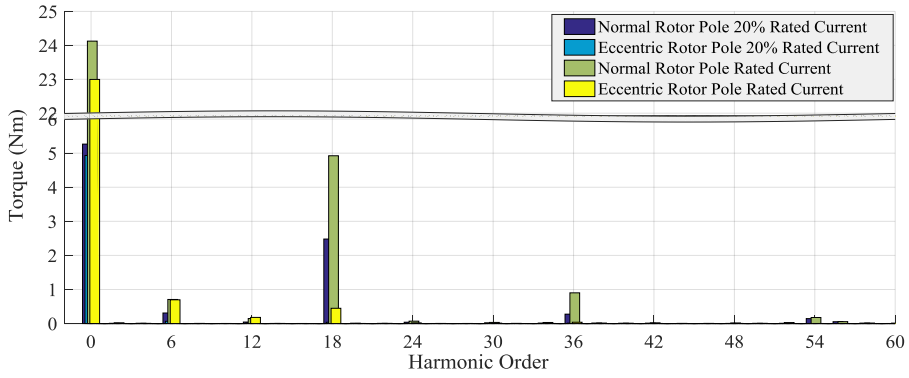

(b)

Figure 4.41. Torque comparison between normal rotor pole and eccentric rotor pole of (a) torque waveforms vs. rotor positon, ζ_m, (b) harmonics analysis.

The base speed voltage waveforms corresponding to torque generation in figure 4.41 are plotted against rotor position, ζ_m in figure 4.42 (a) (b). The harmonics analysis is displayed in figure 4.42 (c). From the figures, the fundamental voltage from the eccentric rotor pole is slightly smaller than normal pole. At 20% rated i_s, all harmonics components are greatly reduced with eccentric poles. At rated i_s, low order harmonics are reintroduced, where eccentric pole reduces the 35th, 37th,53th and 55th order harmonic components, but there are no obvious influence patterns on harmonics order below the 19th.

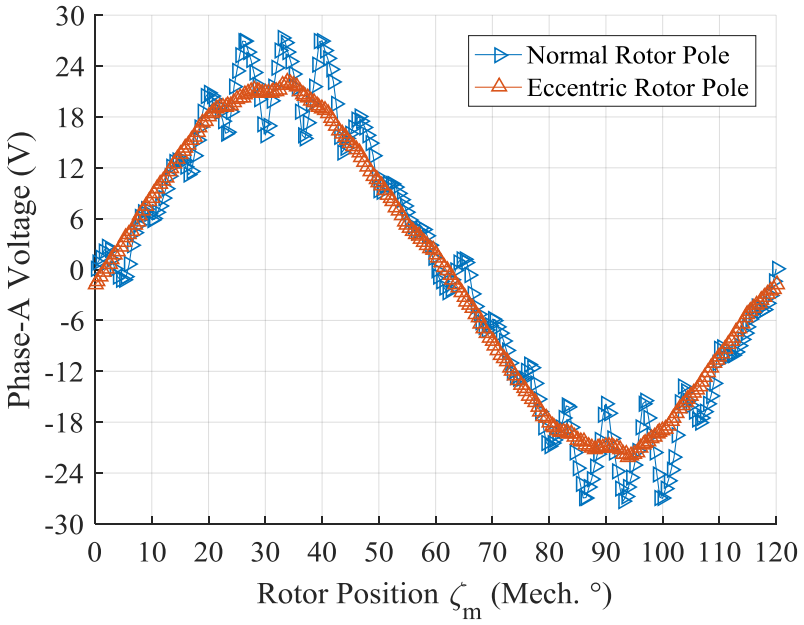

(a)

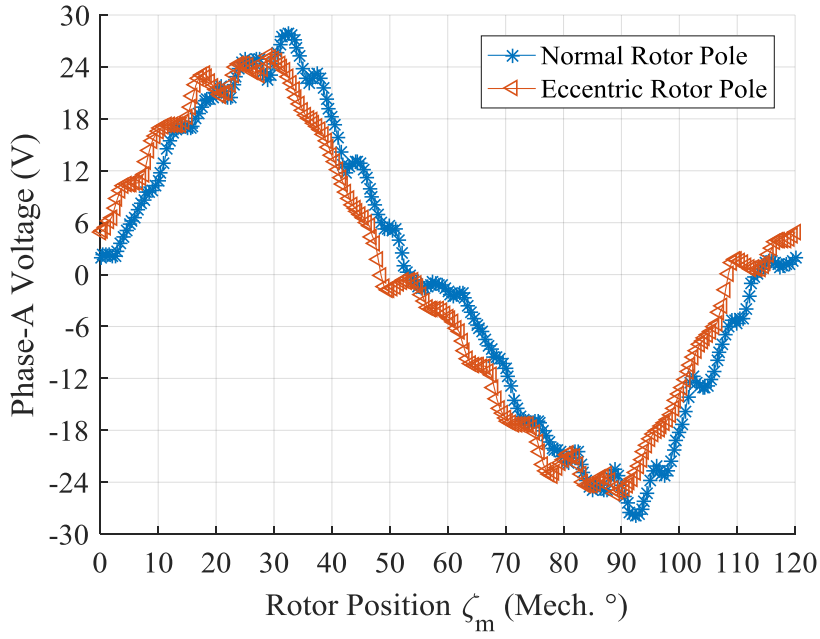

(b)

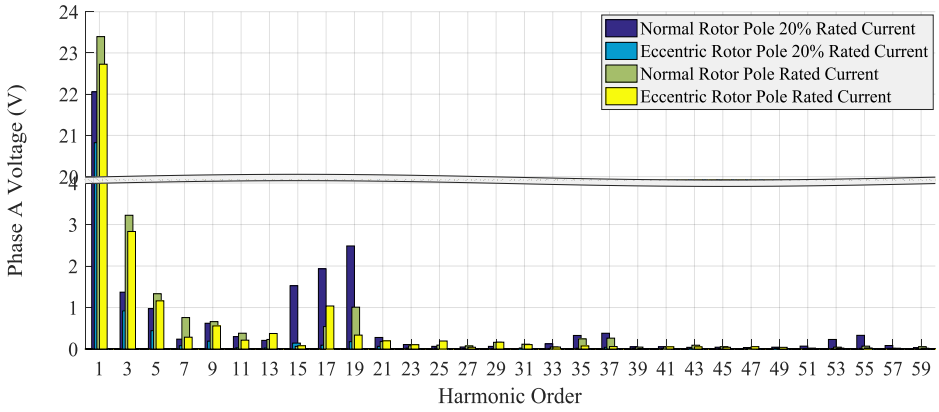

(c)

Figure 4.42. Phase-A voltage comparison between normal rotor pole and eccentric rotor of (a) voltage waveform vs. rotor positon, ζ_m at 20% rated stator current, i_s, (b) voltage waveform vs. rotor positon, ζ_m at rated stator current, i_s and (c) harmonics analysis.

4.4 Summary

In this chapter, the influences of iron core dimensions, rotor pole shape and pole number on the performance of the wound rotor synchronous machine are investigated in terms of loss and torque ripple level. The main contribution is a proposed method to calculate the optimal rotor pole eccentricity for torque ripple minimisation with maximum average torque.

From this study, the following conclusions are drawn:

(1) The rotor pole shoe plays a crucial part in cross saturation, which affects the machine's copper loss performance. With the same rotor flux density, a decrease in rotor pole shoe width helps the machine to maintain its torque capability at high copper loss levels, at the price of increased copper loss at low torque level.

(2) Optimization of the iron core geometry improves machine efficiency, where axial length is the most effective parameter. Excessive increase of axial length may reduce overall machine efficiency, as iron loss increases and the rate of copper loss decrease falls.

(3) Increasing the pole number from four to six shows many enhancements in machine performance. First, a decrease in magnetic reluctance on the rotor excitation magnetic circuit is presented leading to a reduction of rotor current density. Second, both stator and rotor back iron thickness are reduced, so a total winding area increase is realised. Third, shorter stator end winding span reduces stator winding resistance. The combination of these effects allows the six pole machine to be more efficient in operation than four pole machine.

(4) Torque ripple mainly originates from three sources. Cogging, harmonics in rotor flux induced EMF and harmonics in inductances. With a carefully selected eccentric rotor pole, the aforementioned sources are all alleviated, therefore the machine torque ripple can be significantly reduced. This torque ripple reduction is more beneficial under non-saturation conditions. With saturation, some torque ripple is reintroduced.

5. Operation of Wound Rotor Synchronous Machine

Wound Rotor synchronous machine is considering a strong candidate for HEV propulsion mainly due to its theoretically infinite field weakening capability and unity power factor at all field weakening region. Compared with PMSM, the adjustable rotor flux suggests no excessive d-axis current is required to counteract the flux from PM [169], so a good efficiency can be achieved at deep field weakening region, usually high speed and low power. However, the determination of stator and rotor currents for minimum loss criterion with voltage limitation is always a major challenge.

Below the rated speed, MTPA operation with balanced stator and rotor currents for minimum loss provides a good current management method. The details have been discussed in previous chapters. However, the limitation on voltage above base speed introduces another constraint, making the problem difficult to solve.

The conventional way of solving this problem involves Lagrange method with a valid model of the machine, where the dq axis fluxs, λ_d and λ_q, are represented as numerical function of dq axis currents, i_d and i_q, as well as rotor current, i_f. The coefficients in the numerical functions are determined from curve or surface fitting. In this chapter, a novel method based on piecewise interpolation is developed, where the curve fitting is replaced by surface interpolation. This greatly reduces the computation requirement and eliminates errors that may be introduced by data fitting. This novel method is compared with the conventional Lagrange method using finite element analysis. The result from novel method shows higher accuracy with much lower computation time.

5.1 Lagrange Method

Lagrange method is a strategy for finding the local maxima and minima of a function subject to equality constraints using Lagrange function. In this study, the objective function is the loss function, the equality constraints are torque and voltage functions.

To simplify the problem, iron loss is neglected, leaving copper loss the only objective function.

Point (i_d, i_q, i_f) is denoted by x. The objective torque and voltage limits are T_0 and V_0. The objective function is:

$$z(x) = R_r i_f^2 + \frac{3}{2} R_s \left(i_d^2 + i_q^2\right) \tag{5.1}$$

Torque constraint function is:

$$T(x) = \frac{3}{2} p\left(\lambda_d(x) i_q - \lambda_q(x) i_d\right) = T_0 \tag{5.2}$$

If the derived point x^* has a voltage within limit V_0, and the Lagrange function is:

$$L(x, g_1) = z(x) - g_1(T(x) - T_0) \tag{5.3}$$

If the voltage exceeds the limits, another voltage constraint is imposed as:

$$V(x) = \sqrt{V_d^2(x) + V_q^2(x)} = \sqrt{\left(-\omega_e \lambda_q + R_s i_d\right)^2 + \left(\omega_e \lambda_d + R_s i_q\right)^2} = V_0 \tag{5.4}$$

where R_s is the stator phase resistance. R_r is the equivalent rotor coil resistance. ω_e is electric rotational speed. The Lagrange function L becomes:

$$L(x, g_1, g_2) = z(x) - g_1(T(x) - T_0) - g_2(V(x) - V_0) \tag{5.5}$$

where g_1 and g_2 are unspecified constant called the Lagrange multiplier.

With Lagrange function, x^* is a point with local minimum loss subject to equality torque and voltage constraints if:

$$\exists x^*, g_1^*, g_2^*$$

$$\begin{cases} \nabla_{x, g_1, g_2} L\left(x^*, g_1^*, g_2^*\right) = 0 \\ T\left(x^*\right) = T_0 \\ V\left(x^*\right) = V_0 \end{cases} \tag{5.6}$$

5.1.1 Least Square Fitting

The d-axis flux $\lambda_d(i_q, i_d)$ and q-axis flux $\lambda_q(i_q, i_d)$ data generated from Altair Flux at a typical i_f of 600 Aturns are shown below in figure 5.1 (a) (b) as an example. Both flux tables have a size

of 14×27. The definition region for i_d and i_q are both (-213,213), which are determined by power electronics restrictions.

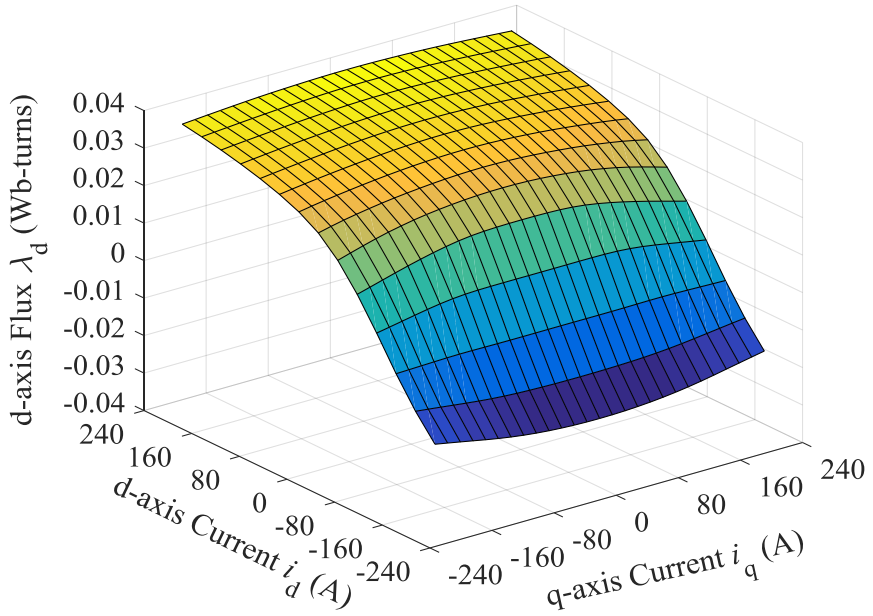

(a)

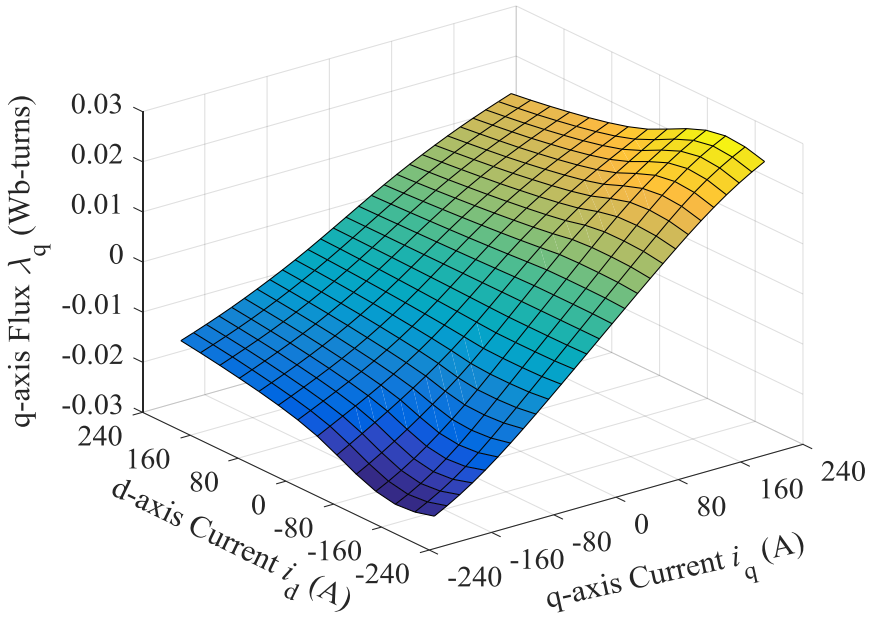

(b)

Figure 5.1. Original data from finite element analysis vs. d-axis current, i_d and q-axis current, i_q of (a) d-axis flux, λ_d and (b) q-axis flux, λ_q, at rotor MMF per coil, i_f of 600 Aturns.

The flux can be modelled as an overdetermined linear system using the Vandermonde matrix as shown in (5.7), where with least square fitting is applied. Matlab provides the fit() function for this purpose, where i+1 and j+1 are the orders of the polynomial in y and x axis. In fit() function, $1 \leqslant i \leqslant 5$ and $1 \leqslant j \leqslant 5$.

$$z = \begin{bmatrix} 1 & x & x^2 & \dots & x^j \end{bmatrix} \begin{bmatrix} p_{00} & p_{10} & p_{20} & \cdots & p_{i-1,0} & p_{i0} \\ p_{01} & p_{11} & p_{21} & \cdots & p_{i-1,1} & 0 \\ p_{02} & p_{12} & p_{22} & \cdots & 0 & 0 \\ \vdots & \vdots & \vdots & \vdots & \vdots & \vdots \\ p_{0j} & 0 & 0 & \dots & 0 & 0 \end{bmatrix} \begin{bmatrix} 1 \\ y \\ y^2 \\ \vdots \\ y^i \end{bmatrix} \tag{5.7}$$

From figure 5.1, λ_d is an even function with respect to $i_q = 0$ plane, so the fitted λ_d polynomial items with odd power of i_q is 0. Similarly, λ_q is an odd function with respect to $i_q = 0$ plane, so λ_q polynomial items with even power of i_q is 0. The fitted functions of λ_d and λ_q versus i_d and i_q are plotted in figure 5.2 (a) (b), both within and outside definition region.

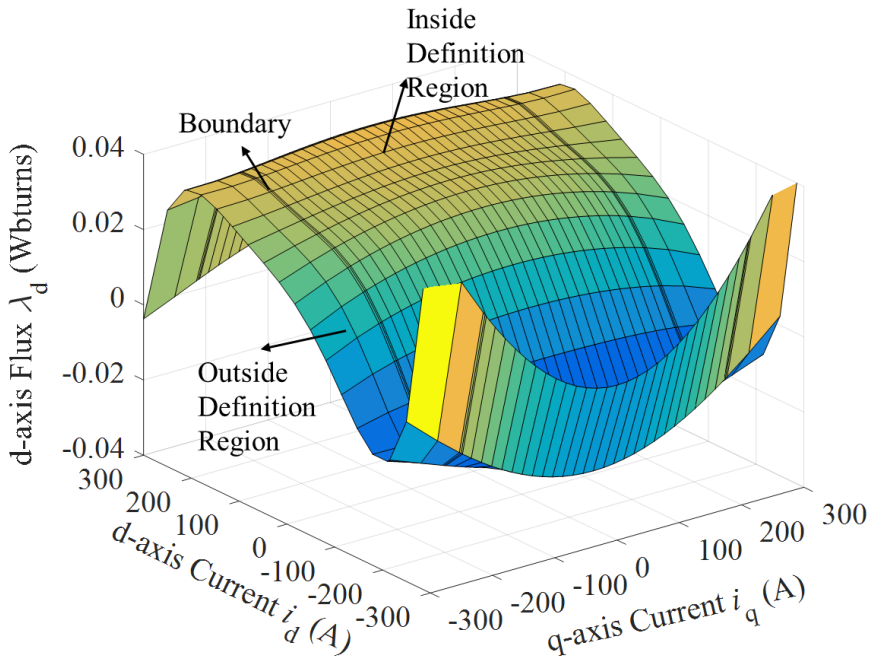

(a)

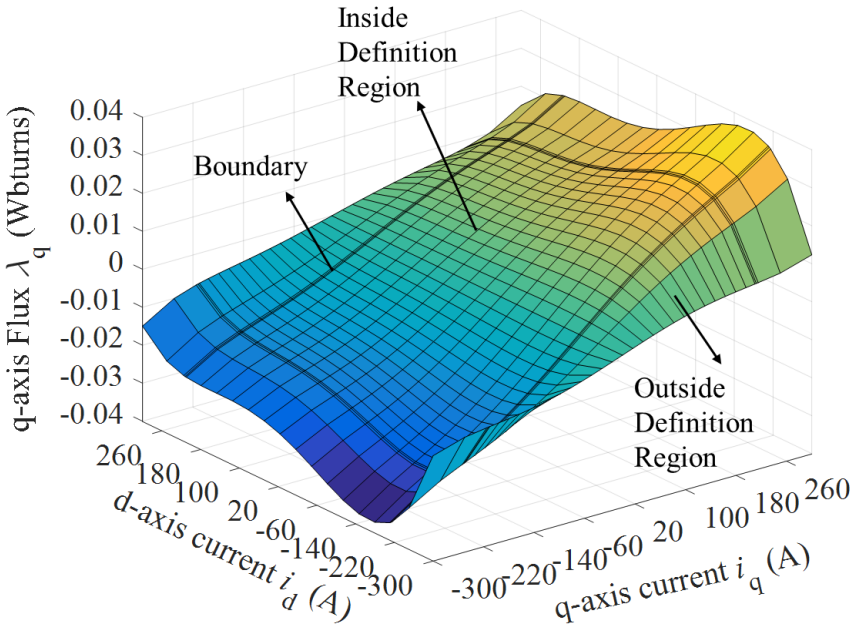

(b)

Figure 5.2. Least square surface fitting equations and data vs. d-axis current, i_d and q-axis current, i_q of (a)d-axis flux, λ_d. The fitted polynomial is $\lambda_d=0.03246+h^4*0.001637+ (0.001061k^2-0.01351)\ h^2 - 0.002005k^2+7.293\times10^{-6}k^4-0.001966h^5+h(7.452\times10^{-5}k^4+0.0006741k^2+0.009217)+h^3(-0.0007442k^2+0.008867)$, where $k=i_q/127.3$ and $h= i_d /131.7$, and (b) q-axis flux, λ_q at rotor MMF per coil i_f of 600Aturns. The fitted polynomial is $\lambda_q=k(0.000133h^3-0.004263h)+0.01566h+k^2(0.0001117h^3+0.00116h)-0.001634h^3+0.0001575h^5+0.0007264hk^3-0.0005528hk^4$, where $k=i_q /127.3$ and $h= i_d /131.7$.

To evaluate the difference between original and fitted data, the raw residual or 'error', is defined as:

$$Raw\_residue = z - z_i \tag{5.8}$$

where z is the actual value from FE analysis and z_i is the fitted value at point x^*.

Percentage of raw residual is defined as:

$$Percentage\_of\_raw\_residue = \frac{z - z_i}{z} \tag{5.9}$$

To evaluate the overall goodness of fitting, adjusted R-square R^2_{adj} is introduced as:

$$R_{adj}^2 = 1 - \left(\frac{n-1}{n-p}\right)\frac{SSE}{SST} \tag{5.10}$$

where p is the number of regression coefficients, SSE is sum of squared error and SST is sum of squared total.

Set i = 5 and j = 5, the R_{adj}^2 of λ_d and λ_q are 0.9991 and 0.9996, suggesting the polynomial models explain 99.91% and 99.96% of the variability in λ_d and λ_q curve data. Figure 5.3 and 5.4 plots the 2D stem charts of the raw residuals of λ_d and λ_q, and their ratio over original grid data. Within definition region, curve fitting introduces randomly distributed raw residuals. The absolute values of raw residuals are generally small, but its percentage over the original data becomes larger as the flux value decreases. Apart from λ_d and λ_q of 0, the percentage of raw residue varies from -8% to 12% for λ_d, and from -5% to 5% for λ_q. Therefore, even with an R_{adj}^2 close to 1, the percentage of raw residue in flux is still considerably large where the flux values are small .

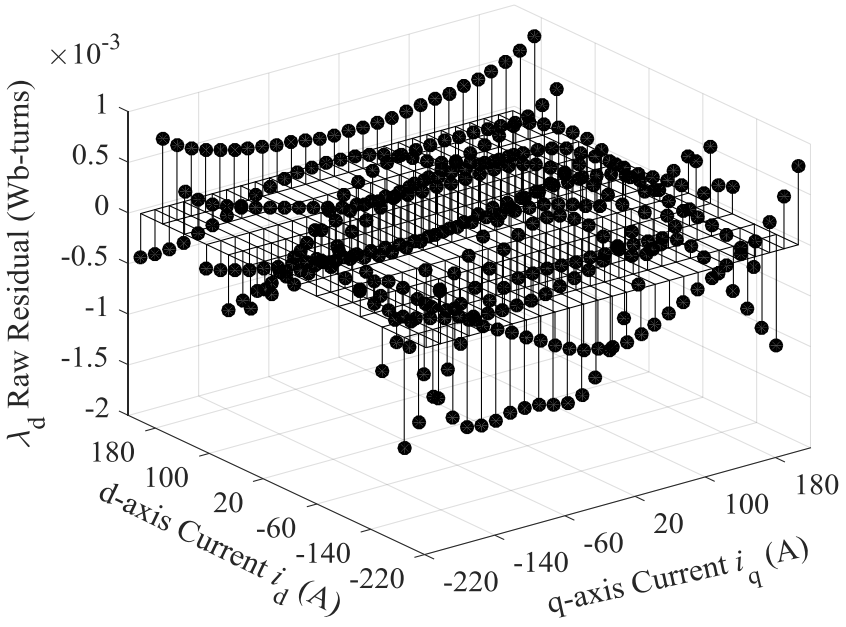

(a)

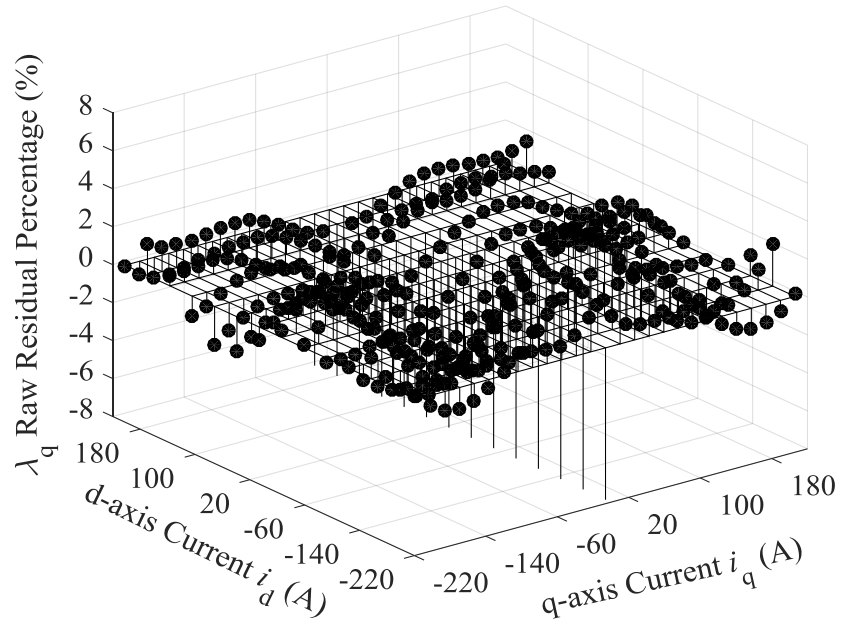

(b)

Figure 5.3. 2D d-axis flux, λ_d, surface fitting residues vs. d-axis current, i_d and q-axis current, i_q (a) raw residues and (b) percentage of raw residues over original data from FE analysis.

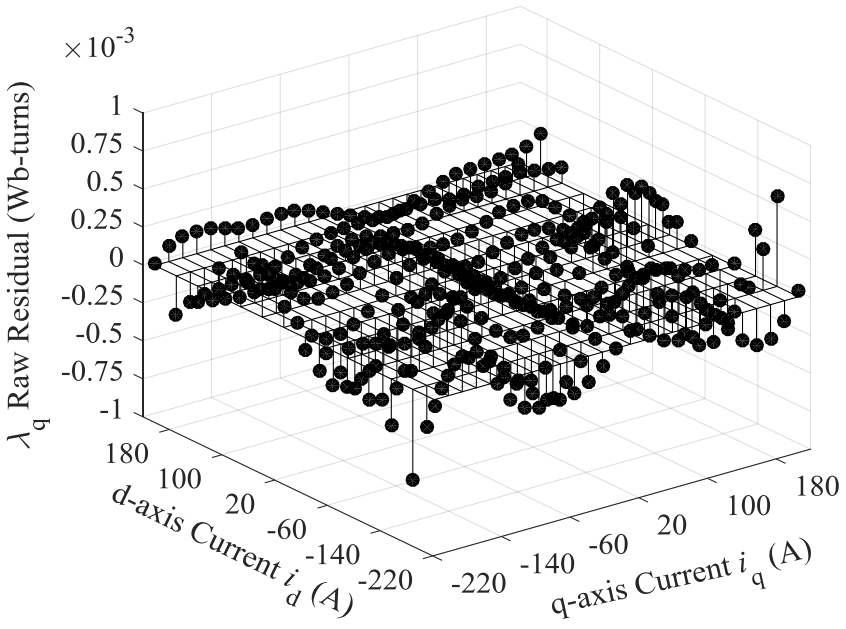

(a)

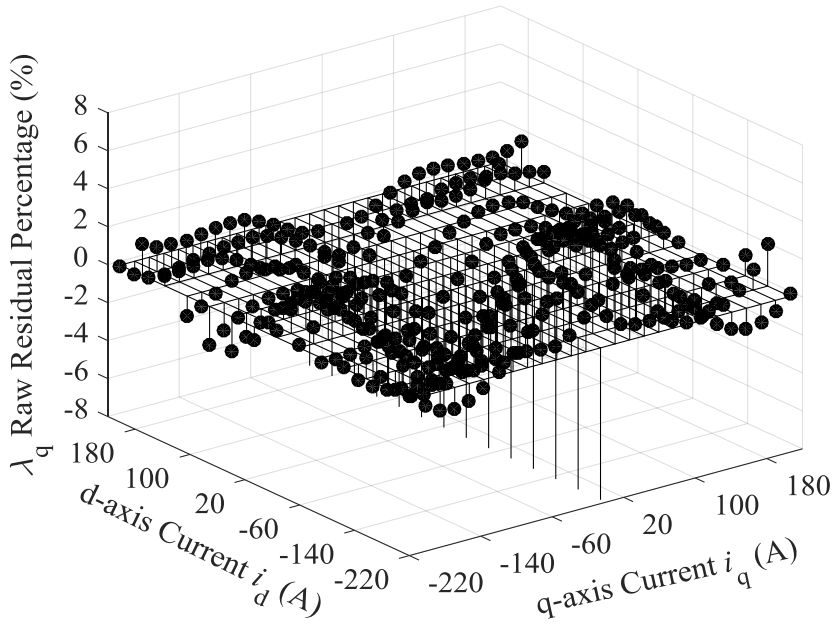

(b)

Figure 5.4. 2D q-axis flux, λ_q, surface fitting residues vs. d-axis current, i_d and q-axis current, i_q (a) raw residues and (b) percentage of raw residues over original data from FE analysis.

When i_d and i_q are beyond the definition region, the polynomials appear a 'random' value as no surface fitting is applied to regulate them. This random distribution may cause calculation error in current by predicting current values outside the definition region.

From the original λ_d and λ_q grid data, the average torque, T_{ave} and induced phase voltage, e can be determined according to (1.16) and (1.17), as shown in figure 5.5 and 5.6. Figure 5.7 and 5.8 plot their raw residuals and percentage from fitted flux polynomials. Clearly, the flux polynomials pass the deviations to torque and voltage. For torque prediction, the raw residuals are between -0.8 Nm to +0.6 Nm. Except zero torque points, the percentage of residue is within -13% to +6%. For voltage prediction, the raw residuals are between -1.0 V to +0.6 V. Besides zero voltage points, the percentage of residue is within -12% to +5%.

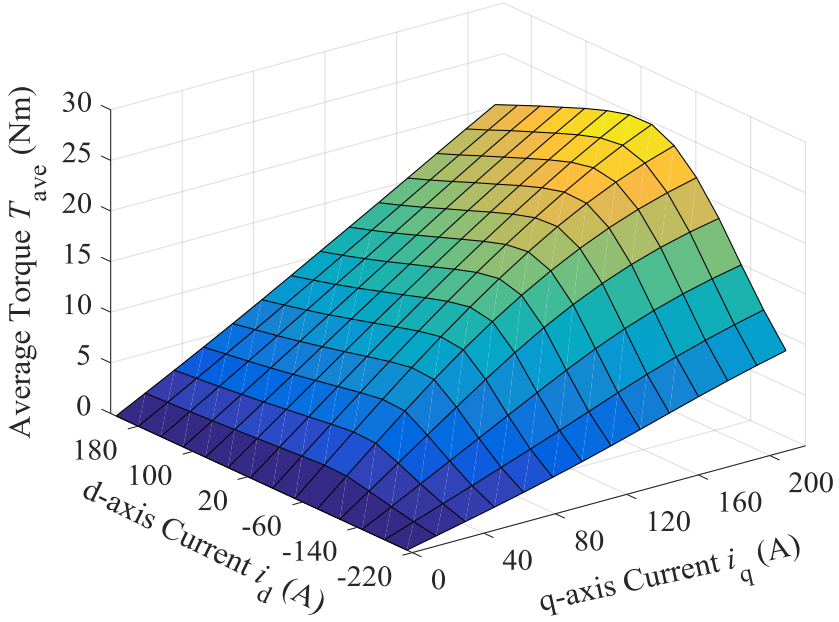

(a)

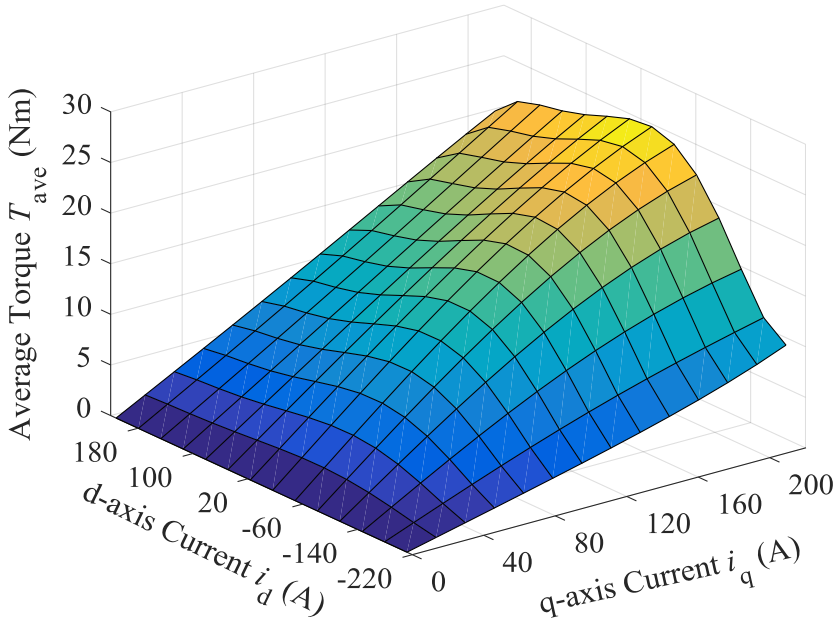

(b)

Figure 5.5. Average torque, T_{ave}, from (a) FE analysis and (b) surface fitting vs. d-axis current, i_d and q-axis current, i_q of at rotor MMF per coil, i_f of 600 Aturns.

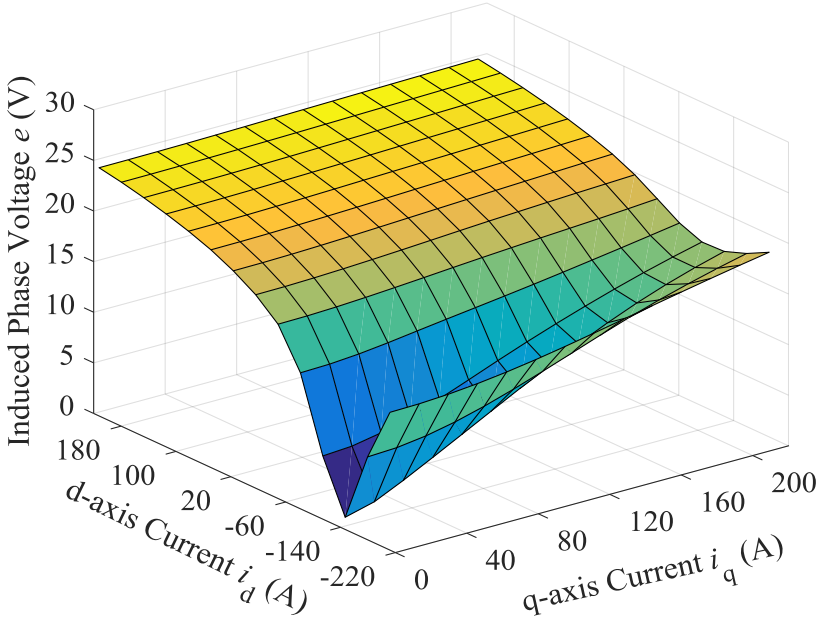

(a)

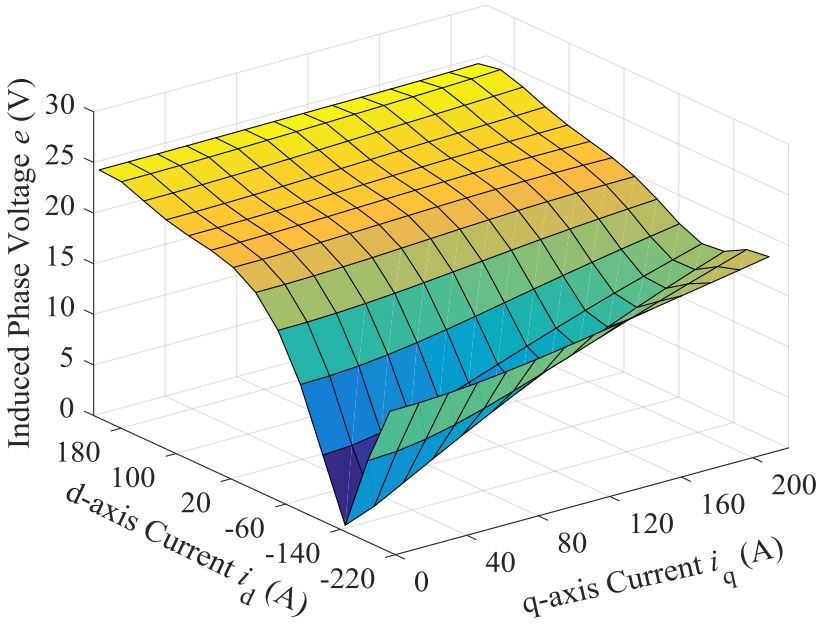

(b)

Figure 5.6. Induced phase voltage, e, from (a) FE analysis and (b) surface fitting vs. d-axis current, i_d and q-axis current, i_q of at rotor MMF per coil, i_f of 600Aturns.

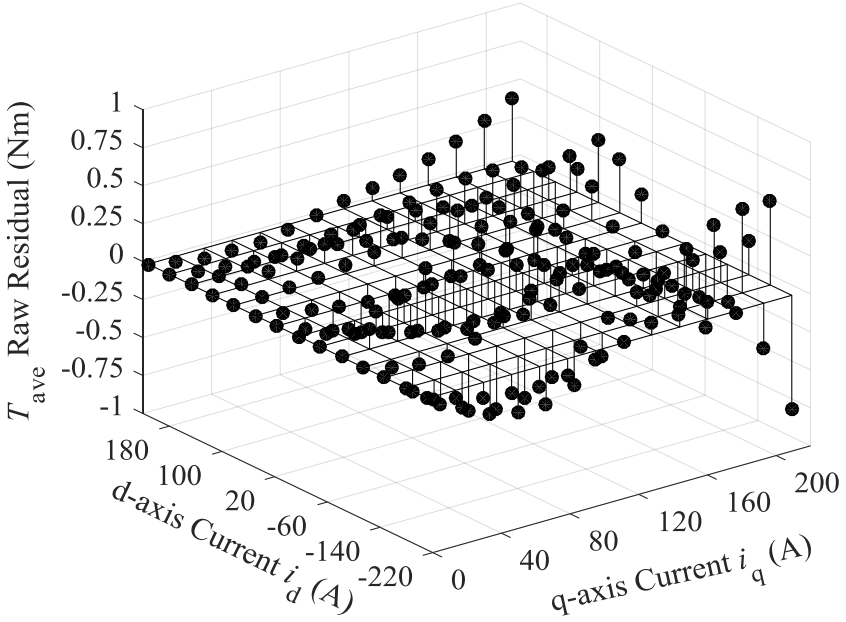

(a)

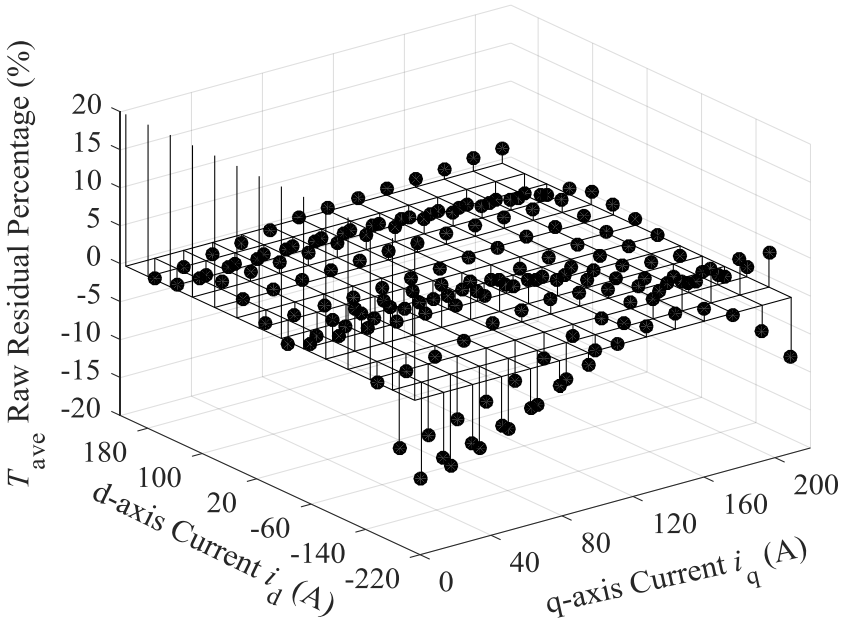

(b)

Figure 5.7. 2D torque residues from flux surface fitting vs. d-axis current, i_d and q-axis current, i_q, (a) raw residues and (b) percentage of raw residues over original data from FE analysis.

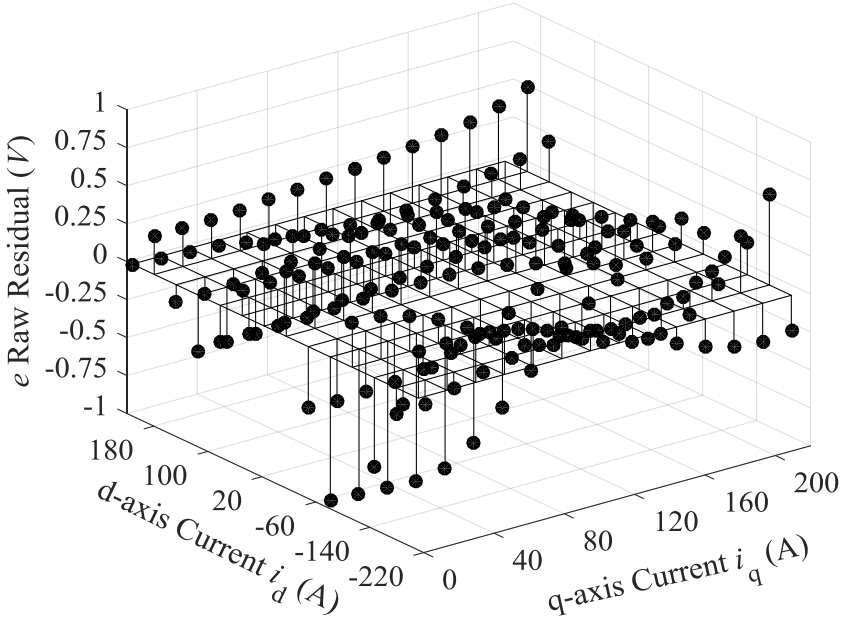

(a)

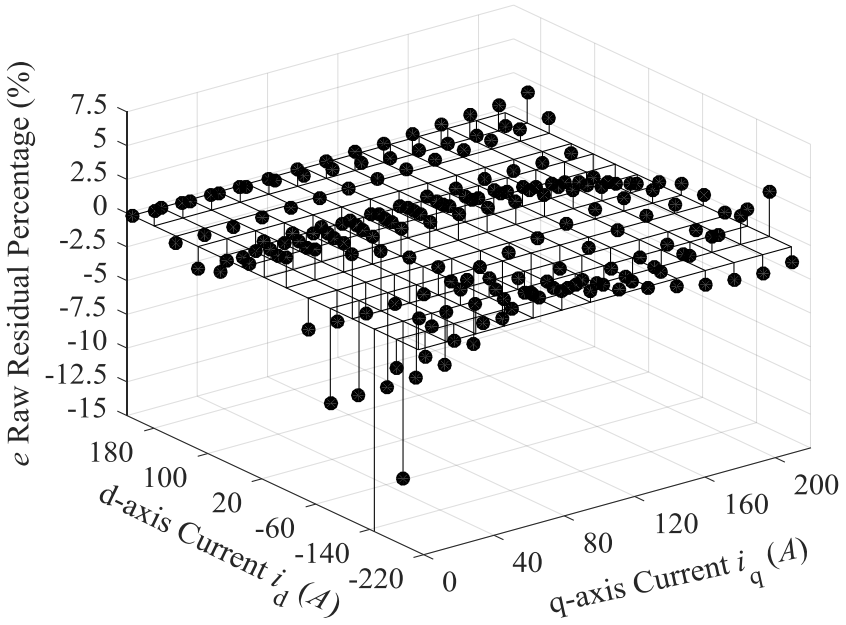

(b)

Figure 5.8. 2D induced voltage residues from flux surface fitting vs. d-axis current, i_d and q-axis current, i_q, (a) raw residues and (b) percentage of raw residues over original data from FE analysis.

The surface fitting procedures for a fixed i_f is now complete. To expand the flux polynomials to describe machine performance across all investigated values of i_f, the surface fitting

described above is repeated at i_f levels from 0 to 1000 Aturns at an interval of 100 Aturns. The undetermined coefficients in (5.7) are plotted against i_f, as shown in figure 5.9.

A 1D least square curve fitting is applied on each coefficient in figure 5.9. The resultant polynomial orders vary from four to eight. These polynomials are then used to replace the corresponding constants displayed in figure 5.2. In this way, 3D polynomials of λ_d and λ_q are derived as functions of i_d, i_q and i_f. From figure 5.2, different polynomial item has different contribution to flux, and their contribution varies considerably with i_f. Some coefficient polynomials are even function with $i_f = 0$ axis, and some are odd functions.

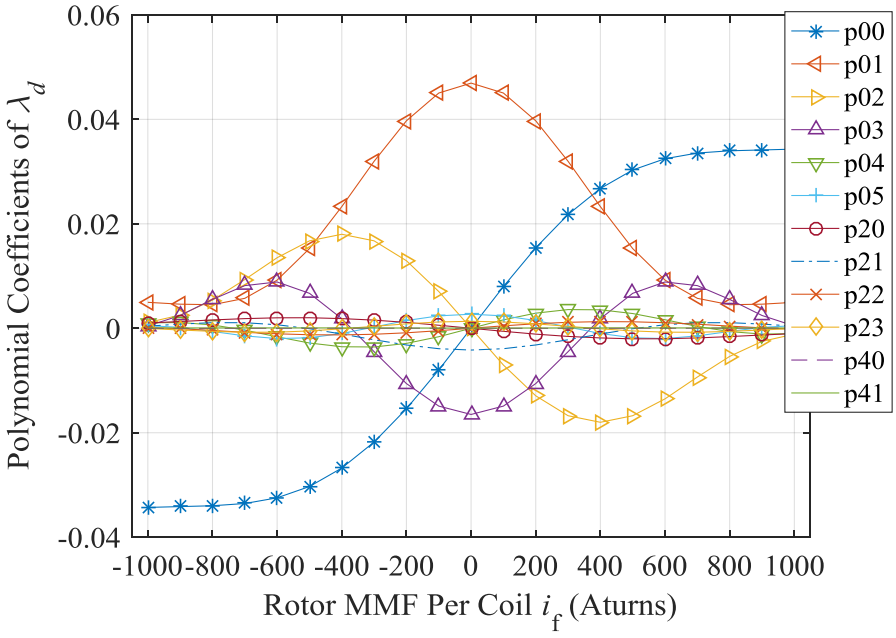

(a)

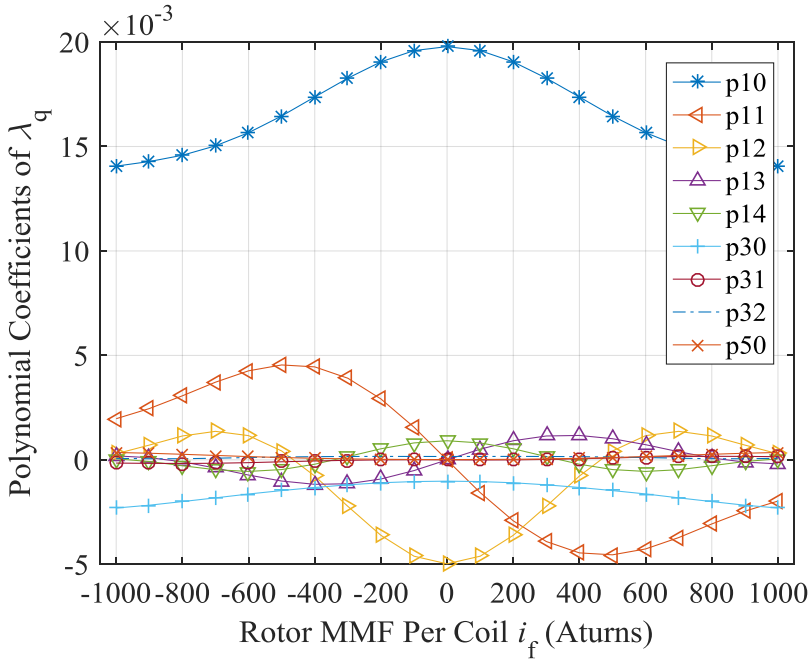

(b)

Figure 5.9. 2D Surface Fitting Polynomial Coefficients vs. rotor MMF per coil, i_f of (a) d-axis flux, λ_d and (b) q-axis flux, λ_q.

5.1.2 Results Analysis

Solving Lagrange function (5.6), the solved i_q^*, i_d^* and i_f^* for speed, ω from 2000 rpm to 10000 rpm and mechanical power, P_{mech} from 1 to 5 kW are plotted in figure 5.10. The boundaries of the definition region are labelled in black dotted line.

From the figure, prediction of i_d at 1 kW under the speed of 4000 rpm and 6000 rpm, and 1 to 5 kW under the speed 7000 rpm lay outside the definition region. This causes error in prediction, and therefore these points are excluded. To evaluate the accuracy of Lagrange method, predicted currents are fed back to FE model, where the generated torque values are compared with their objective values as displayed in figure 5.11. The deviations and percentage of deviations over the objective torque values are shown in figure 5.12. From the figures, deviations vary from -0.8 Nm to 0.5 Nm and their percentage vary from -12 % to 10 %. The fundamental phase voltages, V_{fun} and its limits, V_{fun0} are plotted in figure 5.13, where predicted voltage exceeds V_{fun0} by a maximum of 2.6 V, or 10.5 %.

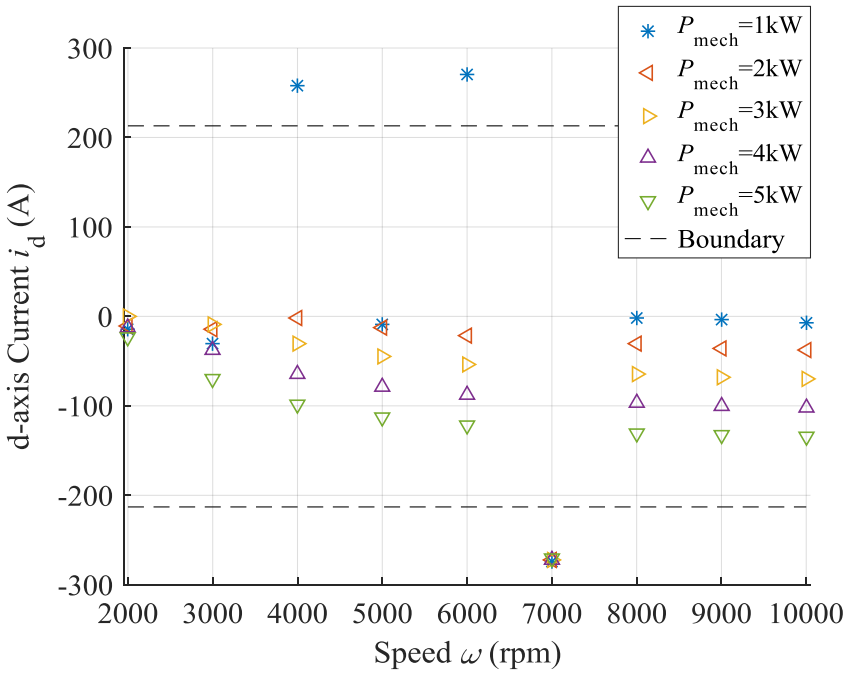
300
200
100
0
-100
-200
-300
2000
3000
4000
5000
6000
7000
8000
9000
10000
d-axis Current i_d (A)
Speed ω (rpm)
P_{mech}=1kW
P_{mech}=2kW
P_{mech}=3kW
P_{mech}=4kW
P_{mech}=5kW
Boundary

(a)

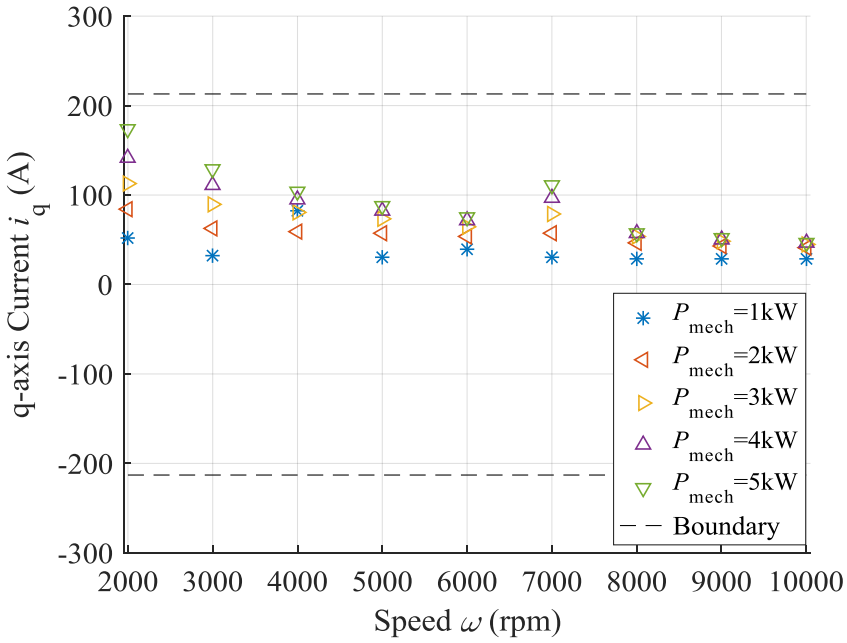
300
200
100
0
-100
-200
-300
2000
3000
4000
5000
6000
7000
8000
9000
10000
q-axis Current i_q (A)
Speed ω (rpm)
P_{mech}=1kW
P_{mech}=2kW
P_{mech}=3kW
P_{mech}=4kW
P_{mech}=5kW
Boundary

(b)

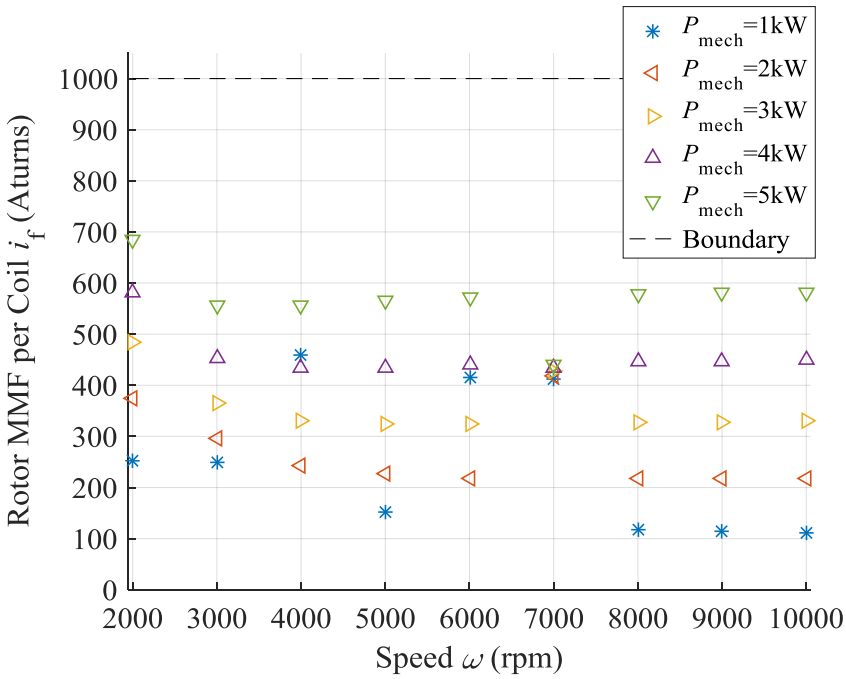

(c)

Figure 5.10. Currents from Lagrange method vs. speed ω of (a) d-axis current i_d (b) q-axis current i_q and (c)rotor MMF per coil i_f at various mechanical power P_{mech}.

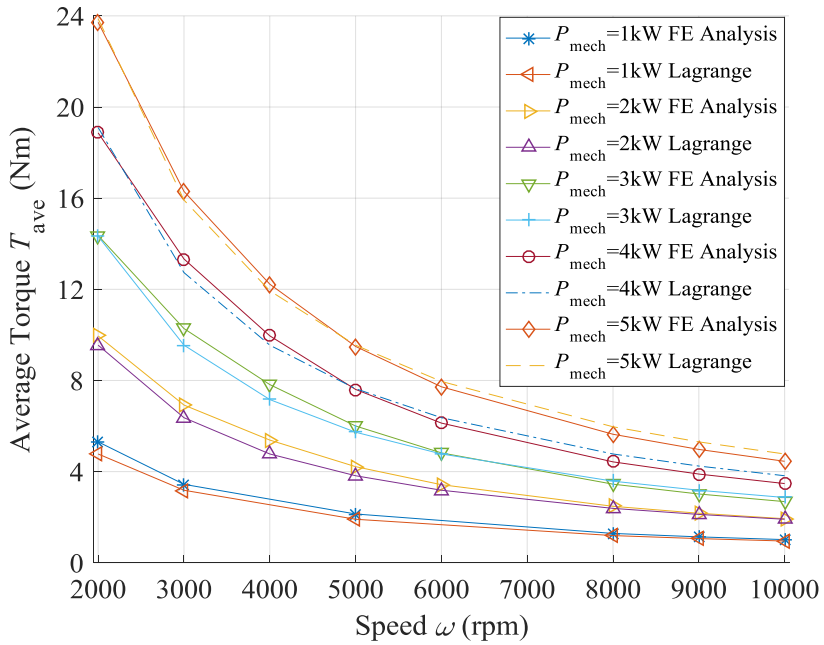

Figure 5.11. Comparisons between and average torque, T_{ave}, prediction from Lagrange method and from FE analysis vs. speed, ω at various mechanical power, P_{mech}.

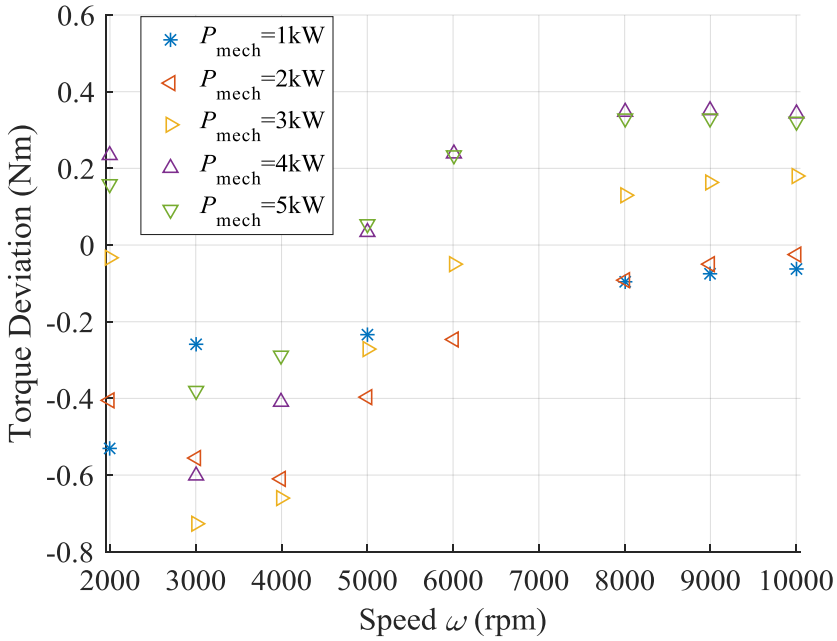

(a)

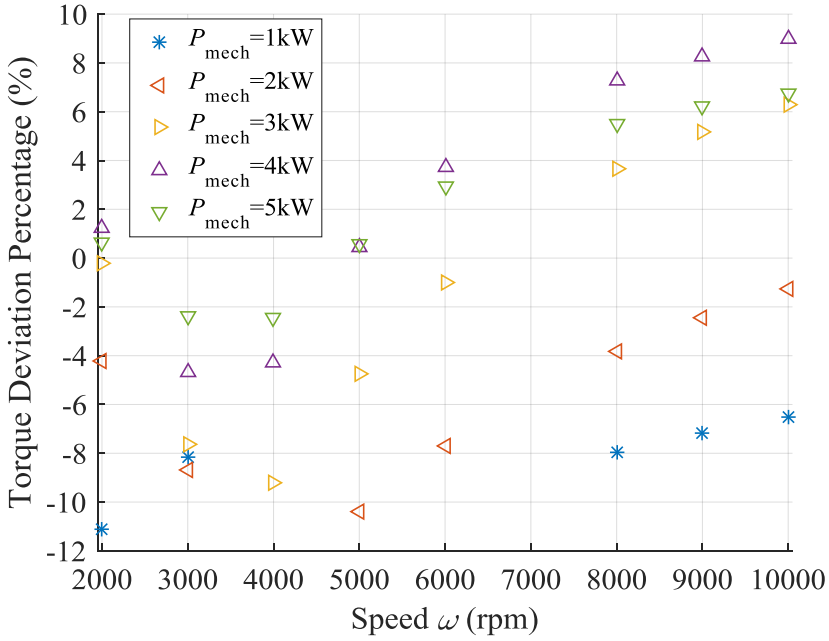

(b)

Figure 5.12. Deviations between average torque, T_{ave}, from Lagrange method and FE analysis vs. speed, ω at various mechanical power, P_{mech} (a) value (b) percentage of deviation over FE analysis.

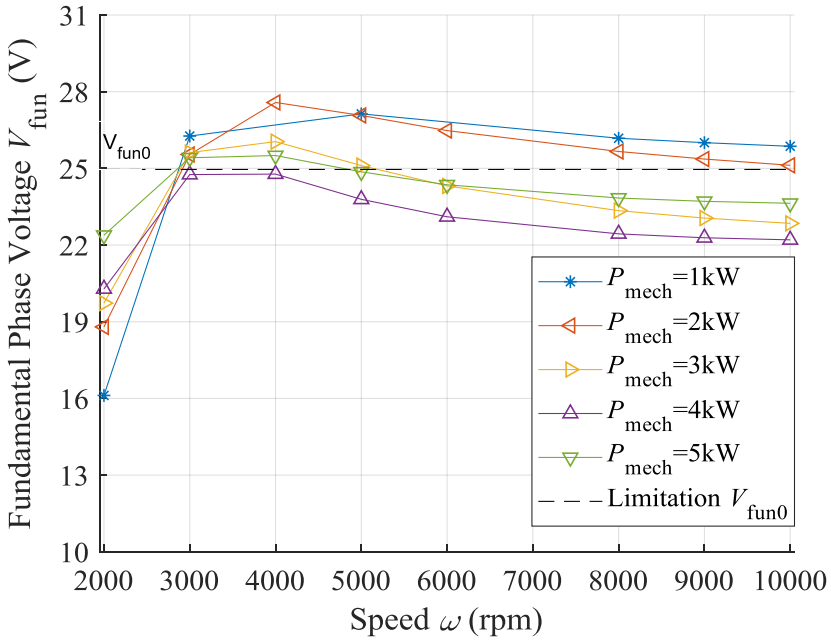

Figure 5.13. Fundamental phase voltage, V_{fun}, vs. speed, ω, with voltage limit, V_{fun0} at various mechanical power, P_{mech}.

In conclusion, this section introduces a detailed procedure to determine the current criterion for minimum copper loss operation of wound rotor synchronous machine with torque and voltage restraints using Lagrange method. The results are validated with finite element analysis, where the predicted torque and voltage results are compared with its FE analysis values.

From the study, Lagrange method has three major drawbacks:

(1) The computer applied for solving the Lagrange functions is equipped with Intel® Xeon® CPU E3-1270 v3 @ 3.50GHz, with 16.0GB of RAM and 64 bit windows 7 professional operation system. Solving each point using Lagrange method takes as long as four hours with Matlab.

(2) From comparison, deviations no more than ±10% of the FE analysis are observed in generally. These deviations come from the inaccuracy between original flux data from finite element analysis and its surface fitted polynomials. To reduce this inaccuracy, polynomials with higher order should be introduced, which adds to the complexity of flux functions and therefore further increase simulation time.

(3) The Lagrange method also introduces errors in prediction if either of the predicted current values are located beyond the definition region, because polynomial coefficients outside definition region are no longer regulated by flux data.

5.2 Proposed Method

In section 5.1, the Lagrange method is applied for solving the problem of minimum copper loss with torque and voltage constraints. This chapter introduces a novel method in searching for minimum loss operation current criterion. Compared with the Lagrange method, the proposed method requires much less computation time, and the results are more accurate.

5.2.1 Introduction

From section 5.1, a major problem in the Lagrange method is the highly non-linear and current dependent λ_d and λ_q. Least squares curve fitting introduces residues at existing points. Errors are also presented in value prediction between existing points. The combination of these effects causes errors in current prediction compared with FE analysis. Moreover, polynomials outside the definition region are not regulated, causing possible errors in the calculations.

To overcome these problems, this section introduces a novel approach. The proposed method uses 2D cubic spline interpolation to replace normal surface fitting. To implement this method, two conditions are applied. First, as cubic spline functions are continuously differentiable twice, the flux model is considered second order continuous everywhere. Second, multi - dimensional interpolation is accomplished by performing one - dimensional interpolation across each dimension.

The piecewise cubic spline interpolation algorithm used in this study is described in [170]. A brief explanation is presented here. For a discrete function $f(\alpha_i)$ with j points, cubic polynomials are applied to each point, where the i^{th} point has a function of

$$s_i(\alpha) = A_i + B_i(\alpha - \alpha_i) + C_i(\alpha - \alpha_i)^2 + D_i(\alpha - \alpha_i)^3 \tag{5.11}$$

To solve for the unknown coefficients A, B, C and D, the following conditions are satisfied. First, (5.11) passes point i and i+1. Second, $s_i'(\alpha)$ and $s_i''(\alpha)$ exists at any α_i ($1 < i < j$). Last, proper boundary conditions are imposed. In this study, 'not-a-knot' conditions are imposed at point 1 and j.

From the statement above, using the interpolation over the least squares fitting has three advantages. First, it eliminates residues at α. Second, no requirement is needed to regulate the data where $i < 1$ and $i > j$. However, interpolation greatly complicates the flux numerical model, where for a m × n table, (m - 1) × (n - 1) polynomials are introduced, giving 4 × (m - 1) × (n - 1) coefficients. To solve this problem, dense points are interpolated in advance, then a searching algorithm is proposed. This approach brings the third advantage, where the solving process is greatly simplified. Unlike Lagrangian method that requires solving of high order polynomials for each calculation, the tables in interpolation method only need to be interpolated once. For each calculation, polynomial solving is then replaced with a simple searching procedure. This greatly reduces calculation effort and time consumption

Using interpolation method to predict MSCRM field weakening performance has been detailed described in section 3.2.2. Based on this method, a searching algorithm for minimum loss of WRSM with equal torque constraint and unequal voltage constraint is developed. To compare with the Lagrange method, the same flux data tables used in section 5.1 are applied.

The symbols used in this chapter are listed below:

T_0, V_0: torque and voltage objective value;

$\lambda_{if}(i_d, i_q)$, $T_{if}(i_d, i_q)$: flux and torque versus i_d and i_q at certain rotor MMF per coil i_f,

T_{acc}, V_{acc}: The accuracy of predicted torque and voltage, where:

$$T_{acc} = \frac{T_{if}(i_d, i_q) - T_0}{T_0} \tag{5.12a}$$

$$V_{acc} = \frac{V_{if}(i_d, i_q) - V_0}{V_0} \tag{5.12b}$$

Δi_d, Δi_q, Δi_f: intervals of original flux data tables between two nearby current points;

$d i_d$, $d i_q$, $d i_f$: intervals between interpolated current points;

i_{dint}, i_{qint}, i_{fint}: interpolated current values;

λ_{ifint} (i_{dint}, i_{qint}), T_{ifint} (i_{dint}, i_{qint}), V_{ifint}(i_{dint}, i_{qint}): interpolated flux, torque and voltage tables;

i_{drec}, i_{qrec}, i_{frec}: current and torque values that satisfy (5.12);

$P_{cop,rec}$: copper loss under i_{drec}, i_{qrec}, i_{frec}.

i_d^*, i_q^* and i_f^*: current and torque values that satisfy (5.12) with minimum copper loss;

$P_{cop,min}^*$: minimum copper loss,

The detailed procedure of searching for minimum loss point with constraints of $V \le V_0$ and $T = T_0$ is described as follows. A flow chart is shown in figure 5.14:

(1) Generate λ_{if} (i_d, i_q) and T_{if} (i_d, i_q) from finite element analysis with interval of Δi_d, Δi_q, at Δi_f apart;

(2) Interpolate all λ_{if} (i_d, i_q) and T_{if} (i_d, i_q) at interval of $d i_d$ and $d i_q$ into λ_{ifint} (i_{dint}, i_{qint}) and T_{ifint} (i_{dint}, i_{qint});

(3) Interpolate all λ_{ifint} and T_{ifint} tables at interval of $d i_f$;

(4) Use λ_{ifint} to generate V_{ifint} (i_d, i_q) tables at speed of ω at all i_{fint} values;

(5) At certain i_{fint}, with certain voltage and torque accuracies of V_{acc} and T_{acc}. $T = T_0$ and $V=V_0$ are located on V_{ifint} (i_{dint}, i_{qint}) and T_{ifint} (i_{dint}, i_{qint}) with a isoline of discrete points, while $V \le V_0$ is described with a region of discrete points. The required operating condition (i_{drec}, i_{qrec}) is any mutual points shared between the $T = T_0$ and $V \le V_0$. If there are multiple mutual points, P_{cop} of each point is calculated, and the one with minimum

copper loss is selected;

(6) Repeat process (5) for throughout i_{fint}, where the minimum loss point (i_d^*, i_q^*, i_f^*) and the minimum copper loss $P_{cop,min}{}^*$ is found;

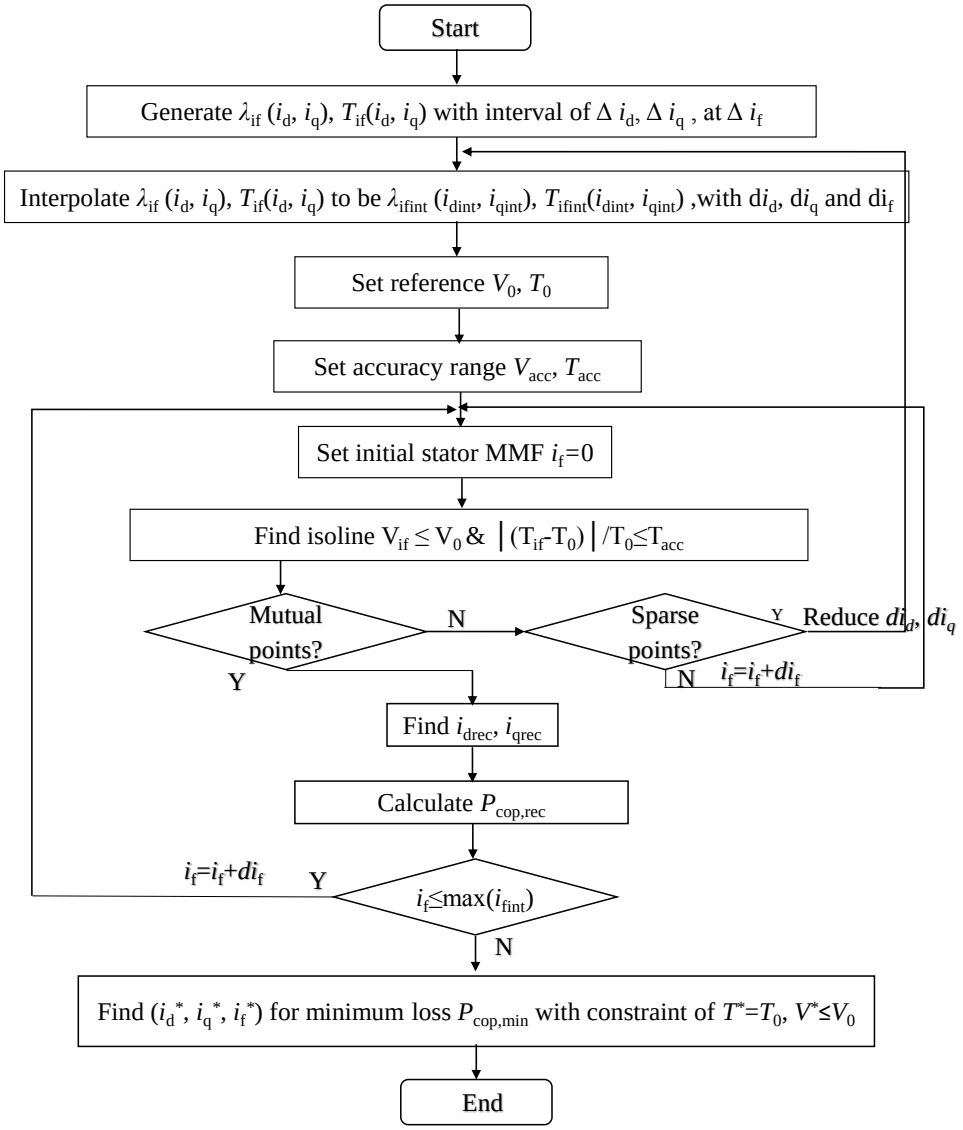

Figure 5.14. Flow chart of interpolation method in searching for stator and rotor current for minimum loss operation of wound rotor synchronous machine, with torque and voltage restraints.

In this process, several things need to be mentioned. In step (5), if there is no intersection between the torque isoline and voltage region within rotor MMF limit, the requirements of $T = T_0$ and $V \le V_0$ exceeds machine current capability. If the torque isoline and voltage region intersect, but there are no common points due to a sparse table, two ways can be adopted to

solve this problem. First, decrease di_d or di_q to increase the density of the interpolated table. Second, decrease T_{acc} or V_{acc} to include more points.

5.2.2 Results Analysis

An example of V_{ifint} (i_{dint}, i_{qint}) and T_{ifint} (i_{dint}, i_{qint}) surfaces are plotted in figure 5.15-5.17, where the interpolated torque surface is shown in figure 5.15, and the interpolated voltage surface in figure 5.16. The constraints are $T_0 = 7.96$ Nm, $V_0 \leq 24.96$ V and $i_f = 580$ Aturn. Points satisfying the requirements of $(T - T_0) / T \leq \pm 0.5\%$ and $V \leq V_0$ are marked in red. Figure 5.17 displays projection of $(T - T_0) / T \leq \pm 0.5\%$ and $V \leq V_0$ on z-plane, where intersection occurs at multiple points. Each intersected point is calculated for copper loss, where a minimum copper loss of 648.8 W is presented at stator current of (-121.24, 74.41).

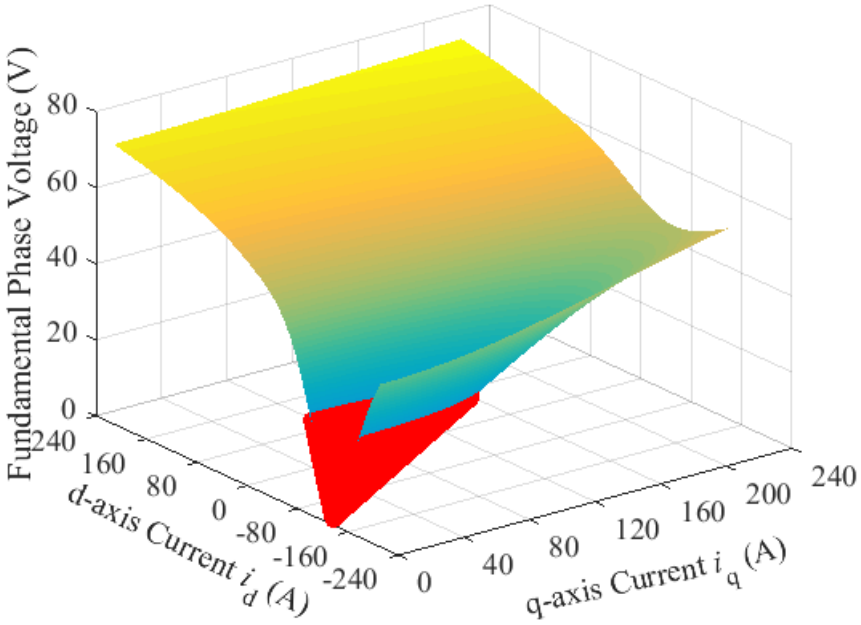

Figure 5.15. Fundamental phase voltage vs. d-axis current, i_d and q-axis current, i_q. Voltage limit, $V_0 \leq 24.96$ V, rotor MMF, $i_f = 580$ Aturns.

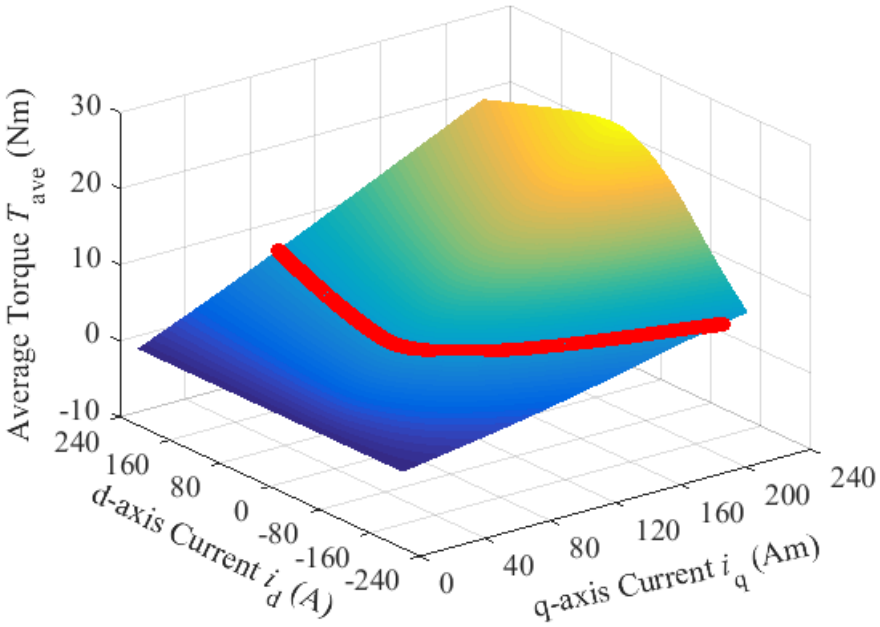

Figure 5.16. Average torque, T_{ave}, vs. d-axis current, i_d and q-axis current, i_q. Objective torque, T_0 = 7.96 Nm, rotor MMF, i_f = 580 Aturns, torque tolerance, T_{acc} = ± 0.5%.

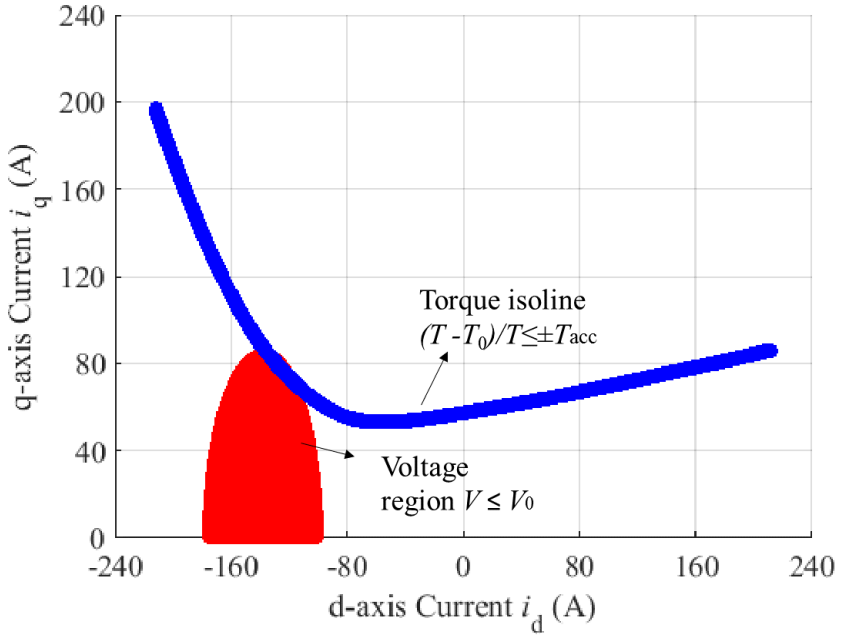

Figure 5.17. Torque region (T - T_0) / T ≤ ± 0.5% and voltage region V ≤ V_0 vs. d-axis curren,t i_d and q-axis current, i_q. Objective torque, T_0 = 7.96 Nm, voltage limitation, V_0=24.96 V, rotor MMF, i_f = 580 Aturns, torque tolerance, T_{acc} = ± 0.5%.

Repeat this process for all i_f, the copper losses, P_{cop} versus i_f for various speed, ω from 2000 rpm to 10000 rpm at 5 kW is shown in figure 5.18. From the figure, a great reduction in optimum

rotor MMF, i_f^* is presented from 2000 rpm to 3000 rpm, and further speed increase does not affect i_f^*.

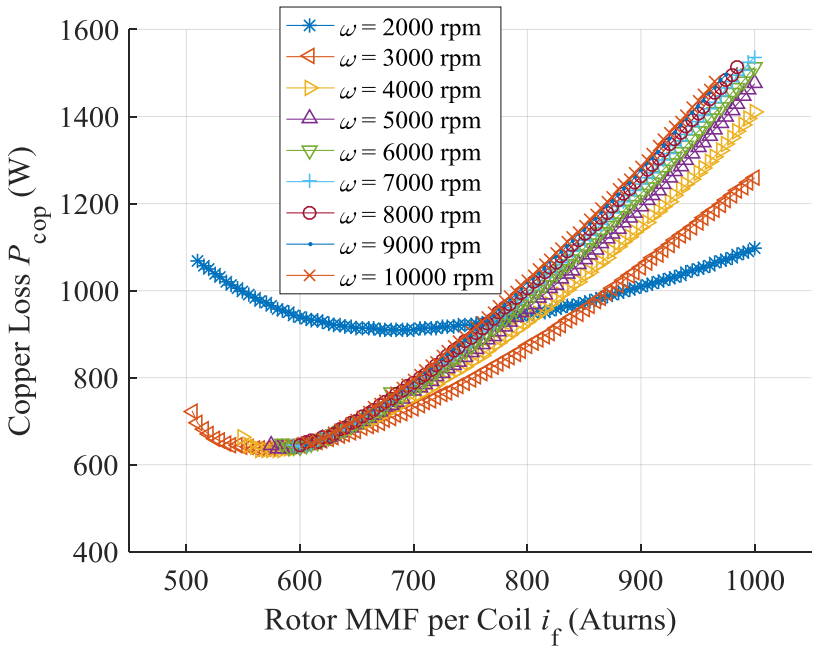

Figure 5.18. Copper loss, P_{cop} at 5 kW vs. rotor MMF per coil, i_f, from speed, ω of 2000 rpm to 10000 rpm at interval of 1000 rpm.

The average torque comparisons between objective and predicted values versus speed are shown in figure 5.19. The average torque deviations and percentage of deviation over objective values are plotted in figure 5.20. From the figures, almost all predicted torque values above 1 kW fall into the defined tolerance region of ±0.5%. For 1 kW, a tolerance region of ±1% is achieved. Compare figure 5.12 and 5.20, the interpolation method increases torque prediction accuracy by a factor of 10. The phase voltage plot for various power and speed is shown in figure 5.21. For minimum copper loss, the operation voltage is below limitation at 1 kW. With increase of power, the voltage approaches its constraint, but does not exceed limitation by more than 0.15%.

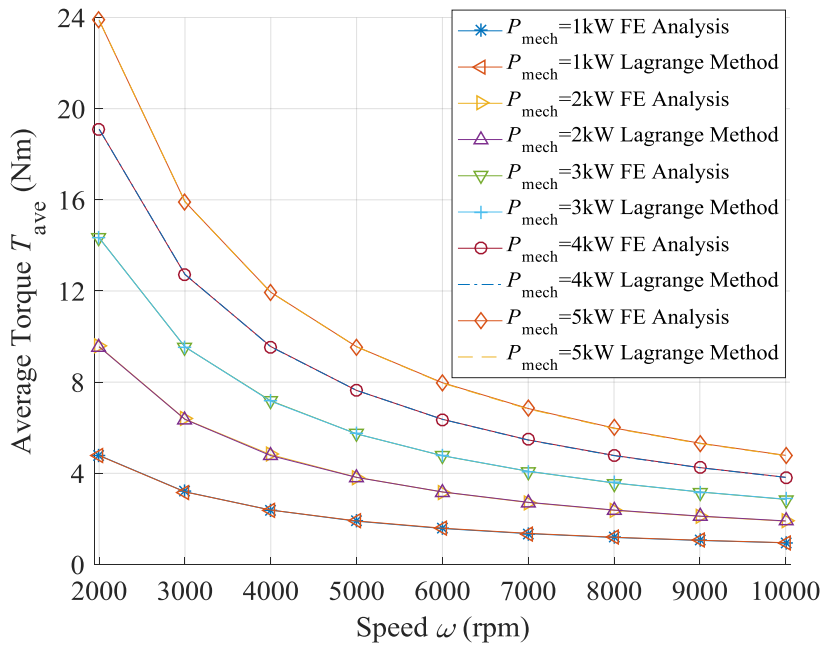

Figure 5.19. Average torque, T_{ave}, comparisons between interpolation method and FE analysis vs. speed, ω at mechanical power, P_{mech}, from 1 to 5 kW at interval of 1 kW.

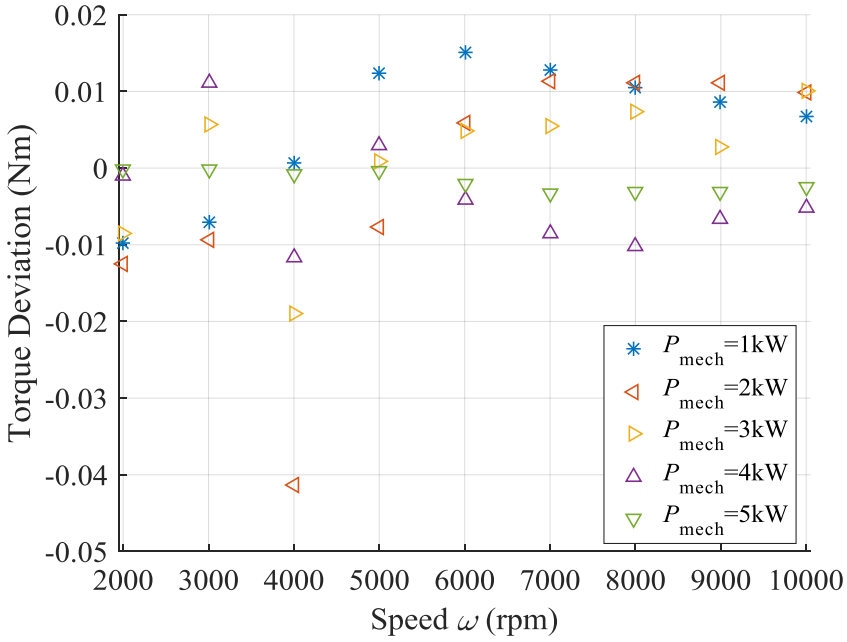

(a)

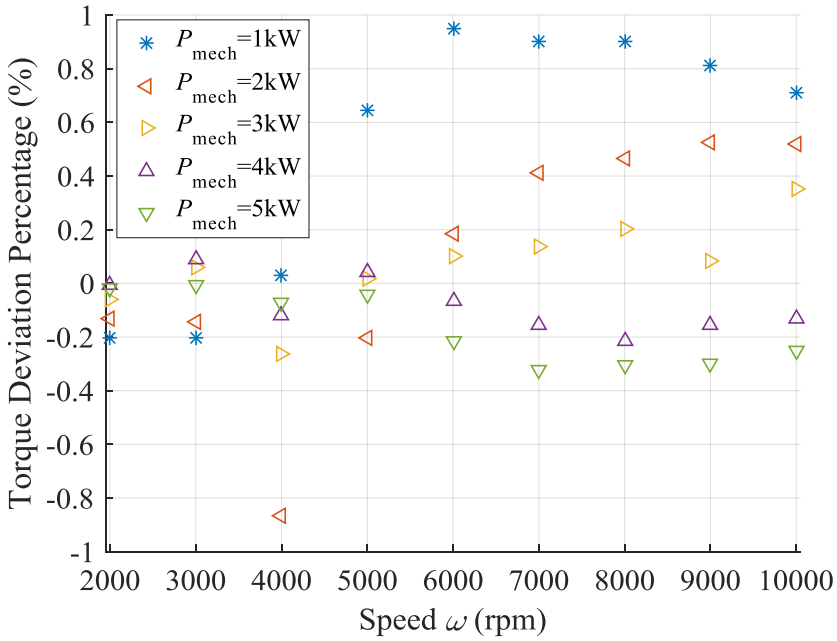

(b)

Figure 5.20. (a) Torque deviations between interpolation method and FE analysis (b) percentage of torque deviations over FE analysis vs. speed, ω at mechanical power, P_{mech}, from 1 to 5 kW at interval of 1 kW.

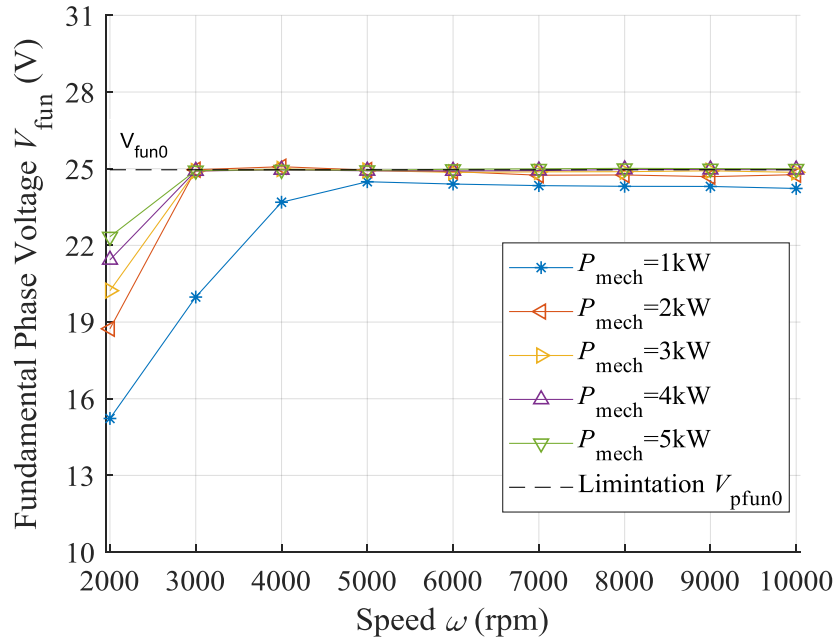

Figure 5.21. Fundamental phase voltages, V_{fun}, from interpolation method and limitation, V_{fun0} vs. speed, ω at mechanical power, P_{mech}, from 1 to 5 kW at interval of 1 kW.

In summary, the interpolation method has the following advantages over Lagrange method:

(1) The predicted results are free from error points beyond definition region;

(2) The predicted results are higher in accuracy, where the discrepancies between predictions and FE analysis reduce from ±10% to ±1%. This indicates that interpolation is more capable in describing flux and torque than polynomials, where residues from surface fitting is avoided;

(4) Once the tables are interpolated, they are stored in computer memory and are readily applied for any optimum operation point calculation with a simple searching algorithm. Therefore, the time and computational effort are greatly reduced. Using the same computer and Matlab, the interpolation method decreases the computational time of solving one point from two to four hours to less than one minute.

5.2.3 Considering Iron Loss

Previous research suggests iron loss is not as influential as copper loss in WRSM operation [111]. In section 5.2.1 and 5.2.2, only copper loss is considered for loss minimization.

The iron loss, P_{ir} to total loss, P_l ratio from minimum copper loss operation versus speed, ω at various mechanical power, P_{mech} levels are plotted in figure 5.22. At different speed and mechanical power level, the ratio of iron loss varies considerably. With increasing mechanical power and decreasing speed, copper loss becomes more dominant. At low power and high speed, however, iron loss is the primary loss source, so reduction on iron loss has a great potential for improvement on total loss minimization. Consequently, an investigation is conducted on the effects of minimum loss operation including iron loss, and its difference compared with minimum copper loss operation.

To achieve this, tables of iron loss, P_{ir} versus d-axis current, i_d, q-axis current, i_q, rotor MMF per coil, i_f and speed, ω are obtained from Altiar Flux and interpolated as described in section 3.2.2. The interpolated iron losses are added to copper loss in step (5) of the procedure described in section 5.2.2 and figure 5.14. Figure 5.23 shows an example of iron loss versus i_f and θ at ω of 6000 rpm and fundamental stator current i_{sfun} of 150 A.

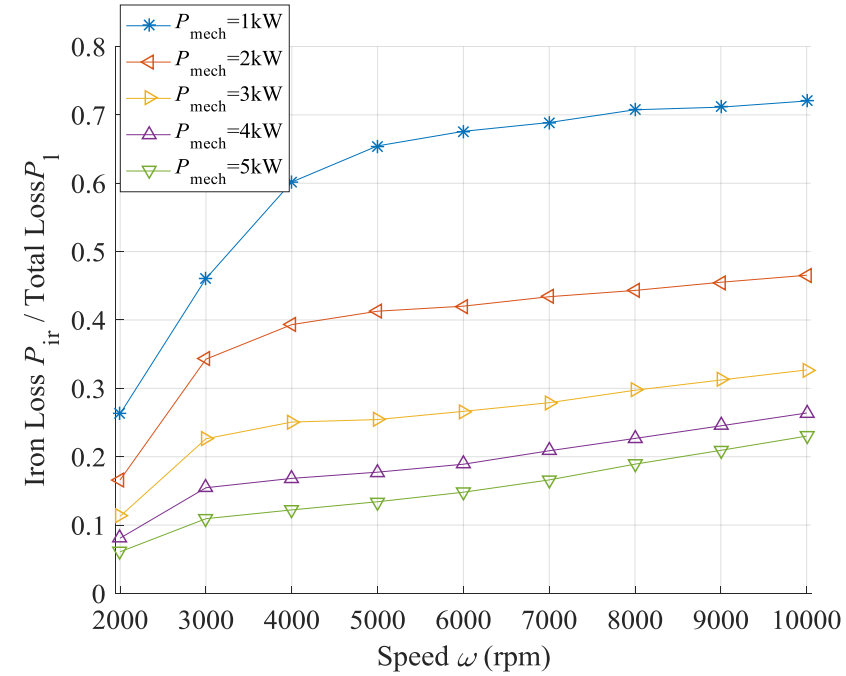

Figure 5.22. Iron loss, P_{ir}, to total loss, P_l, ratio vs. speed, ω for mechanical power, P_{mech}, from 1 to 5 kW at interval of 1 kW.

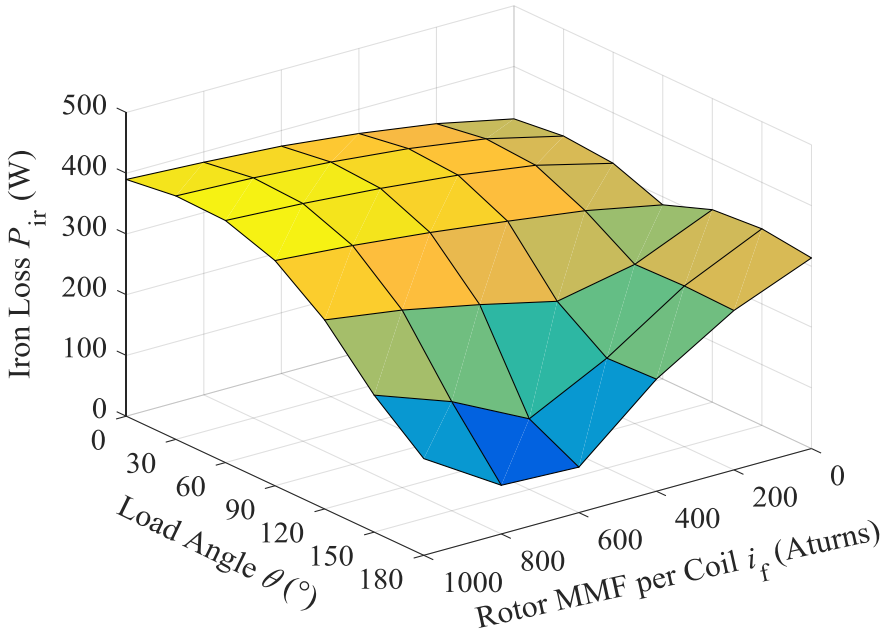

Figure 5.23. Iron loss, P_{ir}, vs. load angle, θ and rotor MMF per coil, i_f at fundamental stator current, i_{sfun} of 150 A and speed, ω of 6000 rpm.

Since the P_{mech} of 1 kW has the highest P_{ir} to P_{cop} ratio, total loss minimization strategy is applied at P_{mech} of 1 kW, where the currents and losses are plotted in comparison with copper

loss minimization strategy. To be specific, comparisons of fundamental stator phase current, i_{sfun}, rotor MMF per coil, i_f, load angle, θ and fundamental phase flux, λ_{fun} are plotted in figure 5.24 - 5.27. Compared with the copper loss minimization strategy, i_{sfun} and i_f in the total loss minimization strategy are both increased, generating a higher P_{cop}. Then with an increased θ, a decrease in λ is achieved, leading to a reduction in P_{ir}. Figure 5.28 compares P_{cop} and P_{ir} from the total loss minimization method with copper loss minimization method and its FE analysis results. From the figure, the total loss minimization method slightly overestimates the iron loss at high speed. Compared with the copper loss minimization method, a maximum loss reduction of about 12% is presented from 3000 rpm to 5000 rpm. However, this reduction quickly diminishes with increase of P_{mech}. At rated P_{mech} of 5 kW, the both methods give the same results.

In conclusion, compared with the copper loss minimization method, the total loss minimization method decreases the iron loss. However, the reduction of iron loss is offset by increases in copper loss, and the total loss only shows slightly improvement at low mechanical power.

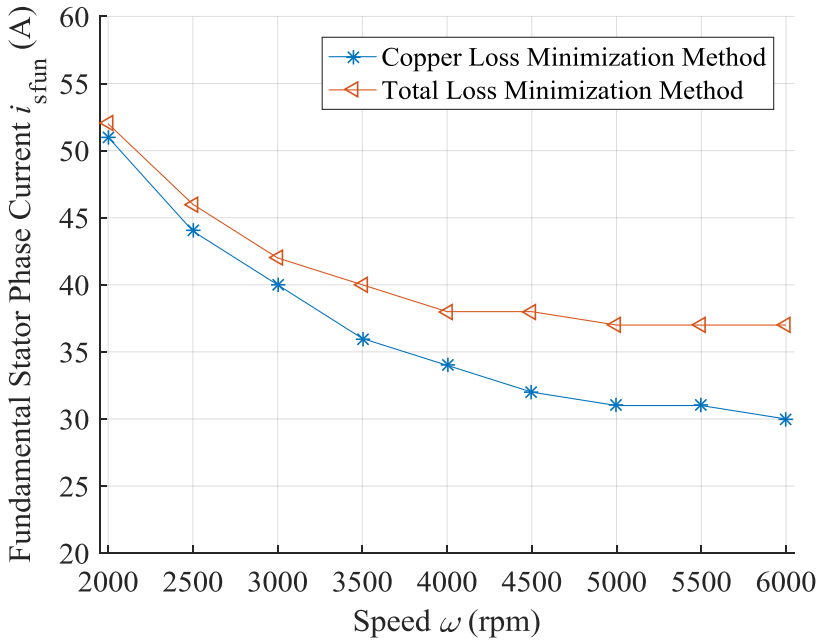

Figure 5.24. Fundamental stator phase current, i_{sfun}, comparisons between copper loss minimization and total loss minimization methods vs. speed, ω at mechanical power, P_{mech} of 1 kW.

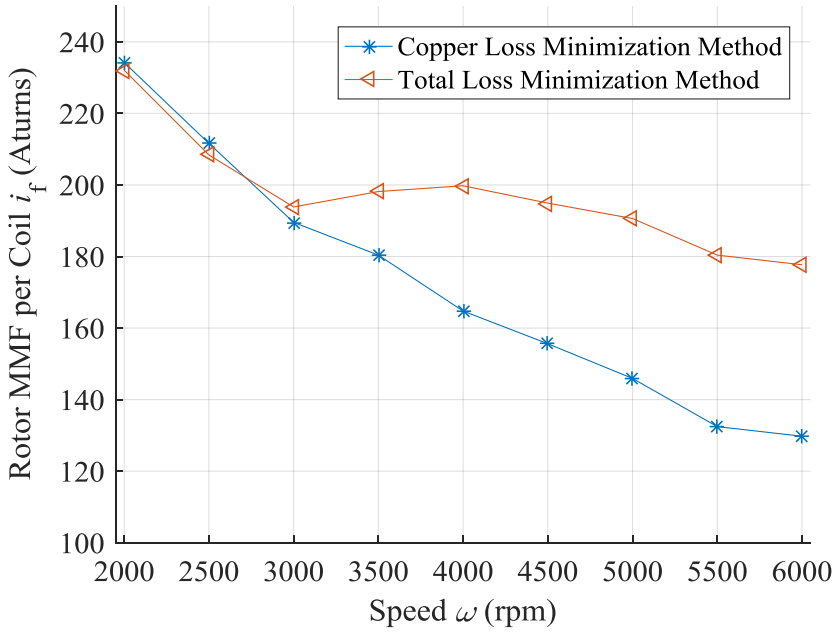

Figure 5.25. Rotor MMF per coil, i_f, comparisons between copper loss minimization and total loss minimization vs. speed, ω at mechanical power, P_{mech} of 1 kW.

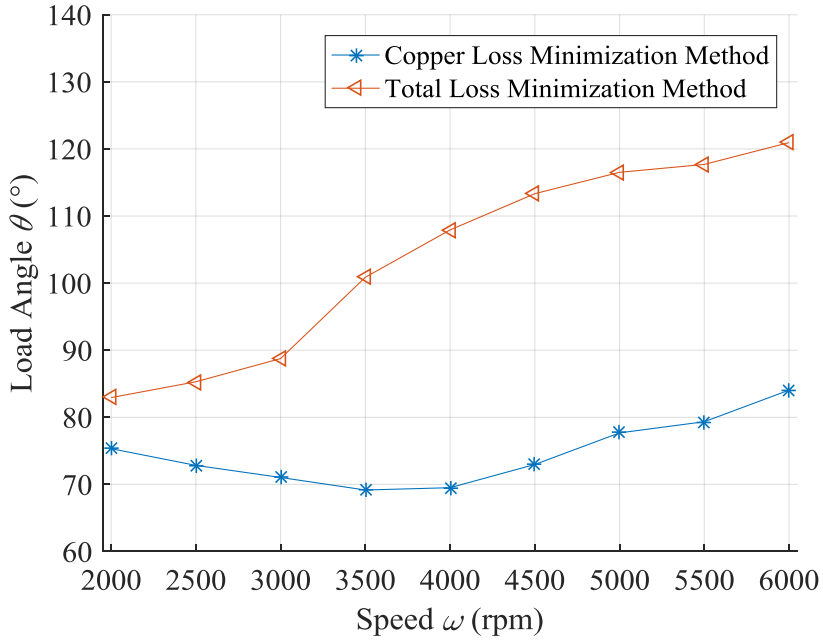

Figure 5.26.Load angle, θ, comparisons between copper loss minimization and total loss minimization vs. speed, ω at mechanical power, P_{mech} of 1 kW.

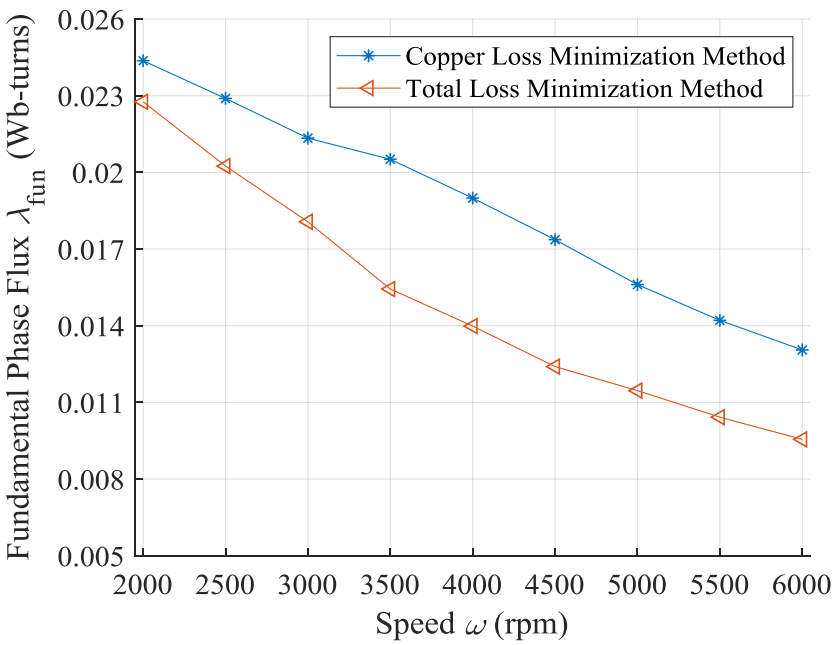

Figure 5.27. Fundamental phase flux, λ_{fun}, comparisons between copper loss minimization and total loss minimization vs. speed, ω at mechanical power, P_{mech}, of 1 kW.

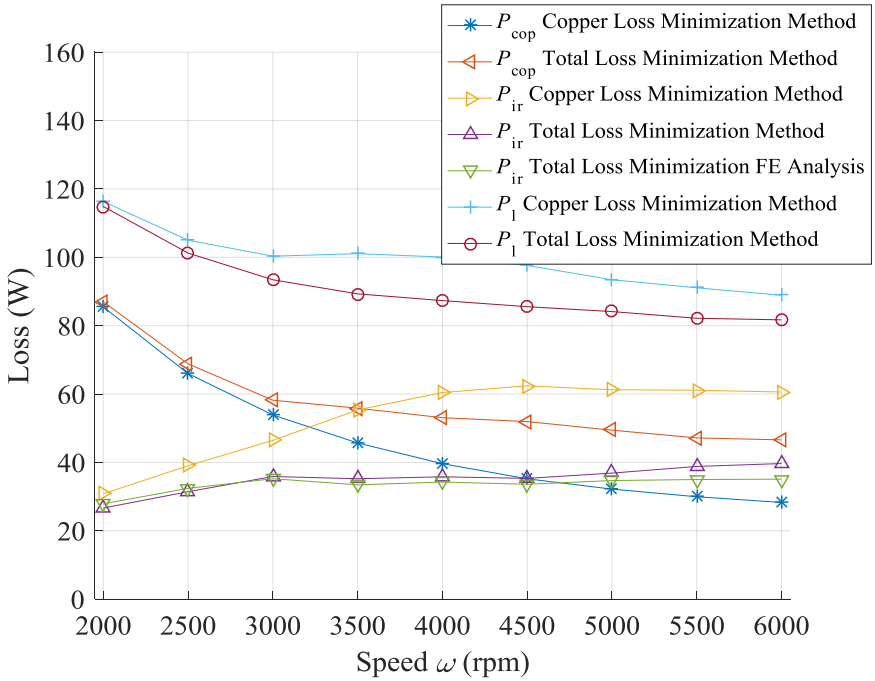

Figure 5.28. Copper losses P_{cop}, iron losses P_{ir} and total losses P_l comparisons between copper loss minimization and total loss minimization methods vs. speed ω at mechanical power P_{mech} of 1 kW.

5.3 Operation Comparison

With an accurate copper loss minimization algorithm for current criterion prediction as described in section 5.2, the influences of geometries on operational losses over all speed range can be investigated.

In section 5.3.1, the operation of four pole and six pole machines are compared. Both machines are geometrically optimized for minimum loss at rated mechanical power of 5 kW as described in section 4.1.3 and 4.2.1. In section 5.3.2, comparisons between six pole machines with normal and eccentric rotor pole are conducted. The geometric specifications of rotor pole eccentricity are described in section 4.3.2. In section 5.3.3, a different lamination material is implemented on the six pole machine with eccentric rotor. The impact of material on iron loss and efficiency are studied. In section 5.4.4, the WRSM performance in terms of loss over a driving cycle is evaluated. The performance is then used to compare with the benchmark Speedstart classical switched reluctance machine.

5.3.1 Comparison Between Four and Six Poles

In this study, a normal rotor pole is applied. The fundamental stator current amplitude, i_{sfun} is limited at 300 A for power electronic components rating, and rotor current density, J_r is limited at 8 A/mm^2 for thermal consideration. The DC-link voltage of inverter is 48 V for motoring mode, and 50 V for generating mode. The efficiency maps of the four pole and the six pole machine versus speed, ω and mechanical power, P_{mech}, in both motoring and generating mode are illustrated in figure 5.29.

According to section 4.2, despite a slightly higher iron loss, the six pole machine has much lower copper loss than the four pole machine, leading to a higher efficiency at low speed. Figure 5.30 and 5.31 show the copper loss, P_{cop} and iron loss, P_{ir} versus speed, ω and mechanical power, P_{mech} for the four and six pole machines over the full speed range. A lower total loss, P_l in the six pole machine is exhibited, leading to a higher efficiency in a wider operation range. Moreover, with same i_{sfun} limit, six pole machine has higher P_{mech} production ability. The peak efficiency of both machines are similar. For the four pole machine, in motoring

mode, the peak efficiency is 90.8% at P_{mech} of 1.5 kW and ω of 4000 rpm. In generating mode, the peak efficiency is 90.5% at P_{mech} of 2 kW and ω of 4000 rpm. For six pole machine, in motoring mode, the peak efficiency is 90.0% at P_{mech} of 2 kW and ω of 4000 rpm. In generating mode, it is 89.8% at P_{mech} of 3 kW and ω of 4000 rpm.

At the rated P_{mech} of 5 kW, the efficiency of the six pole machine is higher than the four pole machine especially at low speed. In generating mode, an approximate 2% increase in efficiency is realized between 2200 rpm to 6000 rpm, which diminishes with increasing speed. In motoring mode, the six pole machine exhibits a significant increase in efficiency of 6.2% at 1200 rpm, and about 3% in the field weakening region.

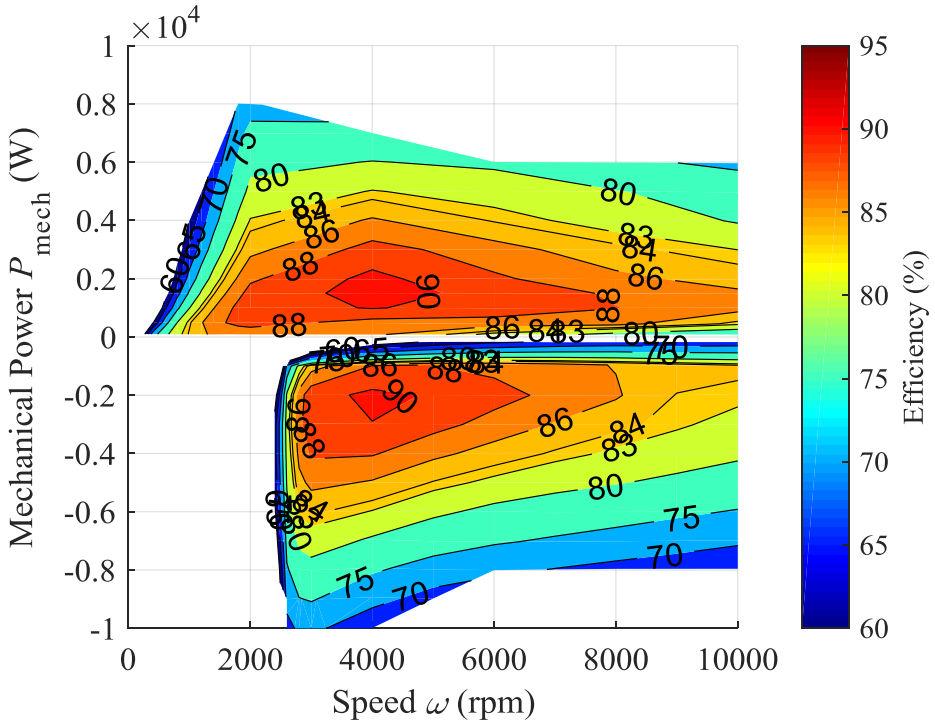

(a)

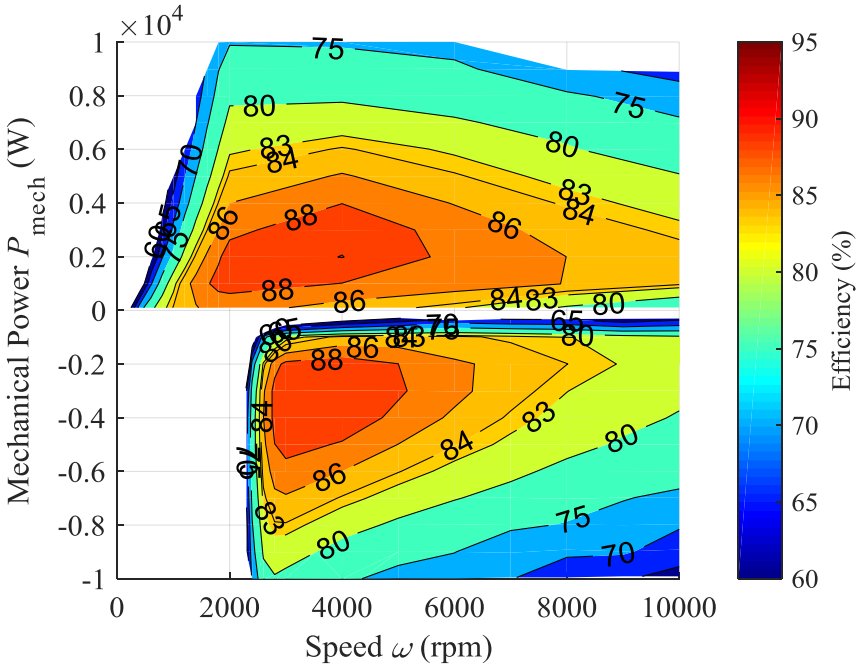

(b)

Figure 5.29. Efficiency map vs. speed, ω and mechanical power, P_{mech} of a geometry optimized (a) four pole and (b) six pole wound rotor synchronous machine.

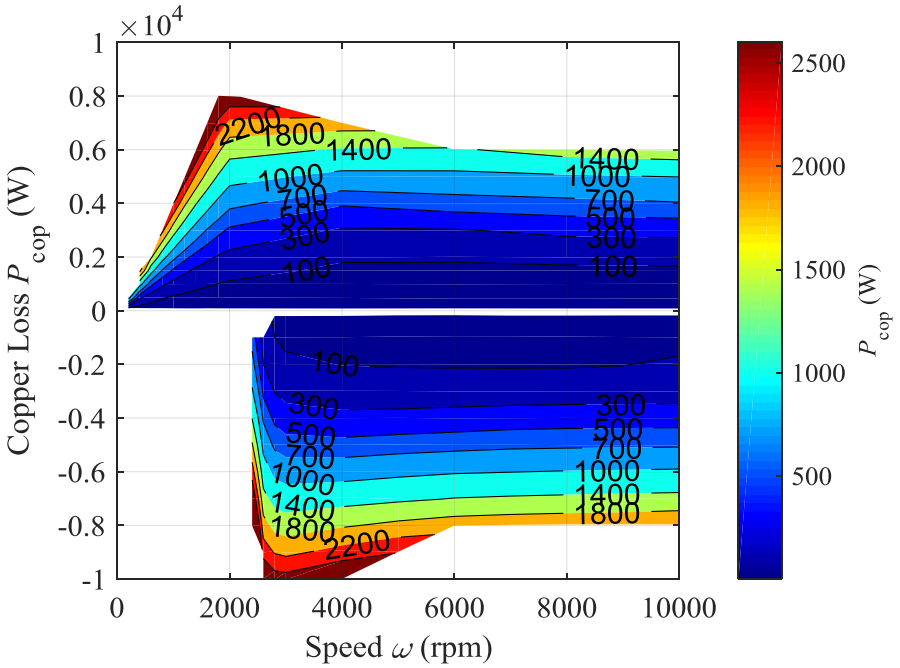

(a)

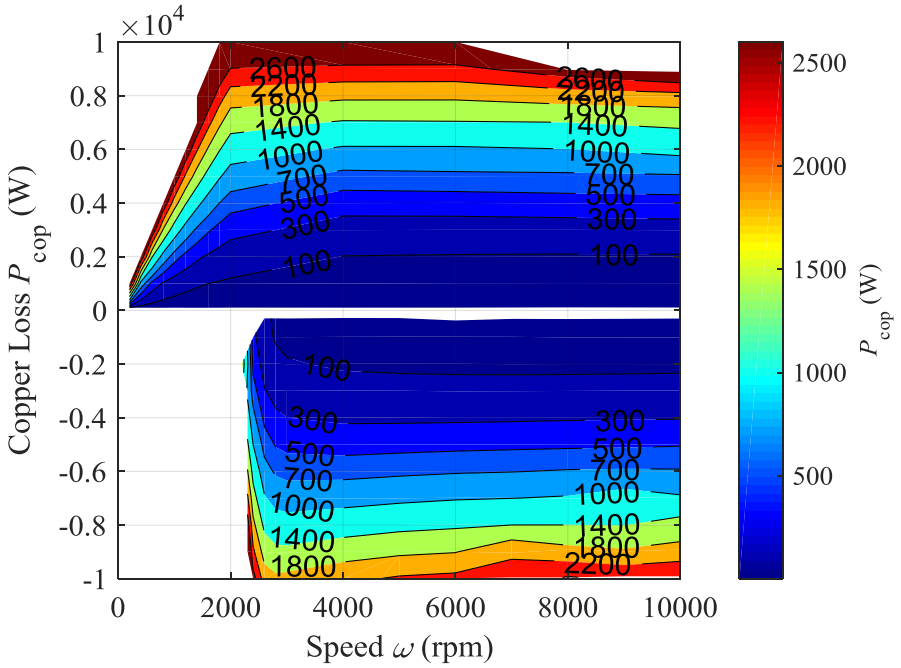

(b)

Figure 5.30. Copper loss, P_{cop}, map vs. speed, ω and mechanical power, P_{mech} of a geometry optimized (a) four pole and (b) four pole wound rotor synchronous machine.

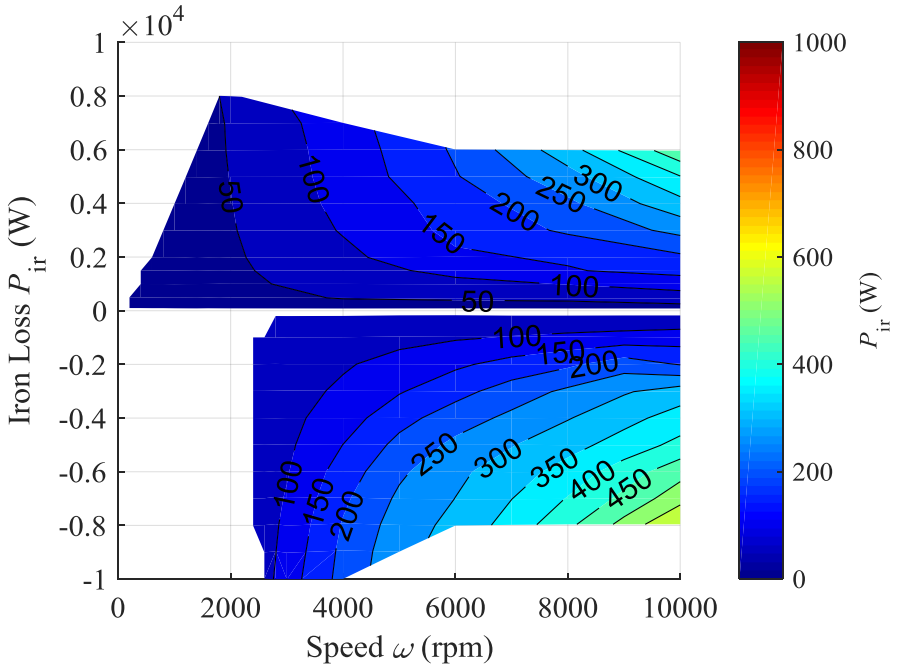

(a)

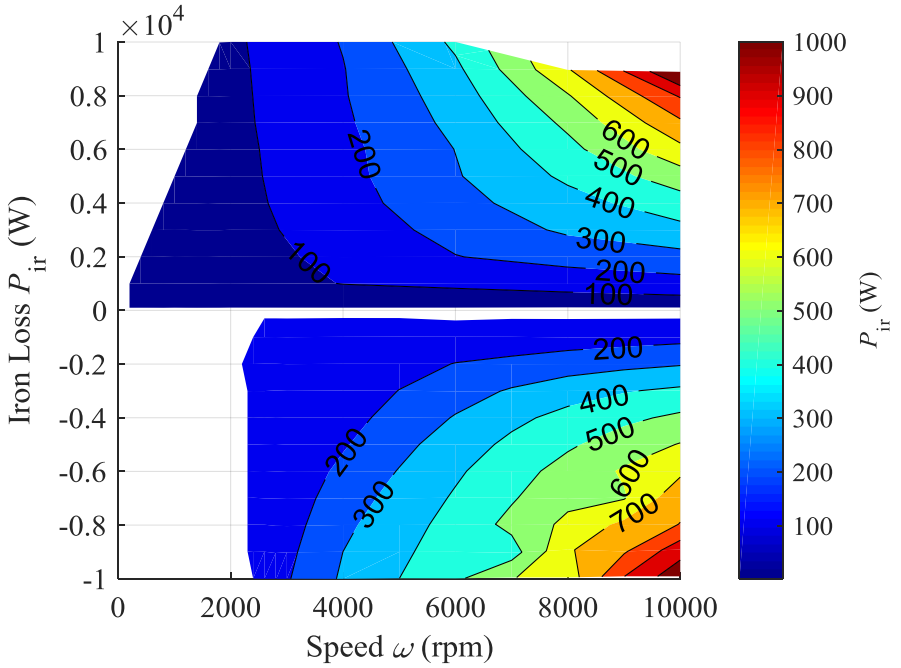

(b)

Figure 5.31. Iron loss, P_{ir}, map vs. speed, ω and mechanical power, P_{mech} of a geometry optimized (a) four pole and (b) six pole wound rotor synchronous machine.

5.3.2 Effect of Eccentric Rotor Pole

From section 4.3, the torque ripple is greatly reduced with eccentric rotor pole, as a significant reduction in high speed airgap harmonics is realized. Since flux harmonics is also a major source for iron loss, introduction of eccentric rotor pole suggests an alleviation in iron loss production. The iron loss, P_{ir} map of six pole eccentric rotor pole machine is plotted in figure 5.32. Compare with P_{ir} of normal rotor pole in figure 5.31 (b), a significant reduction is presented in both motoring and generating mode. At 5 kW, iron loss reduction in field weakening region increase from 20% at based speed up to 65% at high speed.

The efficiency versus speed, ω and mechanical power, P_{mech} of the eccentric rotor pole machine is plotted in figure 5.33. Compared with the normal rotor efficiency map in figure 5.29 (b), the efficiency of eccentric rotor machine is slightly lower below base speed as a result of a higher copper loss from eccentric rotor winding. However, with increasing speed, the reduction in iron loss outweighs the increase in copper loss. The efficiency of eccentric rotor machine quickly surpasses normal rotor machine, and the difference increases with the speed. At 5 kW motoring

mode, the efficiency of the eccentric rotor machine is about 1% lower at 1000 rpm, 0.5% lower at 2000 rpm, 2.57% higher at 6000 rpm, and 4.96% at 10000 rpm. A similar trend is observed in generating mode, where the efficiency of two rotor types intersects at 3000 rpm. The eccentric rotor pole efficiency is about 3.6% higher at 6000 rpm, and 7.7% higher at 10000 rpm.

For peak efficiency, a 92.6% efficiency is reached in motoring mode, and a 92.2% efficiency is achieved, both at 2 kW and 6000 rpm.

5.3.3 Effect of Steel Lamination

The previous section shows that the eccentric rotor pole greatly reduces iron loss on the machine. However, in the field weakening region the iron loss still accounts for a large proportion of the total loss, hampering the achievement of a higher efficiency. To further reduce iron loss, lamination steel with thinner sheet thickness is applied. In this research, M300-35A is applied in comparison with M400-50A on the six pole machine with eccentric rotor pole. Following the curve fitting procedure for iron loss coefficients of Bertotti loss model (1.20) in section 1.2.4, the coefficients for M300-35A are listed in table 5.1:

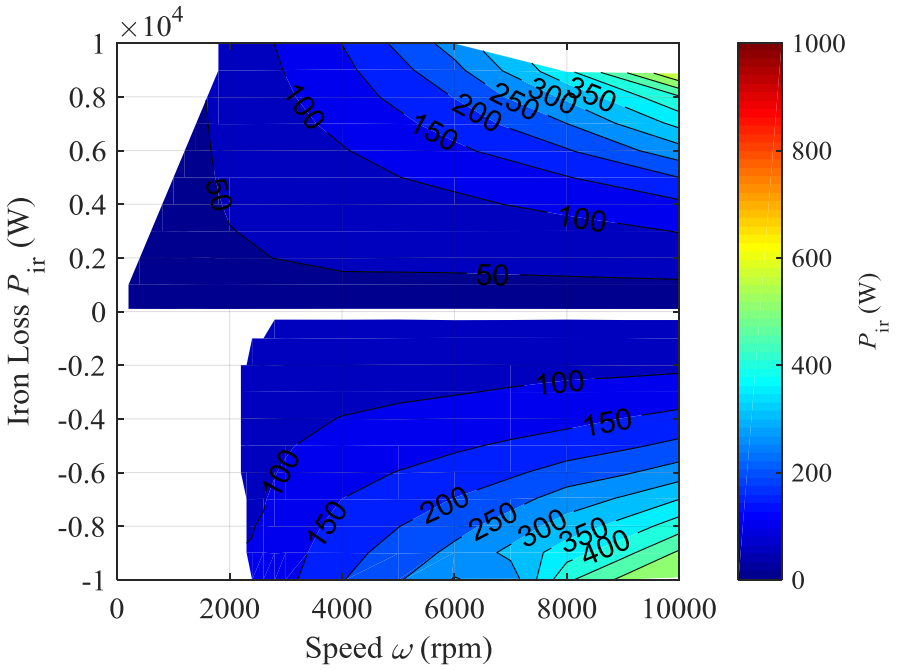

Figure 5.32. Iron loss, P_{ir}, map vs. speed ω and mechanical power, P_{mech} of a geometry optimized six pole wound rotor synchronous machine with eccentric rotor pole.

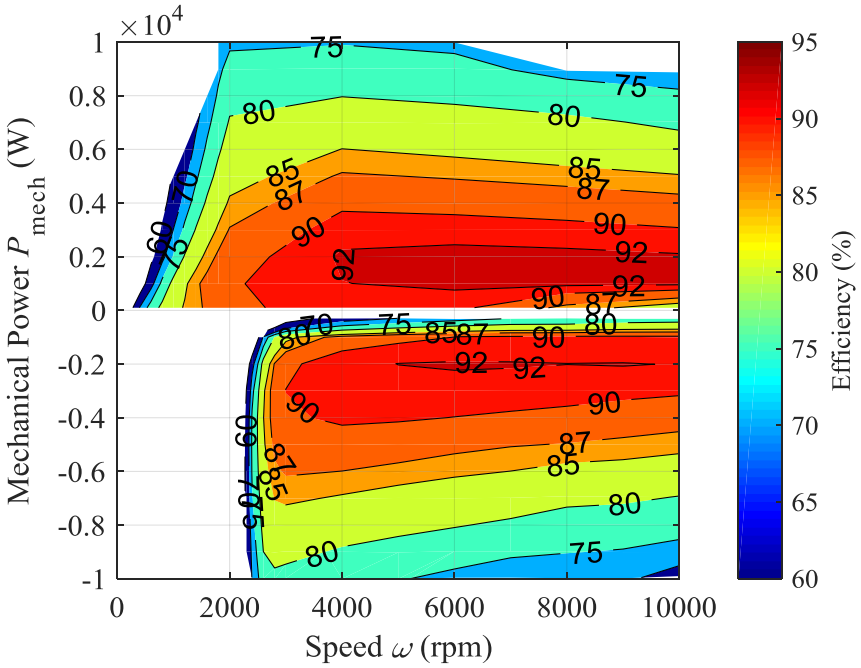

Figure 5.33. Efficiency map vs. speed, ω and mechanical power, P_{mech} of a geometry optimized six pole wound rotor synchronous machine with eccentric rotor pole.

Name of coefficient	Symbol	Value (Unit)
Hysteresis coefficient	k_h	128.0 ($WsT^{-2}m^{-3}$)
Conductivity	σ	2000000 (S/m)
Excess loss coefficient	k_e	0.376 ($W(Ts^{-1})^{-3/2}m^{-3}$)
Power of peak flux density in hysteresis loss	α	2.214

Table 5.1. Bertotti loss coefficients of M300-35A in (1.20).

The efficiency map versus speed, ω and mechanical power, P_{mech} for both motoring and generating mode is illustrated below in figure 5.34. The iron loss, P_{ir} map versus ω and P_{mech} is plotted in figure 5.35. Compared with the M400-50A, implementation of M300-35A lamination cuts iron loss by 35-55%. The reduction in iron loss increases the overall efficiency of machine, and helps to maintain a high efficiency at high speed. With M300-35A lamination material, the peak efficiency of the machine increases to about 95% at 1kW and 9000 rpm in both motoring and generating mode. At rated P_{mech} of 5 kW, the efficiency is between 88% and 90% in generating mode and 84% to 88% in motoring mode under field weakening operation.

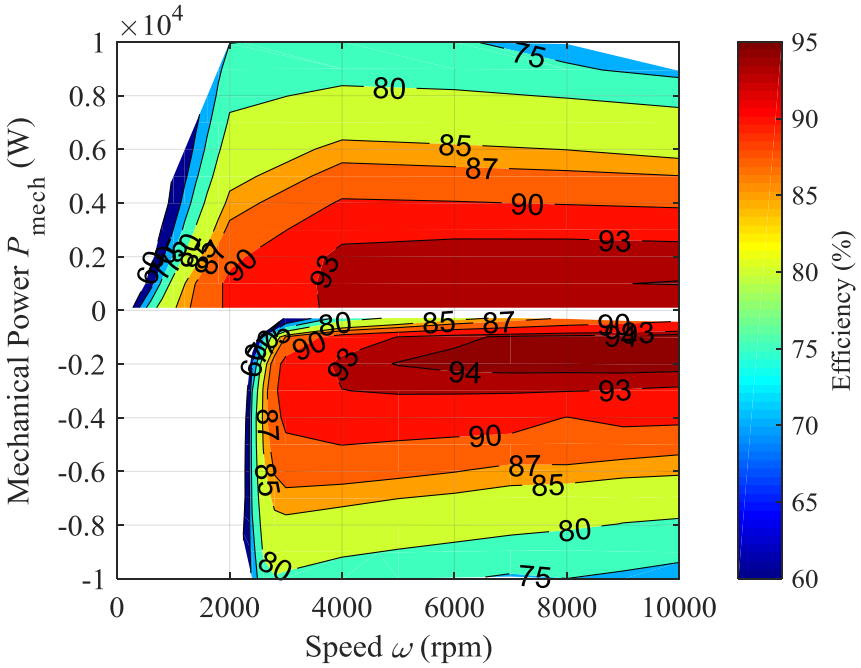

Figure 5.34. Efficiency map vs. speed, ω and mechanical power, P_{mech} of a geometry optimized six pole wound rotor synchronous machine with eccentric rotor pole and lamination material of M300-35A.

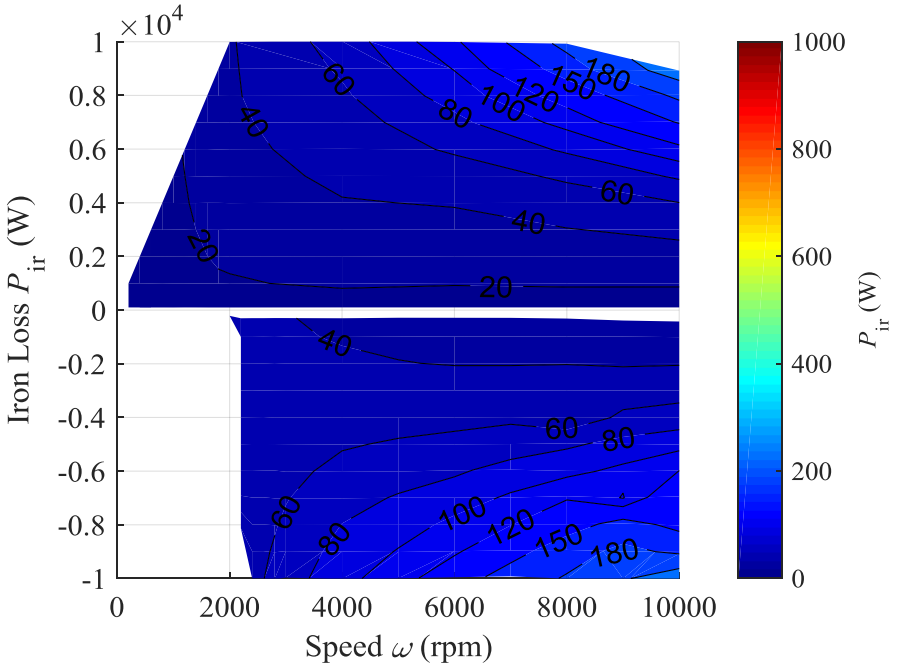

Figure 5.35. Iron loss, P_{ir}, map vs. speed, ω and mechanical power, P_{mech} of a geometry optimized six pole wound rotor synchronous machine with eccentric rotor pole and lamination material of M300-35A.

5.3.4 Operation over New European Driving Cycle

From the efficiency maps of the WRSM and the benchmark SRM shown in figure 1.15, the

wound rotor synchronous machine provides an overall better efficiency performance than the benchmark Speedstart switched reluctance machine. However, to prove the total loss of the WRSM is lower in the specific B-ISG application and operating condition, both machines needs to be simulated through a provided driving cycle.

The machines are simulated on a hybrid electric vehicle and tested in the New European Driving Cycle (NEDC), where the vehicle speed is plotted against time in figure 5.36.

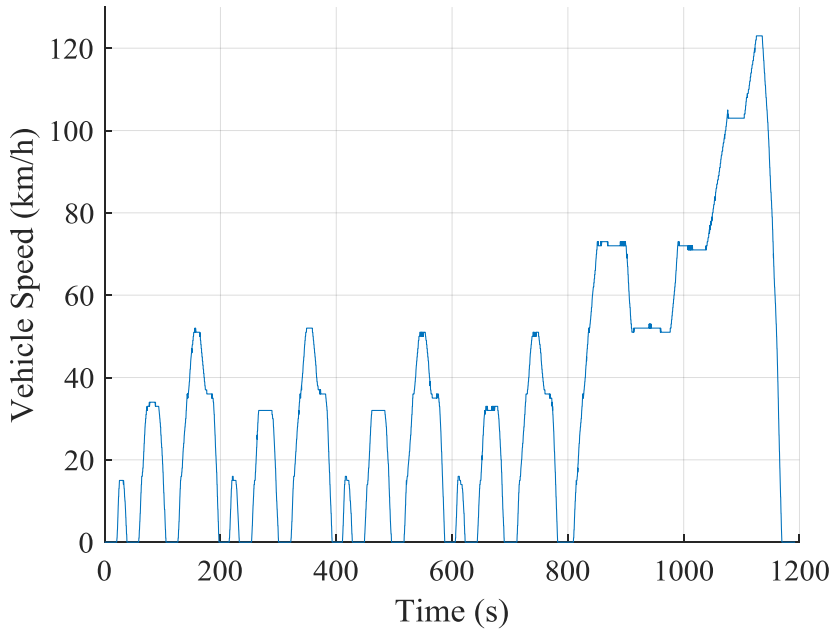

Figure 5.36. The New European Driving Cycle (NEDC).

The electrical machine operational speed, ω over time is plotted in figure 5.37. Its mechanical power, P_{mech} in both motoring and generating mode is shown in figure 5.38.

Under NEDC, the Speedstart operational points are plotted on the efficiency map in figure 5.39.

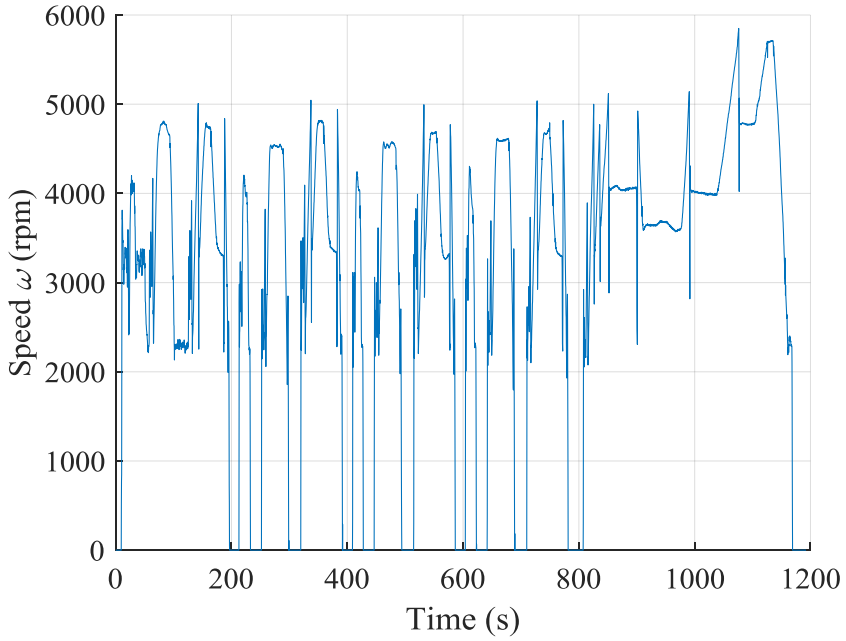

Figure 5.37. The electrical machine speed, ω, vs. time under NEDC.

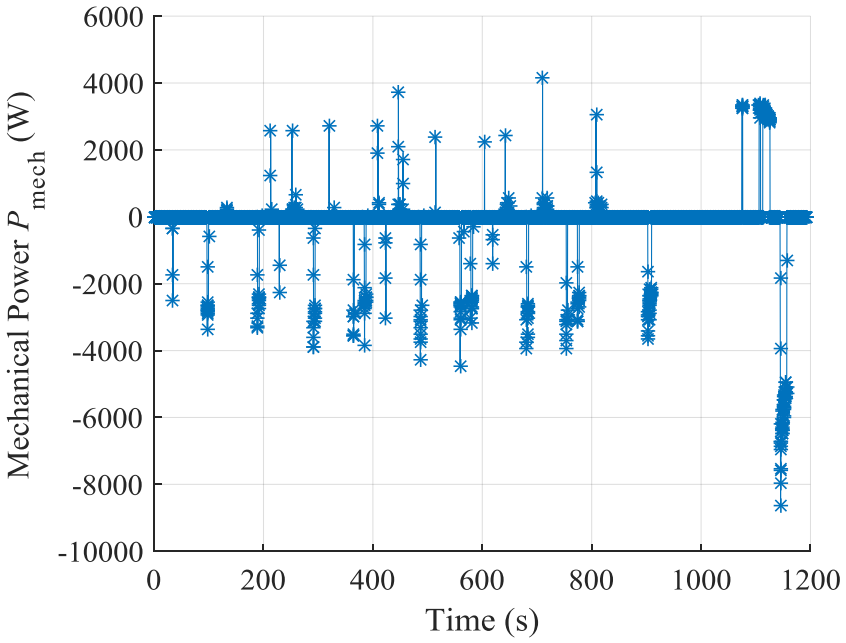

Figure 5.38. The electrical machine mechanical powe,r P_{mech}, vs. time under NEDC.

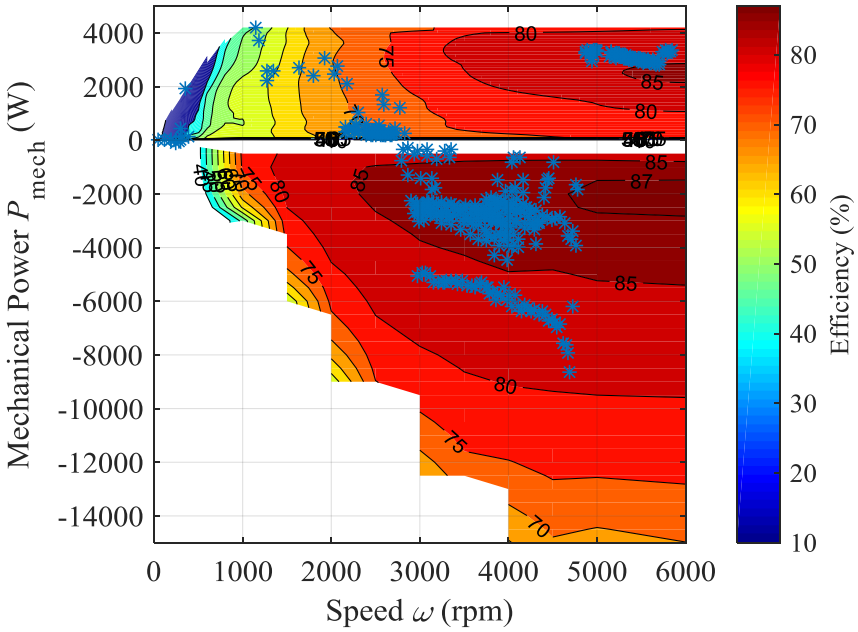

Figure 5.39. The Speedstart classical switched reluctance machine operaitonal points under NEDC on the efficiency map of mechanical power, P_{mech} vs. speed ω.

Figure 5.40 shows the instantaneous loss comparisons between the Speedstart SRM and the optimized six pole wound rotor synchronous machine with eccentric rotor pole over one driving cycle. Both machines use M400-50A lamination. The WRSM has a stator fill factor, c_s of 0.3 and a rotor fill factor, c_r of 0.4. With proper manufacturing process, a c_s of 0.4 and c_r of 0.6 is possible [171], therefore the resultant loss is plotted in comparison. The M300-35A lamination material is also implemented and plotted in figure 5.41 for comparison. The total losses from figure 5.40 and 5.41 and their efficiencies are summarised in table 5.2.

From the figures and table, the benchmark Speedstart CSRM has an overall efficiency of 84.1% over the driving cycle. The WRSM produces much lower loss than Speedstart CSRM under almost all working conditions. With a c_s of 0.3 and c_r of 0.4, a 38.9% of decrease in total loss is achieved, increasing the efficiency to 89.2%. With a c_s of 0.4 and c_r of 0.6, a further loss reduction of 23.3% is realized, and the efficiency is 91.5%. Since the machine speed does not exceed 6000 rpm in the driving cycle, the implementation of M300-35A lamination on loss reduction is not as manifest as expected. Compared with M400-50A, the loss is decreased by 12.6% with a c_s of 0.3 and a c_r of 0.4, and 16.0% with a c_s of 0.4 and a c_r of 0.6. The efficiencies

are 90.5% and 92.9%, respectively.

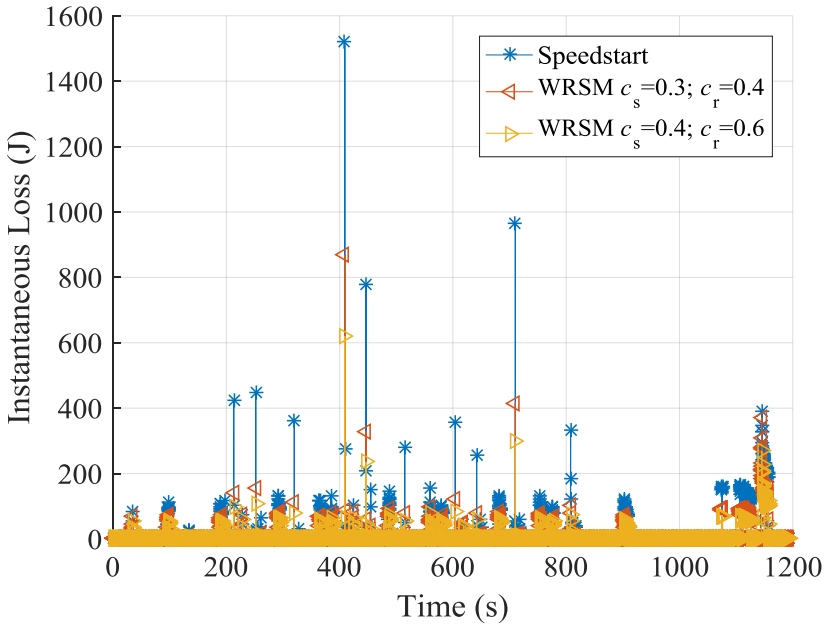

Figure 5.40. The instantaneous loss comparison under NEDC vs. time of Speedstart classical switched reluctance machine; the WRSM with a stator fill factor, c_s of 0.3 and rotor fill factor, c_r of 0.4; the WRSM with a stator fill factor, c_s of 0.4 and rotor fill factor, c_r of 0.6. Lamination material is M400-50A.

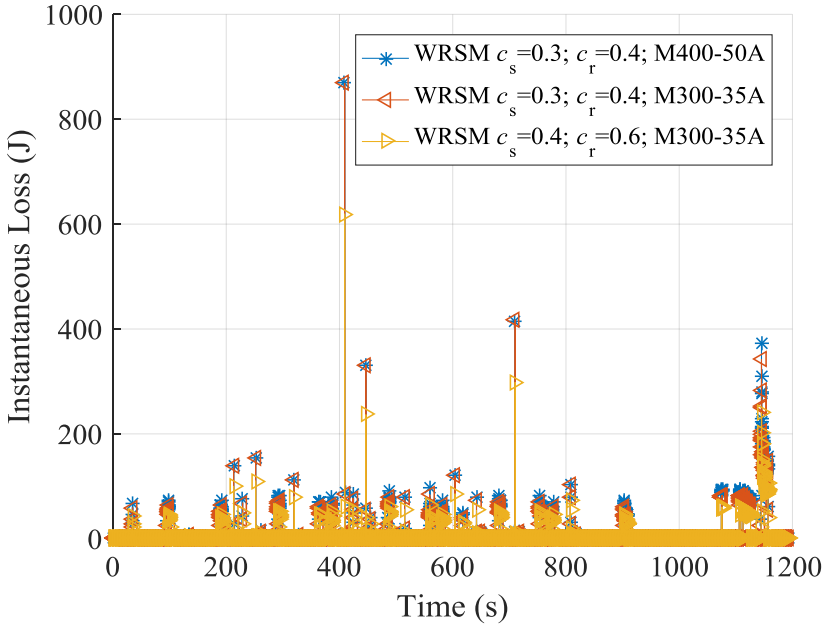

Figure 5.41. The instananuou loss comparison under NEDC vs. time of the WRSM with stator fill factor, c_s of 0.3, rotor fill factor, c_r of 0.4 and M400-50A lamination material; the WRSM with a stator fill factor, c_s of 0.3, rotor fill factor, c_r of 0.4 and M300-35A lamination material; the WRSM with a stator fill factor, c_s of 0.4, rotor fill factor, c_r of 0.6 and M300-35A lamination material.

Stator fill factor c_s	Rotor fill factor c_r	Material	Loss P_l (J)	Efficiency (%)
Speedstart		M400-50A	46760.7	84.1
0.3	0.4	M400-50A	28547.7	89.2
0.4	0.6	M400-50A	22186.5	91.5
0.3	0.4	M300-35A	24944.0	90.5
0.4	0.6	M300-35A	18632.5	92.9

Table 5.2. Total loss, P_l, under NEDC of Speedstart classical switched reluctance machine, the WRSM with different winding fill factor and lamination material.

5.4 Summary

In this chapter, the operation of WRSM is investigated where the contribution to literature is listed as follows. First, a novel look-up table interpolation algorithm for determination of minimum loss copper operation criterion is proposed and compared against the existing Lagrangian method. Second, the impact of iron loss on minimum loss operation is evaluated. Last, a comparative study between the proposed WRSM and the benchmark Speedstart SRM on the B-ISG application over NEDC is conducted in simulation.

From this study, the following conclusions are drawn:

(1) Compared with the Lagrange method, the proposed LUT interpolation method provides a much more accurate result with less computation time.

(2) At low power and high speeds, iron loss contributes a large proportion of the total loss. Compared with the copper loss optimisation method, the total loss optimisation method including iron loss does not show a significant improvement because the reduction in iron loss is offset by a similar increase in copper loss.

(3) Compared with the four pole machine, the six pole machine produces lower copper loss and higher iron loss. Since iron loss is generally lower than copper loss in this application, the six pole machine has a higher efficiency under the majority of operating conditions.

(4) Compared with the normal rotor pole surface, an eccentric rotor pole greatly reduces cogging torque and torque ripple with a small sacrifice in average torque. An eccentric

rotor reduces harmonics in the open circuit airgap flux, allowing a decrease in the harmonics of the back-EMF and the phase voltage. Since flux harmonic induces iron loss, a significantly lower iron loss is observed when using an eccentric rotor pole machine.

(5) If a substitution of M400-50A lamination for M300-35A is made, a further reduction of iron loss is observed, allowing a higher machine efficiency.

(6) Compared with the benchmark Speedstart classical switched reluctance machine, the six pole wound rotor machine produces much lower loss across one NEDC, so the efficiency is significantly increased. This loss can be further reduced by increasing coil fill factor and utilisation of low loss lamination material.

6. Multi-physics Simulation and Experimental Validation of Wound Rotor Synchronous Machine for Starter-Generator Application

In this chapter, the six pole wound rotor synchronous machine for an B-ISG application is built and tested. The machine has an eccentric rotor pole as described in section 4.3, and its geometrical parameters are listed in table 4.2. A lamination steel of M300-35A is applied on both stator and rotor. To remove the heat from the machine, a water cooling mechanism is deployed, where water with added coolant is pumped into a specially made machine case. An overall schematic diagram of the wound rotor synchronous machine and water cooling system is shown in figure 6.1.

To ensure a safe operation of ISG, several aspects need to be considered. The first is thermal management, where the water cooling system greatly enhances the heat conduction, and effectively increases the machine's power and torque ability. However, to estimate the temperature of the windings, and to ensure the maximum temperature is not exceeded the limitation of insulation, temperature distribution inside the machine and their change versus time is required. The second aspect is mechanical strength. During operation, forces are imposed on both lamination and rotor windings, resulting in stresses on the different machine parts. If the stress exceeds material's bearing capacity, fatigue and even failure will occur. To make sure the machine is operated under safe condition, stress distribution in machine is required.

There are three sections in this chapter. In the first section, mechanical stress of the machine is evaluated, based on which the maximum safe operational speed is determined. In the second section, thermal simulation of the machine is applied, where a water cooling jacket is designed. In the third section, a prototype WRSM is built and tested on a dynamometer. The experimental platform and equipment are introduced. Then the experimental results are compared with simulation, and the machine's performance is validated.

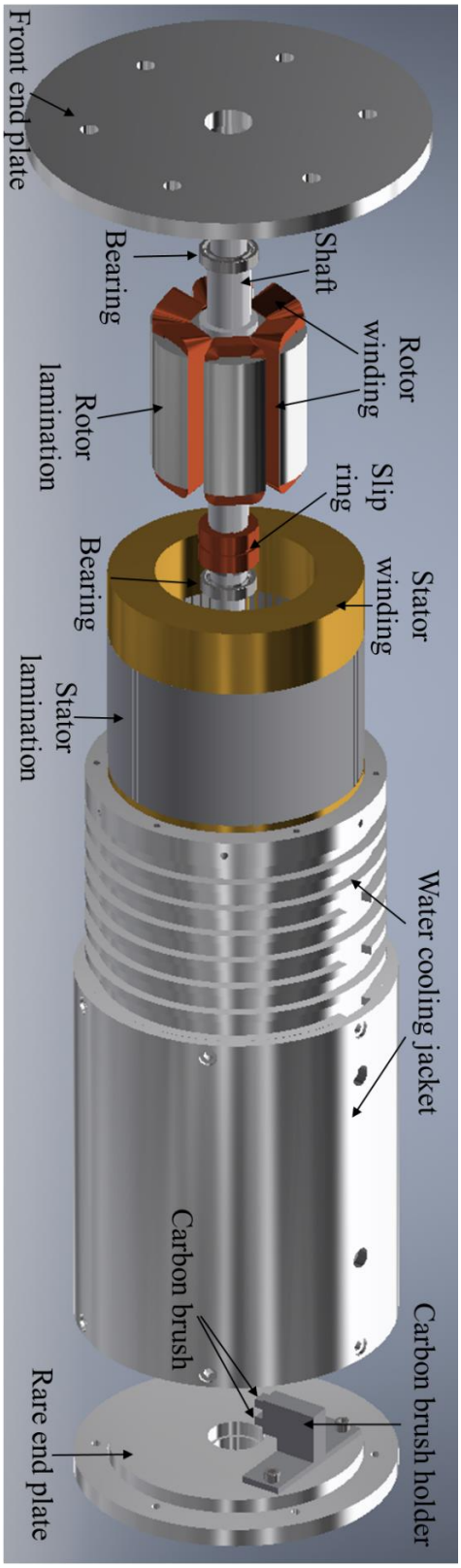

Figure 6.1. An overall schematic diagram of the wound rotor synchronous machine and water cooling system.

6.1 Stress Analysis

In this section, stress analysis of the machine is simulated using Autodesk Inventor Professional 2017. Based on the simulation results, a maximum safety operational speed is determined.

In Autodesk Inventor, a 3D finite element model of stator and rotor is constructed and meshed, the geometry model of stator and rotor and meshing are shown below in figure 6.2. From manufacturing datasheet, the mechanical properties of M300-35A material are listed in table 6.1 [172].

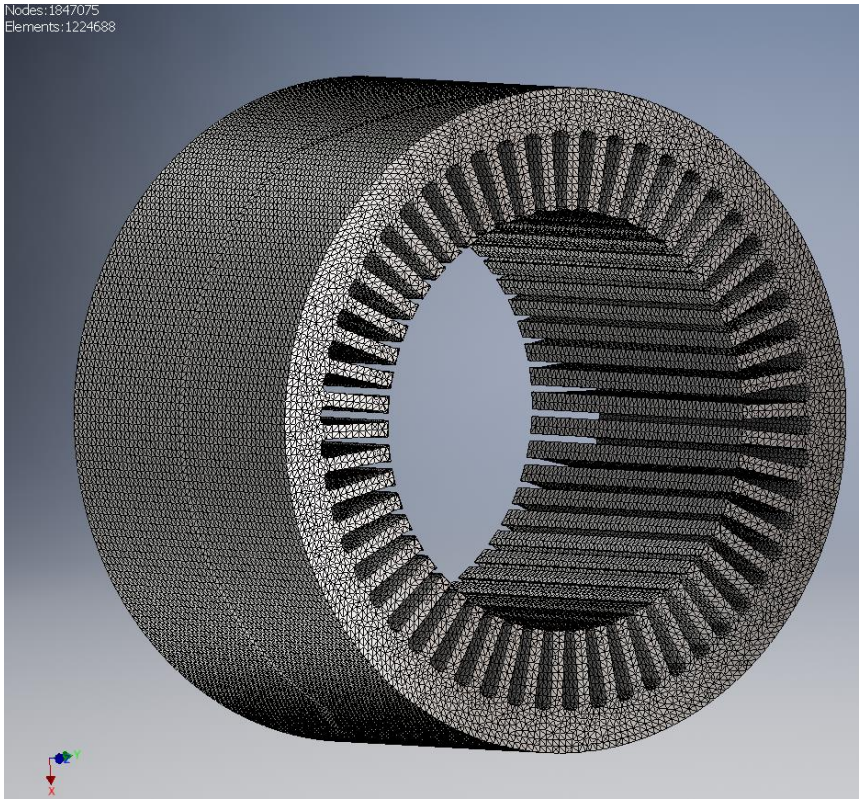

(a)

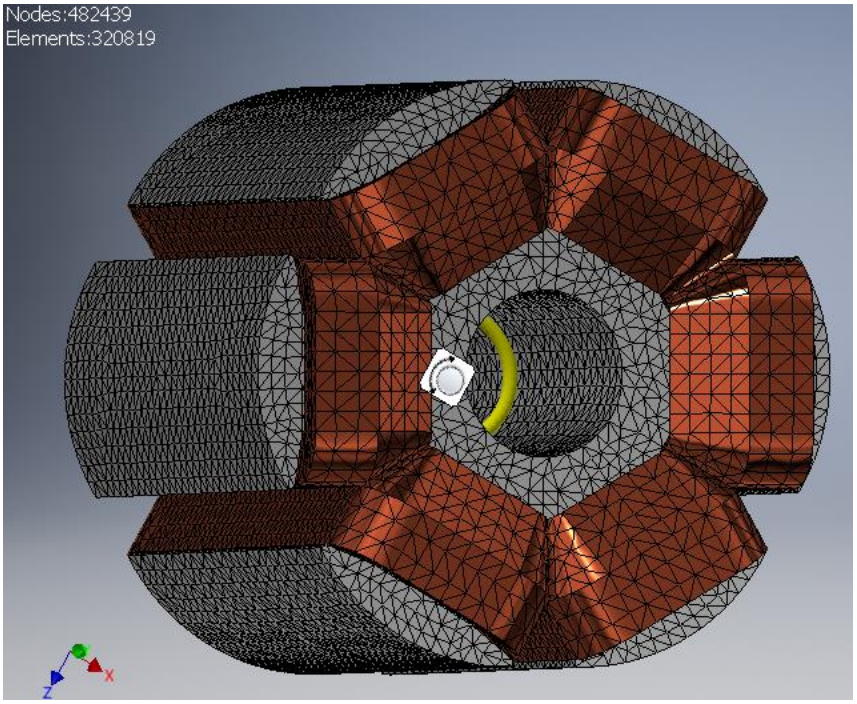

(b)

Figure 6.2. A 3D finite element analysis model with mesh of a wound rotor synchrouous machine (a) stator and (b)rotor with winding , in Autodest Inventor Profssional 2017.

Item	Value	
Density	7.65 kg/dm^2	
Young's Modulus *E*	Rolling direction	Transverse direction
	185000 N/mm^2	200000 N/mm^2
Poisson Ratio *v*	0.3	
Shear Modulus *G*	71154 N/mm^2	
Yield Strength	370 N/mm^2	
Tensile Strength	490 N/mm^2	

Table 6.1. Mechanical properties of M300-35A lamination material.

The stresses on the machine come from two sources. The first is electromagnetic force. This force is mainly imposed to stator and rotor teeth near airgap, which can be estimated by applying Maxwell tensor method on airgap flux distribution. In 2D analysis and cylindrical coordinate, Maxwell tensor method shows the relationship between normal stress σ_n, tangential stress $\sigma_{\tan}$, normal magnetic field strength H_n and tangential magnetic strength $H_{\tan}$ are:

$$\sigma_n = \frac{1}{2}\mu_0\left(H_n^2 - H_{\tan}^2\right) \tag{6.1}$$

$$\sigma_{\tan} = \mu_0 H_n H_{\tan} \tag{6.2}$$

The second source is the centrifugal force from rotation. In rotating motion, the relationship between radius r, mass m, rotation angular velocity ω, linear velocity v and centrifugal force F_c is:

$$F_c = \frac{mv^2}{r} = m\omega^2 r \tag{6.3}$$

Centrifugal force grows proportionally with speed square. Since the rotor windings are fixed on rotor by rotor pole shoes, the forces as a function of speed needs to be inspected to ensure that the pole shoes are strong enough to withstand the forces from the copper wires and its own mass.

6.1.1 Electromagnetic Stress

To estimate the stress from electromagnetic force, several assumptions are made.

(1) The force on each stator or rotor teeth is uniformly distributed on the teeth airgap surface;
(2) The internal stress caused by uneven distribution of flux on each teeth is neglected;
(3) The airgap is evenly divided into small intervals centered by points, and stress calculated from Maxwell tensor method at each point is considered the average stress on that interval.
(4) End effect is neglected.
(5) No rotation is involved.

To evaluate the worst case, a maximum torque of 45.2 Nm is implemented. The airgap is evenly divided into 360 intervals. At the position where rotor pole is fully aligned with phase-A, normal force F_{nor} and tangential force $F_{\tan}$ on each interval is shown in figure 6.3.

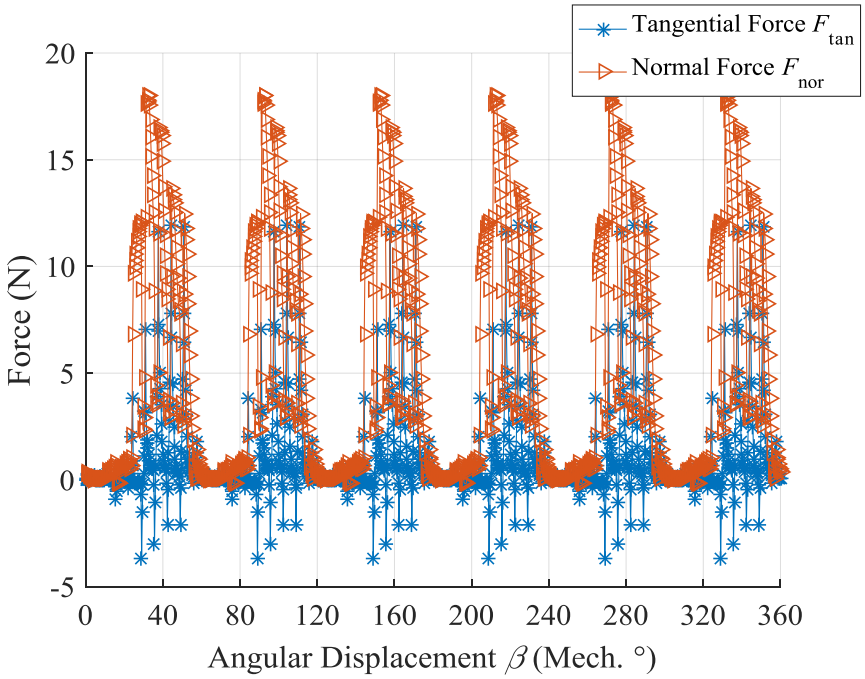

Figure 6.3. Normal force, F_{nor}, and tangential force, F_{tan}, on intervals vs. angular displacement, β, in the airgap of the wound rotor synchronous machine

The total tangential force is 1058.6 N and total normal force is 5538.3 N. On rotor side, the normal and tangential force on each pole is derived by a simply division of total force, where the tangential force is 176.4 N and the normal force is 923.0 N per pole. On stator side, however, since total force is not evenly distributed on teeth, the force is calculated separately for each tooth from figure 6.3.

From FE analysis, the Von Mises stress distribution on stator and rotor are illustrated in figure 6.4. The force is evenly distributed along the axial direction, where the maximum stress on stator and rotor are 10.01 MPa and 4.9 MPa, respectively. Compared with the lamination yield strength of 370 MPa, the stress from electromagnetic force is trivial.

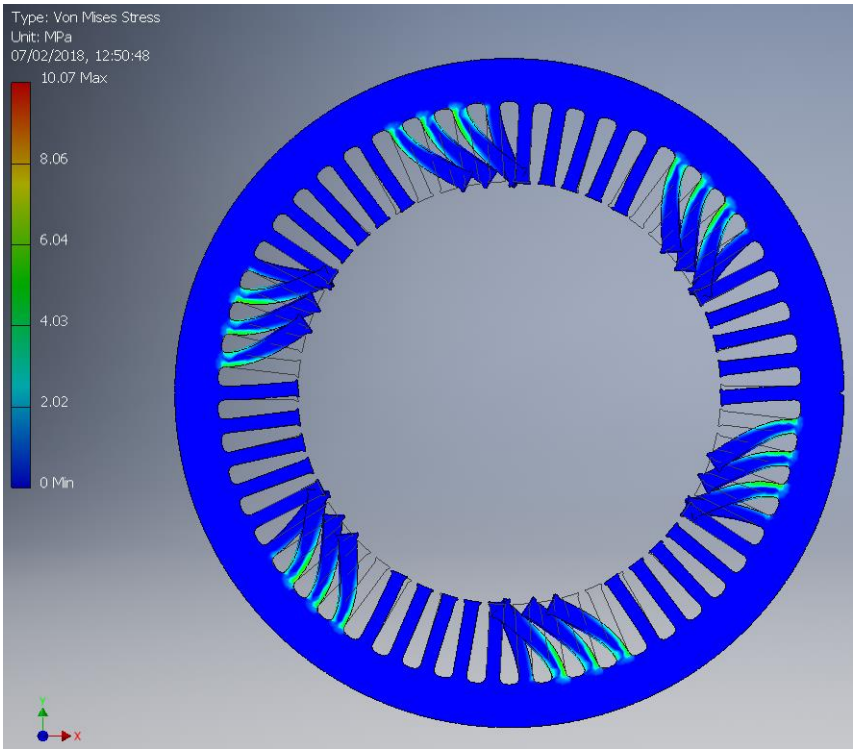

(a)

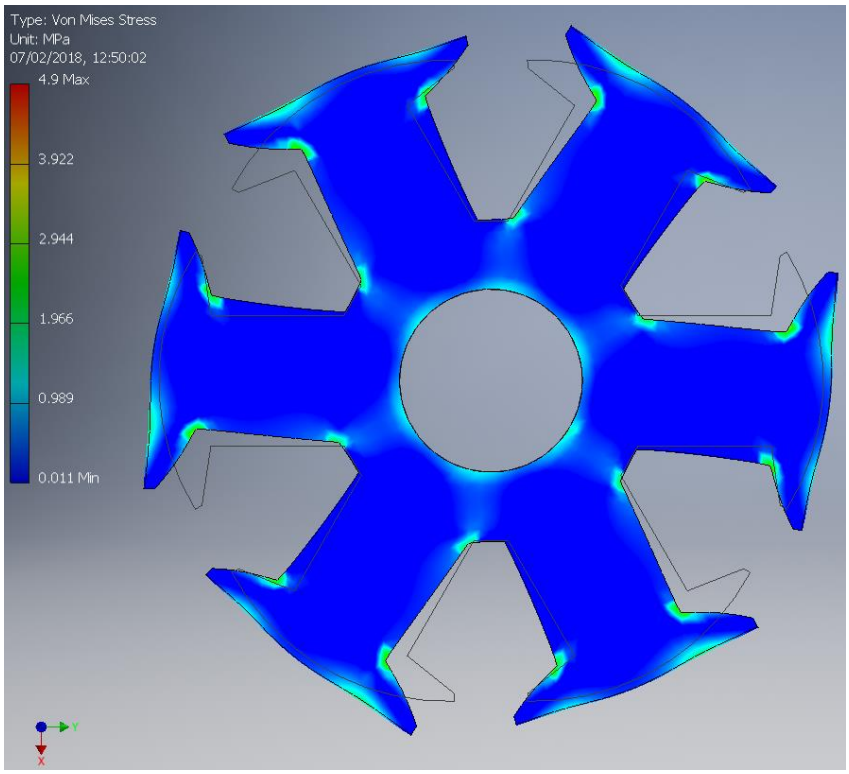

(b)

Figure 6.4. Von Mises stress distribution of (a) stator and (b) rotor from electromagnetic force at torque of 45.2 Nm.

6.1.2 Centrifugal Stress

Since the stress caused by electromagnetic force is generally small and reduces as the speed increase, it is neglected in the study of centrifugal force. The weight of rotor coil is calculated from the length and weight of the wire applied. The mechanical property of the wires is determined by the wire stopper made from fiberglass epoxy resin.

At 10000 rpm, the Von Mises stress distribution on rotor and one coil are displayed in figure 6.5. Unlike electromagnetic force, the stress caused by centrifugal force on rotor is not evenly distributed in axial direction. Instead, the stress significantly increases as it approaches both ends. Similarly, on the coil side the stress concentrates on a small area near both ends. This is caused by the extra weight of the end winding, which bends the coil under centrifugal force, causing the coils and rotor only contacts in a small area. Compared with evenly distributed force, this phenomenon increases local Von Mises stress.

The maximum Von Mises stress, σ_{VM} versus speed, ω for both rotor and coil are plotted in figure 6.6. The maximum Von Mises stress increases with speed, and the local stress on rotor is higher than the coil. However, since different materials have different stress endurance properties, to evaluate the stress capability of different material, the concept of safety factor is introduced as:

$$Safety\_factor = \frac{maximum\_Von\_Mises\_stress}{yield\_strength} \tag{6.4}$$

The safety factor versus speed, ω is plotted in figure 6.7. From the figure, safety factors on rotor and rotor coil are similar, which gradually approach one as speed increases to 20000 rpm. Previous studies suggested a safety factor of 2.7 [173, 174]. To guarantee a safe operation under harsh environments, for this rotor geometry, a safety factor of three should be maintained. The maximum operational speed is therefore 11,000 rpm.

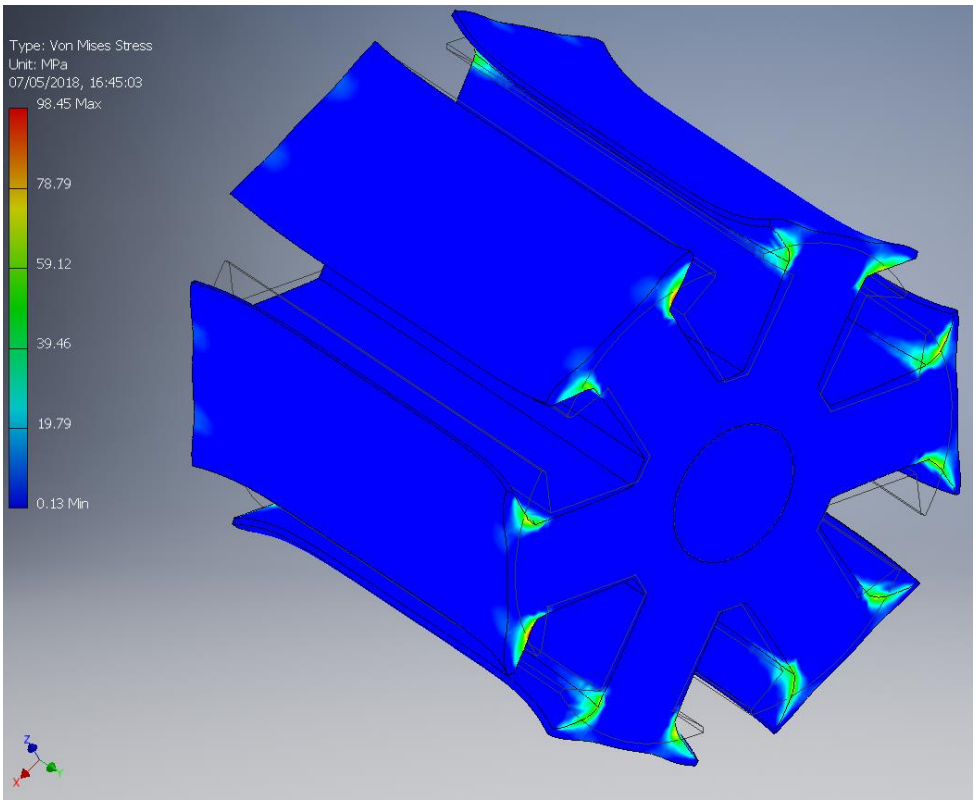

(a)

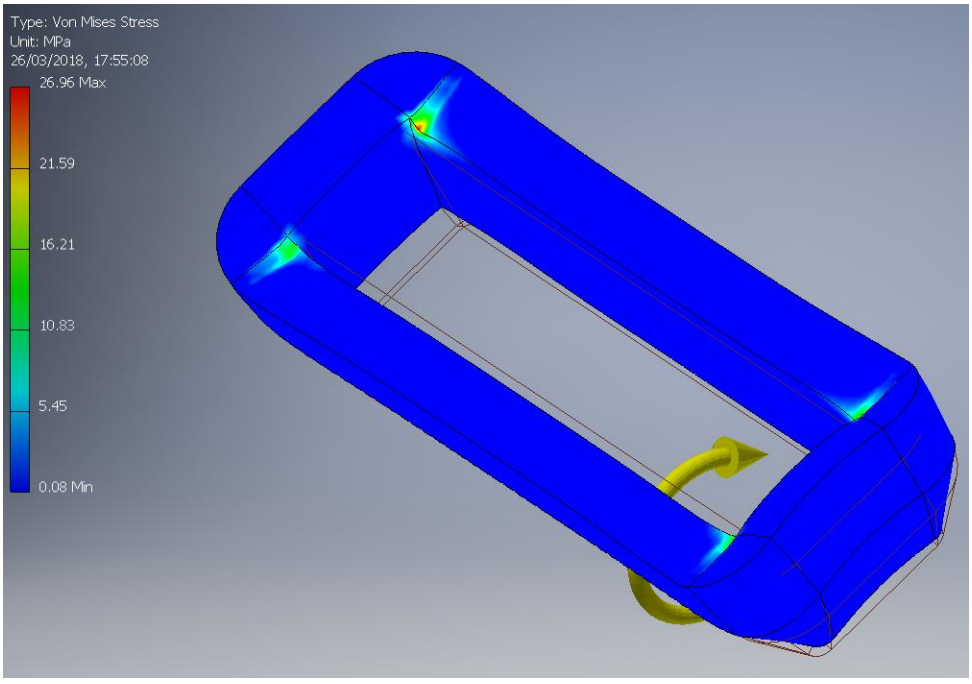

(b)

Figure 6.5. Von Mises stress distribution of (a) stator and (b) rotor from centrigugal force at 10000 rpm.

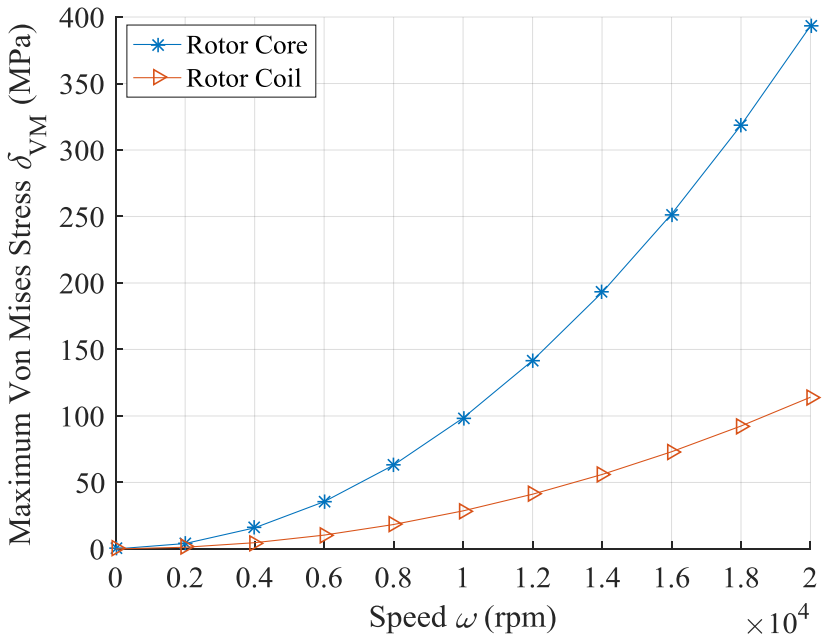

Figure 6.6. Maximum Von Mises stress, σ_{VM}, vs. speed, ω, on both rotor and rotor coil.

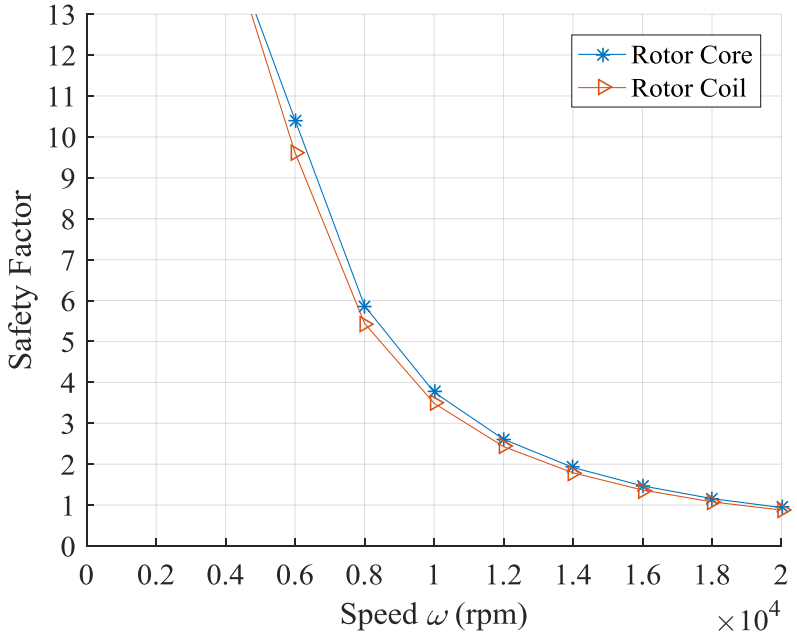

Figure 6.7. Safety factor vs. speed, ω, on both rotor and rotor coil.

6.2 Thermal Consideration

In this section, a water cooling case is designed, where the machine's maximum operation capability within thermal limits is investigated.

The losses from stator and rotor are simulated using the proposed algorithm in Chapter 5. Free from permanent magnets, the maximum allowable temperature is determined by the temperature endurance of winding insulation. As a result, the temperature distribution and maximum temperature on both stator and rotor windings are emphasized.

For thermal modelling, Motor-CAD provides a powerful tool using 3D lumped circuit model to calculate the steady state and transient thermal characteristics of machine and cooling jacket. In this study, Motor-CAD v10.3.10 is applied, where the radial and axial diagram of the machine and cooling system are illustrated in figure 6.9.

The water cooling jacket is made of Aluminium for its ideal thermal and mechanical properties. To enhance thermal conductivity between wires and prevent wire erosion, varnish is applied on winding coils. The materials applied and their thermal properties are either imported from the Motor-CAD library or determined from previous literature as shown below in table 6.2.

Part name	Material	Thermal Conductivity (W/m/°C)	Specific Heat (J/kg/°C)
Water cooling jacket	Aluminium(Cast)	180	963
Winding	Copper	401	385
Winding insulation	Polyamide-imide	0.26	1246
Slot liner		0.13	
Impregnation	Varnish	0.44	1435
Lamination	M300-35A	30	460
Shaft	Shaft steel	25	450
Wedge	Epoxy	0.22	1500

Table 6.2. Materials applied in machine and their thermal properties [175-178].

6.2.1 Water Cooling Jacket Design

The structure of water cooling jacket is illustrated in Autodesk Inventor as shown in figure 6.1. The case consists of two coaxial hollow cylindrical parts. The outer diameter of inner cylinder is slightly smaller than inner diameter of the outer one. The inner cylinder has water trench on the surface, and the dimensions of the trenches are shown in figure 6.8. The outer cylinder has

two holes for water inlet and outlet, where the tube fittings are mounted. To prevent water leakage, rubber seals are applied between cylinders on both ends. Bolts are also fitted to prevent the cylinders from moving.

According to simulation, the machine steady and transient state temperature are mainly influenced by coolant water temperature, ambient environment temperature and water flow rate. The size of water ducts and walls in the jacket do not directly affect cooling performance. However, the size and length of water trenches need to be chosen so that the required water flow rate is possible while being mindful of the available pressure drop. In the current hybrid electric vehicle system, typical coolant water temperature and ambient air temperature are both 90 °C. The water flowing rate is 1×10^{-4} m^3/s, and the available pressure drop on the water jacket is 4 kPa. With the design in figure 6.8, a water pressure drop of only 1.68 kPa is required to achieve the desired flow rate.

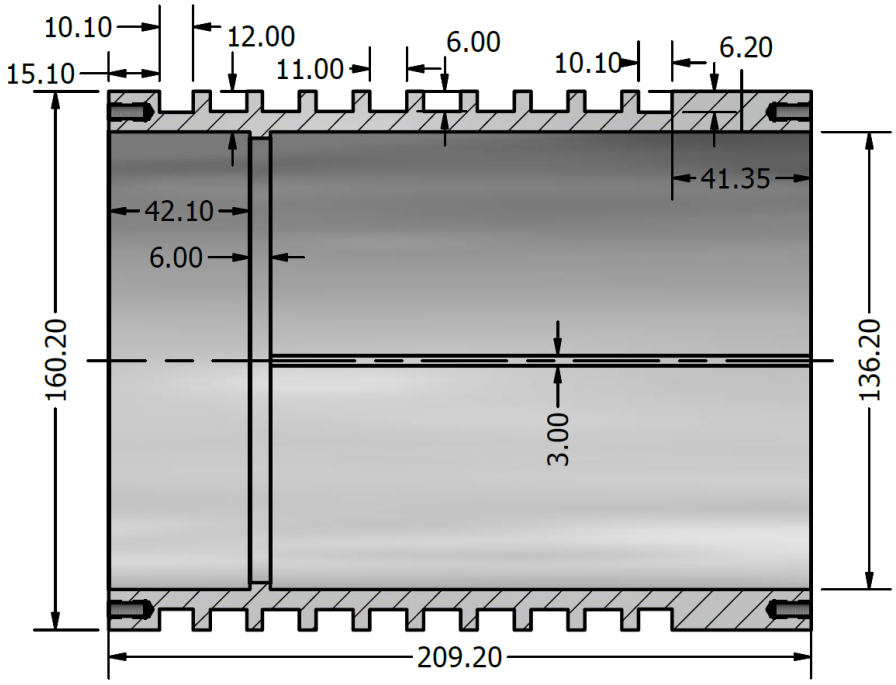

Figure 6.8. Trenches dimensions of the water cooling jacket applied in the ISG system (Unit mm).

6.2.2 Thermal Limitation

In motoring mode, a steady state thermal analysis is conducted at base speed, ω_b, of 2000 rpm and mechanical power, P_{mech}, of 5 kW. The machine's temperature at various positions are shown in figure 6.9. The rotor temperature distribution from FE analysis is illustrated in figure 6.10. Evidently, the highest temperature occurs in the centre of windings, where wound rotor shows a significant higher temperature than stator. On the rotor, the maximum temperature is 284 °C, compared with 173 °C on the stator. The rotor winding applied in this study is a class 200 polyester enamelled copper wire which compiles with IEC 60317-13. According to thermal testing method from IEC60172, this winding has a temperature index of 212 °C, so 284 °C will reduce its insulation life time to a few hundred hours [179].

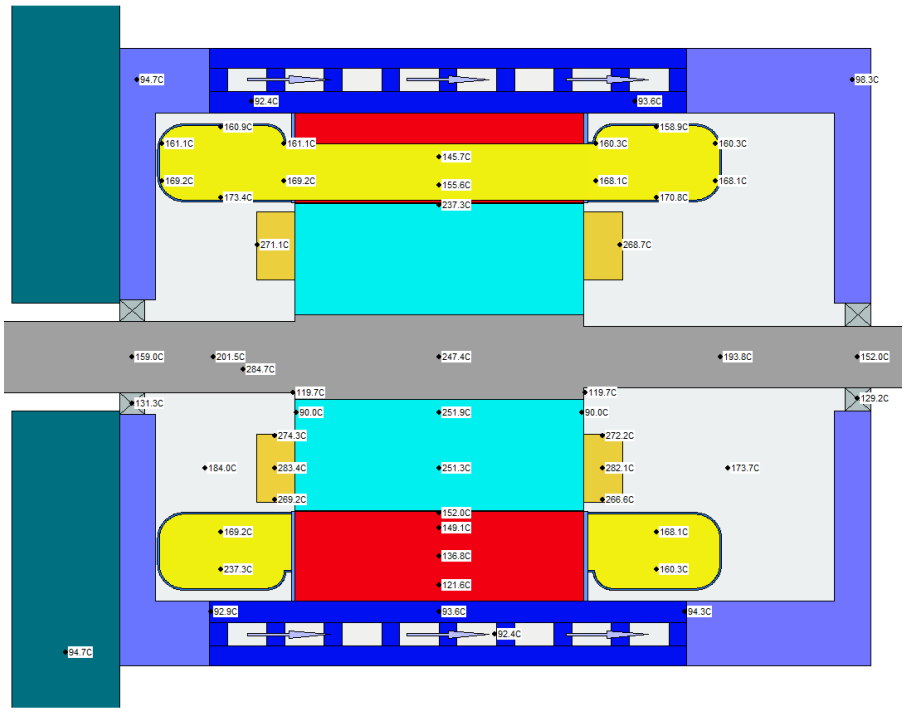

(a)

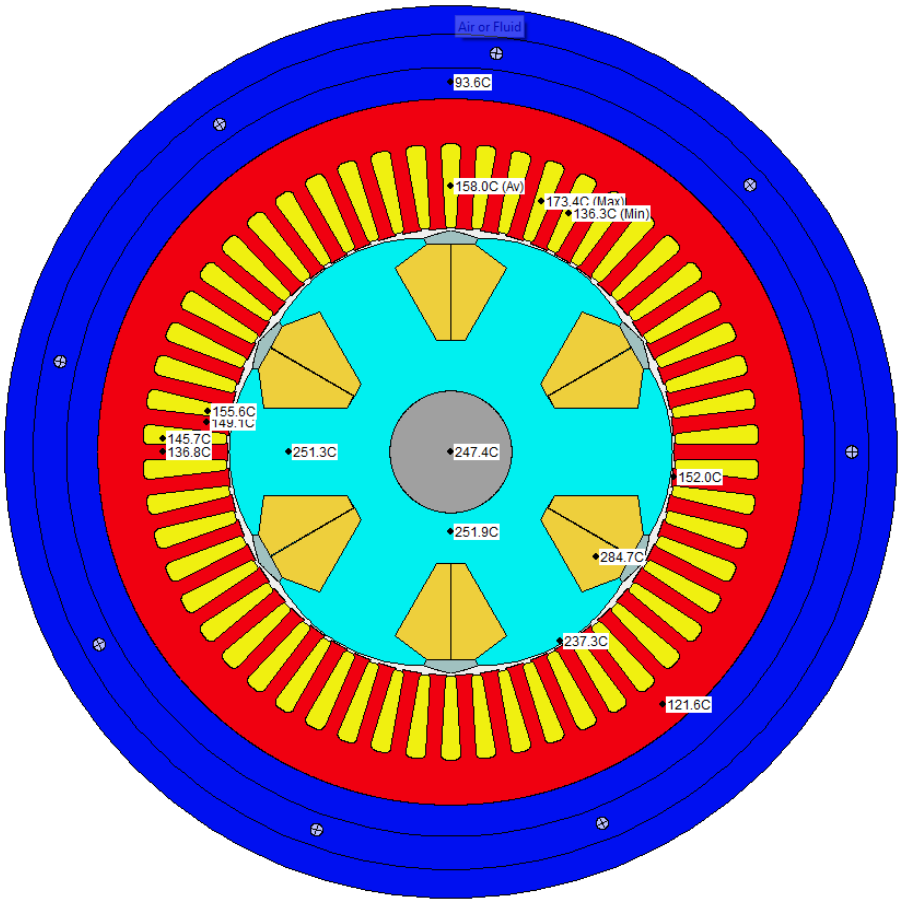

(b)

Figure 6.9. Steady state temperature of the wound rotor synchronous machine and water cooling jacket at mechanical power, P_{mech} of 5 kW and speed, ω of 2000 rpm under minimum loss operation in (a) radial direction and (b) axial direction.

From above analysis, the machine cannot run continuously at 5 kW and 2000 rpm while maintaining a safe temperature. To determine the maximum short term and continuous operational capability at 2000 rpm, a simple testing procedure is conducted. Starting at ambient temperature of 90 °C, losses at P_{mech} of 5 kW and 10 kW are applied on machine until the maximum winding temperature reach 200 °C, then a power reduction is deployed so that the maximum temperature maintains 200 °C. The new mechanical power is the maximum continuous mechanical power at 2000 rpm.

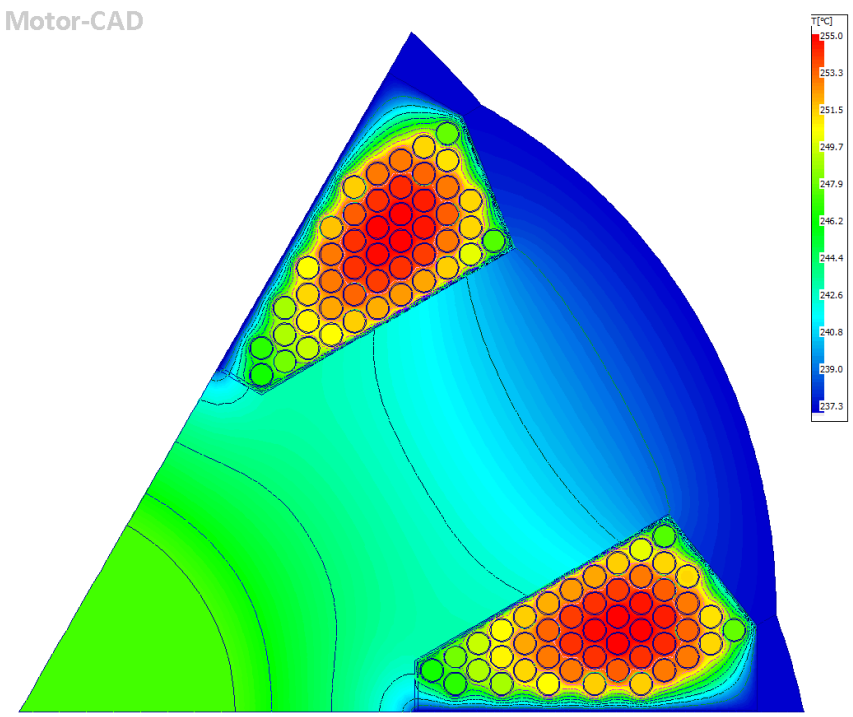

Figure 6.10. Steady state temperature distribution of wound rotor at mechanical power, P_{mech} of 5 kW and speed, ω of 2000 rpm under minimum loss operation.

Figure 6.11 plots the winding temperatures and mechanical power, P_{mech} versus time, where the maximum temperature on rotor coil is about 4 degrees higher than its average value. From the figure, the machine can run for 660 seconds at P_{mech} of 5 kW and 51 seconds at P_{mech} of 10 kW before reaching thermal limitation, and the maximum continuous output power is 3.8 kW. It is worth mentioning that, at 5 kW, rotor winding reaches temperature limit before stator winding, while at 10 kW it is reversed.

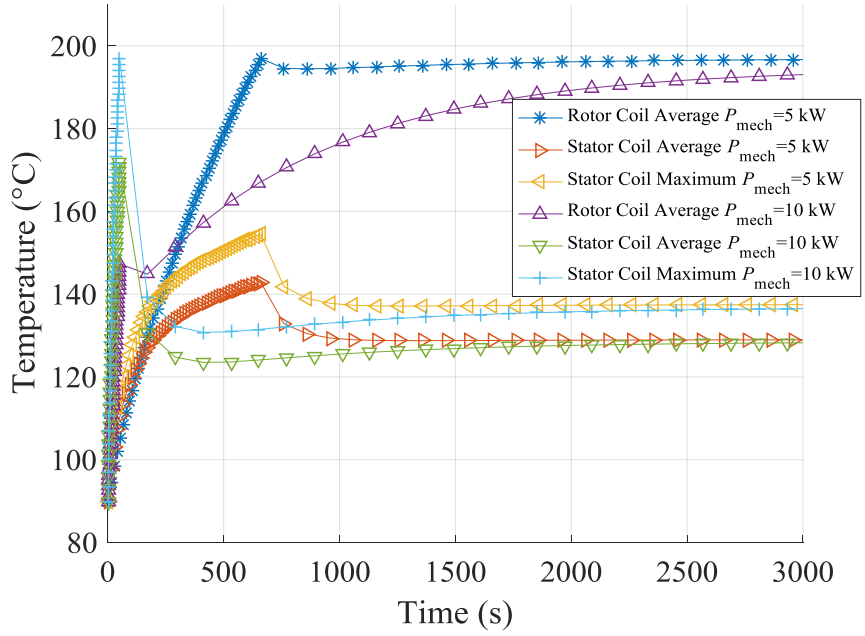

(a)

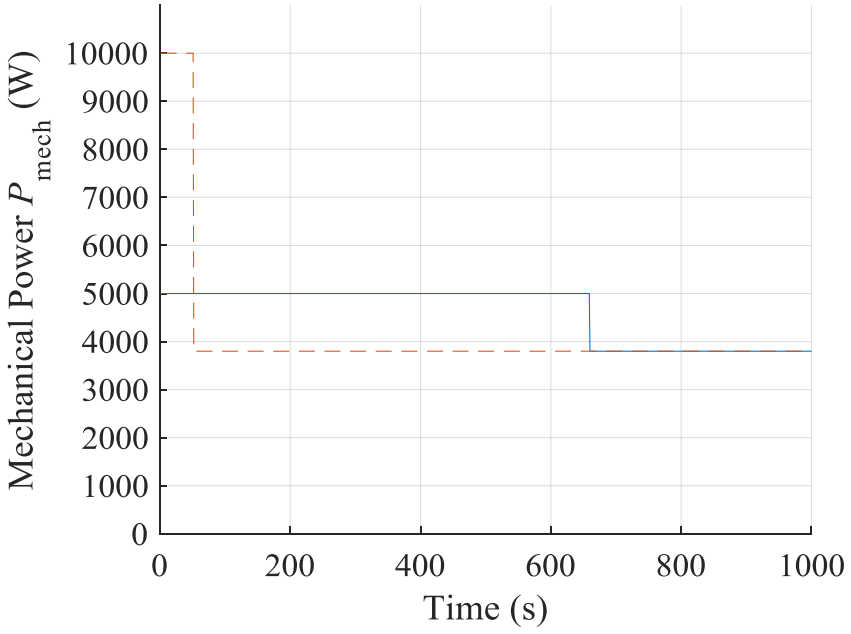

(b)

Figure 6.11. (a) Winding temperatures and (b) mechanical power, P_{mech}, vs. time at 5 kW and 10 kW under speed ω of 2000 rpm in motoring operation mode.

From the machine efficiency map displayed in figure 5.34, machine in high speed field weakening region generates lower losses than low speed MTPA region. Also, at mechanical

power of 5 kW, loss level in generating mode is much lower than motoring mode. The average and maximum winding temperatures in motoring and generating mode versus speed at P_{mech} of 5 kW are plotted in figure 6.12. For the same mechanical power, increase in speed allows a significant reduction in winding temperature on both stator and rotor, so the machine can safely operate at 5 kW. Moreover, winding temperatures in generating mode are generally lower than motoring mode, where machine can operate continuously above 2800 rpm.

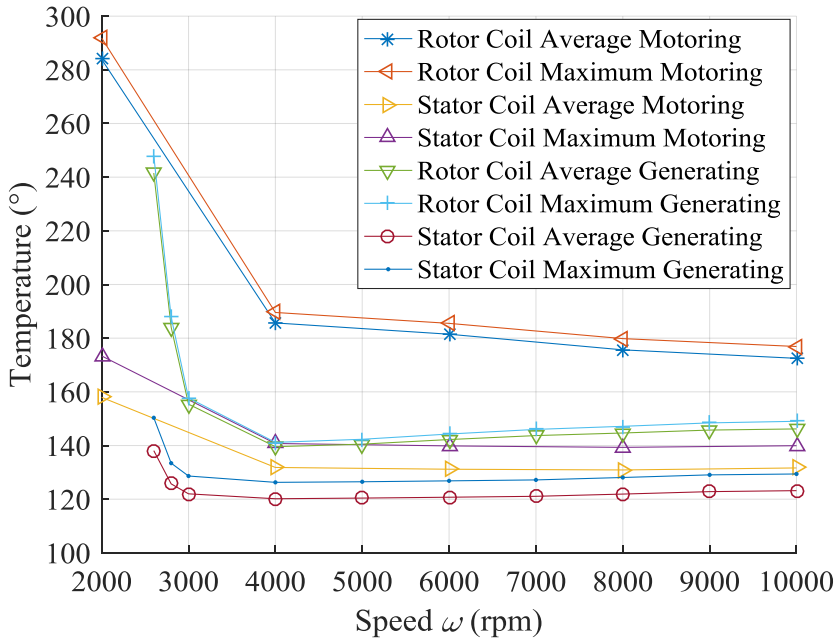

Figure 6.12.Winding temperatures vs. speed ω at mechanical power, P_{mech} of 5 kW in motoring and generating mode.

6.2.3 Proposed Winding Temperature Balancing Method

Results from the prior section indicate that the machine's continuous motoring capability is restricted by rotor winding temperature, where mechanical power reduction or operational speed increase is required for continuous operation. However, in a B-ISG system, the rotor speed is determined by speed of the ICE. To enhance the machine's power ability, an alternative approach is proposed in this section.

Previous simulation suggests that under minimum loss operation, a serious imbalance on winding temperatures are exists between stator and rotor. As a result, the idea of the proposed

method is to reduce rotor winding temperature by rebalancing the stator and rotor losses. To achieve this, the total loss is also likely to increase. At mechanical power, P_{mech} of 5 kW and speed, ω of 2000 rpm, the relationship between stator copper loss, P_{scop} and rotor copper loss, P_{rcop} at fixed winding temperature of 120 °C and temperature from Motor-CAD are shown in figure 6.13. For minimum loss operation, the stator copper loss at 120 °C is 615 W, and rotor copper loss is 301 W. With increase of stator copper loss, rotor copper loss sees a rapid decrease at beginning, but the reduction becomes slower as the total loss increases. If real steady state winding temperature from Motor-CAD is accounted, the both stator and rotor copper loss is significantly increased.

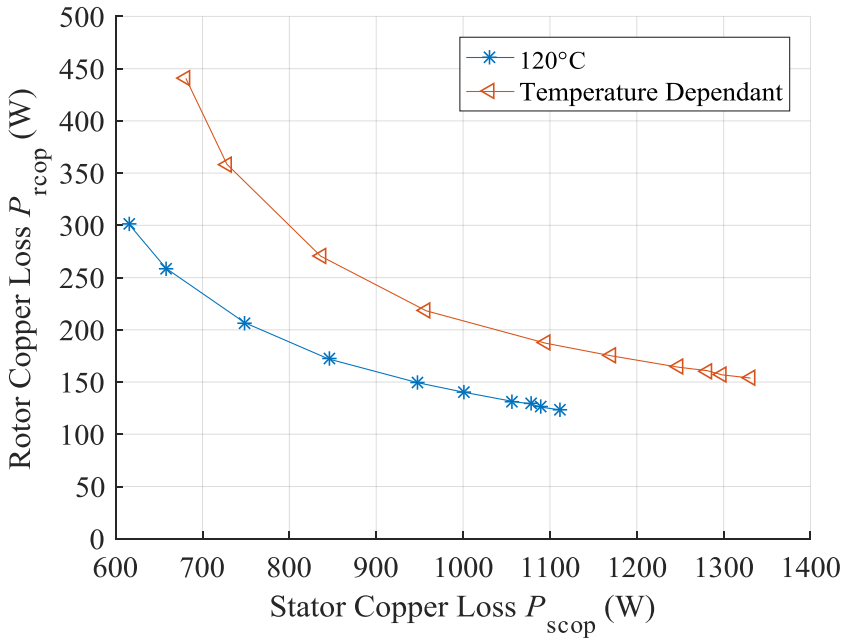

Figure 6.13. Rotor copper loss, P_{rcop}, vs. stator copper loss, P_{scop} at mechanical power, P_{mech} of 5 kW and speed, ω of 2000 rpm, with winding temperature of 120 °C and real temperature from Motor-CAD.

Figure 6.14 plots the real temperatures in stator and rotor winding versus 120 °C stator copper loss, P_{scop}. Clearly, by rebalancing stator and rotor copper losses, the temperatures on rotor windings decreases while the temperature on stator winding increases. Compared with minimum loss operation, increasing the 120 °C stator copper loss to 948 W decreases the 120 °C rotor copper loss to 149 W. This reduces maximum rotor winding temperature from 284 °C to 210 °C and rise maximum stator winding from 173 °C to 200 °C. With the same winding on

rotor and stator, the expected winding lifetime increases to 20000 hours. The total 120 °C copper loss increases from 950 W to 1180 W, and from 1121 W to 1484 W at real steady winding temperature.

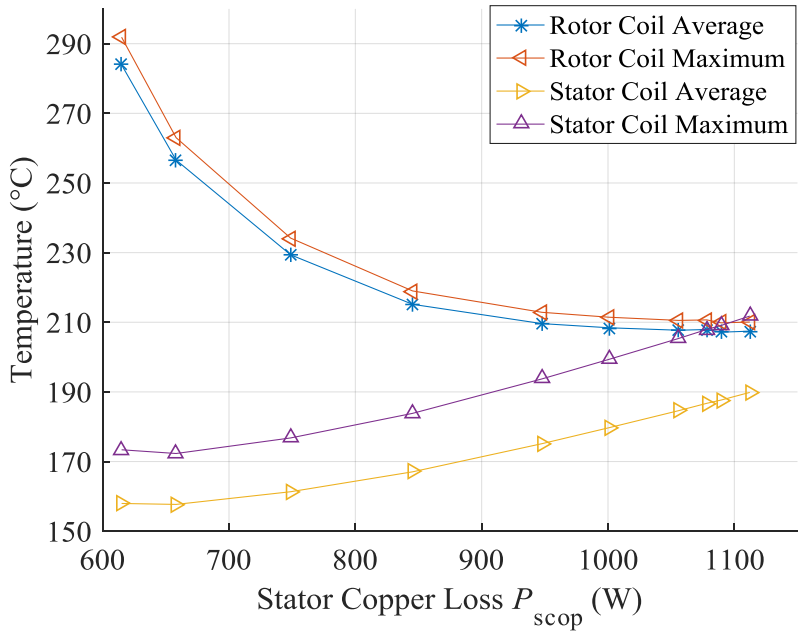

Figure 6.14.Winding temperatures vs. stator copper loss, P_{scop} at 120 °C, at mechanical power, P_{mech} of 5 kW and speed, ω of 2000 rpm.

6.3 Experimental Validation

In this section, a prototype wound rotor synchronous machine is produced. A series of experiments are carried out, where the torque, voltage and loss performances are obtained and compared with FE analysis.

6.3.1 Introduction

Pictures of the different parts of the prototype wound rotor synchronous machine are shown in figure 6.15 (a) (b) and (c), where stator, rotor, shaft, slip ring and carbon brushes are displayed.

Since the stator and rotor are wind by hand, limitations on fill factor, *c* are presented. Moreover, stator currents are restricted by the available machine drive, so a higher number of turns, *N*, are imposed on stator winding to keep the mechanical power unchanged. The parameter change in the prototype machine are listed in table 6.3.

(a) *(b)*

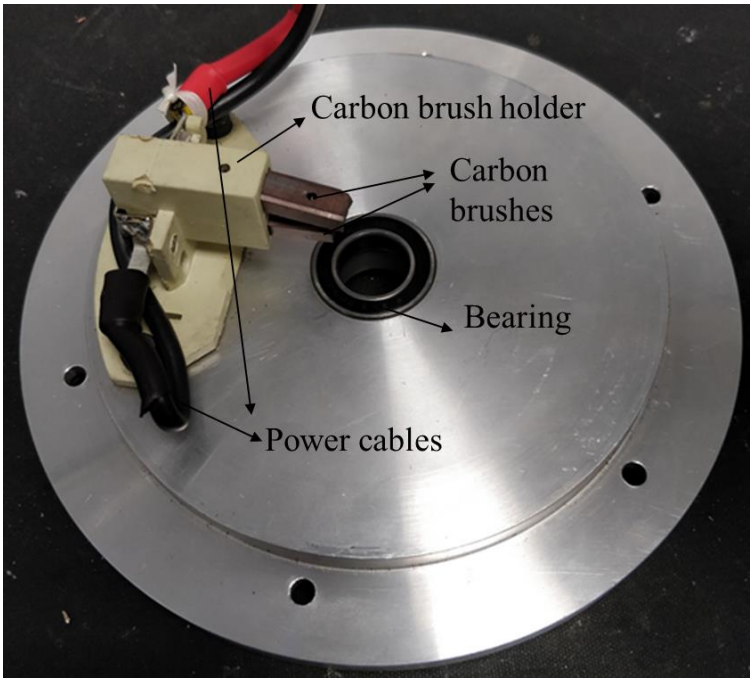

(c)

Figure 6.15. Pictures of the the prototype wound rotor synchronous machine. (a) stator (b) rotor and (c) end plate.

Item	Original Design	Prototype Machine
Stator number of turns per phase N	18	156
Rotor number of turns per coil	72	37
Stator fill factor c_s	0.4	0.3
Rotor fill factor c_r	0.6	0.31
Rated fundamental phase current i_{sfun} (A)	174	16.1
Rated fundamental phase voltage V_{sfun} (V)	29.8	286.2

Table 6.3. Changes between the original design and prototype machine.

Pictures of the experimental platform is displayed in figure 6.16 to 6.17, where all drive and measurement equipment are displayed.

From the pictures, an AVL dynamometer is implemented as the load. The prototype machine is driven with Emerson Unidrive sp3401 on stator side, and excited with TTi QPX1200SP DC power supply on rotor side. To measure the electrical power, Yokogawa WT3000 power analyser is applied, where a matching three-phase current sensor is used. To capture the current and current waveforms, separate current probe and differential probe are also applied. To evaluate the torque and mechanical power, TORQSENSE RWT421 torque transducer is implemented, where both torque and speed can be detected. A water cooling system is also applied, where the water temperature can be controlled.

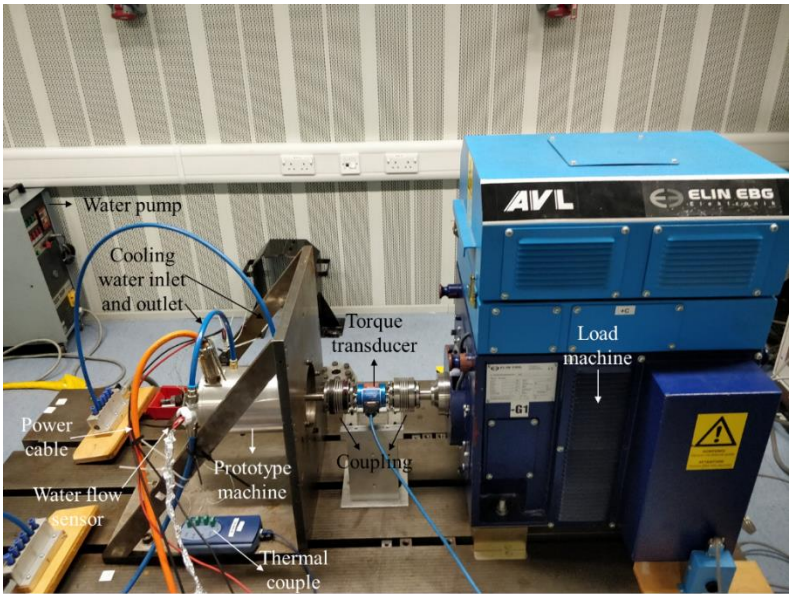

(a)

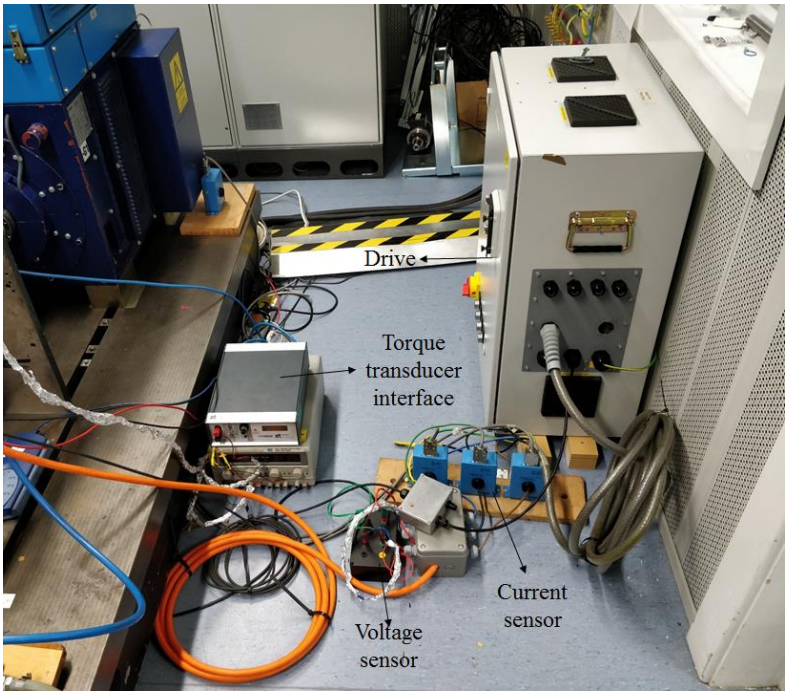

(b)

Figure 6.16. The prototype wound rotor synchronous machine experimental platform. (a) dynomameter and prototype machine, (b) prototype machine driver and sensors.

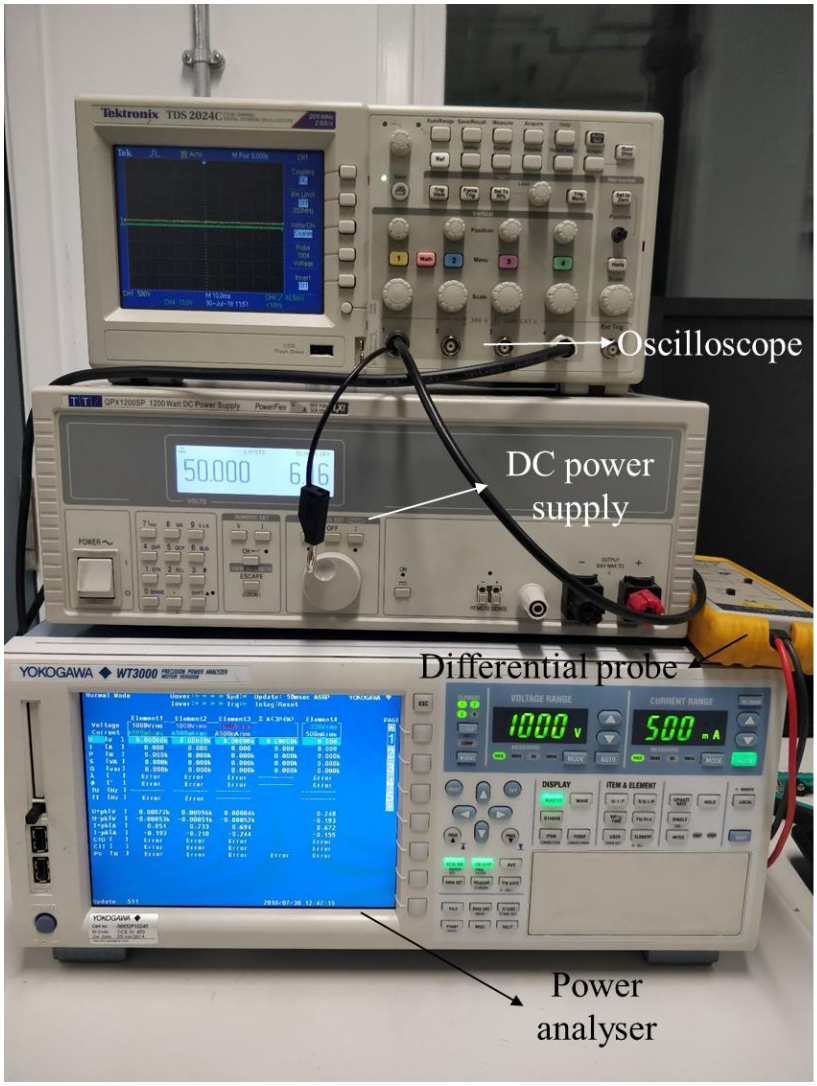

Figure 6.17.Measurement equipment of the prototype wound rotor synchronous machine experimental platform.

6.3.2 Open Circuit

Under open circuit condition and base speed, the back-EMF waveform versus rotor position, ζ_m at various rotor MMF per coil, i_f is plotted below in figure 6.18.

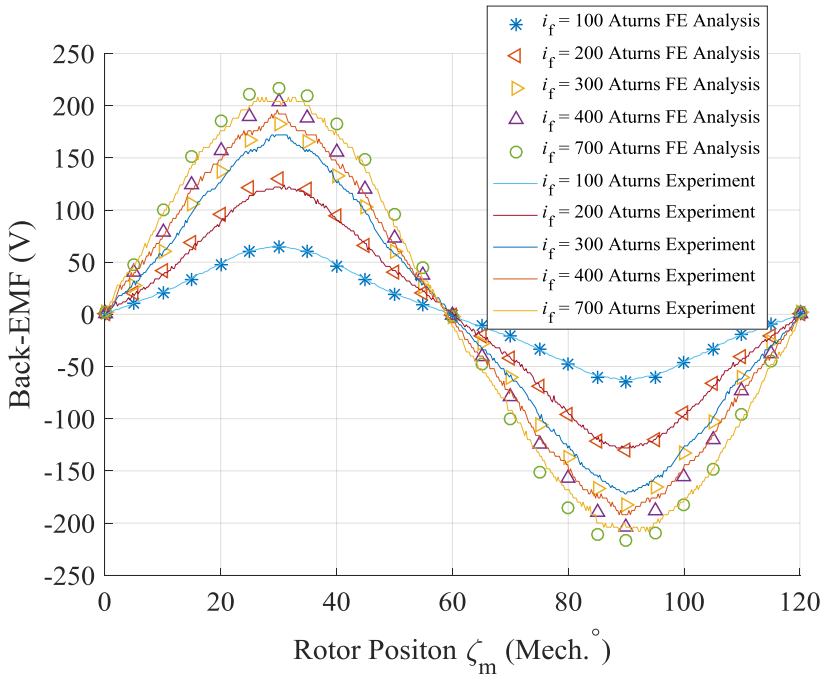

Figure 6.18. Back-EMF waveforms at various rotor MMF per coil, i_f, vs. rotor position, ζ_m at base speed, ω_b of 2000 rpm.

From the FFT results of the back-EMF waveforms, 3rd and 5th harmonics are the main harmonic sources. At different values of i_f, the fundamental, 3rd and 5th harmonics components of the FE analysis and experiments are plotted in figure 6.19. Compared with FE analysis, the experimental results are slightly lower in fundamental component, especially at high i_f. The maximum difference is approximately 6%. This can be explained by the failure to consider the end-effect in 2d FEA [180], and damage to the electrical steel sheets during wire electrical discharge machining (WEDM) [181]. The 3rd and 5th harmonics components changes in a similar pattern with i_f between simulation and experimental results, while a slightly lower amplitude is also exhibited in the experimental results.

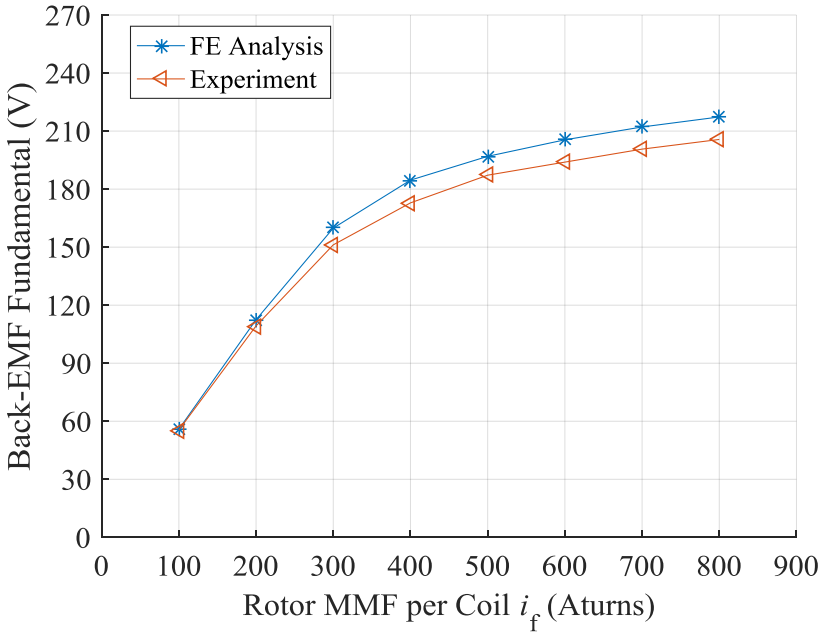

(a)

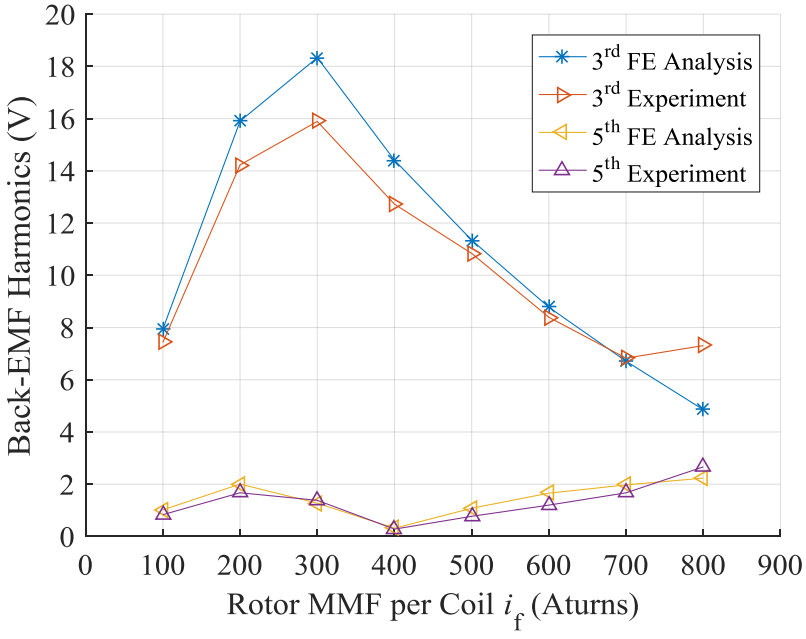

(b)

Figure 6.19. Open circuit back-EMF comparisons between FE analysis and experiment vs. rotor MMF per coil, i_f, (a) fundamental component and (b) 3rd and 5th harmonics components.

6.3.3 Torque Performances

To validate the torque performance of the prototype machine, the torque at different stator and

rotor current are measured. In this process, the load angle, θ, is fixed at 90°, and a low speed is of 100 rpm is applied to avoid any influence of friction or windage.

The measured average torque, T_{ave} at various rotor MMF per coil, i_f versus fundamental stator phase currents, i_{sfun} are plotted with objective value from FE analysis, as shown below in figure 6.20.

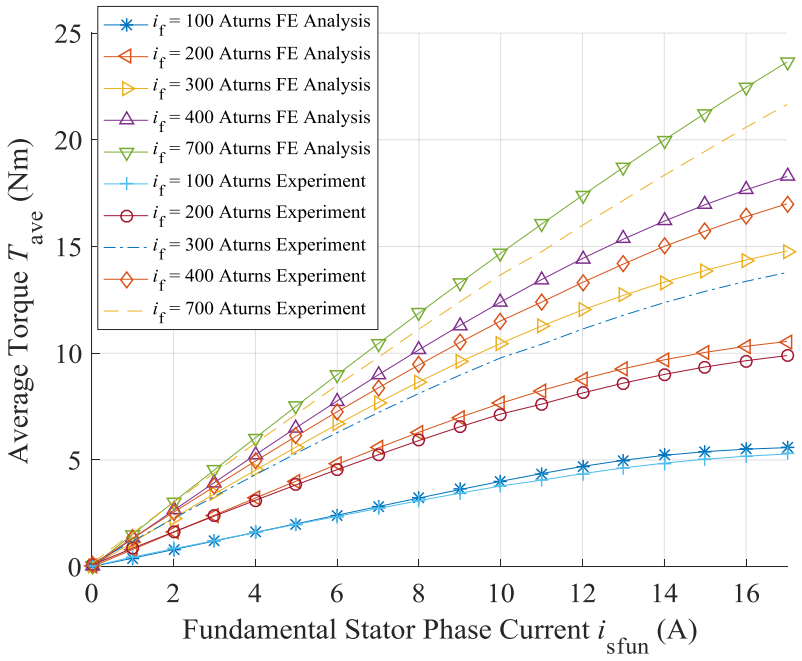

Figure 6.20. Average torque, T_{ave}, comparisons between FE analysis and experiment at various rotor MMF per coil, i_f, vs. fundamental stator phase current, i_{sfun}.

Comparisons indicate the average torque from experiments are generally lower than from FE analysis. The absolute and percentage of difference increase with both i_f and i_{sfun}. At rated objective torque and i_f of 700 Aturns, a typical torque reduction of 8% is presented. This is slightly larger than the reduction in back-EMF, suggesting that the armature reaction from stator current has negative impact on the machine's torque capability.

6.3.4 Maximum Torque per Ampere

In this section, the MTPA performance of the prototype machine is investigated, where the machine's currents and load angles are determined from the minimum loss prediction algorithm proposed in section 5.2. In this way, a minimum loss operating condition is expected. The

mechanical power, P_{mech} and total loss, P_l from experiments are compared with FE analysis.

To validate the minimum loss prediction method, an experiment is designed. To be specific, at the speed of 500 rpm, different stator RMS current, i_{srms}, i_f and θ are applied according to the minimum loss prediction algorithm to maintain a constant P_{mech}. The P_l and P_{mech} from experiment are then compared with FE analysis. At various objective P_{mech}, the P_l and P_{mech} comparisons are plotted in figure 6.21 and 6.22, where the loss is converted to a winding temperature of 120 °C.

From the figures, the proposed algorithm gives a good estimation of the losses, where the minimum loss point can also be accurately predicted. The experimental results are 0 - 4% higher than FE analysis at certain stator current. A constant P_{mech} is also maintained at different i_{srms}, as shown in figure 6.22. Consequently, the proposed minimum loss operation algorithm is validated under MTPA condition.

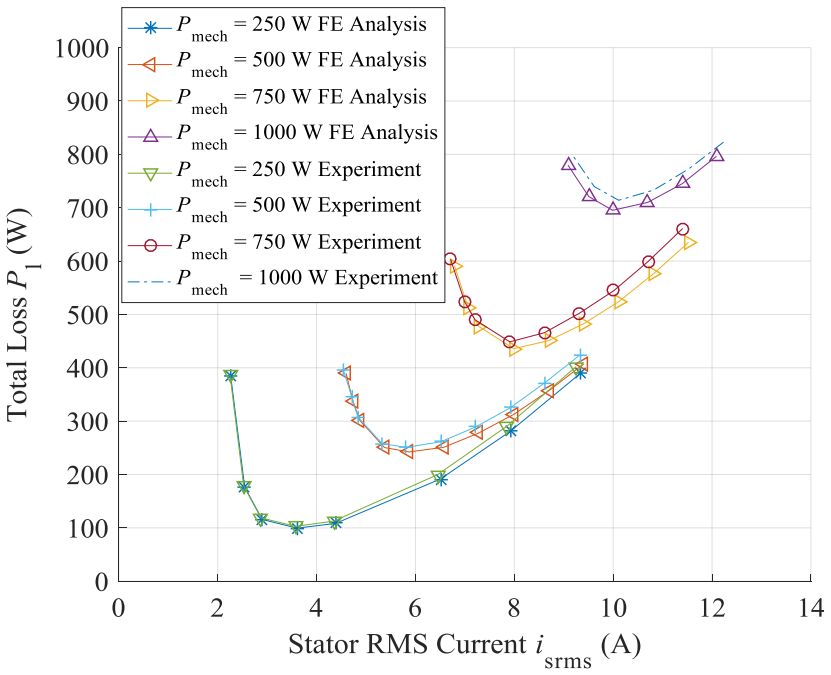

Figure 6.21. Total loss, P_l, comparisons between FE analysis and experiment vs. stator RMS current, i_{srms}, under various objective mechanical power, P_{mech}.

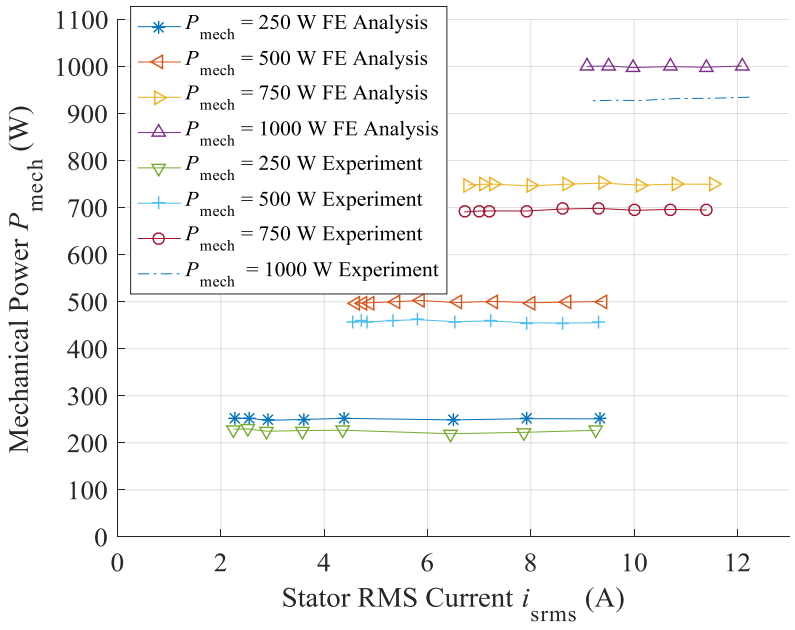

Figure 6.22. Mechanical power, P_{mech}, comparisons between FE analysis and experiments at various objective mechanical power, P_{mech}.

At the speed of 200 rpm, 500 rpm, 1000 rpm and 1500 rpm, P_l versus P_{mech} from experiments are plotted against objective FE analysis in figure 6.23. From the figure, a typical 10% increase of P_l to P_{mech} ratio is exhibit, which is mainly originated from the overestimation of P_{mech}.

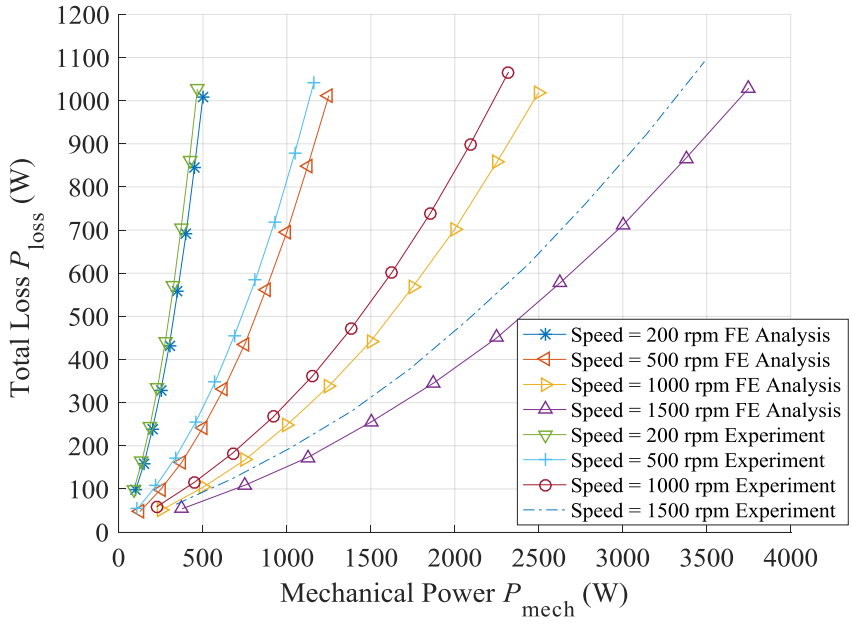

Figure 6.23. Total loss, P_l, comparisons between FE analysis and experiments vs. mechanical power, P_{mech} at various speed, ω.

6.3.5 Field Weakening Operation

In this section, the machine field weakening performance is investigated, where the currents and load angles are determined from the minimum loss prediction algorithm proposed in section 5.2. Compared with section 6.3.4, the difference is that both torque and voltage restrictions are imposed. The mechanical power, P_{mech}, fundamental stator phase voltage, V_{fun} and total loss, P_l from experiments are compared with FE analysis.

For safety concern, the machine speed is limited to 2000 rpm, so the stator phase voltage constraint is lowered accordingly to reduce the new base speed to 200 rpm. To keep a constant rated average torque, the rated mechanical power is reduced to 500 W. At 1000 rpm, the experiments described in section 6.3.4 are repeated with voltage restrictions. The P_l, P_{mech} and V_{fun} from FE analysis and experiments are plotted in comparison in figure 6.24 - 6.26.

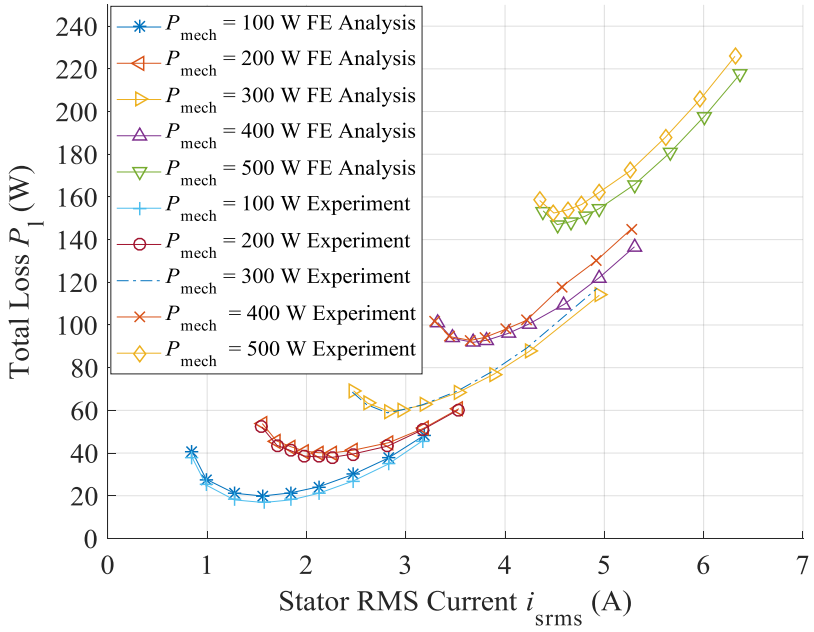

Figure 6.24. Total loss, P_l, comparisons between FE analysis and experiment vs. stator RMS current, i_{srms}, under various objective mechanical power, P_{mech}.

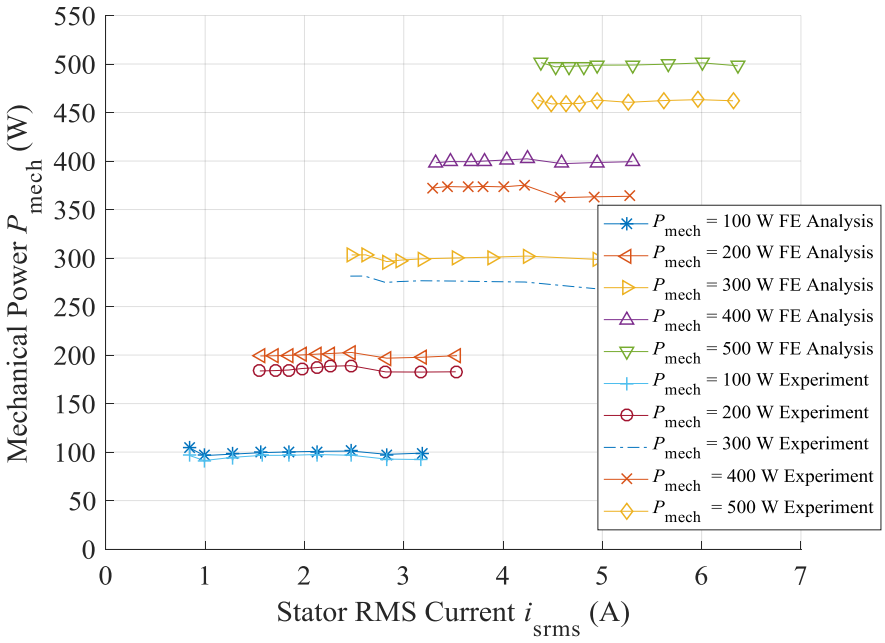

Figure 6.25. Mechanical power, P_{mech}, comparisons between objective from FE analysis and experiments vs. speed, ω.

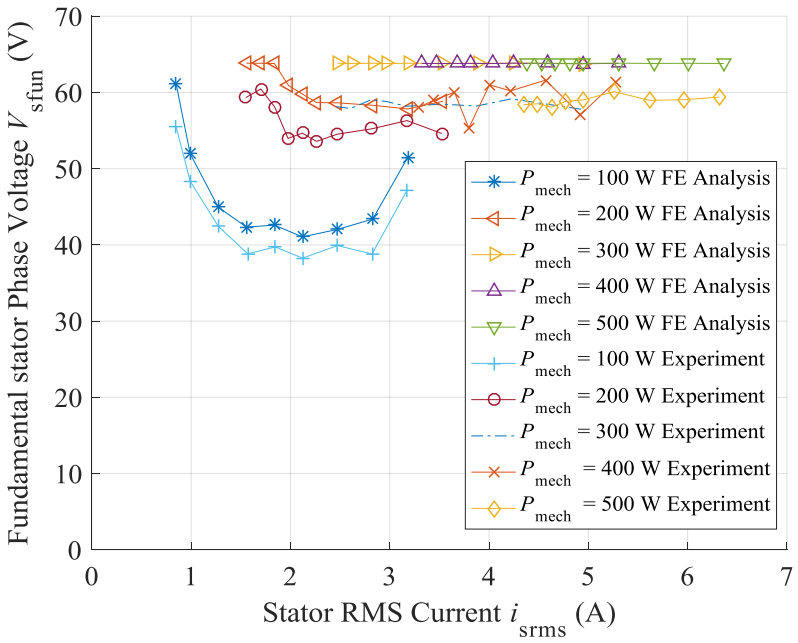

Figure 6.26. Stator fundamental phase voltage, V_{fun}, comparisons between FE analysis and experiment vs. stator RMS current, i_{srms}, under various objective mechanical power, P_{mech}.

From figure 6.24, experimental loss shows a good agreement with FE analysis. At low objective P_{mech}, FE analysis slightly overestimates P_{loss}. At high objective P_{mech}, it tends to underestimate

P_l. The difference between them is no more than 5%. From figure 6.25, P_{mech} is generally constant at various i_{srms} and i_f, which are 4 - 9% lower than the objective P_{mech}. From figure 6.26, V_{fun} versus i_f from FE analysis follows the same trend as the experiments. The experimental V_{fun} values are typically 8% lower than the FE analysis, which is consistent with the P_{mech} difference.

With a validated minimum loss method for field weakening operation, experiments are conducted in the entire field weakening speed range, where the experimental P_{mech}, V_{fun} and P_l from are plotted against the FE analysis data in figure 6.27 - 6.29.

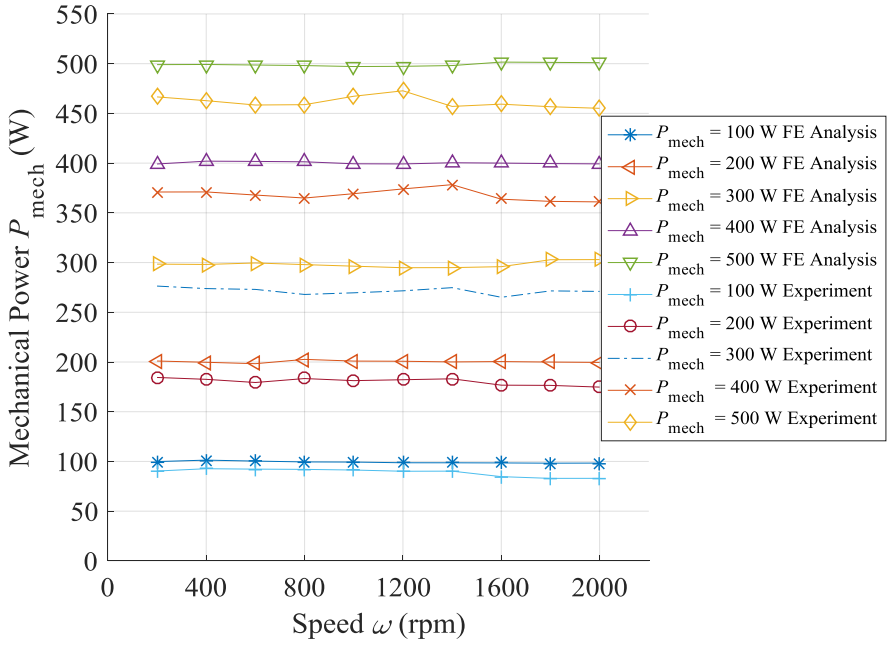

Figure 6.27. Mechanical power, P_{mech}, comparisons between objective from FE analysis and experiments vs. speed, ω.

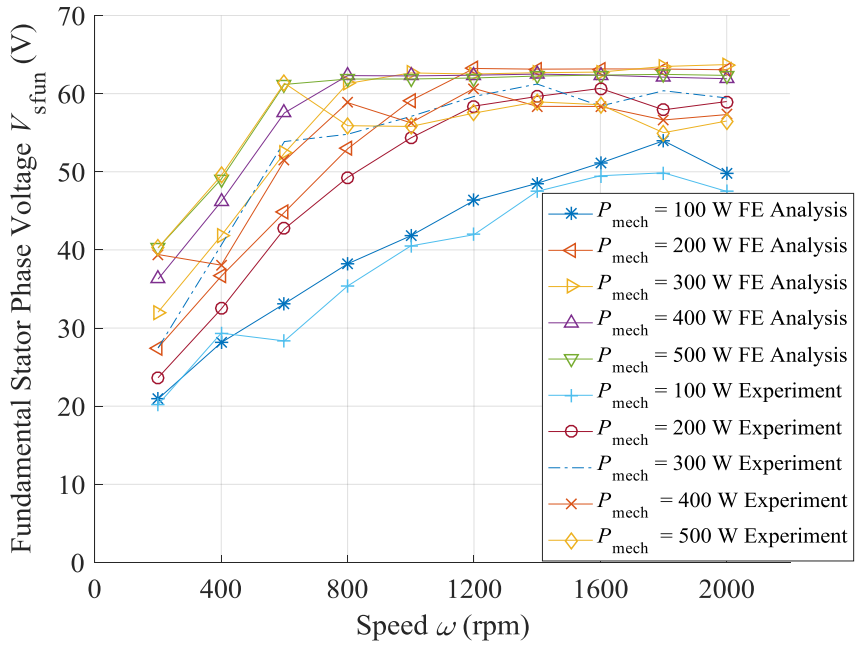

Figure 6.28. Stator fundamental phase voltage, V_{fun}, comparisons between FE analysis and experiment vs. speed, ω, under various objective mechanical power, P_{mech}.

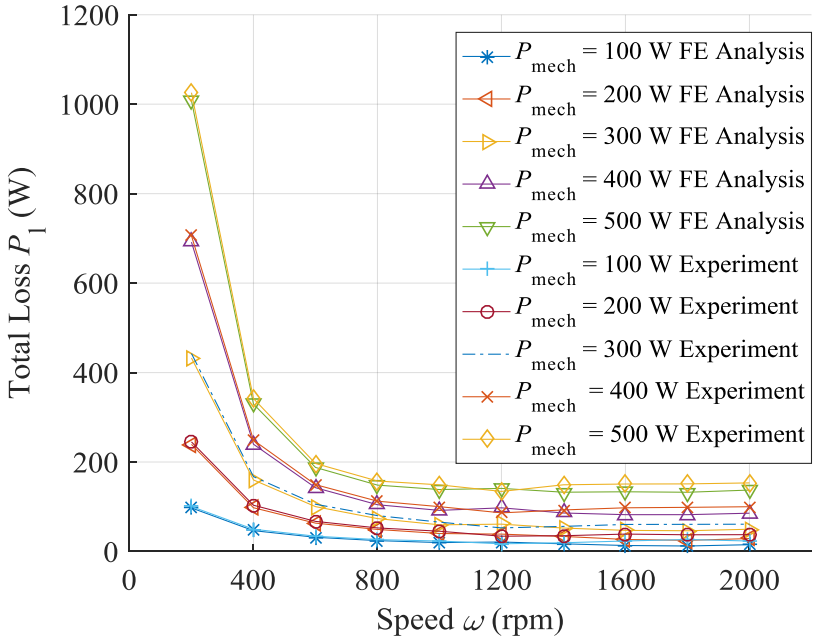

Figure 6.29. Total loss, P_l, comparisons between FE analysis and experiment vs. speed, ω, under various objective mechanical power, P_{mech}.

From these experiments, the wound rotor synchronous machine demonstrates a good field weakening capability, where a CPSR of 10 is possible. To achieve this performance with

minimum loss, the proposed minimum loss algorithm provides good accuracy.

6.4 Summary

In this chapter, thermal and mechanical simulations of the prototype wound rotor synchronous machine are conducted. Then a prototype WRSM with water cooling jacket is constructed and tested on dynamometer. A novel temperature balancing method between stator and rotor is also suggested, where the maximum continuous motoring power can be significantly increased.

From this study, the following conclusions are drawn:

(1) The presence of rotor winding lead to large centrifugal force at high speed, imposing a mechanical speed restriction at 11,000 rpm.

(2) The heat on the rotor is more difficult to dissipate than stator, resulting in a much higher temperature on the rotor winding than stator winding under rated operation conditions. By rebalancing stator and rotor losses, the winding temperatures on rotor windings is reduced, which greatly increases continuous power capability. The cost of this method is an increase in stator winding temperature and total copper loss.

(3) Experiments performed on the prototype machine show a reduced back-EMF and average torque compared with FE analysis, where the differences are no more than 10%. Loss measurements show that the minimum loss prediction method proposed in Chapter 5 gives a good prediction of losses, mechanical power and phase voltage. Taking advantage of this method, the prototype machine delivers good field weakening capability with low losses.

7. Conclusion and Future Work

7.1 Conclusions

Mild hybrid vehicles with B-ISGs enjoy the advantages of a smaller battery, lower cost and greater cruising range compared with an EV, and lower noise, higher fuel efficiency and better dynamic performance compared with ICEV.

For ISG applications, a rare earth permanent magnet synchronous machine is widely implemented due to its unique high torque density, high power density, high efficiency, low maintenance requirements and easy control. However, the presence of rare earth permanent magnets also brings challenges such as high cost, temperature sensitivity and difficulty in field weakening.

To overcome these problems, different types of non-PM machines are evaluated in this thesis. The classical switched reluctance machine is considered for its easy field weakening, low machine cost, robust structure and insensitivity to temperature. However, there are major drawbacks such as low torque density, high torque ripple, low overall efficiency, low power factor, complicated control strategy and high cost power electronics.

This study hopes to partially overcome the problems of torque density, control complexity and power electronics cost by changing the winding configuration and implementing AC sinusoidal current drive. Short pitched mutually coupled winding, fractional pitched classical winding, fractional pitched mutually coupled winding and fully pitched winding topologies are studied using conventional AC machine theory. Among them, the short pitched mutually coupled winding provides the most favourable performances in torque per copper loss, IPF and CPSR.

To validate the AC machine theory on an MCSRM, a co-simulation between three-phase AC inverter and the machine is applied, where six-step operation generates harmonics in the excitation current, as opposed to a pure sinusoidal current in conventional AC theory. These harmonics reduce the power factor and therefore increase the current requirements. The field weakening capability is largely unaffected. Generally speaking, AC sinusoidal excitation results

in low power factor and a poor field weakening ability in SRM, making it unfavourable for B-ISG applications.

The wound rotor synchronous machine is another potential candidate for B-ISG applications. It has good field weakening capability, high efficiency and adopts conventional AC machine theory. Despite the merits, there are also many shortcomings. First, a high efficiency, low torque ripple machine requires a comprehensive determination of machine dimensions. Second, since saturation is manifest in WRSM, the strong nonlinearity brings challenges in machine modelling. Third, an extra rotor excitation current increases complexity in machine control. Fourth, a high centrifugal force from the weight of rotor winding challenges the mechanical strength of rotor at high speed. Last, the rotor copper loss creates problems in thermal management.

To solve the first problem, a comprehensive geometric optimization procedure for minimum loss is applied at base speed and rated power, where the sensitivity of rotor pole shoes is emphasized. To further reduce loss, a six pole rotor is proposed over a four pole structure, where the former exhibits a pleasing reduction in copper loss and increase in efficiency. Further decrease in iron loss can be achieved by using thinner lamination material.

To solve the second problem, an eccentric rotor pole provides an effective solution. To ensure a maximum average torque at certain torque ripple level, a proposed look-up table interpolation method is applied, where a significant decrease in ripple is possible at the price of a small reduction in average torque.

To solve the third problem, the Lagrange method is the most widely used approach. This study proposed an algorithm based on look-up table and interpolation method. Compared with the Lagrange method, the proposed algorithm decreases the deviation of torque and voltage prediction from ±10% to ±1%, and computation time from hours to minutes. The proposed method is then validated with experiments, where a discrepancy of no more than 10% is exhibited on back-EMF, average torque and loss. The minimum copper loss current criteria are

accurately predicted.

With the design and control strategies proposed from our study, the WRSM not only fulfils the requirements for the B-ISG application, but also achieves a better overall performance over the benchmark SRM. From simulation, a total loss reduces of at least 40% over an NEDC driving cycle is presented, and the overall efficiency increases from 84% to over 90%.

The thermal and mechanical limitations of the WRSM is then studied, where the wound rotor structure brings thermal and mechanical challenges. The windings on the rotor creates large centrifugal force, limiting the speed of machine at 11,000 rpm. A desirable level of heat removal on the rotor is much more difficult to implement than on the stator. High temperature on the rotor winding limits the maximum continuous motoring power at base speed to only 3.8 kW. To achieve a desired continuous motoring power of 5 kW, rebalancing of the stator and rotor copper losses is proposed at the expense of an increase in total copper loss.

7.2 Future Work

Despite the contributions in this thesis, there are still limitations for WRSM in B-ISG applications. Therefore, the following suggestions are made for future investigations.

First, despite being a mature technology, the carbon brushes and slip rings not only need regular replacement, but also causes potential contacting problems. The available non-contacting solutions usually adopt a rotational transformer. Compared with slip ring, a reduction in efficiency and increase in cost is presented. Alternatively, harmonics in the airgap are used to transmit power to rotor, where stator windings act as primary winding to generate the harmonics. Auxiliary secondary windings are placed on rotor surface to receive the transmitted power. This approach increases machine structural complexity, reduces efficiency, and the power transmission capability is usually reliant on rotor speed. Therefore, further investigations are required to improve the current power transmission technology, where a high efficiency, low cost non-contacting power supply device or design should be developed for rotor excitation current.

Secondly, as proposed in section 6.1.2, the large centrifugal force limits the machine speed. Since a large proportion of the stress is brought by unevenly distributed force along the axial direction from end-windings. A band or sleeve on the end-winding to support it at high speed is expected to greatly alleviate this problem. However, further study is required to verify this hypothesis.

Thirdly, the optimum loss algorithm proposed in section 5.2 is conducted at a fixed temperature. To guarantee a minimum copper loss considering winding temperatures, a temperature dependant minimum loss algorithm should be developed and evaluated under driving cycles. This involves a multi-physics simulation with coupled magnetic and thermal machine models.

Last, unlike the PM machine, the average temperature of the rotor winding can be easily obtained by measuring the voltage across the rotor windings. Based on both stator and rotor winding temperature, an instantaneous current control guarantees a maximum efficiency at any time and a minimum temperature rise over multiple driving cycles. Therefore, a minimum loss control strategy with temperature consideration should be developed in real-time machine controller.

References

[1] I. Husain, Electric and hybrid vehicles: design fundamentals, CRC press, 2011.
[2] R.W. Bentley, Global oil & gas depletion: an overview, Energy policy, 30 (2002) 189-205.
[3] N.A. Owen, O.R. Inderwildi, D.A. King, The status of conventional world oil reserves—Hype or cause for concern?, Energy policy, 38 (2010) 4743-4749.
[4] A. Sieminski, International Energy Outlook, in, 2013.
[5] T. Thielemann, S. Schmidt, J.P. Gerling, Lignite and hard coal: Energy suppliers for world needs until the year 2100—An outlook, International Journal of Coal Geology, 72 (2007) 1-14.
[6] B. François, Hybrid Vehicles: From Components to System, Editions TECHNIP, 2013.
[7] J. Larminie, J. Lowry, Electric vehicle technology explained, John Wiley & Sons, 2004.
[8] C. Iclodean, B. Varga, N. Burnete, D. Cimerdean, B. Jurchiş, Comparison of Different Battery Types for Electric Vehicles, in: IOP Conference Series: Materials Science and Engineering, IOP Publishing, 2017, pp. 012058.
[9] G. Albright, J. Edie, S. Al-Hallaj, A comparison of lead acid to lithium-ion in stationary storage applications, Published by AllCell Technologies LLC, (2012).
[10] B. Nykvist, M. Nilsson, Rapidly falling costs of battery packs for electric vehicles, Nature Climate Change, 5 (2015) 329-332.
[11] S. Carley, R.M. Krause, B.W. Lane, J.D. Graham, Intent to purchase a plug-in electric vehicle: A survey of early impressions in large US cites, Transportation Research Part D: Transport and Environment, 18 (2013) 39-45.
[12] J.E. Walters, R.J. Krefta, G. Gallegos-Lopez, G.T. Fattic, Technology considerations for belt alternator starter systems, in, SAE Technical Paper, 2004.
[13] R.E. Uhrig, Using plug-in hybrid vehicles, The Bent of Tau Beta Pi, 96 (2005).
[14] S.-K. Sul, Control of electric machine drive systems, John Wiley & Sons, 2011.
[15] S. Kozawa, Trends and Problems in Research of Permanent Magnets for Motors-Addressing Scarcity Problem of Rare Earth Elements, Science and Technology Trends, Quarterly Review, 38 (2011) 40-54.
[16] Y. Zhang, Peak Neodymium: Material Constraints for Future Wind Power Development, in, 2013.
[17] J.d. Santiago, H. Bernhoff, B. Ekergård, S. Eriksson, S. Ferhatovic, R. Waters, M. Leijon, Electrical Motor Drivelines in Commercial All-Electric Vehicles: A Review, IEEE Transactions on Vehicular Technology, 61 (2012) 475-484.
[18] C. Hurst, China's rare earth elements industry: What can the west learn?, in, Institute for the Analysis of Global Security Washington DC, 2010.
[19] S. Hoenderdaal, L. Tercero Espinoza, F. Marscheider-Weidemann, W. Graus, Can a dysprosium shortage threaten green energy technologies?, Energy, 49 (2013) 344-355.
[20] D. Bauer, D. Diamond, J. Li, D. Sandalow, P. Telleen, B. Wanner, US Department of Energy critical materials strategy, (2010).
[21] A.H. Tkaczyk, A. Bartl, A. Amato, V. Lapkovskis, M. Petranikova, Sustainability evaluation of essential critical raw materials: cobalt, niobium, tungsten and rare earth elements, Journal of Physics D: Applied Physics, 51 (2018) 203001.
[22] D.G. Dorrell, A.M. Knight, M. Popescu, L. Evans, D.A. Staton, Comparison of different motor

design drives for hybrid electric vehicles, in: Energy Conversion Congress and Exposition (ECCE), 2010 IEEE, 2010, pp. 3352-3359.
[23] T. Sebastian, Temperature effects on torque production and efficiency of PM motors using NdFeB magnets, Industry Applications, IEEE Transactions on, 31 (1995) 353-357.
[24] C.C. Chan, The state of the art of electric and hybrid vehicles, Proceedings of the IEEE, 90 (2002) 247-275.
[25] W. Cai, Comparison and review of electric machines for integrated starter alternator applications, in: Industry Applications Conference, 2004. 39th IAS Annual Meeting. Conference Record of the 2004 IEEE, 2004, pp. 1-393.
[26] I.-a. Viorel, L. Szabó, L. Lowenstein, C. STET, Integrated starter-generators for automotive applications, Acta Electrotehnica, 45 (2004) 255-260.
[27] B. Fahimi, A switched reluctance machine based starter/generator for more electric cars, in: Electric Machines and Drives Conference, 2001. IEMDC 2001. IEEE International, 2001, pp. 73-78.
[28] J.M. Miller, A.R. Gale, P.J. McCleer, F. Leonardi, J.H. Lang, Starter-alternator for hybrid electric vehicle: comparison of induction and variable reluctance machines and drives, in: Industry Applications Conference, 1998. Thirty-Third IAS Annual Meeting. The 1998 IEEE, 1998, pp. 513-523 vol.511.
[29] L. Chunhua, K.T. Chau, J.Z. Jiang, A Permanent-Magnet Hybrid Brushless Integrated Starter-Generator for Hybrid Electric Vehicles, Industrial Electronics, IEEE Transactions on, 57 (2010) 4055-4064.
[30] F. Leonardi, M. Degner, Integrated starter generator based HEVs: a comparison between low and high voltage systems, in: Electric Machines and Drives Conference, 2001. IEMDC 2001. IEEE International, 2001, pp. 622-628.
[31] T.J.E. Miller, Electronic control of switched reluctance machines, Newnes, 2001.
[32] M. Zeraoulia, M.E.H. Benbouzid, D. Diallo, Electric Motor Drive Selection Issues for HEV Propulsion Systems: A Comparative Study, Vehicular Technology, IEEE Transactions on, 55 (2006) 1756-1764.
[33] S. Taghavi, Design of Synchronous Reluctance Machines for Automotive Applications, in, Concordia University, 2015.
[34] A. Boglietti, M. Pastorelli, Induction and synchronous reluctance motors comparison, in: Industrial Electronics, 2008. IECON 2008. 34th Annual Conference of IEEE, 2008, pp. 2041-2044.
[35] C. Shaotang, B. Lequesne, R.R. Henry, X. Yanhong, J.J. Ronning, Design and testing of a belt-driven induction starter-generator, Industry Applications, IEEE Transactions on, 38 (2002) 1525-1533.
[36] A. Boglietti, A. Cavagnino, M. Pastorelli, A. Vagati, Experimental comparison of induction and synchronous reluctance motors performance, in: Industry Applications Conference, 2005. Fourtieth IAS Annual Meeting. Conference Record of the 2005, 2005, pp. 474-479 Vol. 471.
[37] J.D. Widmer, R. Martin, M. Kimiabeigi, Electric vehicle traction motors without rare earth magnets, Sustainable Materials and Technologies, 3 (2015) 7-13.
[38] K. Yamazaki, M. Shina, Y. Kanou, M. Miwa, J. Hagiwara, Effect of Eddy Current Loss Reduction by Segmentation of Magnets in Synchronous Motors: Difference Between Interior and Surface Types, IEEE Transactions on Magnetics, 45 (2009) 4756-4759.
[39] A. Vagati, G. Pellegrino, P. Guglielmi, Comparison between SPM and IPM motor drives for EV

application, in: Electrical Machines (ICEM), 2010 XIX International Conference on, 2010, pp. 1-6.
[40] K.T. Chau, C.C. Chan, L. Chunhua, Overview of Permanent-Magnet Brushless Drives for Electric and Hybrid Electric Vehicles, Industrial Electronics, IEEE Transactions on, 55 (2008) 2246-2257.
[41] R.-R. Moghaddam, Synchronous reluctance machine (SynRM) in variable speed drives (VSD) applications, in: KTH University, 2011.
[42] W.L. Soong, N. Ertugrul, Field-weakening performance of interior permanent-magnet motors, IEEE Transactions on Industry Applications, 38 (2002) 1251-1258.
[43] R. Vartanian, H.A. Toliyat, B. Akin, R. Poley, Power factor improvement of synchronous reluctance motors (SynRM) using permanent magnets for drive size reduction, in: Applied Power Electronics Conference and Exposition (APEC), 2012 Twenty-Seventh Annual IEEE, 2012, pp. 628-633.
[44] I. Boldea, L. Tutelea, C.I. Pitic, PM-assisted reluctance synchronous motor/generator (PM-RSM) for mild hybrid vehicles: electromagnetic design, Industry Applications, IEEE Transactions on, 40 (2004) 492-498.
[45] G. Pellegrino, A. Vagati, P. Guglielmi, B. Boazzo, Performance comparison between surface-mounted and interior PM motor drives for electric vehicle application, Industrial Electronics, IEEE Transactions on, 59 (2012) 803-811.
[46] I. Boldea, L.N. Tutelea, L. Parsa, D. Dorrell, Automotive electric propulsion systems with reduced or no permanent magnets: An overview, IEEE Transactions on Industrial Electronics, 61 (2014) 5696-5711.
[47] M. Cheng, W. Hua, J. Zhang, W. Zhao, Overview of stator-permanent magnet brushless machines, IEEE Transactions on Industrial Electronics, 58 (2011) 5087-5101.
[48] Y. Liao, F. Liang, T.A. Lipo, A novel permanent magnet motor with doubly salient structure, IEEE Transactions on Industry Applications, 31 (1995) 1069-1078.
[49] R.P. Deodhar, S. Andersson, I. Boldea, T.J. Miller, The flux-reversal machine: A new brushless doubly-salient permanent-magnet machine, IEEE Transactions on Industry Applications, 33 (1997) 925-934.
[50] E. Hoang, H.B. Ahmed, J. Lucidarme, Switching flux permanent magnet polyphased synchronous machines, in: EPE 97, 1997.
[51] C. Ruiwu, C. Mi, C. Ming, Quantitative Comparison of Flux-Switching Permanent-Magnet Motors With Interior Permanent Magnet Motor for EV, HEV, and PHEV Applications, Magnetics, IEEE Transactions on, 48 (2012) 2374-2384.
[52] W.L. Soong, T.J.E. Miller, Field-weakening performance of brushless synchronous AC motor drives, in: IEE Proceedings - Electric Power Applications, 1994, pp. 331-340.
[53] G. Friedrich, Experimental comparison between Wound Rotor and permanent magnet synchronous machine for Integrated Starter Generator applications, in: Energy Conversion Congress and Exposition (ECCE), 2010 IEEE, 2010, pp. 1731-1736.
[54] A. De Vries, Y. Bonnassieux, M. Gabsi, F. D'Oliveira, C. Plasse, A switched reluctance machine for a car starter-alternator system, in: Electric Machines and Drives Conference, 2001. IEMDC 2001. IEEE International, 2001, pp. 323-328.
[55] C.S. Edrington, M. Krishnamurthy, B. Fahimi, Bipolar Switched Reluctance Machines: A Novel Solution for Automotive Applications, Vehicular Technology, IEEE Transactions on, 54 (2005) 795-808.
[56] J. Faiz, K. Moayed-Zadeh, Design of switched reluctance machine for starter/generator of hybrid

electric vehicle, Electric Power Systems Research, 75 (2005) 153-160.
[57] C.A. Ferreira, S.R. Jones, W.S. Heglund, W.D. Jones, Detailed design of a 30-kW switched reluctance starter/generator system for a gas turbine engine application, Industry Applications, IEEE Transactions on, 31 (1995) 553-561.
[58] S.R. MacMinn, W.D. Jones, A very high speed switched-reluctance starter-generator for aircraft engine applications, in: Aerospace and Electronics Conference, 1989. NAECON 1989., Proceedings of the IEEE 1989 National, 1989, pp. 1758-1764 vol.1754.
[59] C. Pollock, H. Pollock, R. Barron, J.R. Coles, D. Moule, A. Court, R. Sutton, Flux-Switching Motors for Automotive Applications, Industry Applications, IEEE Transactions on, 42 (2006) 1177-1184.
[60] K.M. Rahman, B. Fahimi, G. Suresh, A.V. Rajarathnam, M. Ehsani, Advantages of switched reluctance motor applications to EV and HEV: design and control issues, Industry Applications, IEEE Transactions on, 36 (2000) 111-121.
[61] K.M. Rahman, S.E. Schulz, High performance fully digital switched reluctance motor controller for vehicle propulsion, in: Industry Applications Conference, 2001. Thirty-Sixth IAS Annual Meeting. Conference Record of the 2001 IEEE, 2001, pp. 18-25 vol.11.
[62] N. Schofield, S.A. Long, Generator operation of a switched reluctance starter/generator at extended speeds, in: Vehicle Power and Propulsion, 2005 IEEE Conference, 2005, pp. 8 pp.
[63] N. Schofield, S.A. Long, D. Howe, M. McClelland, Design of a Switched Reluctance Machine for Extended Speed Operation, Industry Applications, IEEE Transactions on, 45 (2009) 116-122.
[64] M.S. Islam, M.N. Anwar, I. Husain, Design and control of switched reluctance motors for wide-speed-range operation, in: IEE Proceedings - Electric Power Applications, 2003, pp. 425-430.
[65] X.D. Xue, K.W.E. Cheng, S.L. Ho, Study of power factor in SRM drives under current hysteresis chopping control, in: Fourtieth IAS Annual Meeting. Conference Record of the 2005 Industry Applications Conference, 2005., 2005, pp. 2734-2740 Vol. 2734.
[66] X.D. Xue, K.W.E. Cheng, S.L. Ho, Correlation of modeling techniques and power factor for switched-reluctance machines drives, IEE Proceedings - Electric Power Applications, 152 (2005) 710-722.
[67] X.D. Xue, K.W.E. Cheng, S.L. Ho, Influences of Outputs and Control Parameters upon the Power Factor of Switched Reluctance Motor Drives, Electric Power Components and Systems, 32 (2004) 1207-1223.
[68] K. Young Ahn, S. Kyoo Jae, R. Guen Hie, SRM drive system with improved power factor, in: Proceedings of the IECON'97 23rd International Conference on Industrial Electronics, Control, and Instrumentation (Cat. No.97CH36066), 1997, pp. 541-545 vol.542.
[69] H. Hannoun, M. Hilairet, C. Marchand, Gain-scheduling PI current controller for a Switched Reluctance Motor, in: Industrial Electronics, 2007. ISIE 2007. IEEE International Symposium on, 2007, pp. 1177-1182.
[70] H. Hannoun, M. Hilairet, C. Marchand, Comparison of instantaneous and average torque control for a switched reluctance motor, in: Industrial Electronics, 2008. ISIE 2008. IEEE International Symposium on, 2008, pp. 675-680.
[71] H. Hannoun, M. Hilairet, C. Marchand, Design of an SRM Speed Control Strategy for a Wide Range of Operating Speeds, Industrial Electronics, IEEE Transactions on, 57 (2010) 2911-2921.
[72] H. Hannoun, M. Hilairet, C. Marchand, Experimental Validation of a Switched Reluctance Machine

Operating in Continuous-Conduction Mode, Vehicular Technology, IEEE Transactions on, 60 (2011) 1453-1460.
[73] M. Hilairet, H. Hannoun, C. Marchand, Design of an optimized SRM control architecture based on a hardware/software partitioning, in: Industrial Electronics, 2009. IECON '09. 35th Annual Conference of IEEE, 2009, pp. 4053-4057.
[74] J.S. Lawler, J.M. Bailey, J.W. McKeever, P.J. Otaduy, Impact of continuous conduction on the constant power speed range of the switched reluctance motor, in: Electric Machines and Drives, 2005 IEEE International Conference on, 2005, pp. 1285-1292.
[75] M. Rekik, M. Besbes, C. Marchand, B. Multon, S. Loudot, D. Lhotellier, High Speed Range Enhancement of a Switched Reluctance Motor with Continous Mode, in: EVER 2007, MONACO, Monaco, 2007, pp. 8p.
[76] R. Krishnan, Switched reluctance motor drives: modeling, simulation, analysis, design, and applications, CRC press, 2001.
[77] Ž. Grbo, S. Vukosavić, E. Levi, A novel power inverter for switched reluctance motor drives, Facta universitatis-series: Electronics and Energetics, 18 (2005) 453-465.
[78] M.N. Anwar, I. Husain, Design perspectives of a low acoustic noise switched reluctance machine, in: Industry Applications Conference, 2000. Conference Record of the 2000 IEEE, 2000, pp. 99-106 vol.101.
[79] M.N. Anwar, I. Husain, Radial force calculation and acoustic noise prediction in switched reluctance machines, Industry Applications, IEEE Transactions on, 36 (2000) 1589-1597.
[80] F.-C. Lin, S.-M. Yang, Instantaneous shaft radial force control with sinusoidal excitations for switched reluctance motors, IEEE Transactions on Energy Conversion, 22 (2007) 629-636.
[81] C.-Y. Wu, C. Pollock, Analysis and reduction of vibration and acoustic noise in the switched reluctance drive, IEEE transactions on industry applications, 31 (1995) 91-98.
[82] G.J. Li, X. Ojeda, S. Hlioui, E. Hoang, M. Gabsi, C. Balpe, Comparative study of Switched Reluctance Motors performances for two current distributions and excitation modes, in: Industrial Electronics, 2009. IECON '09. 35th Annual Conference of IEEE, 2009, pp. 4047-4052.
[83] G. Li, J. Ojeda, E. Hoang, M. Lécrivain, M. Gabsi, Comparative studies between classical and mutually coupled switched reluctance motors using thermal-electromagnetic analysis for driving cycles, IEEE Transactions on magnetics, 47 (2011) 839-847.
[84] X. Liang, G. Li, J. Ojeda, M. Gabsi, Z. Ren, Comparative study of classical and mutually coupled switched reluctance motors using multiphysics finite-element modeling, IEEE Transactions on Industrial Electronics, 61 (2014) 5066-5074.
[85] L. Guangjin, J. Ojeda, S. Hlioui, E. Hoang, M. Lecrivain, M. Gabsi, Modification in Rotor Pole Geometry of Mutually Coupled Switched Reluctance Machine for Torque Ripple Mitigating, Magnetics, IEEE Transactions on, 48 (2012) 2025-2034.
[86] L. Yue, T. Yifan, Switched reluctance motor drives with fractionally-pitched winding design, in: PESC97. Record 28th Annual IEEE Power Electronics Specialists Conference. Formerly Power Conditioning Specialists Conference 1970-71. Power Processing and Electronic Specialists Conference 1972, 1997, pp. 875-880 vol.872.
[87] B.C. Mecrow, New winding configurations for doubly salient reluctance machines, Industry Applications, IEEE Transactions on, 32 (1996) 1348-1356.

[88] X.Y. Ma, G.J. Li, G.W. Jewell, Z.Q. Zhu, H.L. Zhan, Performance Comparison of Doubly Salient Reluctance Machine Topologies Supplied by Sinewave Currents, IEEE Transactions on Industrial Electronics, 63 (2016) 4086-4096.
[89] M.A. Kabir, I. Husain, Mutually coupled switched reluctance machine (MCSRM) for electric and hybrid vehicles, in: PES General Meeting| Conference & Exposition, 2014 IEEE, IEEE, 2014, pp. 1-5.
[90] B.C. Mecrow, Fully pitched-winding switched-reluctance and stepping-motor arrangements, Electric Power Applications, IEE Proceedings B, 140 (1993) 61-70.
[91] J. Malan, M.J. Kamper, Performance of hybrid electric vehicle using reluctance synchronous machine technology, in: Industry Applications Conference, 2000. Conference Record of the 2000 IEEE, 2000, pp. 1881-1887 vol.1883.
[92] M. Morandin, E. Fornasiero, N. Bianchi, S. Bolognani, A robust integrated starter/alternator drive adopting a synchronous reluctance machine for automotive applications, in: Transportation Electrification Conference and Expo (ITEC), 2014 IEEE, 2014, pp. 1-6.
[93] J.K. Kostko, Polyphase reaction synchronous motors, American Institute of Electrical Engineers, Journal of the, 42 (1923) 1162-1168.
[94] A. Vagati, The synchronous reluctance solution: a new alternative in AC drives, in: Industrial Electronics, Control and Instrumentation, 1994. IECON '94., 20th International Conference on, 1994, pp. 1-13 vol.11.
[95] W.L. Soong, T.J.E. Miller, Field-weakening performance of brushless synchronous AC motor drives, IEE Proceedings - Electric Power Applications, 141 (1994) 331-340.
[96] L. Xu, X. Xu, T.A. Lipo, D.W. Novotny, Vector control of a synchronous reluctance motor including saturation and iron loss, IEEE Transactions on Industry Applications, 27 (1991) 977-985.
[97] T. Matsuo, T.A. Lipo, Field oriented control of synchronous reluctance machine, in: Power Electronics Specialists Conference, 1993. PESC '93 Record., 24th Annual IEEE, 1993, pp. 425-431.
[98] H.F. Hofmann, S.R. Sanders, A. El-Antably, Stator-flux-oriented vector control of synchronous reluctance Machines with maximized efficiency, Industrial Electronics, IEEE Transactions on, 51 (2004) 1066-1072.
[99] D. Platt, Reluctance motor with strong rotor anisotropy, IEEE transactions on industry applications, 28 (1992) 652-658.
[100] A. Vagati, M. Pastorelli, G. Franceschini, C. Petrache, Design of low-torque-ripple synchronous reluctance motors, in: Industry Applications Conference, 1997. Thirty-Second IAS Annual Meeting, IAS '97., Conference Record of the 1997 IEEE, 1997, pp. 286-293 vol.281.
[101] C. Oprea, A. Dziechciarz, C. Martis, Comparative analysis of different synchronous reluctance motor topologies, in: Environment and Electrical Engineering (EEEIC), 2015 IEEE 15th International Conference on, 2015, pp. 1904-1909.
[102] N. Balbo, R. D'Andrea, L. Malesani, P. Tomasin, Synchronous reluctance motors for low-cost, medium performance drives, in: Power Electronics and Applications, 1993., Fifth European Conference on, IET, 1993, pp. 77-81.
[103] H. Kiriyama, S. Kawano, Y. Honda, T. Higaki, S. Morimoto, Y. Takeda, High performance synchronous reluctance motor with multi-flux barrier for the appliance industry, in: Industry Applications Conference, 1998. Thirty-Third IAS Annual Meeting. The 1998 IEEE, IEEE, 1998, pp. 111-117.

[104] D.A. Staton, W.L. Soong, T.J. Miller, Unified theory of torque production in switched reluctance and synchronous reluctance motors, IEEE Transactions on Industry Applications, 31 (1995) 329-337.
[105] A. Vagati, A. Fratta, G. Franceschini, P. Rosso, AC motors for high-performance drives: a design-based comparison, IEEE Transactions on Industry Applications, 32 (1996) 1211-1219.
[106] G. Pellegrino, E. Armando, P. Guglielmi, A. Vagati, A 250kW transverse-laminated Synchronous Reluctance motor, in: Power Electronics and Applications, 2009. EPE '09. 13th European Conference on, 2009, pp. 1-10.
[107] C. Rossi, D. Casadei, A. Pilati, M. Marano, Wound rotor salient pole synchronous machine drive for electric traction, in: Industry Applications Conference, 2006. 41st IAS Annual Meeting. Conference Record of the 2006 IEEE, IEEE, 2006, pp. 1235-1241.
[108] D.G. Dorrell, Are wound-rotor synchronous motors suitable for use in high efficiency torque-dense automotive drives?, in: IECON 2012 - 38th Annual Conference on IEEE Industrial Electronics Society, 2012, pp. 4880-4885.
[109] G. Friedrich, A. Girardin, INTEGRATED STARTER GENERATOR Design, principle, constraints, and optimal control, Ieee Industry Applications Magazine, 15 (2009) 26-34.
[110] F.W. Klatt, Qualitative analysis: Brushless Wound-rotor [Synchronous] Doubly-Fed Electric Machine for electric propulsion, in: 2013 IEEE Transportation Electrification Conference and Expo (ITEC), 2013, pp. 1-8.
[111] G.-H. Lee, H.-H. Lee, Q. Wang, Development of Wound Rotor Synchronous Motor for Belt-Driven e-Assist System, 2013.
[112] A. Vignaud, H. Fennel, H. Hakvoort, W. Hackmann, Efficient Electric Powertrain with Externally Excited Synchronous Machine without Rare Earth Magnets using the Example of the Renault System Solution, in: Vienna Motor Symposium, 2012.
[113] R.D. Hall, R.P. Roberge, Carbon brush performance on slip rings, in: Pulp and Paper Industry Technical Conference (PPIC), Conference Record of 2010 Annual, IEEE, 2010, pp. 1-6.
[114] A.K. Jain, V. Ranganathan, Modeling and field oriented control of salient pole wound field synchronous machine in stator flux coordinates, IEEE Transactions on Industrial Electronics, 58 (2011) 960-970.
[115] Y. Kim, K. Nam, Copper-Loss-Minimizing Field Current Control Scheme for Wound Synchronous Machines, IEEE Transactions on Power Electronics, 32 (2017) 1335-1345.
[116] P.G. Friedrich, Modelling of a wound rotor salient pole synchronous machine and its converter in the constant power zone.
[117] D. Uzel, V. Šmídl, Z. Peroutka, Gradient descent maximum torque control up to the base speed of wound rotor synchronous motors, in: Mechatronics-Mechatronika (ME), 2016 17th International Conference on, IEEE, 2016, pp. 1-6.
[118] M. Mabhula, M.J. Kamper, Saliency and mutual inductance effect in cylindrical wound-rotor synchronous motor, in: 2017 IEEE Workshop on Electrical Machines Design, Control and Diagnosis (WEMDCD), 2017, pp. 152-157.
[119] A. Rambetius, S. Luthardt, B. Piepenbreier, Modeling of wound rotor synchronous machines considering harmonics, geometric saliencies and saturation induced saliencies, in: Power Electronics Conference (IPEC-Hiroshima 2014-ECCE-ASIA), 2014 International, IEEE, 2014, pp. 3029-3036.
[120] C.D. Nguyen, W. Hofmann, Self-tuning adaptive copper-losses minimization control of externally

excited synchronous motors, in: Electrical Machines (ICEM), 2014 International Conference on, IEEE, 2014, pp. 897-902.
[121] R. Mbayed, G. Salloum, L. Vido, E. Monmasson, M. Gabsi, Hybrid excitation synchronous motor control in electric vehicle with copper and iron losses minimization, in: IECON 2012-38th Annual Conference on IEEE Industrial Electronics Society, IEEE, 2012, pp. 4886-4891.
[122] R. Wang, S. Pekarek, M. Bash, Alternative excitation strategies for a wound rotor synchronous machine drive, in: Energy Conversion Congress and Exposition (ECCE), 2012 IEEE, IEEE, 2012, pp. 2300-2307.
[123] O. Haala, B. Wagner, M. Hofmann, M. März, Optimal current control of externally excited synchronous machines in automotive traction drive applications, International Journal of Electrical, Computer, Energetic, Electronic and Communication Engineering, 7 (2013) 1133-1139.
[124] H.-S. Seol, J.-M. Jeong, J. Lee, C.-S. Jin, Current control of WRSM considering magnetic saturation phenomenon, IEEE Transactions on Magnetics, 52 (2016) 1-4.
[125] I. Jeong, B.G. Gu, J. Kim, K. Nam, Y. Kim, Inductance Estimation of Electrically Excited Synchronous Motor via Polynomial Approximations by Least Square Method, Ieee Transactions on Industry Applications, 51 (2015) 1526-1537.
[126] A. Radun, Analytical calculation of the switched reluctance motor's unaligned inductance, Magnetics, IEEE Transactions on, 35 (1999) 4473-4481.
[127] A. Radun, Analytically computing the flux linked by a switched reluctance motor phase when the stator and rotor poles overlap, Magnetics, IEEE Transactions on, 36 (2000) 1996-2003.
[128] P. Vijayraghavan, Design of switched reluctance motors and development of a universal controller for switched reluctance and permanent magnet brushless DC motor drives, in, Virginia Polytechnic Institute and State University, 2001.
[129] T.A. Lipo, Synchronous reluctance machines-a viable alternative for ac drives?, Electric Machines and Power Systems, 19 (1991) 659-671.
[130] G. Bertotti, General properties of power losses in soft ferromagnetic materials, IEEE Transactions on magnetics, 24 (1988) 621-630.
[131] K. Atallah, Z. Zhu, D. Howe, An improved method for predicting iron losses in brushless permanent magnet DC drives, IEEE Transactions on magnetics, 28 (1992) 2997-2999.
[132] J. Lavers, P. Biringer, H. Hollitscher, A simple method of estimating the minor loop hysteresis loss in thin laminations, IEEE Transactions on magnetics, 14 (1978) 386-388.
[133] S.D. Calverley, G.W. Jewell, R.J. Saunders, Prediction and measurement of core losses in a high-speed switched-reluctance machine, IEEE transactions on magnetics, 41 (2005) 4288-4298.
[134] Y. Hayashi, T.J. Miller, A new approach to calculating core losses in the SRM, IEEE transactions on Industry Applications, 31 (1995) 1039-1046.
[135] T. Yifan, Switched reluctance motor with fractionally pitched windings and bipolar currents, in: Industry Applications Conference, 1998. Thirty-Third IAS Annual Meeting. The 1998 IEEE, 1998, pp. 351-358 vol.351.
[136] G. Li, X. Ma, G. Jewell, Z. Zhu, P. Xu, Influence of Conduction Angles on Single-Layer Switched Reluctance Machines, IEEE Transactions on Magnetics, 52 (2016) 1-11.
[137] J. Haataja, A comparative performance study of four-pole induction motors and synchronous reluctance motors in variable speed drives, Acta Universitatis Lappeenrantaensis, (2003).

[138] J.M. Stephenson, J. Corda, Computation of torque and current in doubly salient reluctance motors from nonlinear magnetisation data, Electrical Engineers, Proceedings of the Institution of, 126 (1979) 393-396.

[139] M. Mohr, O. Bíró, A. Stermecki, F. Diwoky, An improved physical phase variable model for permanent magnet machines, in: 2012 XXth International Conference on Electrical Machines, 2012, pp. 53-58.

[140] L. Queval, H. Ohsaki, Nonlinear abc-Model for Electrical Machines Using N-D Lookup Tables, IEEE Transactions on Energy Conversion, 30 (2015) 316-322.

[141] K. Byung-Il, W. Kyung-Il, K. Sol, Finite element analysis of direct thrust-controlled linear induction motor, IEEE Transactions on Magnetics, 35 (1999) 1306-1309.

[142] M.A. Jabbar, L. Zhejie, D. Jing, Time-stepping finite-element analysis for the dynamic performance of a permanent magnet synchronous motor, IEEE Transactions on Magnetics, 39 (2003) 2621-2623.

[143] G.H. Jang, J.H. Chang, D.P. Hong, K.S. Kim, Finite-element analysis of an electromechanical field of a BLDC motor considering speed control and mechanical flexibility, IEEE Transactions on Magnetics, 38 (2002) 945-948.

[144] F. Parasiliti, M. Villani, A. Tassi, Dynamic Analysis of Synchronous Reluctance Motor Drives Based on SimulinkÂ® and Finite Element Model, in: IECON 2006 - 32nd Annual Conference on IEEE Industrial Electronics, 2006, pp. 1516-1520.

[145] O.A. Mohammed, S. Liu, Z. Liu, Physical modeling of PM synchronous motors for integrated coupling with Machine drives, IEEE Transactions on Magnetics, 41 (2005) 1628-1631.

[146] X. Cao, A. Kurita, H. Mitsuma, Y. Tada, H. Okamoto, Improvements of numerical stability of electromagnetic transient simulation by use of phase‐domain synchronous machine models, Electrical Engineering in Japan, 128 (1999) 53-62.

[147] L. Wang, J. Jatskevich, H.W. Dommel, Re-examination of Synchronous Machine Modeling Techniques for Electromagnetic Transient Simulations, IEEE Transactions on Power Systems, 22 (2007) 1221-1230.

[148] T. Herold, D. Franck, E. Lange, K. Hameyer, Extension of a d-q model of a permanent magnet excited synchronous machine by including saturation, cross-coupling and slotting effects, in: 2011 IEEE International Electric Machines & Drives Conference (IEMDC), 2011, pp. 1363-1367.

[149] G. Stumberger, B. Stumberger, D. Dolinar, Identification of linear synchronous reluctance motor parameters, IEEE transactions on industry applications, 40 (2004) 1317-1324.

[150] M.B. Salles, J.R. Cardoso, K. Hameyer, Dynamic modeling of transverse flux permanent magnet generator for wind turbines, Journal of Microwaves, Optoelectronics and Electromagnetic Applications, 10 (2011) 95-105.

[151] F. Poltschak, W. Amrhein, A dynamic nonlinear model for permanent magnet synchronous machines, in: 2008 IEEE International Symposium on Industrial Electronics, 2008, pp. 724-729.

[152] X. Ling, B. Li, L. Gong, Y. Huang, C. Liu, Simulation of Switched Reluctance Motor Drive System Based on Multi-Physics Modeling Method, IEEE Access, 5 (2017) 26184-26189.

[153] F. Soares, P.J. Costa Branco, Simulation of a 6/4 switched reluctance motor based on Matlab/Simulink environment, Aerospace and Electronic Systems, IEEE Transactions on, 37 (2001) 989-1009.

[154] W. Soong, Sizing of electrical machines, Power Engineering Briefing Note Series, 9 (2008) 17-18.
[155] T.A. Lipo, Introduction to AC machine design, John Wiley & Sons, 2017.
[156] M.G. Say, E.N. Pink, The performance and design of alternating current machines: transformers, three-phase induction motors and synchronous machines, Pitman London, 1958.
[157] F. Fu, X. Tang, Induction machine design handbook, in, Chine Machine Press, 2002.
[158] F. Magnussen, C. Sadarangani, Winding factors and Joule losses of permanent magnet machines with concentrated windings, in: Electric Machines and Drives Conference, 2003. IEMDC'03. IEEE International, 2003, pp. 333-339 vol.331.
[159] M. Say, Performance and design of AC machines: Pitman, London, ISBN, 273 (1970) 8.
[160] V. Petrovi, A.M. Stankovic, Modeling of PM synchronous motors for control and estimation tasks, in: Decision and Control, 2001. Proceedings of the 40th IEEE Conference on, IEEE, 2001, pp. 2229-2234.
[161] F. Magnussen, H. Lendenmann, Parasitic effects in PM machines with concentrated windings, IEEE transactions on industry applications, 43 (2007) 1223-1232.
[162] S.A. Evans, Salient pole shoe shapes of interior permanent magnet synchronous machines, in: Electrical Machines (ICEM), 2010 XIX International Conference on, IEEE, 2010, pp. 1-6.
[163] Y. Li, J. Xing, T. Wang, Y. Lu, Programmable design of magnet shape for permanent-magnet synchronous motors with sinusoidal back EMF waveforms, IEEE transactions on magnetics, 44 (2008) 2163-2167.
[164] S.-M. Jang, H.-I. Park, J.-Y. Choi, K.-J. Ko, S.-H. Lee, Magnet pole shape design of permanent magnet machine for minimization of torque ripple based on electromagnetic field theory, IEEE Transactions on Magnetics, 47 (2011) 3586-3589.
[165] Z. Chen, C. Xia, Q. Geng, Y. Yan, Modeling and analyzing of surface-mounted permanent-magnet synchronous machines with optimized magnetic pole shape, IEEE Transactions on Magnetics, 50 (2014) 1-4.
[166] P. Zheng, J. Zhao, J. Han, J. Wang, Z. Yao, R. Liu, Optimization of the magnetic pole shape of a permanent-magnet synchronous motor, IEEE Transactions on Magnetics, 43 (2007) 2531-2533.
[167] I. Boldea, Synchronous Generators-The Electric Generator Handbook, 2006, in, Taylor & Francis Group, Boca Raton, New York, London, 2006.
[168] A. Frias, P. Pellerey, A.K. Lebouc, C. Chillet, V. Lanfranchi, G. Friedrich, L. Albert, L. Humbert, Rotor and stator shape optimization of a synchronous machine to reduce iron losses and acoustic noise, in: Vehicle Power and Propulsion Conference (VPPC), 2012 IEEE, IEEE, 2012, pp. 98-103.
[169] F.G. Capponi, G. Borocci, G. De Donato, F. Caricchi, Flux regulation strategies for hybrid excitation synchronous machines, Ieee Transactions on Industry Applications, 51 (2015) 3838-3847.
[170] R. Keys, Cubic convolution interpolation for digital image processing, IEEE Transactions on Acoustics, Speech, and Signal Processing, 29 (1981) 1153-1160.
[171] A. El-Refaie, Fractional-slot concentrated-windings: A paradigm shift in electrical machines, in: 2013 IEEE Workshop on Electrical Machines Design, Control and Diagnosis (WEMDCD), 2013, pp. 24-32.
[172] Typical data for SURA® M300-35A - Cogent Power, (2008).
[173] W.-H. Kim, A stress analysis method for the rotor design of an IPMSM considering radial force, Journal of Electrical Engineering and Technology, 9 (2014) 888-892.

[174] A. Schofield, R. S. Steedman, Safety Factor Analysis for Centrifuge Systems, 1991.
[175] Torlon PAI design guide (Solvay Advanced Polymers), in, 2014.
[176] W. Soong, Thermal analysis of electrical machines: Limits and heat transfer principles, Power Engineering Briefing Note Series, Lipiec, (2008) 19-10.
[177] D.E. Tsatis, Thermal diffusivity of GE‐7031 varnish, Journal of applied physics, 62 (1987) 302-302.
[178] K. Jayasuriya, A. Stewart, S. Campbell, The specific heat capacity of GE varnish (200-400K), Journal of Physics E: Scientific Instruments, 15 (1982) 885.
[179] S. Ohta, Temperature classes of electrical insulators, Three Bond Technical News, 13 (1985).
[180] K. Yamazaki, Induction motor analysis considering both harmonics and end effects using combination of 2D and 3D finite element method, IEEE Transactions on Energy Conversion, 14 (1999) 698-703.
[181] Ş. Bayraktar, Y. Turgut, Effects of different cutting methods for electrical steel sheets on performance of induction motors, Proceedings of the Institution of Mechanical Engineers, Part B: Journal of Engineering Manufacture, 232 (2018) 1287-1294.